Focusing the Field of a HIFU Array Transducer through Human Ribs

by

Pierre Nicolas Spiridon Elie Gélat

A dissertation submitted for
the degree of Doctor of Philosophy
at University College London

Department of Mechanical Engineering
University College London
Torrington Place
London WC1E 7JE

Declaration

I, Pierre Gélat, confirm that the work presented in this thesis is my own. Where information has been derived from other sources, I confirm that this has been indicated in the thesis.

Abstract

High intensity focused ultrasound (HIFU) enables highly localised, non-invasive tissue ablation, and its efficacy in the treatment of a range of cancers, including those of the kidney, prostate and breast has been demonstrated. HIFU offers the ability to treat deep-seated tumours locally, and potentially bears fewer side effects than more established treatment modalities such as resection, chemotherapy and ionising radiation. There remain, however, a number of significant challenges which currently hinder its widespread clinical application. One of these challenges is the need to transmit sufficient energy through the ribcage to ablate tissue at the required foci whilst minimising the formation of side lobes and sparing healthy tissue. Ribs both absorb and reflect ultrasound strongly. This sometimes results in overheating of bone and overlying tissue during treatment, leading to skin burns. Successful treatment of a patient with tumours in the upper abdomen therefore requires a thorough understanding of the way acoustic and thermal energy is deposited. In this thesis, an approach which predicts the acoustic field of a multi-element HIFU array scattered by human ribs, the topology of which was obtained from CT scan data, has been developed, implemented and validated. It is based on the boundary element method (BEM). Dissipative mechanisms were introduced into the propagating medium, along with a complex surface impedance condition at the surface of the ribs. A reformulation of the boundary element equations as a constrained optimisation problem was carried out to solve the inverse problem of determining the complex surface normal velocities of a multi-element HIFU array that best fitted a required acoustic pressure distribution in a least-squares sense. This was done whilst ensuring that an acoustic dose rate parameter at the surface of the ribs was kept below a specified threshold. The methodology was tested at an excitation frequency of 1 MHz on a spherical section multi-element array in the presence of human ribs. It was compared on six array-rib topologies against other methods of focusing through the ribs, including binarised apodisation based on geometric ray tracing, phase conjugation and the DORT method (*décomposition de l'opérateur de retournement temporel*). The constrained optimisation approach offers greater potential than the other focusing methods in terms of maximising the ratio of acoustic pressure magnitudes at the focus to those on the surface of the ribs whilst taking full advantage of the dynamic range of the phased array.

Table of Contents

Acknowledgements

I would like to extend my thanks and gratitude towards my supervisor Nader Saffari. Throughout the duration of this work, his support, guidance, assistance and friendship have been invaluable. I would also like to thank Susan Dowson, my line manager at the National Physical Laboratory (NPL) and Bajram Zeqiri, Knowledge Leader of the NPL Acoustics and Ionising Radiation Division, for their support and encouragement.

I am very grateful to Patrick Macey and John King from PACSYS Ltd. for supplying stand-alone executable files of the Program for Automatic Finite Element Calculations boundary element routines as well as for useful discussions. I owe much to Gail ter Haar for her support, encouragement and feedback on the thesis material and manuscript. I would like to thank Simon Woodford who was instrumental in helping me get started on the parallelisation of the boundary element routines. I would also like to thank Tristan Clark from the UCL Department of Computer Science for his extensive IT support. I am grateful to Peter Lovelock for producing the meshes used in the boundary element calculations. I would like to thank my colleague Adam Shaw for his continuing feedback on my work and for sharing his expertise in the area of HIFU metrology. I would equally like to thank Minh Hoang for his advice on inverse methods and help with NAG Numerical Library solvers and Andy Robinson for help with the Geomagic® software. I am grateful to John Platt for reviewing the material in chapter 3. I would like to extend my gratitude to Alan Green and everyone from the NPL graphics team.

I am grateful to Simon Arridge, Jean-François Aubry, John Ballard, Dean Barratt, Timo Betcke, Svetlana Bobkova, David Cosgrove, Constantin Coussios, David Cranston, Lianghao Han, Anthony Harker, Vera Khokhlova, Claire Prada, Lise Rétat, Erik-Jan Rijkhorst, Ian Rivens, David Sinden, Richard Symonds-Taylor, Mickael Tanter and Gregory Vilensky for useful discussions. I would also like to thank Neelaksh Sadhoo and Claudie Chevillon for their help with proofreading.

I would like to thank my parents, friends and work colleagues for their support. Most of all, I would like to express gratitude to my fiancée, Ulrike Wirth, for putting up with my busy schedule over the last four years and for her support throughout my endeavours.

Funding

I would like to acknowledge funding from National Measurement Systems Directorate of the UK Department of Business, Innovation and Skills and EPSRC EP/F025750/1. This work was supported in parts by the European Metrology Research Programme (Joint Research Project HLT03, which is jointly funded by the EMRP participating countries within EURAMET and the European Union) and by the Acoustics and Ionising Radiation programme of the UK National Measurement Office.

List of acronyms

BEM	boundary element modelling
BIE	boundary integral equation
CT	computed tomography
DORT	decomposition of the time reversal operator (from French: *decomposition de l'opérateur de retournement temporel*)
FDTD	finite difference time domain
FEM	finite element modelling
FFT	fast Fourier transform
GMRES	generalised minimal residual method
HIFU	high-intensity focused ultrasound
KZK	Khokhlov-Zabolotskaya-Kuznetsov
MR	magnetic resonance
PDE	partial differential equation
PML	perfectly matched layer
PZT	lead zirconate titanate
RAM	random access memory
SVD	singular value decomposition
TRO	time reversal operator

List of symbols

A	first coefficient in Taylor series expansion of the pressure as a function density
$\boldsymbol{A}$	**s**quare matrix (GMRES description)
$[A]$	matrix used in the definition of the constraints on the surface of the scatterers
A_n	coefficients in series expansions
a	radius of an element on the HIFU array
a_α	constant in ultrasonic attenuation coefficient power law
B	second coefficient in the Taylor series expansion of the pressure as a function density
$\boldsymbol{b}$	column vector (GMRES description)
b_α	exponent in ultrasonic attenuation coefficient power law
$[C]$	matrix used in the definition of the objective function
$\boldsymbol{C}_n$	matrix given by $[\boldsymbol{e}_2, \boldsymbol{e}_3, \cdots, \boldsymbol{e}_n, -\boldsymbol{c}]$ (GMRES description)
c	complex speed of sound
$\boldsymbol{c}$	negative of last column of $\boldsymbol{AK}_n$ (GMRES description)
c_0	equilibrium speed of sound
c_1	complex speed of sound in the medium of the scatterer
c_j	element of Givens rotation matrix (GMRES description)
c_p	specific heat capacities at constant pressure
c_v	specific heat capacities at constant volume
$E_m(\omega)$	Fourier transform of $e_m(t)$
$\{E^0(\omega)\}$	initial input vector in the phase conjugation process
$\{E^1(\omega)\}$	updated input vector in phase conjugation which focuses on the target
$\boldsymbol{e}_i$	unit vector along the i^{th} direction (GMRES description)
$e_m(t)$	input signal corresponding to the m^{th} element of the array
F	focal distance of the spherical-section HIFU source
$\boldsymbol{F}_j$	Givens rotation matrix (GMRES description)
f	frequency
G	Green's function
$[G]$	boundary element matrix pre-multiplying the vector of acoustic pressure normal derivatives

$\bar{G}$	static case Green's function
g	function defining the $\frac{\partial p(\vec{r})}{\partial n}$ boundary condition on *S*
$\boldsymbol{g}_n$	transformed right hand side in GMRES scheme equal to $\left(\prod_{j=n}^{1} \boldsymbol{F_j}\right)\|\boldsymbol{b}\|\boldsymbol{e_1}$ (GMRES description)
$\boldsymbol{H}$	upper Hessenberg matrix (GMRES description)
$[H]$	boundary element matrix pre-multiplying the vector of acoustic pressures
$h_n^{(2)}$	spherical Hankel function of order *n* of the second kind
$\boldsymbol{I}$	identity matrix (GMRES description)
i	unit imaginary number
i	integer variable
$i_{\max}$	number of eigenvectors associated with the higher singular values of the singular value decomposition of $[K(\omega)]$
J_e	Jacobian used in the transformation from global coordinates on a boundary element to local coordinates
J_n	Bessel function of the first kind of order *n*
j	integer variable
j_n	spherical Bessel function of order *n*
$[K(\omega)]$	HIFU array inter-element transfer matrix also known as the time reversal operator
$K_{lm}(\omega)$	Fourier transform of $k_{lm}(t)$
$\boldsymbol{K}_n$	Krylov sequence (GMRES description)
K_n	n^{th} order Krylov subspace (GMRES description)
k	acoustic wave number
$\vec{k}$	propagation vector
k_x	propagation vector component along the *x*-direction
$k_{lm}(t)$	impulse response from element *m* to element *l* of the HIFU array
k_y	propagation vector component along the *y*-direction
k_z	propagation vector component along the *z*-direction
$\mathcal{L}$	Lagrangian density
l	integer variable
$[M]$	boundary element shape function matrix
m	integer variable
n	integer variable

N	total number of elements on the HIFU array
N_p	number of patches on surface of scatterer after discretisation
$\vec{n}$	unit normal vector
$\vec{n}_q$	unit normal vector
P	thermodynamic pressure
P_n	Legendre polynomial
p	is the acoustic pressure
$\{p_{\text{ext}}\}$	vector of acoustic pressures in the exterior domain.
$p_{\text{far field}}$	far field acoustic pressure
p_i	incident acoustic pressure
$p_{\text{near field}}$	near field acoustic pressure
p_s	scattered component of acoustic pressure
$p_{\text{surf}_{\max}}$	threshold for the maximum pressure magnitude on the surface of the scatterer in the constrained optimisation
$\{p_{\text{surf}}\}$	vector of acoustic pressures on the surface of the scatterer
Q	acoustic source term
$[Q]$	matrix of weighting coefficients relating the scattered acoustic pressures on the surface of the scatterer to the field pressures
$\boldsymbol{Q}$	unitary matrix (GMRES description)
$\boldsymbol{Q}_n$	orthogonal matrix (GMRES description)
$\boldsymbol{q}_n$	n^{th} column of $\boldsymbol{Q}$ (GMRES description)
q_v	rate of energy absorption per unit mass or specific absorption rate (SAR)
R_j	variable defined so that $R_j = \sqrt{x_j'^2 + y_j'^2}$
$R_l(\omega)$	Fourier transform of $r_l(t)$
$\boldsymbol{R}_n$	upper-triangular matrix (GMRES description)
$\{R^0(\omega)\}$	resulting output vector from $\{E^0(\omega)\}$ in the phase conjugation process
$\{R^1(\omega)\}$	resulting output signal vector from $\{E^1(\omega)\}$ in the phase conjugation process
r	radius in polar coordinate axis set
$\vec{r}$	position vector
$\overrightarrow{r'}$	position vector defined by (x', y', z')
$r_l(t)$	output signal at l^{th} element of the HIFU array element resulting from the convolution of $e_m(t)$ by $k_{lm}(t)$

$\boldsymbol{r}_n$	residual at the n^{th} iteration of the GRMES scheme (GMRES description)
$\vec{r}_q$	position vector
S_0	acoustic source term
S	closed surface defining a scatterer
S_1	surface quantity invoked in the derivation of the Kirchhoff-Helmholtz equation
S_2	surface quantity invoked in the derivation of the Kirchhoff-Helmholtz equation
s	specific entropy
s'	is the entropy perturbation
s_j	element of Givens rotation matrix (GMRES description)
T	the absolute temperature
t	time
$\{U\}$	vector of HIFU array element source velocities
U_e	function involving the Green's function or its normal derivatives
$\{U_{\text{focus}}\}$	normal velocity spherical focusing vector
$U_{\max}$	normal velocity magnitude defining the upper bound of the dynamic range of each element on the HIFU array.
U_n	normal surface velocity magnitude the n^{th} element of a multi-element HIFU array
$\{U_{projected}\}$	orthogonal projection of the array element normal velocity focusing vector
$\vec{u}$	fluid particle velocity vector
u_n	inward normal component of $\vec{u}$ on S
V	volume defined by exterior domain in boundary element formulation
$[V(\omega)]$	unitary matrix arising from the singular value decomposition of $[K(\omega)]$
$[W(\omega)]$	unitary matrix arising from the singular value decomposition of $[K(\omega)]$
$\{W_i\}$	i^{th} column of $[W(\omega)]$
$\boldsymbol{X}_n$	matrix invoked in GMRES scheme equal to $\left(\prod_{j=n}^{1} \boldsymbol{F_j}\right)\boldsymbol{H}_n$ (GMRES description)
$\boldsymbol{x}$	column vector (GMRES description)
$\tilde{\boldsymbol{x}}_n$	approximate solution to $\boldsymbol{Ax} = \boldsymbol{b}$, member of the n^{th} order Krylov subspace

x	coordinate along the first axis of a Cartesian coordinate system for a three-dimensional space
x'	coordinate along the first axis of a local Cartesian coordinate system for a three-dimensional space
y	coordinate along the second axis of a Cartesian coordinate system for a three-dimensional space
$\boldsymbol{y}$	column vector invoked in GMRES scheme (GMRES description)
y'	coordinate along the second axis of a local Cartesian coordinate system for a three-dimensional space
z	coordinate along the third axis of a Cartesian coordinate system for a three-dimensional space
z'	coordinate along the third of a local Cartesian coordinate system for a three-dimensional space
z_1	is the acoustic impedance of the surface of the scatterer
α	the ultrasonic attenuation coefficient
α_0	is the absorption coefficient
α_a	is the absorption coefficient arising from relaxation mechanisms when the shear viscosity is set to zero
α_c	is the coupling coefficient in the Burton-Miller formulation
α_j	angle of rotation about the global Cartesian *y*-axis defining the location of j^{th} element on the HIFU array
β	coefficient of nonlinearity
$[\beta]$	matrix relating the acoustic pressures on the surface of the scatterer to the element source velocity vector $\{U\}$
β_j	angle of rotation of about the global Cartesian *y*-axis the defining the location of j^{th} element on the HIFU array
$[\gamma]$	matrix relating the acoustic field pressures in the exterior domain to the element source velocity vector $\{U\}$, in absence of the scatterers
ΔS_e	elemental of area arising from the discretisation of the transducer surface
δ	Dirac delta function
δ_0	diffusivity of sound
δ_{ij}	Kronecker delta
ε_n	variable invoked in the series expansion of a plane wave
η	ordinate in local coordinate system on a boundary element patch

θ	angle in polar coordinate axis set
κ	is the thermal conductivity
Λ	surface at infinity
$[\Lambda(\omega)]$	real diagonal matrix arising from the singular value decomposition of
μ	shear viscosity
μ_B	bulk or volume viscosity
ξ	abscissa in local coordinate system on a boundary element patch
ρ	mass density
ρ_0	equilibrium mass density
ρ_1	density of the medium of the scatterer
ρ'	is the density perturbation
τ	retarded time
ω	angular frequency

List of figures

Figure 4.6 Burton-Miller formulation on a perfectly spherical scatterer of 5 mm radius in a non-attenuating medium for α_c = 0.1. Incident field: unit amplitude plane wave travelling in positive x direction. Acoustic pressure magnitude on the surface of the sphere at (5, 0, 0) mm as a function of the number of GMRES iterations. Comparison with analytical solution.

Figure 4.7 Percentage difference between acoustic pressure results in figure 4.6 and the analytical solution.

Figure 4.8 Surface Helmholtz formulation for a perfectly rigid spherical scatterer of 5 mm radius in an attenuating medium with properties representative of human liver. Incident field: unit amplitude plane wave travelling in positive x direction. Acoustic pressure magnitudes along the x-axis on the side of the shadow zone. Solid lines: BEM. Dotted lines: analytical solution.

Figure 4.9 Percentage difference between acoustic pressure results in figure 4.6 and analytical solution. Comparison along x-axis on the side of the shadow zone at seven first eigenfrequencies corresponding to interior modes of sphere against analytical solution.

Figure 4.10 Surface Helmholtz formulation on a locally reacting spherical scatterer of 5 mm radius with properties representative of rib bone in an attenuating medium with properties representative of human liver. Incident field: unit amplitude plane wave travelling in positive x direction. Acoustic pressure magnitudes along the x-axis on the side of the shadow zone. Solid lines: BEM. Dotted lines: analytical solution.

Figure 4.11 Percentage difference between acoustic pressure results in figure 4.8 and analytical solution. Comparison along x-axis on the side of the shadow zone at seven first eigenfrequencies corresponding to interior modes of sphere against analytical solution.

Figure 4.12 Surface Helmholtz formulation on a locally reacting spherical scatterer of 5 mm radius with properties representative of rib bone immersed in an attenuating medium with properties representative of human liver. Incident field: 1 MHz unit

amplitude plane wave travelling in positive x direction. Acoustic pressure magnitudes along the x-axis on the side of the shadow zone.

Figure 4.13 Percentage difference between acoustic pressure results in figure 4.10 and analytical solution. Comparison along x-axis on the side of the shadow zone at 1 MHz.

Figure 4.14 Acoustic pressure magnitude on the surface of a locally reacting 5 mm radius sphere insonated by a 1 MHz plane wave travelling in the positive x direction in a dissipative medium. Element dimensions: 0.5 mm (three elements per wavelength mesh density).

Figure 4.15 Acoustic pressure magnitude on the surface of a locally reacting 5 mm radius sphere insonated by a 1 MHz plane wave travelling in the positive x direction in a dissipative medium. Element dimensions: 0.25 mm (six elements per wavelength mesh density).

Figure 4.16 Cylindrical scatterer with hemispherical end-caps used for BEM validation: height 22cm and radius 1 cm.

Figure 4.17 Burton-Miller formulation on a perfectly rigid cylindrical scatterer with hemispherical end-caps with α_c = 0.1. Cylinder height: 22 cm. Cylinder radius: 1cm. Incident field: unit amplitude 1 MHz plane wave travelling in positive z direction in a non-attenuating medium. Acoustic pressure magnitudes along the z-axis on the side of the shadow zone. The analytical solution for an infinite cylinder is shown for comparison.

Figure 4.18 Burton-Miller formulation on a perfectly rigid cylindrical scatterer with hemispherical end-caps with α_c = 0.1. Cylinder height: 22 cm. Cylinder radius: 1cm. Incident field: unit amplitude 1 MHz plane wave travelling in positive z direction in a non-attenuating medium. Acoustic pressure magnitude on the surface of the scatterer is shown.

Figure 4.19 Burton-Miller formulation on a perfectly rigid cylindrical scatterer with hemispherical end-caps with α_c = 0.1. Cylinder height: 22 cm. Cylinder radius: 1cm. Incident field: unit amplitude 1 MHz plane wave travelling in positive z direction in a non-attenuating medium. Acoustic pressure magnitude in the y-z plane.

Figure 4.20 Surface Helmholtz formulation on a perfectly rigid cylindrical scatterer with hemispherical end-caps (α_c = 0). Cylinder height: 22 cm. Cylinder radius: 1cm. Incident field: unit amplitude 1 MHz plane wave travelling in positive *z* direction in an attenuating medium. Acoustic pressure magnitudes along the *z*-axis on the side of the shadow zone. Comparison against analytical solution for an infinite cylinder.

Figure 4.21 Surface Helmholtz formulation on a perfectly rigid cylindrical scatterer with hemispherical end-caps with α_c = 0.1. Cylinder height: 22 cm. Cylinder radius: 1cm. Incident field: unit amplitude 1MHz plane wave travelling in positive *z* direction in an attenuating medium. Acoustic pressure magnitude on the surface of the scatterer is displayed.

Figure 4.22 Surface Helmholtz formulation on a perfectly rigid cylindrical scatterer with hemispherical end-caps. Cylinder height: 22 cm. Cylinder radius: 1cm. Incident field: unit amplitude 1 MHz plane wave travelling in positive *z* direction in an attenuating medium. Acoustic pressure magnitude in the *y*-*z* plane.

Figure 4.23 Surface Helmholtz formulation on a locally reacting cylindrical scatterer with hemispherical end-caps. Cylinder height: 22 cm. Cylinder radius: 1cm. Incident field: unit amplitude 1 MHz plane wave travelling in positive *z* direction in an attenuating medium. Mesh density: three elements per wavelength. Acoustic pressure magnitudes along the *z*-axis on the side of the shadow zone. Comparison against analytical solution for an infinite cylinder.

Figure 4.24 Surface Helmholtz formulation on a locally reacting cylindrical scatterer with hemispherical end-caps. Cylinder height: 22 cm. Cylinder radius: 1cm. Incident field: unit amplitude 1 MHz plane wave travelling in positive *z* direction in an attenuating medium. Mesh density: three elements per wavelength. Acoustic pressure magnitude on the surface of the scatterer.

Figure 4.25 Surface Helmholtz formulation on a locally reacting cylindrical scatterer with hemispherical end-caps. Cylinder height: 22 cm. Cylinder radius: 1cm. Incident field: unit amplitude 1 MHz plane wave travelling in positive *z* direction in an

attenuating medium. Mesh density: three elements per wavelength. Acoustic pressure magnitude in the *y*-*z* plane.

Figure 4.26 Surface Helmholtz formulation on a locally reacting cylindrical scatterer with hemispherical end-caps. Cylinder height: 22 cm. Cylinder radius: 1cm. Incident field: unit amplitude 1 MHz plane wave travelling in positive *z* direction in an attenuating medium. Mesh density: six elements per wavelength. Acoustic pressure magnitudes along the *z*-axis on the side of the shadow zone. Comparison against analytical solution.

Figure 4.27 Surface Helmholtz formulation on a locally reacting cylindrical scatterer with hemispherical end-caps. Cylinder height: 22 cm. Cylinder radius: 1cm. Incident field: unit amplitude 1 MHz plane wave travelling in positive *z* direction in an attenuating medium. Mesh density: six elements per wavelength. Acoustic pressure magnitude on the surface of the scatterer.

Figure 4.28 Surface Helmholtz formulation on a locally reacting cylindrical scatterer with hemispherical end-caps. Cylinder height: 22 cm. Cylinder radius: 1cm. Incident field: unit amplitude 1 MHz plane wave travelling in positive *z* direction in an attenuating medium. Mesh density: six elements per wavelength. Acoustic pressure magnitude in the *y*-*z* plane.

Figure 4.29 Scattered acoustic pressure magnitude in the *y*-*z* plane. Mesh density: three elements per wavelength. Surface Helmholtz formulation on a locally reacting cylindrical scatterer with hemispherical end-caps. Cylinder height: 22 cm. Cylinder radius: 1cm. Incident field: unit amplitude 1 MHz plane wave travelling in positive *z* direction in an attenuating medium.

Figure 4.30 Scattered acoustic pressure magnitude in the *y*-*z* plane. Mesh density: six elements per wavelength. Surface Helmholtz formulation on a locally reacting cylindrical scatterer with hemispherical end-caps. Cylinder height: 22 cm. Cylinder radius: 1cm. Incident field: unit amplitude 1 MHz plane wave travelling in positive *z* direction in an attenuating medium.

Figure 4.31 Near field and far field calculation of the on-axis acoustic pressure magnitude generated by a plane circular piston rigidly vibrating in an infinite baffle.

Figure 4.32 Frontal view of 256 element HIFU phased array with regular spatial arrangement of elements. 6 mm element diameter, 4 cm diameter central aperture, 16 cm array diameter, 18 cm focal length, 1 MHz frequency of operation.

Figure 4.33 Acoustic pressure magnitude in *x*-*z* plane resulting from field of 256 element 1 MHz multi-element array with regular spatial arrangement of elements. Uniform unit amplitude velocity and zero phase.

Figure 4.34 Acoustic pressure magnitude in *y*-*z* plane resulting from field of 256 element 1 MHz multi-element array with regular spatial arrangement of elements. Uniform unit amplitude velocity and zero phase.

Figure 4.35 Frontal view of 256 element HIFU random phased array configuration. 6 mm element diameter, 4 cm diameter central aperture, 16 cm array diameter, 18 cm focal length, 1 MHz frequency of operation.

Figure 4.36 Acoustic pressure magnitude in *x*-*z* plane resulting from field of 256 element 1 MHz multi-element array with pseudo-random spatial arrangement of elements. Uniform unit amplitude velocity and zero phase.

Figure 4.37 Acoustic pressure magnitude in *y*-*z* plane resulting from field of 256 element 1 MHz multi-element array with pseudo-random spatial arrangement of elements. Uniform unit amplitude velocity and zero phase.

Figure 4.38 STL representation of ribs 8-12 of the right side of an adult male attached to the spine.

Figure 4.39 Section of ribs 9-12 of the right side of an adult male.

Figure 4.40 Position of ribs with respect to HIFU array looking through the ribs towards the transducer face, in the negative *z* direction.

Figure 4.41 Position of ribs with respect to the HIFU array. Dotted lines join the centroid of each array element to the geometric focus of the array.

Figure 4.42 Incident acoustic pressure magnitude generated by the 1 MHz random phased HIFU array for spherical focusing case in the *y*-*z* plane.

Figure 4.43 Acoustic pressure magnitude on the surface of the ribs resulting from sonication by the 1 MHz random phased HIFU array for an intercostal treatment location approximately 3 cm behind the ribcage, between ribs 10 and 11 on right side. Spherical focusing case on perfectly rigid ribs in a non-attenuating medium.

Figure 4.44 Acoustic pressure magnitude on the rib surface resulting from sonication by the 1 MHz random phased HIFU array for an intercostal treatment location approximately 3 cm behind the ribcage, between ribs 10 and 11 on right side. Spherical focusing case on perfectly rigid ribs in a non-attenuating medium. Contour of ribs shown in bone colour.

Figure 4.45 Magnitude of scattered acoustic pressure in the *y*-*z* plane resulting from sonication by the 1 MHz random phased HIFU array for an intercostal treatment location approximately 3 cm deep into ribcage between ribs 10 and 11 on right side. Spherical focusing case on perfectly rigid ribs in a non-attenuating medium. Contour of ribs shown in bone colour.

Figure 4.46 Acoustic pressure magnitude on the surface of the ribs resulting from sonication by the 1 MHz random phased HIFU array for an intercostal treatment location approximately 3 cm deep into ribcage between ribs 10 and 11 on right side. Spherical focusing case on perfectly rigid ribs in an attenuating medium.

Figure 4.47 Acoustic pressure magnitude on the rib surface resulting from sonication by the 1 MHz random phased HIFU array for an intercostal treatment location approximately 3 cm behind the ribcage, between ribs 10 and 11 on right side. Spherical focusing case on perfectly rigid ribs in an attenuating medium. Contour of ribs shown in bone colour.

Figure 4.48 Magnitude of scattered acoustic pressure in the *y*-*z* plane resulting from sonication by the 1 MHz random phased HIFU array for an intercostal treatment location approximately 3 cm deep into ribcage between ribs 10 and 11 on right side. Spherical focusing case on perfectly rigid ribs in an attenuating medium. Contour of ribs shown in bone colour.

Figure 4.49 Acoustic pressure magnitude on the surface of the ribs resulting from sonication by the 1 MHz random phased HIFU array for an intercostal treatment location approximately 3 cm deep into ribcage between ribs 10 and 11 on right side. Spherical focusing case on locally reacting ribs in an attenuating medium.

Figure 4.50 Acoustic pressure magnitude on the rib surface resulting from sonication by the 1 MHz random phased HIFU array for an intercostal treatment location approximately 3 cm behind the ribcage, between ribs 10 and 11 on right side. Spherical focusing case on locally reacting ribs in an attenuating medium. Contour of ribs shown in bone colour.

Figure 4.51 Magnitude of scattered acoustic pressure in the *y*-*z* plane resulting from sonication by the 1 MHz random phased HIFU array for an intercostal treatment location approximately 3 cm deep into ribcage between ribs 10 and 11 on right side. Spherical focusing case on locally reacting ribs in an attenuating medium. Contour of ribs shown in bone colour.

Figure 4.52 Acoustic pressure magnitude on the surface of the ribs resulting from sonication by the 1 MHz random phased HIFU array for an intercostal treatment location approximately 3 cm deep into ribcage between ribs 10 and 11 on right side. Spherical focusing case on locally reacting ribs in an attenuating medium. Fine mesh (six elements per wavelength).

Figure 4.53 Acoustic pressure magnitude on the rib surface resulting from sonication by the 1 MHz random phased HIFU array for an intercostal treatment location approximately 3 cm behind the ribcage, between ribs 10 and 11 on right side. Spherical focusing case on locally reacting ribs in an attenuating medium. Contour of ribs shown in bone colour. Fine mesh (six elements per wavelength).

Figure 5.1. Frontal view of HIFU multi-element array configuration used for the reduced complexity problem. 1 cm element diameter, 60 cm array diameter, 50 cm focal length, 100 kHz frequency of operation.

Figure 5.2 Position of cylindrical scatterer with respect to focused array.

Figure 5.3. Acoustic pressure magnitude in *y-z* plane resulting from field of 100 kHz multi-element array. Uniform unit amplitude velocity and zero phase. Contour of cylinder shown in black.

Figure 5.4. Incident acoustic pressure magnitude in *y-z* plane resulting from field of 100 kHz multi-element array (no scatterer). Uniform unit amplitude velocity and zero phase.

Figure 5.5 Acoustic pressure magnitude on surface of cylinder resulting from field of 100 kHz multi-element array. Uniform unit amplitude velocity and zero phase.

Figure 5.6. Source velocity magnitudes resulting from constrained minimisation.

Figure 5.7. Source velocity phases resulting from constrained minimisation.

Figure 5.8. Acoustic pressure magnitude on surface of cylinder resulting from field of 100 kHz multi-element array. Source velocity distribution obtained from constrained minimisation.

Figure 5.9. Acoustic pressure magnitude in *y-z* plane resulting from field of 100 kHz multi-element array. Source velocity distribution obtained from constrained minimisation.

Figure 5.10 Normalised acoustic pressure magnitude in *y-z* plane resulting from field of 100 kHz multi-element array. Uniform unit amplitude velocity and zero phase (spherical focusing).

Figure 5.11 Normalised acoustic pressure magnitude in *y-z* plane resulting from field of 100 kHz multi-element array. Source velocity distribution obtained from constrained minimisation.

Figure 6.9 Source velocity magnitudes resulting from phase conjugation. Array-rib configuration 1.

Figure 6.12 Acoustic pressure magnitude in *y-z* plane resulting from field of 1 MHz multi-element array. Phase conjugation. Array-rib configuration 1.

Figure 6.13 Source velocity magnitudes resulting from DORT method. Array-rib configuration 1.

Figure 6.14 Source velocity phases resulting from DORT method. Array-rib configuration 1.

Figure 6.15 Acoustic pressure magnitude on surface of ribs resulting from field of 1 MHz multi-element array. DORT method. Array-rib configuration 1.

Figure 6.16 Acoustic pressure magnitude in *y-z* plane resulting from field of 1 MHz multi-element array. DORT method. Array-rib configuration 1.

Figure 6.17 Source velocity magnitudes resulting from constrained optimisation. Array-rib configuration 1.

Figure 6.18 Source velocity phases resulting from constrained optimisation. Array-rib configuration 1.

Figure 6.19 Acoustic pressure magnitude on surface of ribs resulting from field of 1 MHz multi-element array. Constrained optimisation.

Figure 6.20 Acoustic pressure magnitude in *y-z* plane resulting from resulting. Constrained optimisation. Array-rib configuration 1.

Figure 6.21 Position of ribs with respect to HIFU array for configuration 2.

Figure 6.22 Acoustic pressure magnitude on surface of ribs resulting from field of 1 MHz multi-element array. Spherical focusing. Array-rib configuration 2.

Figure 6.23 Acoustic pressure magnitude in *y-z* plane resulting from field of 1 MHz multi-element array. Spherical focusing. Array-rib configuration 2.

Figure 6.24 Source velocity magnitudes resulting from binarised apodisation based on ray tracing. Array-rib configuration 2.

Figure 6.25. Source velocity phases resulting from binarised apodisation based on ray tracing. Array-rib configuration 2.

Figure 6.26 Acoustic pressure magnitude on surface of ribs resulting from field of 1 MHz multi-element array. Binarised apodisation based on geometric ray tracing. Array-rib configuration 2.

Figure 6.27 Acoustic pressure magnitude in *y-z* plane resulting from field of 1 MHz multi-element array. Binarised apodisation based on geometric ray tracing. Array-rib configuration 2.

Figure 6.28 Acoustic pressure magnitude in *y-z* plane resulting from field of 1 MHz point source of unit source strength, positioned at the global origin. Array-rib configuration 2.

Figure 6.29 Source velocity magnitudes resulting from phase conjugation. Array-rib configuration 2.

Figure 6.30 Source velocity magnitudes resulting from phase conjugation. Array-rib configuration 2.

Figure 6.31 Acoustic pressure magnitude on surface of ribs resulting from field of 1 MHz multi-element array. Phase conjugation. Array-rib configuration 2.

Figure 6.32 Acoustic pressure magnitude in *y-z* plane resulting from field of 1 MHz multi-element array. Phase conjugation. Array-rib configuration 2.

Figure 6.33 Source velocity magnitudes resulting from DORT method. Array-rib configuration 2.

Figure 6.34 Source velocity phases resulting from DORT method. Array-rib configuration 2.

Figure 6.35 Acoustic pressure magnitude on surface of ribs resulting from field of 1 MHz multi-element array. DORT method. Array-rib configuration 2.

Figure 6.36 Acoustic pressure magnitude in *y*-*z* plane resulting from field of 1 MHz multi-element array. DORT method. Array-rib configuration 2.

Figure 6.37 Source velocity magnitudes resulting from constrained optimisation. Array-rib configuration 2.

Figure 6.38 Source velocity phases resulting from constrained optimisation. Array-rib configuration 2.

Figure 6.39 Acoustic pressure magnitude on surface of ribs resulting from field of 1 MHz multi-element array. Constrained optimisation. Array-rib configuration 2.

Figure 6.40 Acoustic pressure magnitude in *y*-*z* plane resulting from resulting. Constrained optimisation. Array-rib configuration 2.

Figure 6.41 Position of ribs with respect to HIFU array for configuration 3.

Figure 6.42 Acoustic pressure magnitude on surface of ribs resulting from field of 1 MHz multi-element array. Spherical focusing. Array-rib configuration 3.

Figure 6.43 Acoustic pressure magnitude in *y*-*z* plane resulting from field of 1 MHz multi-element array. Spherical focusing. Array-rib configuration 3.

Figure 6.44 Source velocity magnitudes resulting from binarised apodisation based on ray tracing. Array-rib configuration 3.

Figure 6.45. Source velocity phases resulting from binarised apodisation based on ray tracing. Array-rib configuration 3.

Figure 6.46 Acoustic pressure magnitude on surface of ribs resulting from field of 1 MHz multi-element array. Binarised apodisation based on geometric ray tracing. Array-rib configuration 3.

Figure 6.47 Acoustic pressure magnitude in *y-z* plane resulting from field of 1 MHz multi-element array. Binarised apodisation based on geometric ray tracing. Array-rib configuration 3.

Figure 6.48 Acoustic pressure magnitude in *y-z* plane resulting from field of 1 MHz point source of unit source strength, positioned at the global origin. Array-rib configuration 3.

Figure 6.49 Source velocity magnitudes resulting from phase conjugation. Array-rib configuration 3.

Figure 6.50 Source velocity magnitudes resulting from phase conjugation. Array-rib configuration 3.

Figure 6.51 Acoustic pressure magnitude on surface of ribs resulting from field of 1 MHz multi-element array. Phase conjugation. Array-rib configuration 3.

Figure 6.52 Acoustic pressure magnitude in *y-z* plane resulting from field of 1 MHz multi-element array. Phase conjugation. Array-rib configuration 3.

Figure 6.53 Source velocity magnitudes resulting from DORT method. Array-rib configuration 3.

Figure 6.54 Source velocity phases resulting from DORT method. Array-rib configuration 3.

Figure 6.55 Acoustic pressure magnitude on surface of ribs resulting from field of 1 MHz multi-element array. DORT method. Array-rib configuration 3.

Figure 6.56 Acoustic pressure magnitude in *y-z* plane resulting from field of 1 MHz multi-element array. DORT method. Array-rib configuration 3.

Figure 6.57 Source velocity magnitudes resulting from constrained optimisation. Array-rib configuration 3.

Figure 6.58 Source velocity phases resulting from constrained optimisation. Array-rib configuration 3.

Figure 6.59 Acoustic pressure magnitude on surface of ribs resulting from field of 1 MHz multi-element array. Constrained optimisation. Array-rib configuration 3.

Figure 6.60 Acoustic pressure magnitude in *y-z* plane resulting from resulting. Constrained optimisation. Array-rib configuration 3.

Figure 6.61 Position of ribs with respect to HIFU array for configuration 4.

Figure 6.62 Acoustic pressure magnitude on surface of ribs resulting from field of 1 MHz multi-element array. Spherical focusing. Array-rib configuration 4.

Figure 6.63 Acoustic pressure magnitude in *y-z* plane resulting from field of 1 MHz multi-element array. Spherical focusing. Array-rib configuration 4.

Figure 6.64 Source velocity magnitudes resulting from binarised apodisation based on ray tracing. Array-rib configuration 4.

Figure 6.65. Source velocity phases resulting from binarised apodisation based on ray tracing. Array-rib configuration 4.

Figure 6.66 Acoustic pressure magnitude on surface of ribs resulting from field of 1 MHz multi-element array. Binarised apodisation based on geometric ray tracing. Array-rib configuration 4.

Figure 6.67 Acoustic pressure magnitude in *y-z* plane resulting from field of 1 MHz multi-element array. Binarised apodisation based on geometric ray tracing. Array-rib configuration 4.

Figure 6.68 Acoustic pressure magnitude in *y-z* plane resulting from field of 1 MHz point source of unit source strength, positioned at the global origin. Array-rib configuration 4.

Figure 6.69 Source velocity magnitudes resulting from phase conjugation. Array-rib configuration 4.

Figure 6.70 Source velocity magnitudes resulting from phase conjugation. Array-rib configuration 4.

Figure 6.71 Acoustic pressure magnitude on surface of ribs resulting from field of 1 MHz multi-element array. Phase conjugation. Array-rib configuration 4.

Figure 6.72 Acoustic pressure magnitude in *y-z* plane resulting from field of 1 MHz multi-element array. Phase conjugation. Array-rib configuration 4.

Figure 6.73 Source velocity magnitudes resulting from DORT method. Array-rib configuration 4.

Figure 6.74 Source velocity phases resulting from DORT method. Array-rib configuration 4.

Figure 6.75 Acoustic pressure magnitude on surface of ribs resulting from field of 1 MHz multi-element array. DORT method. Array-rib configuration 4.

Figure 6.76 Acoustic pressure magnitude in *y-z* plane resulting from field of 1 MHz multi-element array. DORT method. Array-rib configuration 4.

Figure 6.77 Source velocity magnitudes resulting from constrained optimisation. Array-rib configuration 4.

Figure 6.78 Source velocity phases resulting from constrained optimisation. Array-rib configuration 4.

Figure 6.79 Acoustic pressure magnitude on surface of ribs resulting from field of 1 MHz multi-element array. Constrained optimisation. Array-rib configuration 4.

Figure 6.80 Acoustic pressure magnitude in *y-z* plane resulting from resulting. Constrained optimisation. Array-rib configuration 4.

Figure 6.81 Position of ribs with respect to HIFU array for configuration 5.

Figure 6.82 Acoustic pressure magnitude on surface of ribs resulting from field of 1 MHz multi-element array. Spherical focusing. Array-rib configuration 5.

Figure 6.83 Acoustic pressure magnitude in *y*-*z* plane resulting from field of 1 MHz multi-element array. Spherical focusing. Array-rib configuration 5.

Figure 6.84 Source velocity magnitudes resulting from binarised apodisation based on ray tracing. Array-rib configuration 5.

Figure 6.85. Source velocity phases resulting from binarised apodisation based on ray tracing. Array-rib configuration 5.

Figure 6.86 Acoustic pressure magnitude on surface of ribs resulting from field of 1 MHz multi-element array. Binarised apodisation based on geometric ray tracing. Array-rib configuration 5.

Figure 6.87 Acoustic pressure magnitude in *y*-*z* plane resulting from field of 1 MHz multi-element array. Binarised apodisation based on geometric ray tracing. Array-rib configuration 5.

Figure 6.88 Acoustic pressure magnitude in *y*-*z* plane resulting from field of 1 MHz point source of unit source strength, positioned at the global origin. Array-rib configuration 5.

Figure 6.89 Source velocity magnitudes resulting from phase conjugation. Array-rib configuration 5.

Figure 6.90 Source velocity magnitudes resulting from phase conjugation. Array-rib configuration 5.

Figure 6.91 Acoustic pressure magnitude on surface of ribs resulting from field of 1 MHz multi-element array. Phase conjugation. Array-rib configuration 5.

Figure 6.104 Source velocity magnitudes resulting from binarised apodisation based on ray tracing. Array-rib configuration 6.

Figure 6.105. Source velocity phases resulting from binarised apodisation based on ray tracing. Array-rib configuration 6.

Figure 6.106 Acoustic pressure magnitude on surface of ribs resulting from field of 1 MHz multi-element array. Binarised apodisation based on geometric ray tracing. Array-rib configuration 6.

Figure 6.107 Acoustic pressure magnitude in *y*-*z* plane resulting from field of 1 MHz multi-element array. Binarised apodisation based on geometric ray tracing. Array-rib configuration 6.

Figure 6.108 Acoustic pressure magnitude in *y*-*z* plane resulting from field of 1 MHz point source of unit source strength, positioned at the global origin. Array-rib configuration 6.

Figure 6.109 Source velocity magnitudes resulting from phase conjugation. Array-rib configuration 6.

Figure 6.110 Source velocity magnitudes resulting from phase conjugation. Array-rib configuration 6.

Figure 6.111 Acoustic pressure magnitude on surface of ribs resulting from field of 1 MHz multi-element array. Phase conjugation. Array-rib configuration 6.

Figure 6.112 Acoustic pressure magnitude in *y*-*z* plane resulting from field of 1 MHz multi-element array. Phase conjugation. Array-rib configuration 6.

Figure 6.113 Source velocity magnitudes resulting from DORT method. Array-rib configuration 6.

Figure 6.114 Source velocity phases resulting from DORT method. Array-rib configuration 6.

Figure 6.115 Acoustic pressure magnitude on surface of ribs resulting from field of 1 MHz multi-element array. DORT method. Array-rib configuration 6.

Figure 6.116 Acoustic pressure magnitude in *y*-*z* plane resulting from field of 1 MHz multi-element array. DORT method. Array-rib configuration 6.

Figure 6.117 Source velocity magnitudes resulting from constrained optimisation. Array-rib configuration 6.

Figure 6.118 Source velocity phases resulting from constrained optimisation. Array-rib configuration 6.

Figure 6.119 Acoustic pressure magnitude on surface of ribs resulting from field of 1 MHz multi-element array. Constrained optimisation. Array-rib configuration 6.

Figure 6.120 Acoustic pressure magnitude in *y*-*z* plane resulting from resulting. Constrained optimisation. Array-rib configuration 6.

Figure 6.121 Acoustic pressure magnitude along the *x*-axis for all focusing methods. Array-rib configuration 1.

Figure 6.122 Acoustic pressure magnitude along the *y*-axis for all focusing methods. Array-rib configuration 1.

Figure 6.122 Acoustic pressure magnitude along the *x*-axis for all focusing methods. Array-rib configuration 2.

Figure 6.123 Acoustic pressure magnitude along the *y*-axis for all focusing methods. Array-rib configuration 2.

Figure 6.124 Acoustic pressure magnitude along the *x*-axis for all focusing methods. Array-rib configuration 3.

Figure 6.125 Acoustic pressure magnitude along the *y*-axis for all focusing methods. Array-rib configuration 3.

Figure 6.126 Acoustic pressure magnitude along the *x*-axis for all focusing methods. Array-rib configuration 4.

Figure 6.127 Acoustic pressure magnitude along the *y*-axis for all focusing methods. Array-rib configuration 4.

Figure 6.128 Acoustic pressure magnitude along the *x*-axis for all focusing methods. Array-rib configuration 5.

Figure 6.129 Acoustic pressure magnitude along the *y*-axis for all focusing methods. Array-rib configuration 5.

Figure 6.130 Acoustic pressure magnitude along the *x*-axis for all focusing methods. Array-rib configuration 6.

Figure 6.131 Acoustic pressure magnitude along the *y*-axis for all focusing methods. Array-rib configuration 6.

Figures in appendices

Figure A.1 Cylindrical scatterer with hemispherical end-caps. 1 cm radius, total height 22 cm (including an additional 0.5 cm radius for the hemispherical end-caps at either end). Meshed to include at least 3 elements per wavelength at 1 MHz.

Figure B.1 Position of spherical scatterers with respect to focused array.

Figure B.2 Acoustic pressure magnitude on the surface of the spheres. Spherical focusing case.

Figure B.3 Acoustic pressure field resulting from the spherical focusing.

Figure B.4 Singular values of diagonal matrix

Figure B.5 Acoustic pressure on surface of spheres resulting from the focusing vector obtained from the first column of $[W(\omega)]$. This vector focuses on the most reflective scatterer.

Figure B.6 Acoustic pressure field resulting from the focusing vector obtained from the first column of $[W(\omega)]$. This vector focuses on the most reflective scatterer.

Figure B.7 Acoustic pressure on surface of spheres resulting from the focusing vector obtained from the second column of $[W(\omega)]$. This vector focuses on the least reflective scatterer.

Figure B.8 Acoustic pressure field resulting from the focusing vector obtained from the second column of $[W(\omega)]$. This vector focuses on the least reflective scatterer.

Figure B.9 Acoustic pressure on surface of spheres resulting from the focusing vector obtained from the third column of $[W(\omega)]$.

Figure B.10 Acoustic pressure field resulting from the focusing vector obtained from the third column of $[W(\omega)]$.

Figure B.11 Acoustic pressure on surface of spheres resulting from the focusing vector obtained from the fourth column of $[W(\omega)]$.

Figure B.12 Acoustic pressure field resulting from the focusing vector obtained from the fourth column of $[W(\omega)]$.

Figure B.13 Acoustic pressure on surface of spheres resulting from the focusing vector obtained from the fifth column of $[W(\omega)]$.

Figure B.14 Acoustic pressure field resulting from the focusing vector obtained from the fifth column of $[W(\omega)]$.

Figure B.15 Acoustic pressure on surface of spheres resulting from the focusing vector obtained from the sixth column of $[W(\omega)]$.

Figure B.16 Acoustic pressure field resulting from the focusing vector obtained from the sixth column of $[W(\omega)]$.

Figure B.17 Acoustic pressure magnitude on the surface of the spheres. DORT method.

Figure B.18 Acoustic pressure field resulting from the DORT method.

Figure B.19 Acoustic pressure field in the vicinity of the focus resulting from the spherical focusing.

Figure B.20 Acoustic pressure field in the vicinity of the focus resulting from the application of the DORT method.

List of tables

List of refereed journal papers

Reprints of the papers have been included in Appendix D.

Gélat P, ter Haar G and Saffari N 2011 Modelling of the acoustic field of a multi-element HIFU array scattered by human ribs *Phys. Med. Biol.* **56** 5553–5581.

Gélat P, ter Haar G and Saffari N 2012 Scattering of the field of a multi-element phased array by human ribs *J. Phys. Conf. Ser.* **353** Proceedings of the 10th Anglo-French Physical Acoustics Conference (AFPAC 2011) 19–21 January 2011, Fréjus, France.

Gélat P, ter Haar G and Saffari N 2012 The optimisation of acoustic fields for ablative therapies of tumours in the upper abdomen *Phys. Med. Biol.* **57** 8471–8497.

Gélat P, ter Haar G and Saffari N 2013 Towards the optimisation of acoustic fields for ablative therapies of tumours in the upper abdomen *J. Phys. Conf. Ser.* **457** Proceedings of the 11th Anglo-French Physical Acoustics Conference (AFPAC 2012) 18–20 January 2012, Brighton, UK.

Chapter 1

Introduction

1.1 Overview

The liver is a common site of occurrence for both primary and secondary tumours (Yan and Hart 2009, Vaezy *et al* 2001). Hepatocellular carcinoma, the most common form of liver cancer, is the third most common cause of cancer related death worldwide (Bridges *et al* 2011). The incidence of liver cancer is on the rise in Europe (Piorkowsky 2009) and in 2010, there were 4241 people in the UK diagnosed with liver cancer (Cancer Research UK website). High-intensity focused ultrasound (HIFU) enables highly localised, non-invasive tissue ablation and its efficacy has been demonstrated in the treatment of a range of cancers, including those of the kidney, prostate and breast. HIFU offers the ability to treat deep-seated tumours locally, and potentially bears fewer side effects than more established treatment modalities such as resection, chemotherapy and ionising radiation. In the context of treating liver tumours, there remain a number of significant challenges which currently hinder its widespread clinical application, mainly arising from the interaction of the ribs with the ultrasonic field from the HIFU transducer.

Existing theoretical descriptions of trans-costal HIFU are often inadequate, in that they do not provide a rigorous 3D treatment of how an ultrasonic field is scattered by human ribs. Furthermore, existing approaches to solving the inverse problem of focusing the field of a multi-element HIFU array through the ribcage, whilst sparing the ribs and maintaining ablative pressures at the focus, may not be optimal. There is consequently substantial scope for improving HIFU treatment planning strategies for tumours of the liver, through the use of validated theoretical models. The first aim of this work is to investigate a forward model based on the boundary element method (BEM) to predict the scattering of the acoustic field of a multi-element HIFU by human ribs, the topology of which may be obtained from MR or CT scan data. The second aim is to use this forward model to investigate the inverse problem of focusing the field of a HIFU array inside the ribcage, whilst sparing the ribs, using existing

and novel methods. In this chapter, background information on the treatment of tumours of the liver will be outlined. A brief description and history of HIFU will be provided. The challenges of trans-costal HIFU and the deficiencies of current approaches will be mentioned. The specific objectives of the work will be defined.

1.2 Background

1.2.1 Challenges of treating liver tumours

The first choice of therapy for liver cancer is either surgical resection or transplantation (Vaezy *et al* 2001, Cha *et al* 2010). The suitability of a patient for surgical resection is highly dependent on the size, location and number of tumours (Vaezy *et al* 2001, Carpizo and D'Angelica 2009). The prognosis for patients having undergone a resection remains poor, often due to the fact that other tumours may have been present during surgery, but remained undetected due to their small size (Vaezy *et al* 2001, Tomlinson *et al* 2007). Moreover, the risks associated with conventional surgical treatments render them unsuitable for the majority of patients: resection is an invasive procedure which involves the loss of large amounts of blood. Thus, the ability to ablate tumours accurately and non-invasively within the liver will have considerable clinical impact.

1.2.2 HIFU

HIFU is a medical procedure which uses high amplitude ultrasound to heat and ablate a localised region of tissue. High energy may be accurately targeted within a well-defined and predetermined volume and tissue destruction may be achieved without damaging the overlying tissue (ter Haar *et al* 1989). Early work on high-intensity focused ultrasound (HIFU) was carried out in the 1940s by Lynn *et al* (1942, 1944) in the context of neurosurgery, and involved targeting areas in the brains of cats, monkeys and dogs with ultrasound, after a section of skull bone had been removed, and observing resulting lesions. Subsequent work performed by Fry *et al* (1954) involved concentrating high-energy ultrasound into a target volume and indicated the ability to produce isolated deep-seated legions in the brain using four quartz transducers, arranged to allow their beams to overlap within the tissue target. Griffith *et al* (1967) carried out an experimental study in pigs to test the feasibility of producing arterial damage from trackless lesions in the spinal cord by

focused ultrasound, with the intention of reducing pelvic pain. Their conclusions were positive, suggesting that this could be an effective and safe surgical intervention in humans. Lizzi *et al* (1978) employed HIFU to seal tears in the retina, and for glaucoma treatment. The ability to produce high-intensity focused beams improved substantially with the introduction of piezoceramic and piezocomposite transducers. This, combined with increasingly higher resolution imaging modalities such as MR, has led to the efficacy of HIFU being demonstrated for the treatment of a range of different cancers (Crum *et al* 2010), including those of the liver (Wu *et al* 2003, Wu *et al* 2004, Illing *et al* 2005, Leslie *et al* 2012), prostate (Sanghvi *et al* 1996, Ahmed *et al* 2012), kidney (Illing *et al* 2005, Ritchie *et al* 2010) and breast (ter Haar and Coussios 2007). It is currently estimated that there have been over 47000 prostate cancer treatments and more than 50000 treatments for abdominal tumours, osteosarcoma, uterine fibroids and thyroid worldwide (ter Haar 2013 personal communication). HIFU has received FDA approval for the treatment of uterine fibroids, and its safety and efficacy continues to be established (Voogt *et al* 2012).

1.2.3 Challenges of trans-costal HIFU treatment

As a non-invasive focused therapy, HIFU offers considerable advantages over techniques such as chemotherapy and surgical resection, in terms of its low risk of harmful side effects (ter Haar *et al* 1989). Despite this, there are a number of difficulties which currently hinder its more widespread clinical application in the context of trans-costal treatment. One of these difficulties is the need to transmit sufficient energy through the ribcage to induce tissue necrosis at the required location whilst minimising the formation of side lobes. This is true not only of liver cancers, but also of renal cancers and pancreatic tumours. Rib bones both absorb and reflect ultrasound strongly. As such, a common side effect of focusing ultrasound in regions located behind the ribcage is the overheating of bone and surrounding tissue, which can lead to skin burns (Wu *et al* 2004, Li *et al* 2007).

Multi-element random spherical phased arrays are currently showing great promise in overcoming the limitations, such as side lobe formation, lack of electronic steering and lack of beam shaping capabilities of single-element transducers (Gavrilov and Hand 2000, Pernot *et al* 2003, Tanter *et al* 2007, Aubry *et al* 2008, Hand *et al* 2009). Nevertheless, the successful treatment of intra-abdominal cancers requires a thorough understanding of the way in which the ultrasonic pressure field from a HIFU array is scattered by the ribcage. This is

likely to rely on a treatment planning strategy which uses a numerical solution to ultrasonic wave propagation problems on anatomical data, the topology of which has been obtained from computed tomography (CT) or magnetic resonance (MR) scans. Hence, a model capable of predicting the pressure distribution both on the ribs and in the surrounding tissue must form an important part of treatment planning.

There have been several attempts to investigate the theoretical and experimental feasibility and efficacy of trans-costal HIFU. Due to the computational challenges involved for large domain dimensions at megahertz frequencies, many models have relied on simplified shadowing techniques (Botros *et al* 1998, Bobkova *et al* 2010, Li *et al* 2007, Yuldashev *et al* 2013). Whilst these techniques may replicate features of wave propagation during trans-costal HIFU treatments, they do not accurately address the actual scattering and diffraction mechanisms involved in complex 3D structures and are likely to be of limited use for treatment planning applications. Moreover, full wave 3D models for propagation in heterogeneous media in the presence of bone still present major computational challenges.

1.3 Aims and objectives

1.3.1 Statement of problem

HIFU offers the ability to treat deep-seated tumours locally, and potentially bears fewer side effects than more established treatment. There remain however a number of significant challenges which currently hinder its widespread clinical application. Successful HIFU treatment of intra-abdominal tumours requires transmitting sufficient energy through the ribcage to ablate tissue at the required foci, whilst also minimising the formation of side lobes and sparing healthy tissue. It was discussed in section (1.2.3) that ultrasound is both strongly absorbed and reflected by ribs, and how this sometimes results in overheating of bone and overlying tissue during treatment, leading to skin burns. Successful treatment of a patient with tumours in the upper abdomen therefore requires a thorough understanding of the way acoustic and thermal energy is deposited. In the context of trans-costal HIFU applications, full wave 3D models for propagation in heterogeneous media in the presence of bone still present major computational challenges. As such, linear models capable of accurately modelling effects of scattering by human ribs in 3D have an important role to play in an

initial evaluation of the feasibility of treatment planning, particularly where transducer field optimisation is required.

1.3.2 Objectives

The first overall aim of this work is to develop, implement and validate a forward modelling approach based on BEM to predict the acoustic field of a multi-element HIFU array scattered by human ribs, the topology of which may be obtained from MR or CT scan data. The second aim is to use this forward model to investigate approaches to solving the inverse problem of focusing the field of multi-element HIFU array whilst sparing the ribs.

The specific objectives are as follows:

- to review existing approaches to modelling ultrasonic fields in the presence of ribs
- to justify the role of BEM in modelling HIFU fields in the presence of ribs
- to provide a theoretical description of BEM applied to acoustic scattering problems
- to implement and validate the BEM code and to apply it to an acoustic scattering problem involving a multi-element HIFU source in the presence of human ribs
- to review existing methods for focusing HIFU fields through ribs and to propose a novel method based on constrained optimisation
- to compare the efficacy of different focusing methods on a range of array-rib configurations
- to define areas suitable for further development.

1.3.3 Outline

Prior work on the modelling of HIFU beams will be reviewed in Chapter 2, with emphasis placed on trans-costal simulations. The limitations of existing methods in dealing accurately with the scattering of the field of a HIFU array by human ribs will be outlined, and it will be explained why BEM is particularly suited to this application. Chapter 3 will provide a theoretical description of BEM applied to acoustic scattering problems. The model assumptions will be stated and justified. The description and implementation of the BEM code used in this thesis (supplied by PACSYS Ltd, PAFEC Program for Automatic Finite

Element Calculations website) was originally written as a separate chapter but it was decided to confine it to Appendix A. Chapter 4 will describe the validation of the BEM code against known analytical solution. This chapter will also feature a review of HIFU sources alongside a description of the multi-element transducer used in this thesis. Finally, forward BEM calculations on human ribs will be presented. Chapter 5 will feature a review of the existing focusing methods which have been used in the literature in the context of trans-costal HIFU for sparing the ribs. A novel constrained optimisation method using BEM as the forward model will be suggested and described, and an example on a reduced complexity model presented. Chapter 6 will compare the efficacy of the inverse methods described in Chapter 5 on six array-rib configurations in an aim to assess which method is most effective at sparing the ribs whilst maintaining high focal pressures. Chapter 7 will present the conclusions from this thesis work followed by a discussion of areas for future work.

1.4 Summary

The efficacy of HIFU for treating a range of cancers has been clearly demonstrated. In the case of treatment of liver tumours, HIFU shows promise in overcoming some of the limitations of established treatment modalities. However, there remain a number of difficulties which currently hinder its more widespread clinical application, which include overheating of the ribs and overlying tissue, and the formation of side lobes. It has been discussed that successful treatment of tumours of the liver and, more generally, of the upper abdomen, is likely to rely on a planning strategy which uses a numerical solution to ultrasonic wave propagation problems on anatomical data. This thesis will initially review existing studies which address this problem, and suggest an approach, based on BEM, which can overcome the limitations of these existing approaches. The first overall aim of this work is to develop, implement and validate a forward BEM model to predict the acoustic field of a multi-element HIFU array scattered by human ribs, the topology of which may be obtained from MR or CT scan data. The second aim is to use this forward model to investigate approaches to solving the inverse problem of focusing the field of multi-element HIFU array whilst sparing the ribs.

Chapter 2

Review of Numerical Methods for Modelling HIFU Fields in the Presence of Bone

2.1 Overview

Over the past fifty years, computational methods have gained widespread acceptance and made significant contributions in many fields of science and engineering, including medical ultrasound. In complex systems where physical behaviour cannot be readily underpinned by analytical solutions, numerical solutions must be sought. This is particularly true when attempting to devise treatment planning strategies based on anatomical data. Numerical solutions usually involve constructing a quantitative mathematical model of the system where the behaviour of infinitesimally small elements (or regions) is established based on the relationships between the system variables, defined by the governing differential equations. A solution to the problem is then obtained within a defined domain for specific conditions, expressed on the boundary of the domain.

In this chapter, approaches to modelling the propagation of ultrasonic waves in soft tissue in the presence of bone will be reviewed. In HIFU applications, the propagation of an ultrasonic wave in tissue is generally nonlinear. As the wave propagates forward it distorts, creating harmonics and in some cases, acoustic shocks. Initially, some of the nonlinear acoustic wave equations more widely used in HIFU will be reviewed. Whilst a rigorous theoretical treatment of attenuation in biological media remains beyond the scope of this thesis, a brief overview of the topic will be provided. In the context of trans-costal HIFU applications, it will be explained why full wave 3D models for propagation in heterogeneous media in the presence of bone still present major computational challenges. It will be argued that linear models capable of accurately modelling effects of scattering by human ribs in 3D have an important role to play in an initial evaluation of the feasibility of treatment planning. This may be particularly important in applications where transducer field optimisation is required: since several

runs of the forward propagation model may be required to solve an inverse problem, and thus, linear models may be of value.

Studies involving simulations of trans-costal and trans-skull HIFU will be reviewed and it will be explained why existing modelling methods and approaches used are inadequate for achieving the aims and objectives stated in section 1.3. It will be argued why the boundary element method (BEM) is particularly suited to attaining these objectives.

2.2 Review of acoustic equations for propagation of ultrasound in tissue

2.2.1 Constitutive equations

The dynamics of a viscous, heat-conducting fluid are described by four equations. These are (Hamilton and Blackstock 1998, p42):

- the conservation of mass or continuity equation
- the conservation of momentum equation
- the energy or entropy balance equation
- the equation of thermodynamic state.

In Eulerian coordinates, i.e. relative to fixed spatial coordinates, these equations are expressed below.

The conservation of mass equation is expressed as:

$$\frac{D\rho}{Dt} + \rho\vec{\nabla} \cdot \vec{u}=0 \tag{2.1}$$

where

- ρ is the mass density
- t denotes time
- $\vec{u}$ is the fluid particle velocity vector
- $\frac{D}{Dt} = \frac{\partial}{\partial t} + \vec{u} \cdot \vec{\nabla}$ is the material time derivative
- $\vec{\nabla}= \vec{\imath}\frac{\partial}{\partial x} + \vec{\jmath}\frac{\partial}{\partial y} + \vec{k}\frac{\partial}{\partial z}$

The conservation of momentum equation is given by:

$$\rho \frac{D\vec{u}}{Dt} + \vec{\nabla} P = \mu \nabla^2 \vec{u} + \left(\mu_B + \frac{1}{3}\mu\right) \vec{\nabla}\left(\vec{\nabla} \cdot \vec{u}\right) \tag{2.2}$$

where

- P is the thermodynamic pressure
- μ is the shear viscosity
- μ_B is the bulk or volume viscosity.

The shear viscosity accounts for momentum diffusion between adjacent fluid particles of differing velocity. The bulk viscosity describes losses arising from changes in volume in the fluid. At low frequencies, the bulk viscosity provides an approximate description of non-equilibrium deviations between the actual local pressure and P (Hamilton and Blackstock 1998, p43). A more general form of the conservation of momentum equation would involve acknowledging that non-equilibrium deviations involve relaxation. This is discussed further in section 2.2.6. If we assume that relaxation times are much shorter than the timescale of the acoustic disturbance, the entropy equation is given by:

$$\rho \frac{Ds}{Dt} = \kappa \nabla^2 T + \mu_B \left(\vec{\nabla} \cdot \vec{u}\right)^2 + \frac{1}{2}\mu \left(\frac{\partial u_i}{\partial x_j} + \frac{\partial u_j}{\partial x_i} - \frac{2}{3}\delta_{ij}\frac{\partial u_k}{\partial x_k}\right)^2 \tag{2.3}$$

where

- s is the specific entropy
- T is the absolute temperature
- κ is the thermal conductivity.

Cartesian tensor notation (Brillouin 1964, p36) was used to express the final term in equation (2.3), where u_i denotes the particle velocity vector component along direction x_i and δ_{ij} is the Kronecker delta. $\delta_{ij} = 1$ for $i = j$ and $\delta_{ij} = 0$ for $i \neq j$.

The equation of state is written as:

$$P = P(\rho, s) \tag{2.4}$$

In this chapter, we are concerned with nonlinearities up to, and including, second order terms. The order is defined in terms of the acoustic Mach number which, in turn, is defined as the ratio of the peak particle velocity to the equilibrium speed of sound. If it is assumed that the entropy perturbations generated as a by-product of the sound field are of second order, a second order expansion of the equation of state in the form of a Taylor series about the equilibrium state (ρ_0, s_0) yields:

$$p = c_0^2\rho' + \frac{c_0^2}{\rho_0}\frac{B}{2A}\rho'^2 + \left(\frac{\partial P}{\partial s}\right)_{\rho,0} s' \tag{2.5}$$

where

- p is the acoustic pressure
- c_0 is the equilibrium speed of sound
- ρ' is the density perturbation
- s' is the entropy pertubation
- $\frac{B}{A} = \left(\frac{\rho_0}{c_0^2}\right)\left(\frac{\partial^2 P}{\partial \rho^2}\right)_{s,0}$ is the nonlinear parameter.

2.2.2 The Westervelt equation

By discarding terms of third order and higher in equations (2.1), (2.2), (2.3) and (2.4), and by neglecting the Lagrangian density term $\mathcal{L}$ (Westervelt 1963, Aanonsen *et* al 1984, Hamilton and Blackstock 1998, p55),

$$\mathcal{L} = \frac{\rho_0 u^2}{2} - \frac{p^2}{2\rho_0 c_0^2} \tag{2.6}$$

a second order wave equation known as the Westervelt equation (2.7) may be derived.

$$\nabla^2 p - \frac{1}{c_0^2}\frac{\partial^2 p}{\partial t^2} + \frac{\delta_0}{c_0^4}\frac{\partial^3 p}{\partial t^3} = -\frac{\beta}{\rho_0 c_0^4}\frac{\partial^2 p^2}{\partial t^2} \tag{2.7}$$

where

- δ_0 is the diffusivity of sound
- $\beta = 1 + B/2A$ is the coefficient of nonlinearity.

The diffusivity of sound is given by:

$$\delta_0 = \frac{1}{\rho_0}\left(\frac{4}{3}\mu + \mu_B\right) + \frac{\kappa}{\rho_0}\left(\frac{1}{c_v} - \frac{1}{c_p}\right) \tag{2.8}$$

where c_v and c_p are the specific heat capacities at constant volume and constant pressure, respectively. To second order, for a progressive plane, spherical or cylindrical wave, $\mathcal{L} = 0$. The extent to which the Lagrangian density term may be neglected in the case of a general beam depends on whether cumulative nonlinear effects dominate local nonlinear effects (Aanonsen *et* al 1984).

2.2.3 The Khokhlov-Zabolotskaya-Kuznetsov (KZK) equation

In cases where the acoustic waves propagate primarily in a single direction, it is common to make the parabolic approximation on the diffraction operator (Kuznetsov 1971). This approximation is justified as follows: if the positive z-axis denotes the nominal axis of the sound beam and a is the source radius, it is assumed that $ka \gg 1$, where k is the acoustic wave number. This implies that the beam is reasonably directional and located in the vicinity of the z-axis. In a retarded frame of reference, the wave profile is perceived to vary more slowly spatially in the direction of the beam than in directions transverse to the beam. This is described in more detail by Hamilton and Blackstock (1998, p60). The KZK equation is expressed as follows (Zabolotskaya and Khokhlov 1969, Kuznetsov 1971):

$$\frac{\partial^2 p}{\partial z \partial \tau} - \frac{c_0}{2}\left(\frac{\partial^2 p}{\partial x^2} + \frac{\partial^2 p}{\partial y^2}\right) - \frac{\delta_0}{2c_0^3}\frac{\partial^3 p}{\partial \tau^3} = \frac{\beta}{2\rho_0 c_0^3}\frac{\partial^2 p^2}{\partial \tau^2} \tag{2.9}$$

where $\tau = t - \frac{z}{c_0}$ is the retarded time.

The KZK equation is perhaps the most commonly used equation for modelling HIFU fields, owing mainly to the ease with which it can be implemented compared with full wave equations. Many efficient algorithms exist which solve the KZK equation both in the frequency domain and in the time domain (Aanonsen *et al* 1984, Lee and Hamilton 1995). More recently, Hajihasani *et al* (2009) developed a generalised time domain numerical algorithm to solve the diffraction term of the KZK equation, allowing for a

3D solution. However, as the KZK equation assumes that field variations transverse to the direction of propagation are slow compared to axial variations, the parabolic approximation limits the equation's validity to about 15° from the axis of propagation (Tappert 1977, p224). Additionally, the KZK equation is a one-way wave equation and thus does not model reflections, scattering, and heterogeneities. Furthermore, many HIFU transducers have an aperture diameter of similar dimension to their focal length. Analysis of such transducers may also be limited when using the parabolic approximation, and their fields are better described by the Westervelt equation (Yuldashev and Khokhlova 2011).

2.2.4 Mechanisms of attenuation in soft tissue

Attenuation mechanisms in pure water are primarily viscous in nature, and result in a pressure amplitude attenuation coefficient of plane waves proportional to the frequency squared for frequencies between 3 MHz and 70 MHz (Duck 1990, p99). Experimental observation indicates that α, the ultrasonic attenuation coefficient in tissue, has a power law dependence on frequency of form (Duck 1990, p101):

$$\alpha = a_\alpha f^{b_\alpha} \tag{2.10}$$

where a_α and b_α are constants determined experimentally. The power law exponent b_α is typically between 1 and 1.5 (Szabo 2004, p4–6). Attenuation of ultrasonic waves in tissue results from two mechanisms: acoustic scattering due to inhomogeneities in the medium, and acoustic absorption. Attenuation in tissue is known to be dominated by absorption. In the low megahertz frequency range, the scatter component of attenuation in soft tissue accounts for about 10% to 15% of the total attenuation (Duck 1990, p121). The losses in tissue due to absorption are known to be dominated by relaxation mechanisms (Markham *et al* 1951, Nachman *et al* 1990, Duck 1990, p100). Relaxation refers to the time required for a medium to establish equilibrium in a new thermodynamic state produced by a change in one or more of the state variables (Landau and Lifshitz 2011, p308). The physical description of ultrasound attenuation in soft tissue is not straightforward and there is no universal theoretical explanation of observed relaxation processes, although the equations derived using different approaches are of similar form once linearised (Nachman *et al* 1990). An augmented form of the one-dimensional nonlinear wave equation (Burgers' equation) was derived

by Pierce (1989, p591) to include an arbitrary number of relaxation mechanisms. For linear acoustic propagation in inhomogeneous media, Nachman *et al* (1990) proposed an equation suitable for accounting for relaxation losses in tissue. A formulation accounting for an arbitrary number of relaxation losses was implemented in a nonlinear full wave model by Pinton *et al* (2011), based on a seismic wave field model (Emmerich and Korn 1987).

Involving the sum of the relaxation absorption terms to account for effects of attenuation in tissue can be both memory-intensive and expensive from a computational time point of view. An approach which involves a spatially varying fractional derivative can be a more computationally efficient approach to modelling attenuation in lossy media which follows an arbitrary power law. Such an approach was proposed by Chen and Holm (2004). This approach was later refined to include an extended operator which accounted for power law absorption as required by the Kramers-Kronig relations (Treeby *et al* 2012). The Kramers-Kronig relations, which link attenuation and dispersion (i.e. the dependence of the phase velocity in the medium with frequency), ensure that causality of the system is satisfied (O'Donnel *et al* 1981).

2.2.5 Linear acoustic wave equation in heterogeneous absorbing media

The wave equations considered thus far for the modelling of ultrasound propagation in tissue have included effects of nonlinearity to second order. Whilst the propagation of ultrasonic waves in tissue in applications such as HIFU is indeed nonlinear, there is some justification for considering linear approaches to modelling. It has been shown that correcting for aberrations introduced by the presence of bone need not require nonlinear propagation models and that linear approaches generally suffice (Pinton *et al* 2011). Furthermore, nonlinear behaviour in HIFU applications is likely to be mainly confined to the central focal lobe (Yuldashev and Khokhlova 2011). Hence, although a more rigorous treatment of the focal region may be required, useful information can be obtained from linear models when investigating HIFU fields. Moreover, for problems which may be computationally challenging to solve when accounting for nonlinearities, linear propagation models can act as an initial guess and provide a benchmark against which more sophisticated models may be compared. This is particularly true of field optimisation problems.

Differing biological tissues will have properties which may be dissimilar in terms of their density, speed of sound and attenuation. For example, there is a large difference in the properties of soft tissue such as liver, and hard tissue such as ribs (Duck 1990, p103–110). Being able to account for such heterogeneities in ultrasound simulations in humans is of importance in applications such as trans-skull HIFU and trans-costal HIFU. The linear wave equation in heterogeneous absorbing media may be used for this (Aubry *et al* 2003):

$$\left(1+\alpha_0(\vec{r})\frac{\partial}{\partial t}\right)\left[\rho_0(\vec{r})\vec{\nabla}\cdot\left(\frac{1}{\rho_0(\vec{r})}p(\vec{r},t)\right)\right]-\frac{1}{c_0(\vec{r})^2}\frac{\partial^2 p(\vec{r},t)}{\partial t^2}=S_0(\vec{r},t) \qquad (2.11)$$

where

- α_0 is the absorption
- S_0 is an acoustic source term
- $\vec{r}$ is the position vector.

2.3 Ultrasonic propagation modelling in biological media in the presence of bone

2.3.1 Approaches based on nonlinear acoustic modelling

Li *et al* (2007) describe a theoretical and experimental study to assess the effect of ribs on the field of a HIFU transducer 36 mm diameter focal length 143 mm 1.13 MHz. The ribs were modelled as idealised cuboid objects and were assumed to be perfect absorbers. An alternating direction implicit backward finite difference scheme (Lapidus and Pinder 1989) was used to solve the KZK equation in the frequency domain in 3D. Porcine ribs were used experimentally. Good agreement was obtained between theory and experiment for the first and second harmonics in the focal plane.

Yuldashev *et al* (2013) carried out a theoretical study on the effects of nonlinear propagation associated with the field of a HIFU source in the presence of idealised perfectly absorbing ribs, consisting of parallel strips. A 1 MHz phased array consisting of 254 elements was used. A 3D implementation of the Westervelt equation (Westervelt 1963) on a parallel computing platform was used. This was implemented using an operator splitting approach described by Yuldashev and Khokhlova (2011). Simulations

in water and in water backed by soft tissue were carried out in the presence of the idealised ribs.

The methods of modelling the trans-costal HIFU process proposed by Li *et al* (2007) and Yuldashev *et al* (2013) account for effects of nonlinearities and frequency-dependent absorption. Inclusion of the full Laplacian operator by Yuldashev *et al* (2013) in the form of the Westervelt equation described in section (2.2.5) allows for more accurate modelling of the field of highly focused sources. There are nevertheless some simplifications in these formulations regarding the modelling of the ribs. The first simplification is that the ribs are considered to be perfect absorbers. In reality, whilst it is true that ribs possess an attenuation coefficient higher than that of soft tissue and water (Mast *et al* 1999, Aubry *et al* 2008 and El-Brawany *et al* 2009), the velocity of propagation of longitudinal waves in, and the density of, rib bone are respectively 4080 m s^{-1} and 1912 kg m^{-3} (Wein *et al* 2008). For water and soft tissue, these properties are approximately 1500 m s^{-1} and 1000 kg m^{-3}. It may easily be shown (Kinsler *et al* 1982, p126) that the resulting pressure reflection coefficient at the interface between a semi-infinite medium of soft tissue and a semi-infinite medium of rib bone is of the order of 0.7. This indicates that, for a simple interface and in the case of normal incidence, most of the acoustic energy is in fact reflected rather than absorbed. In the context of accurately evaluating the acoustic pressure on the surface of ribs for quantification of the rate of energy absorption per unit volume, it is clear that assuming the ribs to be either perfect reflectors or perfect absorbers is likely to lead to large uncertainties. The implementation of a boundary condition on the surface of the ribs may be desirable and is precluded by these approaches. The second simplification in the studies by Li *et al* (2007) and Yuldashev *et al* (2013) is related to the idealisation of the shape of the ribs. These were assumed to be parallel thin strips or cuboid objects. Simulations on such simplified shapes may reveal features of the effects of scattering which occur when a HIFU source is insonating human ribs. However, as human ribs are intricate 3D objects, it is likely that simulations on parallel strips are of limited use for treatment planning applications. One of the goals of this thesis involves a rigorous treatment of the ribs and of how these scatter the incident field of a HIFU source. Whilst investigating idealised ribs is certainly of interest, it is a prerequisite to achieving this goal to use a method which allows for anatomical data obtained from MR or CT scans to be imported into the forward model of acoustic propagation.

Pinton *et al* (2011) implemented a 3D finite difference time domain (FDTD) model of the full wave equation on a distributed computing platform to study the effects of nonlinear ultrasound propagation on HIFU exposures inside a dessicated human skull placed in a water tank. Anatomical data from CT scans was used. The wave equation used enabled the effects of nonlinearity, attenuation, multiple scattering, reflection and refraction to be accounted for. A 20-cycle Gaussian pulse with a fundamental frequency of 1 MHz was used in this study. Numerical results were compared against experiment, demonstrating good agreement up to the third harmonic.

Whilst full wave 3D FDTD techniques could, in principle, be used to model ultrasound propagation in the context of trans-rib HIFU propagation, this would result in large domain sizes, which may be challenging from a computational point of view. This and other limitations of FDTD will be discussed further in section 2.4. These may be partially overcome through the use of more computationally efficient approaches, such as *k*-space pseudospectral methods (Tabei *et al* 2002). In pseudospectral methods, the calculation of the partial derivatives in the governing equation for ultrasound propagation is carried out using Fourier collocation methods, which involve computing the derivatives of the interpolating polynomial basis functions using a fast Fourier transform. This significantly relaxes the requirement on the density of the computational grid compared to FDTD methods. The *k*-space pseudospectral method is discussed in more detail by Tabei *et al* (2002). It has been applied to model the nonlinear propagation of ultrasonic waves in 3D in heterogeneous media using a modified Westervelt equation with power law absorption (Treeby *et al* 2012). Whilst the *k*–space pseudospectral method can deal somewhat with weak inhomogeneities in the propagating medium, it becomes increasingly inaccurate when dealing with large local spatial variations in the speed of sound, such as at a soft tissue/bone interface (Treeby *et al* 2012).

2.3.2 Approaches based on linear acoustic modelling

FDTD methods have been successfully applied to modelling a range of linear HIFU problems in the context of treatment planning based on simulations on anatomical data involving soft tissue and bone. FDTD methods are attractive in that they can readily be applied to any set of differential equations by approximating the differential operators with simpler localised algebraic expressions at given nodal locations of the domain.

Mast *et al* (1999) produced FDTD simulations which modelled the propagation of pulsed waves through the ribcage. Using cross-sections obtained from cadaver scanned anatomical data, ultrasonic propagation of longitudinal waves through fat, muscle, connective tissue, cartilage and bone was simulated in 2D.

Aubry *et al* (2003) carried out an experimental demonstration of non-invasive trans-cranial adaptive focusing based on data from prior CT scans. The linear wave equation for propagation of acoustic waves in heterogeneous media (see equation 2.11) was solved in three dimensions in a cuboid volume of dimensions 70 mm × 10 mm × 30 mm. Simulations were carried out using an in-house FDTD solver at a fundamental frequency of 1.5 MHz. On the computing platform used at the time, simulations took approximately 20 hours to complete.

Further work on the simulation of trans-skull ultrasound has been carried out by Deffieux and Konofagou (2010). This was carried out in view of studying the effects of different transducer parameters on targeting areas of the brain relevant to Parkinson's and Alzheimer's disease, for the opening the blood-brain-barrier for targeted drug delivery. CyberLogic Wave3000, (CyberLogic website) a commercially available full wave visco-elastic FDTD solver, was used to perform simulations on anatomical data from human and primate skulls, obtained from CT scans. Wave3000 produces a solution to the 3D linear visco-elastic wave equation in heterogeneous media (Kauffman *et al* 2008). Whilst the software features the ability to model shear wave propagation in both solids and liquids, Deffieux and Konofagou (2010) only considered the propagation of longitudinal waves, as mode conversion from compressional to shear waves inside the skull is not deemed significant at an incidence angle less than 20° (White *et al* 2006). Pulsed excitation from a single-element HIFU transducer was used, with a fundamental frequency ranging from 100 kHz to 1 MHz. The authors concluded that treatment planning using an experimentally validated numerical model offers a means of evaluating trans-cranial focusing to induce opening of the blood-brain barrier through human and primate skulls, at the centre of the targeted brain region.

Aubry *et al* (2008) produced two-dimensional FDTD simulations on cross-sections of human ribs immersed in water, the topology of which was obtained from CT scans. The bone was modelled as an isotropic solid. These simulations were carried out in an effort to improve the understanding of the way in which the acoustic beam from a multi-

element HIFU phased array is affected by the ribs. Three periods of a 1 MHz fundamental frequency pulse were used.

2.4 Limitations of existing approaches to ultrasonic propagation modelling in biological media in the presence of bone

As discussed in section 2.3.1 modelling approaches based on one-way wave propagation which involve the KZK or the Westervelt equation are of limited use for rigorously investigating the way in which human ribs scatter the field of a HIFU transducer. Whilst full wave approaches based on FDTD methods have the advantage of being relatively straightforward to realise for purely acoustic problems, and can be generalised to three dimensions and easily be implemented using cluster computing, they possess a number of disadvantages when applied to trans-costal HIFU simulations.

FDTD simulations require the entire computational domain to be discretised, and the grid spatial discretisation must be sufficiently fine to resolve both the shortest acoustic wavelength and the smallest geometrical feature in the model. For 3D trans-costal applications, this results in large computational domains, which in turn leads to long solution times. For example, the guidelines in the Wave3000 manual (CyberLogic website) imply that approximately 100 GB of RAM would be required to solve a 1 MHz FDTD problem in a 20 cm^3 volume of water. It will be seen in Chapter 4 that a spatial domain size of that order is required for trans-costal HIFU simulations. A computing platform with such RAM specifications was not available in the context of this work. Additionally, FDTD methods will require the computational domain to be truncated, generally using a perfectly acoustically matched layer (PML) or an absorbing boundary condition. A PML is an absorbing layer that encloses the computational domain. It is governed by a nonphysical set of equations that cause anisotropic absorption (Berenger 1994, Berenger 1996, Yuan *et al* 1997). Whilst perfectly matched layers are reflectionless for the exact wave equation, numerical reflections are often present once the equations have been discretised.

HIFU simulations employing FDTD techniques have relied on pulsed wave excitations. For example, Aubry *et al* (2008) employed three periods at a central frequency of 1 MHz. Nevertheless, HIFU exposure times are generally of the order of several seconds for a single thermal ablation (Wang *et al* 2009). This effectively results in quasi-

continuous wave conditions. At megahertz frequencies, impractical computational times may ensue when using FDTD methods to simulate quasi-continuous wave conditions. Another option is to use a pulse which contains the frequency of interest and to let the solution time extend so that effects of multiple scattering eventually decay due to dissipative mechanisms. The resulting response at the required frequency may then be obtained using a Fourier transform. This may however necessitate long solution times for media such as water, where effects of attenuation are small compared with tissue.

As of result of truncation errors in the finite difference approximations, there is an impact on the accuracy of the numerical solution. This leads to effects of numerical dispersion as the waves propagate through the computational grid (Chung 2002, p88). A choice of 10 to 20 grid points per acoustic wavelength at the maximum frequency of interest is often used to minimise such effects (Treeby *et al* 2012). This is nevertheless dependent on the size of the computational domain, together with the order of the finite difference scheme.

Finally, since FDTD methods are generally implemented on a domain approximated using a Cartesian grid, boundaries of complex shape become difficult to define. A consequence of this is that the vector normal to boundary surfaces of complex shape, such as ribs, cannot be accurately defined at a given location. This makes boundary conditions on such surfaces difficult to express accurately (Banerjee 1994, p2). Finite element modelling (FEM) techniques can overcome such issues. FEM involves discretising the system by non-infinitesimal finite elements where the system variables are locally approximated by shape functions and the elements are then assembled, thus providing an approximation to the physical system (Zienkiewicz and Taylor 1994). In FEM, the discretisation of the domain is not usually restricted to elements of cuboid shape, which provides a more accurate means of dealing with boundaries of complex shape. Nevertheless, both FEM and FDTD require the entire computational domain to be meshed, which inevitably renders them computationally expensive on large three-dimensional systems.

2.5 The case for the boundary element method

The boundary element method (BEM) is a numerical analysis technique used to obtain the solution of partial differential equations (PDE) associated with a particular physical

problem with well-defined boundary conditions. In BEM, the PDE is essentially reformulated into an integral equation that is defined on the boundary of the domain and an integral that relates the boundary solution to the solution at any point in the domain. The former is referred to as the boundary integral equation (BIE). The BIE may then be solved by discretising the surfaces defined by the domain boundaries into smaller regions known as boundary elements. A major advantage of BEM over other numerical schemes such as FEM or FDTD is that the discretisation occurs only over the surfaces rather than over the entire domain. This eliminates the need to consider domain truncation effects and substantially reduces the problem size as it is reduced from 3D to 2D. Furthermore, boundaries of complex shape can be accurately modelled and conditions on the boundary defined in a more precise fashion than FDTD methods. BEM can readily handle radiation, scattering and interior acoustic problems.

Hence, BEM has the potential to produce a 3D solution to the scattering of continuous waves by ribs of arbitrary shape at megahertz frequencies, without some of the disadvantages associated with the other numerical schemes described in this chapter. Furthermore, BEM enables the definition of a boundary condition on the surface of the scatterer in the form of a surface impedance condition. This implies that analyses involving ribs do not have to be restricted to perfectly absorbing or reflecting objects. This is crucial if calculating a dose-related quantity at a location on the surface of the ribs is required, since this quantity is likely to be related to acoustic pressure (Duck 2009).

From the point of view of planning the treatment of tumours of the upper abdomen, as was discussed in Chapter 1, there is a requirement to investigate methodologies for solving the following inverse problem: focusing the field of a HIFU array inside the ribcage such that it results in ablative pressures at the required locations whilst ensuring that an ultrasonic dose-related quantity on the surface of the ribs does not exceed a given damage threshold. This requires the use of a suitable forward model capable of addressing the effects of scattering on 3D anatomical data. Solving this type of inverse problem is likely to require the use of constrained optimisation techniques. As discussed in section 2.2.6, for problems which present computational challenges to solve when accounting for nonlinearities, linear propagation models can act as an initial guess and provide a benchmark against which more sophisticated models can be assessed. Solving inverse problems will generally require more computational time than a single run of a

forward model. Hence, a good starting point to tackling this inverse problem is to use a forward model which assumes linear propagation of ultrasound. The reduced number of degrees of freedom generated by BEM when compared against methods which require the entire computational domain to be discretised reinforces the case for the use of BEM in the forward propagation model.

Care must be taken in implementing BEM since the transformed BIE is often less well behaved than the original differential equation, where problems of singularity and non-uniqueness may arise, particularly in scattering problems. Furthermore, the matrices derived from the discretisation of the BIE are often complex, non-symmetric and fully-populated. These issues will be discussed further in Chapter 3.

2.6 Summary

In this chapter, existing approaches to modelling the propagation of ultrasonic waves in soft tissue in the presence of bone have been reviewed. Widely used equations describing the nonlinear propagation of ultrasonic waves in tissue have been reviewed, and a brief description of attenuation mechanisms in biological media was provided. In the context of trans-costal HIFU applications, it has been explained why full wave 3D models for propagation in heterogeneous media in the presence of bone still present major computational challenges. It has been argued that linear models capable of accurately modelling effects of scattering by human ribs in 3D have an important role to play in an initial evaluation of the feasibility of treatment planning particularly where transducer field optimisation is required. Prior modelling approaches used in the context of trans-skull and trans-rib HIFU have been reviewed and it was found that they were ill-suited for describing the scattering of the field of a HIFU array by human ribs under continuous wave conditions. A brief description of BEM has been presented with emphasis on why this method is particularly attractive for solving the problem described above. The advantages of BEM include only having to mesh the surface of the scatterer rather than the entire computational domain, not having to deal with domain truncation effects, the lack of numerical dispersion, the ability to model complex scatterer geometries and to apply the relevant boundary conditions on the surface of these scatterers. The suitability of BEM as a forward model for solving transducer field optimisation problems presence in the presence of ribs has been outlined. Details of BEM will be described in Chapter 3.

Chapter 3

Methodology: Boundary Element Methods

3.1 Overview

This chapter presents an overview of the forward mathematical modelling method employed within this body of work. A method of simulating the forward problem of the scattering of an ultrasonic wave by ribs, the topology of which will be obtained from anatomical data, is required. It was shown why boundary element methods are particularly well-suited to describe such a problem in Chapter 2. The boundary integral form of the Helmholtz equation, also known as the Kirchhoff-Helmholtz equation will be derived for scattering problems. The boundary conditions on the surface of the scatterer will be discussed. Issues of singularity and non-uniqueness associated with the Kirchhoff-Helmholtz equation and its discretisation will be reviewed, and how they may be overcome will be described. It will then be shown that the problem to be solved takes the form of a system of linear algebraic equations. The underlying assumptions will be reviewed and discussed in the context of trans-costal HIFU simulations.

3.2 The Kirchhoff-Helmholtz equation

This work will be restricted to the linearised wave equation. Only time harmonic waves with a time dependence of $e^{\mathrm{i}\omega t}$ will be considered, where

- $\mathrm{i}^2 = -1$
- $\omega = 2\pi f$, where f is the frequency
- t is time.

Unless specified, all analyses will be carried out in three-dimensional Cartesian space, so that a location inside the domain is defined in terms of the coordinates x, y and along the global Cartesian axes, by a position vector $\vec{r}$ as follows:

$$\vec{r} = \begin{pmatrix} x \\ y \\ z \end{pmatrix} \tag{3.1}$$

Real physical quantities such as the acoustic pressure, p, and the particle velocity vector, $\vec{u}$, are represented as follows:

$$p(\vec{r}, t) = Re\left[p(\vec{r})e^{\mathrm{i}\omega t}\right] \tag{3.2}$$

$$\vec{u}(\vec{r}, t) = Re\left[\vec{u}(\vec{r})e^{\mathrm{i}\omega t}\right] \tag{3.3}$$

$p(\vec{r})$ and $\vec{u}(\vec{r})$ are complex functions of the position vector $\vec{r}$. Since the analyses will be confined to the frequency domain, the acoustic pressure and particle velocity may therefore be considered only in terms of their dependency on the position vector.

The starting point of the BEM for the acoustic scattering problems considered in this work will be the Helmholtz equation, which describes the propagation of time-harmonic acoustic waves in a homogeneous isotropic inviscid medium.

$$\nabla^2 p(\vec{r}) + k^2 p(\vec{r}) = 0 \tag{3.4}$$

k is the wave number, defined as $k = 2\pi f/c$, where c is the (complex) velocity of propagation of acoustic waves in the medium. k may be a complex quantity.

For analyses carried out in the time domain, a causality condition is required to reflect the fact that an acoustic event cannot physically have an effect before it has occurred. In the frequency domain, the causality condition cannot be expressed as a condition in time, and takes the form of the Sommerfeld radiation condition. Causality is then expressed by the integrability condition, implicit in assuming that a Fourier representation of the wave exists, and becomes a condition in space, in this case a boundary condition at infinity (Pierce 1989, p178). The Sommerfeld radiation condition may be defined in terms of the acoustic pressure as follows (Pierce 1989, p178):

$$\lim_{\|\vec{r}\|\to\infty} |\vec{r}| \left(\frac{\partial p(\vec{r})}{\partial \|\vec{r}\|} + \mathrm{i}kp(\vec{r}) \right) \to 0 \tag{3.5}$$

The Sommerfeld radiation condition essentially implies that acoustic disturbances tend to zero at infinity. Consider an exterior domain V bounded by an imaginary surface Λ and by a closed surface S. Let Λ be at a sufficiently large distance from the acoustic sources, and from S, that the boundary condition on Λ satisfies the Sommerfeld acoustic radiation condition (see figure 3.1).

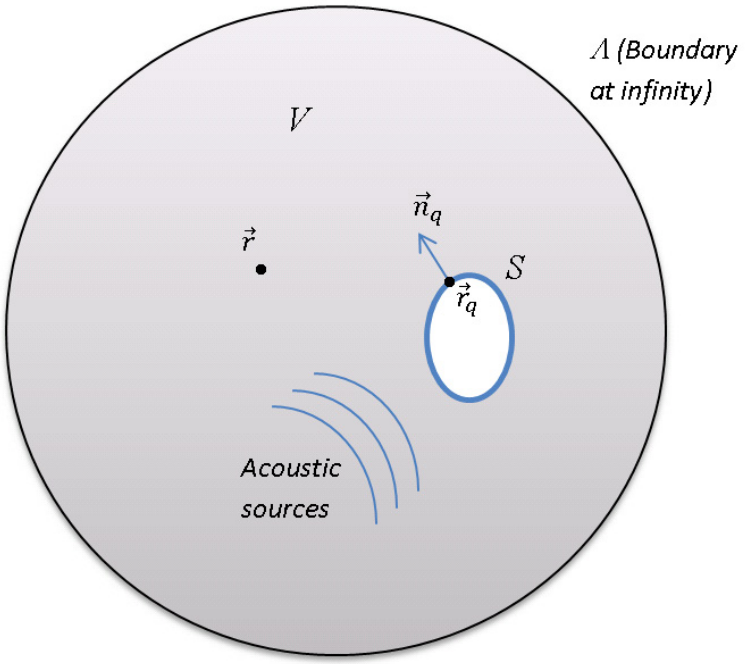

Figure 3.1 Diagram of domain for exterior scattering problem.

Consider an acoustic pressure field $p(\vec{r})$ generated in V by a source term $Q(\vec{r})$, described by the inhomogeneous Helmholtz equation as follows:

$$\nabla^2 p(\vec{r}) + k^2 p(\vec{r}) = -Q(\vec{r}), \forall \vec{r} \in V \tag{3.6}$$

Let the Green's function be defined as a solution to the Helmholtz equation with a singularity at the source point (i.e. a point source of unit source strength):

$$\nabla^2 G(\vec{r}|\vec{r}_q) + k^2 G(\vec{r}|\vec{r}_q) = -\delta(\vec{r} - \vec{r}_q), \forall \vec{r} \in V \tag{3.7}$$

where $\delta(\vec{r} - \vec{r}_q)$ is the Dirac delta function. The Green's function represents the effect of a unit source at any field point $\vec{r}_q$ on the point of observation $\vec{r}$. In three-dimensional space, the Green's function is given by:

$$G(\vec{r}|\vec{r}_q) = \frac{e^{-ik\|\vec{r}-\vec{r}_q\|}}{4\pi\|\vec{r}-\vec{r}_q\|} \tag{3.8}$$

By virtue of the reciprocity of the Green's function, i.e. $G(\vec{r}|\vec{r}_q) = G(\vec{r}_q|\vec{r})$, equation (3.7) is also valid if the derivatives are taken with respect to $\vec{r}_q$. Hence,

$$\nabla_q{}^2 G(\vec{r}|\vec{r}_q) + k^2 G(\vec{r}|\vec{r}_q) = -\delta(\vec{r} - \vec{r}_q), \forall \vec{r}_q \in V \tag{3.9}$$

where

$$\nabla_q{}^2 \equiv \frac{\partial^2}{\partial x_q^2} + \frac{\partial^2}{\partial y_q^2} + \frac{\partial^2}{\partial z_q^2} \tag{3.10}$$

By multiplying equation (3.6) (written in terms of $\vec{r}_q$) by $G(\vec{r}|\vec{r}_q)$ and equation (3.9) by $p(\vec{r}_q)$, and subtracting one from the other, we have:

$$G(\vec{r}|\vec{r}_q)\nabla_q{}^2 p(\vec{r}_q) - p(\vec{r}_q)\nabla_q{}^2 G(\vec{r}|\vec{r}_q) = p(\vec{r}_q)\delta(\vec{r} - \vec{r}_q) - G(\vec{r}|\vec{r}_q)Q(\vec{r}_q) \tag{3.11}$$

By integrating equation (3.11) over *V*, $\vec{r}_q$ being the variable of integration, and by making use of the sifting property of the Dirac delta function, we have:

$$\int_V \left[G(\vec{r}|\vec{r}_q)\nabla_q{}^2 p(\vec{r}_q) - p(\vec{r}_q)\nabla_q{}^2 G(\vec{r}|\vec{r}_q)\right]dV = p(\vec{r}) - p_i(\vec{r}), \forall \vec{r} \in V \tag{3.12}$$

where the incident acoustic pressure $p_i(\vec{r})$, i.e. the pressure in absence of the scatterer, is given by

$$p_i(\vec{r}) = \int_V G(\vec{r}|\vec{r}_q)Q(\vec{r}_q)dV \tag{3.13}$$

By applying Green's second theorem to equation (3.12), the volume integral may be transformed into a surface integral over the area defined by the union of the surface *S* of the scatterer and the surface Λ at infinity. By virtue of the Sommerfeld radiation condition being satisfied at infinity, the integral over Λ tends to zero, and only the integral over *S* need be considered. Hence, equation (3.12) may be written as:

$$\int_S \left[p(\vec{r}_q) \frac{\partial G(\vec{r}|\vec{r}_q)}{\partial n_q} - \frac{\partial p(\vec{r}_q)}{\partial n_q} G(\vec{r}|\vec{r}_q) \right] dS = p(\vec{r}) - p_i(\vec{r}), \forall \vec{r} \in V \tag{3.14}$$

where

$$\frac{\partial}{\partial n_q} \equiv \vec{n}_q \cdot \vec{\nabla} \tag{3.15}$$

and $\vec{n}_q$ denotes a unit vector normal to S at $\vec{r}_q$ and pointing from the surface into the exterior volume V. The total acoustic pressure $p(\vec{r})$ may be expressed as the sum of the incident pressure $p_i(\vec{r})$ and the pressure scattered by the surface S, $p_s(\vec{r})$, $\forall \vec{r} \in V$. Equation (3.14) is known as the Kirchhoff-Helmholtz equation. This integral form of the Helmholtz equation has important applications in calculating the field induced by sources scattered by finite boundaries and is valid $\forall \vec{r} \in V$. For locations on the surface S, the Kirchhoff-Helmholtz equation takes a slightly different form. Consider a hemisphere of radius ε surrounding the observation point $\vec{r}$ on S and let ε tend to zero. Let the surface defined by this hemisphere be S_2 (see figure 3.2).

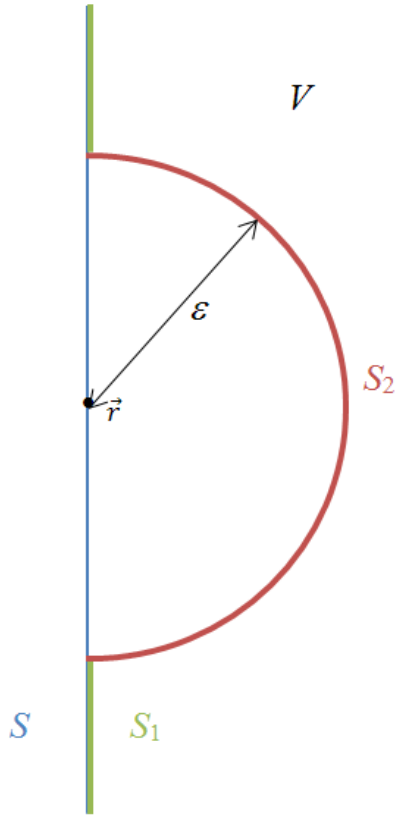

Figure 3.2 Hemisphere of radius ε surrounding the observation point $\vec{r}$ on S.

Let the S_1 be defined so that $S = S_1 \cup S_2$ in the limit of $\varepsilon \to 0$. Since the Dirac delta function is zero at all locations on S_2, we have:

$$\nabla_q{}^2 G(\vec{r}|\vec{r}_q) + k^2 G(\vec{r}|\vec{r}_q) = 0, \forall \vec{r} \in S_2 \tag{3.16}$$

Consider now an observation point lying on S. By following the same procedure as for an observation point located in V and by carrying out the surface integration over $S_1 \cup S_2 \cup \Lambda$, recalling that the integral over Λ vanishes, we have:

$$\int_{S_1} \left[p(\vec{r}_q) \frac{\partial G(\vec{r}|\vec{r}_q)}{\partial n_q} - \frac{\partial p(\vec{r}_q)}{\partial n_q} G(\vec{r}|\vec{r}_q) \right] dS_1 + \int_{S_2} \left[p(\vec{r}_q) \frac{\partial G(\vec{r}|\vec{r}_q)}{\partial n_q} - \frac{\partial p(\vec{r}_q)}{\partial n_q} G(\vec{r}|\vec{r}_q) \right] dS_2 = -p_i(\vec{r}), \forall \vec{r} \in S \tag{3.17}$$

The second integral on the left hand side of equation (3.17) is calculated as follows:

$$\int_{S_2} \left[p(\vec{r}_q) \frac{\partial G(\vec{r}|\vec{r}_q)}{\partial n_q} - \frac{\partial p(\vec{r}_q)}{\partial n_q} G(\vec{r}|\vec{r}_q) \right] dS = \lim_{\varepsilon \to 0} \left[p(\vec{r}) \frac{\partial}{\partial \varepsilon} \left(\frac{e^{ik\varepsilon}}{4\pi\varepsilon} \right) 2\pi\varepsilon^2 \right] = -\frac{1}{2} p(\vec{r}) \tag{3.18}$$

For scattering problems, the integral representation of the solution to the inhomogeneous Helmholtz equation is therefore given by:

$$\begin{cases} \int_S \left[p(\vec{r}_q) \frac{\partial G(\vec{r}|\vec{r}_q)}{\partial n_q} - \frac{\partial p(\vec{r}_q)}{\partial n_q} G(\vec{r}|\vec{r}_q) \right] dS = \frac{1}{2} p(\vec{r}) - p_i(\vec{r}), \forall \vec{r} \in S \\ \int_S \left[p(\vec{r}_q) \frac{\partial G(\vec{r}|\vec{r}_q)}{\partial n_q} - \frac{\partial p(\vec{r}_q)}{\partial n_q} G(\vec{r}|\vec{r}_q) \right] dS = p(\vec{r}) - p_i(\vec{r}), \forall \vec{r} \in V \end{cases} \tag{3.19}$$

3.3 Boundary conditions on the surface of the scatterer

The boundary conditions on S express the constraints of the field value and its normal derivative on the surface. These are associated with the properties of the surface. For perfectly reflective surfaces, two types of boundary condition are possible: the Neumann condition,

$$\frac{\partial p(\vec{r})}{\partial n} = 0, \forall \vec{r} \in S \tag{3.20}$$

and the Dirichlet condition,

$$p(\vec{r}) = 0, \forall \vec{r} \in S \tag{3.21}$$

The Neumann condition corresponds to an acoustically perfectly rigid boundary whilst the Dirichlet condition corresponds to a pressure-release or acoustically soft boundary. Most physical interfaces are not accurately described by either the Neumann or the Dirichlet conditions. In the case of a locally reacting surface, the normal derivative of the acoustic pressure on *S* may be obtained by considering the linearised conservation of momentum equation for harmonic excitation:

$$-\vec{\nabla} p = \mathrm{i}\omega\rho_0\vec{u} \tag{3.22}$$

where ρ_0 is the density of the medium in the exterior domain and $\vec{u}$ the particle velocity vector. Assuming continuity of the normal component of the particle velocity vector and continuity of the acoustic pressure, equation (3.22) must be satisfied in *V* as well as on *S*. By taking the scalar product of each side of equation (3.22) with the inward normal vector on *S*, we have:

$$-\vec{\nabla} p \cdot \vec{n} = \mathrm{i}\omega\rho_0\vec{u} \cdot \vec{n} \tag{3.23}$$

or

$$\frac{\partial p}{\partial n} = \mathrm{i}\omega\rho_0 u_n \tag{3.24}$$

where u_n is the inward normal component of $\vec{u}$ on *S*. The boundary condition on a locally reacting surface is given by Morse and Ingard (1968, p422):

$$\frac{p}{u_n} = z_1 = \rho_1 c_1 \tag{3.25}$$

where z_1 is the acoustic impedance of the surface and ρ_1 and c_1 are respectively the density and speed of sound associated with the medium of the scatterer. Hence, a locally reacting impedance condition on the surface of the scatterer may be defined as follows.

$$\frac{\partial p(\vec{r})}{\partial n} = \mathrm{i}k\frac{\rho_0 c}{\rho_1 c_1}p(\vec{r}), \forall \vec{r} \in S \tag{3.26}$$

In the context of this work, the boundary conditions on *S* which are of interest are the Neumann condition (acoustically hard surface) and the locally reacting impedance condition in equation (3.26).

3.4 Discretisation of the Kirchhoff-Helmholtz equation

We require a solution $p(\vec{r})$ which satisfies:

- the Helmholtz equation in *V*
- the Sommerfeld radiation condition at infinity
- the boundary condition $\frac{\partial p(\vec{r})}{\partial n} = g(\vec{r}), \forall \vec{r} \in S$, where $g(\vec{r}) = \mathrm{i}k\frac{\rho_0 c}{\rho_1 c_1}p(\vec{r})$ is assumed to be a continuous function defined on *S* and is assumed to have a continuous first derivative.

The above set of conditions describes what is known as an exterior Neumann boundary value problem, which can be solved by discretisation of the Kirchhoff-Helmholtz equation. Difficulties arise, however, as the solution of the integral equation relies on the numerical evaluation of singular, oscillatory integrands. On the surface of the scatterer, the Green's function along with its normal derivative becomes singular as the source location $\vec{r}_q$ approaches the observation location $\vec{r}$. Despite the singularity in the integration kernel, the integrals on the left hand side of equation (3.19) are regular, although care must be taken in their numerical evaluation (Meyer *et al* 1978). In addition to the singularity issues associated with the integration kernel for observation locations on *S*, the problem as described by the Kirchhoff-Helmholtz equation suffers from non-uniqueness at frequencies of excitation approaching an eigenvalue of one of the (fictitious) modes of the cavity inside the scatterer. The discretised form of the Kirchhoff-Helmholtz equation (3.19) is often referred to as the surface-Helmholtz integral formulation. The fully populated square matrix formed by discretising equation (3.19) for observation points on *S* then becomes close to singular. The method which appears to offer the best compromise in terms of application of the Helmholtz integral equation to exterior acoustic problems involving scatterers of arbitrary shape remains the Burton-Miller formulation (Chien *et al* 1990). This formulation solves for a linear

combination of equation (3.19) for observation points on S and its derivative with respect to the outward normal vector on S at source locations $\vec{r}$ (Burton and Miller 1971):

$$\int_S \left[p(\vec{r}_q)\left(\frac{\partial G(\vec{r}|\vec{r}_q)}{\partial n_q} + \alpha_c \frac{\partial^2 G(\vec{r}|\vec{r}_q)}{\partial n_q \partial n}\right) - \frac{\partial p(\vec{r}_q)}{\partial n_q}\left(G(\vec{r}|\vec{r}_q) + \alpha_c \frac{\partial G(\vec{r}|\vec{r}_q)}{\partial n}\right)\right] dS = \frac{1}{2}p(\vec{r}) + \frac{\alpha_c}{2}\frac{\partial p(\vec{r})}{\partial n} - p_i(\vec{r}) - \alpha_c \frac{\partial p_i(\vec{r})}{\partial n}, \forall \vec{r} \in S \quad (3.27)$$

where α_c is the coupling coefficient, which can be chosen as i/k (Kress R 1985), although the optimal value for this coefficient is problem-specific. For example, in a problem involving the scattering of a plane wave by a perfectly rigid sphere at a natural frequency of the interior problem, Liu and Rizzo (1991) find that α_c = 0.3333i/k appears to generate better agreement with the analytical solution than α_c = i/k for a fixed number of C^1 continuous elements. C^1 continuity implies that the element shape functions and their slope are required to be continuous (Zienkiewicz and Taylor 1994, p32). Some numerical experimentation is therefore likely to be required for scatterers with known analytical solutions, in order to help underpin values of α_c suitable for the problem being solved.

Burton and Miller (1971) have demonstrated that issues of non-uniqueness are overcome using the formulation in equation (3.27) and that a unique solution is obtained for every wave number. Although the solutions of the surface integral equation and of the normal derivative equation are non-unique at characteristic frequencies of the interior Dirichlet and Neumann problems, respectively, both solution spaces have a null space at their intersection. However, if the wave number associated with the medium in the exterior volume has a non-zero imaginary part, solving the discretised form of equation (3.19) for observation points on S may be sufficient, as the fictitious modes of the cavity inside the scatterer are likely to be dampened (Colton and Kress 1983, p81 and p84). Again, this is likely to be problem-specific and numerical experimentation with complex wave speeds of interest may be required to assess the validity of proceeding without the normal derivative formulation in equation (3.27). This validation would have to be carried out at frequencies corresponding to eigenfrequencies of the interior problem, for scattering problems with known analytical solution.

The surface S will now be discretised into a finite number N_p of patches. By using a shape function $[M]$ over each boundary element to interpolate the acoustic pressure and its derivative, the Kirchhoff-Helmholtz equation on S may be represented as follows:

$$\sum_{j=1}^{N_p}\{p(\vec{r}_{q,j})\}\int_{S_j}\left(\frac{\partial G(\vec{r}|\vec{r}_{q,j})}{\partial n_{q,j}}+\alpha_c\frac{\partial^2 G(\vec{r}|\vec{r}_q)}{\partial n_{q,j}\partial n}\right)[M]dS_j-\sum_{j=1}^{N_p}\left\{\frac{\partial p(\vec{r}_{q,j})}{\partial n_{q,j}}\right\}\int_{S_j}\left(G(\vec{r}|\vec{r}_{q,j})+\alpha_c\frac{\partial G(\vec{r}|\vec{r}_{q,j})}{\partial n}\right)[M]dS_j=\frac{1}{2}p(\vec{r})+\frac{\alpha_c}{2}\frac{\partial p(\vec{r})}{\partial n}-p_i(\vec{r})-\alpha_c\frac{\partial p_i(\vec{r})}{\partial n},\forall\vec{r}\in S \tag{3.28}$$

where N_p is the total number of boundary elements. In the case of constant pressure patches, $[M]$ is simply equal to 1. More generally, the shape function for an n node element is of the following form: for eight-noded quadratic isoparametric C^0 continuity patches, the shape function $[M]$ is established as follows (Zienkiewicz and Taylor 1994, p153).

$$\begin{pmatrix}x\\y\\z\end{pmatrix}^{\mathrm{T}}=\lfloor M_1 \quad M_2 \quad \cdots \quad M_n\rfloor\begin{bmatrix}x_1 & y_1 & z_1\\ x_2 & y_2 & z_2\\ \vdots & \vdots & \vdots\\ x_n & y_n & z_n\end{bmatrix} \tag{3.29}$$

n is the number of element nodes, $^{\mathrm{T}}$ denotes the transpose and (x_i, y_i, z_i) represents the coordinates in the global Cartesian axis set at node i. In this case, $n = 8$. C^0 continuity implies that the element shape functions are continuous (Zienkiewicz and Taylor 1994, p32). Unlike C^1 elements, no such condition is imposed on their slope. The term 'isoparametric' refers to the fact that the element geometry and the acoustic pressure interpolation function on the element are governed by the same shape function $[M]$. Hence,

$$p(x,y,z)=\sum_{i=1}^{n}p(\xi_i,\eta_i)M_i \tag{3.30}$$

Let the local coordinate system on a curvilinear element be defined in terms of the variables ξ and η, as shown in figure 3.3:

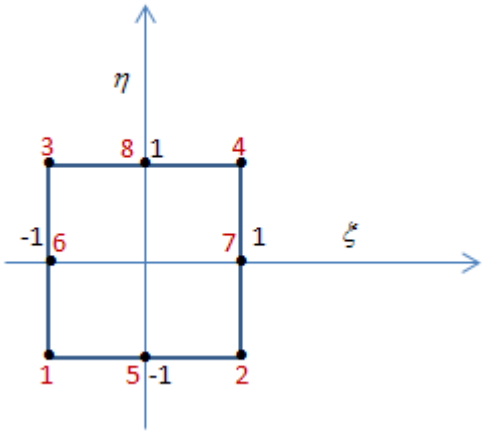

Figure 3.3 Eight node isoparametric quadrilateral element. Node numbers are shown in black. Local coordinate values are displayed in red.

Integrals over a quadrilateral patch in equation (3.28) take the form:

$$\int_{S_j} U_e(\vec{r}, \vec{r}_{q,j})[M] dS_j \tag{3.31}$$

where U_e is a function involving the Green's function or its normal derivatives. After a transformation to local coordinates, the above integral may be expressed as follows:

$$\int_{-1}^{1}\int_{-1}^{1} U_e(\vec{r}, \vec{r}_{q,j})[M]|J_e| d\xi d\eta \tag{3.32}$$

The expression for the Jacobian J_e is given as follows (Wu 2000, p53):

$$|J_e| = \left|\frac{\partial \vec{r}}{\partial \xi} \times \frac{\partial \vec{r}}{\partial \eta}\right| \tag{3.33}$$

The shape function may be shown to take the form below for eight node isoparametric quadrilateral patches. For corner nodes (i.e. nodes 1, 2, 3 and 4), we have (Lachat and Watson 1976):

$$M_i = \frac{1}{4}(1 + \xi\xi_i)(1 + \eta\eta_i)(\xi\xi_i + \eta\eta_i - 1) \tag{3.34}$$

At mid-side nodes, we have:

$$M_i = \frac{1}{4}(1-\xi^2)(1+\eta\eta_i),\ \xi_i = 0 \tag{3.35}$$

$$M_i = \frac{1}{4}(1-\eta^2)(1+\xi\xi_i), \eta_i = 0 \tag{3.36}$$

The hypersingular integrand in equation (3.27), involving the second derivative of the Green's function is strongly singular and cannot be integrated numerically in its current form (Meyer *et al* 1978). It may be regularised following the procedure outlined by Liu and Rizzo (1991), by rewriting as follows:

$$\begin{aligned}
&\int_S\ p(\vec{r}_q)\frac{\partial^2 G(\vec{r}|\vec{r}_q)}{\partial n_q \partial n} dS \\
&= \int_S\ \frac{\partial^2}{\partial n_q \partial n}\left[G(\vec{r}|\vec{r}_q) - \bar{G}(\vec{r}|\vec{r}_q)\right]p(\vec{r}_q)dS + \int_S\ \frac{\partial^2 G(\vec{r}|\vec{r}_q)}{\partial n_q \partial n}p(\vec{r}_q)dS \\
&= \int_S\ \frac{\partial^2}{\partial n_q \partial n}\left[G(\vec{r}|\vec{r}_q) - \bar{G}(\vec{r}|\vec{r}_q)\right]p(\vec{r}_q)dS \\
&\qquad + \int_S\ \frac{\partial^2 \bar{G}(\vec{r}|\vec{r}_q)}{\partial n_q \partial n}\left[p(\vec{r}_q) - p(\vec{r}) - (\vec{r}_q - \vec{r})\cdot\vec{\nabla}p(\vec{r})\right]dS \\
&\qquad\quad + p(\vec{r})\int_S\ \frac{\partial^2 \bar{G}(\vec{r}|\vec{r}_q)}{\partial n_q \partial n}dS + \vec{\nabla}p(\vec{r})\cdot\int_S\ (\vec{r}_q - \vec{r})\frac{\partial^2 \bar{G}(\vec{r}|\vec{r}_q)}{\partial n_q \partial n}dS\,, \forall \vec{r} \in V
\end{aligned} \tag{3.37}$$

where $\bar{G}(\vec{r}|\vec{r}_q)$ is the static case Green's function and is equal to $\frac{1}{4\pi\|\vec{r}_q - \vec{r}\|}$.

According to Liu and Rudolphi (1991), when $\vec{r}$ is in the exterior volume, the last two integrals in equation (3.29) are given by:

$$\int_S\ \frac{\partial^2 \bar{G}(\vec{r}|\vec{r}_q)}{\partial n_q \partial n}dS = 0 \tag{3.38}$$

and

$$\int_S\ (\vec{r}_q - \vec{r})\frac{\partial^2 \bar{G}(\vec{r}|\vec{r}_q)}{\partial n_q \partial n}dS = \int_S\ \vec{n}_q\frac{\partial \bar{G}(\vec{r}|\vec{r}_q)}{\partial n}dS \tag{3.39}$$

Substituting equations (3.38) and (3.39) into equation (3.37), and then back into the normal derivative component of equation (3.27), and placing $\vec{r}$ on *S* gives:

$$\frac{\partial p(\vec{r})}{\partial n} + \int_S \frac{\partial^2 G(\vec{r}|\vec{r}_q)}{\partial n_q \partial n}\left[p(\vec{r}) - p(\vec{r}_q) - \vec{\nabla} p(\vec{r}) \cdot (\vec{r}_q - \vec{r})\right] dS$$
$$+ \int_S \frac{\partial^2}{\partial n_q \partial n}\left[G(\vec{r}|\vec{r}_q) - \bar{G}(\vec{r}|\vec{r}_q)\right] p(\vec{r}_q) dS = \int_S \frac{\partial G(\vec{r}|\vec{r}_q)}{\partial n}\left[\vec{\nabla} p(\vec{r}_q) - \vec{\nabla} p(\vec{r})\right] \cdot \vec{n}_q dS$$
$$+ \int_S \frac{\partial}{\partial n}\left[G(\vec{r}|\vec{r}_q) - \bar{G}(\vec{r}|\vec{r}_q)\right] \vec{n}_q \cdot \vec{\nabla} p(\vec{r}_q) dS + \frac{\partial p_i(\vec{r})}{\partial n}, \forall \vec{r} \in S \qquad (3.40)$$

The integrals in equation (3.40) are weakly singular integrals at most. These, as well as the other integrands in equation (3.27), can be treated for 3D eight node quadrilateral isoparametric elements using the Lachat-Watson transformation (Lachat and Watson 1976). This involves subdividing the quadrilateral elements into triangular patches each with a local coordinate system and a modified Jacobian. This transformation has the advantage of causing the modified Jacobian in the integral over the triangular patch containing the singularity to vanish (Gaul *et al* 2003, p191). The remaining integrals may then be solved using Gaussian-Legendre quadrature (Zienkiewicz and Taylor 1994, p172).

It is well known that theory imposes a C^1 smoothness requirement (i.e. continuity of the slope of the unknown quantity occurring between elements) on the density function (in this case $p(\vec{r})$) of the hypersingular BIEs (Chien *et al* 1990). After discretisation of equation (3.40), the normal derivative of the acoustic pressure may be discontinuous across element boundaries when employing C^0 elements. Chien *et al* (1990) and Liu and Rizzo (1991) have nevertheless suggested that this requirement may be relaxed and that the C^0 smoothness requirement, though mathematically unjustifiable, may suffice. This requirement may be somewhat eschewed by using the approach described by Francis (1993), in which the normal derivative terms are computed at the element centroids. This is then combined with the regular BIE by association of each normal derivative equation with the eight nodes of the element on which the calculation point for that equation is located.

By formulating equation (3.40) for all position vectors $\vec{r}$ on S corresponding to each node on the mesh of the surface, a linear system of equations may be generated.

$$[H]\{p\} - [G]\left\{\frac{\partial p}{\partial n}\right\} + \{p_i\} + \alpha_c \left\{\frac{\partial p_i}{\partial n}\right\} = \{0\} \qquad (3.41)$$

The BEM formulation described by equation (3.41) is known as the collocation BEM, where the approximated BIE is evaluated at the interpolation nodes. After discretisation of the surface into a number of discrete patches defined by nodal points, it is assumed that the BIE is satisfied at these points. It is the earliest variant of BEM (Yu *et* al 2010). It should be noted that there are other BEM formulations which exist, including the Galerkin BEM. The Galerkin BEM discretisation procedure employs a weighted residual technique and is particularly advantageous in dealing with surface geometries which are not smooth, including sharp edges and cracks (Yu *et al* 2010). Forming the Galerkin BEM matrices however requires the evaluation of 4D integrals, which may be costly from a computational point of view. The investigation of Galerkin and other BEM was considered beyond the scope of this thesis.

For a Neumann condition on S, the normal derivative vector of acoustic pressures at nodal locations on S is $\{0\}$. For a locally reacting impedance condition on S, it is related to the acoustic pressure by equation (3.26). Equation (3.41) need therefore only be solved for the acoustic pressures $\{p\}$ at nodal positions on S. From knowledge of the incident pressure field and its normal derivative on S, together with the boundary element matrices $[H]$ and $[G]$, $\{p\}$ may be obtained through matrix inversion. $[H]$ and $[G]$ are generally complex, fully-populated and non-symmetric. Hence, for large problem sizes, storing all the elements of $[H]$ and $[G]$ simultaneously may potentially become problematic due to limited availability of RAM on a computing platform. In such cases, the generalised minimal residual method (Saad and Schultz 1986) may be used. This is discussed in Appendix A.

Once the acoustic pressures on the surface S of the scatterer are known, the pressure $p(\vec{r})$ at any location in the exterior volume V_{ext} may then be obtained by solving:

$$\int_S \left[p(\vec{r}_q) \frac{\partial G(\vec{r}|\vec{r}_q)}{\partial n_q} - \frac{\partial p(\vec{r}_q)}{\partial n_q} G(\vec{r}|\vec{r}_q) \right] dS = p(\vec{r}) - p_i(\vec{r}), \forall \vec{r} \in V \tag{3.42}$$

The acoustic pressures and their normal derivatives at locations on S are known from solving equation (3.41) and from the boundary condition on S. The integral in equation (3.42) does not present any particular problems and may be solved by Gaussian quadrature: there are no non-uniqueness issues and singularities do not occur since the observation location is located in the exterior volume V. Nevertheless, at field locations

close to the surface *S*, it may be necessary to increase the integration order to obtain an accurate solution, as the integration kernels may become close to singular.

3.5 Underlying assumptions

3.5.1 Heterogeneity of soft tissue surrounding the scatterers

In the boundary element formulation described in this chapter, the acoustic medium surrounding the ribs is assumed to extend to infinity and the soft tissue (i.e. muscle, skin and fat) is treated as a homogeneous medium. The speed of propagation of longitudinal waves is generally comparable in different soft tissues, and is approximately 1500 m s^{-1} (Duck 1990, p75 and p95). The same is true of the density (Duck, 1990 p137). Furthermore, Hynynen and Fan (1992) developed and tested a computational model based on a Rayleigh-Sommerfeld diffraction integral which took reflection and refraction of an ultrasound beam at tissue interfaces into account, and concluded that the effect of the interfaces between soft tissues was small and could often be ignored. It may therefore not be unreasonable to consider the acoustic medium surrounding the bone as homogeneous. If multiple tissue volumes need modelling, this could in principle be achieved using BEM through a combination of interior and exterior formulations (Elysée 2011). This would necessitate meshing the closed surfaces associated with each region (e.g. skin, fat, liver tissue, bone). Such a formulation is beyond the scope of this thesis.

During HIFU treatment, the ultrasonic transducer is not usually coupled directly to the abdomen of the patient as it is generally of spherical-section shape, as will be discussed in Chapter 4. Instead, a water coupling region is placed between the transducer and the abdomen. Whilst the density and speed of sound in water are not dissimilar to those in soft tissue, the attenuation coefficient in liver tissue is approximately three orders of magnitude higher than that in water at 20°C at 1 MHz (Duck 1990, p75 and p104, Fan and Hynynen 1994). Neglecting this will have an impact on the acoustic pressures calculated at the focus, which may be considerably underestimated. A correction for the acoustic pressure transmitted at the water/tissue interface could be applied using a Rayleigh-Sommerfeld diffraction integral (Hynynen and Fan 1992 and 1994), but this is beyond the scope of this work.

3.5.2 Normal velocity boundary condition at the location of the ultrasonic sources

In the context of using BEM for the simulation of trans-costal HIFU, a number of assumptions have to be made. It is assumed that the ultrasonic sources are defined simply in terms of an incident acoustic pressure field. As such, no normal velocity boundary condition is imposed at the surface of the HIFU transducer, therefore making it impossible to account for multiple reflections between the surface of the source and the ribs.

3.5.3 Acoustic nonlinearity

The effects of nonlinear propagation are not considered in this thesis. It is however well known that HIFU fields can result in highly nonlinear behaviour in the focal region leading to distortion of the acoustic waveform and transfer of energy from the fundamental frequency towards higher order harmonics (Wu *et al* 2004). Nevertheless, from the point of view of treatment planning, it has been shown that correcting for aberrations introduced by the presence of bone need not require nonlinear propagation models and that linear approaches generally suffice (Pinton *et al* 2011). Furthermore, nonlinear behaviour is likely to be confined mainly to the central focal lobe (Yuldashev *et al* 2013). However, at the focus, nonlinear behaviour is a certainty if tissue necrosis is induced. Hence, although a more rigorous treatment of the focal region may be required, useful information can be obtained from linear models when investigating energy depositions at the surface of the ribs. A full-wave nonlinear 3D model for propagation of ultrasound in tissue allowing for shock wave formation and for sharp discontinuities at the media interfaces (e.g. tissue/bone) would be required to deal with nonlinearities in the presence of ribs. Such a model is beyond the scope of this work.

3.5.4 Through-bone transmission

It has been discussed that the interface between the exterior medium and the bone would be modelled by either assuming the ribs are perfectly rigid, or by using a locally reacting surface impedance condition (see section 3.3). Considering the ribs as perfectly rigid objects was deemed a necessary initial stage before adding more complexity to the model, in the form locally reacting boundary condition. Nevertheless, a locally reacting surface impedance condition neglects any transmission through the bone medium, and this could contribute to the total acoustic pressure in the exterior domain inside the

ribcage. This assumption is however not unreasonable. Indeed, Aubry *et al* (2008) confirmed the shadowing effect of the ribs through two-dimensional finite difference numerical simulations and measurement. It was noted that the ratio between the amplitude of the waves propagating between the ribs and the waves propagating through the ribs was equal to 6.03 in the experiment and to 7.04 in the simulations. This result is perhaps not surprising owing to the high attenuation coefficient of bone relative to that of soft tissue (El-Brawany *et al* 2009, Duck 1990, p104).

3.5.5 Generation of shear waves in bone

It is well known that both longitudinal and shear waves can be generated in bone (Kohles *et al* 1997, Mast *et al* 1999). As bone is a highly attenuating medium compared to soft tissue, absorption of shear waves may play an important part in heating of the bone. Indeed, Nell and Myers (2010) produced axisymmetric calculations describing an 8 cm diameter 1.1 MHz HIFU transducer insonating a water/soft tissue/bone interface, predicting an off-axis temperature rise of up to 30% higher when absorption of shear waves was included in the bone medium.

A full elastodynamic formulation would be required to deal with this phenomenon accurately. This could in principle be achieved using an elastodynamic BEM frequency domain formulation such as that proposed by Chaillat *et al* (2007). Another candidate approach would consist of using a FEM/BEM method (Macey 1987), where the exterior domain would be modelled using BEM patches, and the interior domain using structural finite elements. These formulations are likely to be computationally expensive and remain beyond the scope of this thesis. It is acknowledged that this is a limitation of the method proposed for the forward model.

3.6 Summary

An overview of BEM for exterior scattering problems, for which the integral representation of the solution to the inhomogeneous Helmholtz equation was derived, has been provided. This equation is also referred to as the Kirchhoff-Helmholtz integral equation.

Two formulations describing the boundary condition on the ribs are considered as part of this work.

- A Neumann boundary condition, where the ribs are considered as perfectly rigid surfaces where the normal derivative of the acoustic pressure is zero throughout their surface.
- A locally reacting boundary condition, where it is assumed that the surface is locally reacting, and where the normal derivative of the acoustic pressure on the surface of the ribs is a linear function of the acoustic pressure.

It has been explained how the discretisation of the Kirchhoff-Helmholtz integral equation gives rise to issues of singularity and non-uniqueness when the exterior medium is attenuating. It was shown how a Burton-Miller formulation (Burton and Miller 1971) could overcome the non-uniqueness problem. This formulation solves for a linear combination of the Kirchhoff-Helmholtz integral equation for observation points on the surface S of the scatterer, and its derivative with respect to the outward normal vector on S. This nevertheless gives rise to a hypersingular integrand involving the second derivative of the Green's function, which cannot be integrated numerically in its current form (Meyer *et al* 1978). It has been shown how using the procedure described by Liu and Rizzo (1991) could help regularise this integral, thus giving rise to integrals which are weakly singular at most, and which can be solved using Gaussian-Legendre quadrature after a coordinate transformation. When the medium is attenuating and the imaginary part of the wave number is non-zero, Colton and Kress (1983, p81 and p84) suggest that a Burton-Miller formulation may not be required. Whether or not this applies to the problems addressed in this thesis will have to be determined using numerical experiments. It has been shown that the discretised problem takes the form of a system of linear equations involving fully-populated and complex matrices.

Finally, the assumptions made in the forward modelling method were stated and discussed. These included the following:

- heterogeneity of soft tissue surrounding the scatterers
- no normal velocity boundary condition is imposed at the surface of the HIFU transducer
- linearity of acoustic wave propagation
- no through-bone transmission
- no generation of shear waves in rib bone.

A description of the computational implementation using the PAFEC software can be found in Appendix A. This also includes details of the parallelisation of the software on a dedicated Linux computer cluster. Details of the programme code can be found in Appendix E.

Chapter 4

The Forward Problem: Results

4.1 Overview

In this chapter, the forward problem of predicting the scattering of the acoustic pressure field generated by a HIFU source by human ribs will be described. The modelling method used relies on the BEM approach described in Chapter 3. A description of its implementation on a dedicated computer cluster, using the generalised minimal residual (GMRES) method can be found in Appendix A.

When using a numerical method to solve a given problem, it is crucial to test its implementation on configurations for which known analytical solutions exist. Whilst this may not be a sufficient condition to assess the validity of the implementation, particularly on more complex problems for which there may not be any known analytical solutions, this testing is a necessary step and helps provide an assessment of the method. There are well-established solutions which describe the scattering of a time-harmonic plane wave by spheres analytically (Morse and Ingard 1968, p418). These analytical solutions exist for a range of boundary conditions on the surface of the sphere, including a Neumann boundary condition for which the normal derivative of the acoustic pressure is zero throughout the surface, and a Dirichlet boundary condition, where it is assumed that the surface is locally reacting, and where the normal derivative of the acoustic pressure on the surface of the sphere is a linear function of the acoustic pressure. As discussed in Chapter 3, both these boundary conditions on the surface of the ribs will be considered.

A known analytical solution for a time-harmonic plane wave scattered by an infinite cylinder, when the direction of the propagation vector is perpendicular to the axis of the cylinder, exists (Morse and Ingard 1968, p401). This solution can be useful in benchmarking the BEM formulation for trans-costal HIFU applications. Indeed, long cylinders, where the height is much greater than the radius, possess a shape not unlike

ribs. Furthermore, the acoustic pressure close to the surface of a long finite cylinder halfway along its height should display features of the results provided by the analytical solution for an infinite cylinder. Hence, this comparison can serve as a useful validation tool alongside analyses of spheres. Additionally, comparison of the analytical solution of the scattering of a plane wave by an infinite cylinder with equivalent BEM results for a finite cylinder may yield important conclusions for analyses on ribs. This is particularly valid if the height of the cylinder is much greater than its diameter.

The comparison of BEM results against known analytical solutions is also important in that it may help underpin any numerical issues that result from a poor choice of model input parameters related to the accuracy and convergence of the solution. These model input parameters are as follows:

- the mesh density of the surface of the scatterer(s)
- the number of iterations employed in the GMRES algorithm (see Appendix A)
- the value of the coupling coefficient α_c employed in the Burton-Miller formulation
- the integration order used in the Gaussian-Legendre quadrature routines (Zienkiewicz and Taylor 1994, p172) when evaluating the integrals in the Kirchhoff-Helmholtz equation for receiver locations in the exterior domain.

It is well known that, for eight node isoparametric quadrilateral elements, the rule of thumb of using a mesh density of at least three elements per wavelength corresponding to the wave speed in the exterior domain is generally required to mesh the surface of the scatterer (Hughes 2001, p101). This criterion may nevertheless be problem-dependent and it will need to be assessed by comparing BEM results against analytical solutions. Also, the finer the mesh, the more closely it will match the topology of the surface under investigation. For scatterers of complex shape, the mesh density may have to be increased in certain regions to capture the topology of the surface. This may however result in too large a number of degrees of freedom, thus increasing run times and computational requirements. Furthermore, if the outer surface of the scatterer is obtained from MR or CT data, it is also possible that additional uncertainty may be introduced when refining the mesh, particularly if the boundary element patches are of dimensions which are of the order of the spatial resolution of the imaging modality. The effects of uncertainties in a mesh topology could be assessed by producing modified

meshes in which the coordinates of nodal locations are varied within the bounds of the spatial uncertainties of the imaging modality. The impact of these coordinate modifications on the BEM results could then be examined and quantified. Such analyses, whilst relevant, will remain beyond the scope of this thesis.

As discussed in Appendix A, the GMRES scheme will converge after m iterations when solving a linear system of equations of the form $\boldsymbol{Ax} = \boldsymbol{b}$, where $\boldsymbol{A}$ is of dimension $m \times m$. We have seen that m is likely to be of the order of 10^5 for human rib topologies meshed for an excitation frequency of 1 MHz. Full convergence of the solution may however not necessarily be required to achieve the desired accuracy in the surface acoustic pressures and the acoustic pressures in the exterior domain. Numerical experiments on scattering problems for which there are known analytical solutions are therefore vital to establishing this. The element dimensions in the mesh in figure A.1 (Appendix A) are approximately of dimension 0.5 mm × 0.5 mm, making them of the order of the spatial resolution that is achievable using MR or CT imaging. This is a limitation that must be acknowledged and accepted as part of this work.

As discussed in section 3.4, the value of α_c employed in the Burton-Miller formulation may have an impact on the accuracy of the solution when using a fixed number of surface patches. Furthermore, it was mentioned that a Burton-Miller formulation may not be necessary in cases where the imaginary part of the speed of sound in the exterior domain is non-zero. Again, carrying out numerical experiments on scattering problems for which there are known analytical solutions will help establish which value of $\boldsymbol{\alpha_c}$ to use.

When evaluating the acoustic pressure at locations in the exterior domain, the integration kernel in equation (3.19) at a receiver $\vec{\boldsymbol{r}}$ may become close to singular when $\vec{\boldsymbol{r}}$ is very close to the surface S of the scatterer. In the context of this work, we will generally not be interested in determining acoustic pressures at locations very close to S accurately. Rather, we are interested in pressures on the surface of the scatterer and those at the vicinity of the focus of the HIFU transducer. Fourth order Gaussian-Legendre quadrature routines were therefore maintained throughout the calculations in this thesis. It will be demonstrated that this is indeed sufficient for the field locations of interest.

Here, once the requirements regarding the modelling input parameters affecting accuracy and convergence of the solution have been demonstrated as underpinned through numerical experiments, a section will be devoted to the modelling of the HIFU source. The transducer throughout this thesis is of spherical-section, multi-element type, with a pseudo-random arrangement of the elements on its surface. The transducer type and its specifications (i.e. its dimensions and frequency of operation) will be detailed and a justification as to why this type of source has been used will be provided. The transducer modelling methodology will also be described.

Finally, the incident transducer acoustic pressure field will be used as input data for BEM analyses using a mesh of scatterers derived from human rib data. These analyses will feature gradual added complexity with regards to the ribs and the propagating medium, as follows:

- perfectly rigid ribs in a homogeneous non-attenuating medium (Neumann boundary condition)
- perfectly rigid ribs in a homogeneous attenuating medium (Neumann boundary condition)
- locally reacting ribs with a surface impedance condition in a homogeneous attenuating medium (Dirichlet boundary condition).

4.2 Analytical solutions for scattering of time-harmonic plane acoustic waves by simple scatterers

4.2.1 Spherical scatterers

4.2.1.1 Perfectly rigid spherical scatterer in a homogeneous medium

It is assumed that the centre of the sphere is at the global origin. Let a be the radius of the sphere. The spatial component of the acoustic pressure generated by a plane wave of unit amplitude travelling to the right along a polar axis, so that $x = r\cos\theta$ and $y = r\sin\theta$, may be expressed as (Abramowitz and Stegun 1964, p440):

$$p_i = e^{-ikr\cos\theta} = \sum_{n=0}^{\infty}(2n+1)(-\mathrm{i})^n j_n(kr)P_n(\cos\theta) \tag{4.1}$$

where j_n denotes the spherical Bessel function of order *n* and P_n denotes the Legendre polynomial. The scattered component of the wave, p_s, is given by (Morse and Ingard 1968, p419):

$$p_s = \sum_{n=0}^{\infty} A_n h_n^{(2)}(kr) P_n(\cos\theta) \tag{4.2}$$

where $h_n^{(2)}$ denotes the spherical Hankel function of order *n* of the second kind and A_n are coefficients to be determined.

The total acoustic pressure in the exterior domain is given by the sum of the incident and scattered pressures.

$$p(r,\theta) = \sum_{n=0}^{\infty}(2n+1)(-\mathrm{i})^n j_n(kr) P_n(\cos\theta) + \sum_{n=0}^{\infty} A_n h_n^{(2)}(kr) P_n(\cos\theta) \tag{4.3}$$

For a perfectly rigid sphere, $\frac{\partial p}{\partial r} = 0$ for $r = a$. By differentiating equation (4.3) with respect to *r* and using the orthogonality of the Legendre polynomial (Kreyszig, p241), we have:

$$A_n = -\frac{(2n+1)(-\mathrm{i})^n j_n{}'(ka)}{h_n^{(2)\prime}(ka)} \tag{4.4}$$

where $'$ denotes the derivative of the spherical Bessel and Hankel functions with respect to the function argument.

The expressions derived in this section are also valid for wave numbers with a non-zero imaginary part.

4.2.1.2 Locally reacting spherical scatterer in a homogeneous medium

For a sphere with a locally reacting surface impedance condition, we have $\frac{\partial p}{\partial r} = \mathrm{i}k\frac{\rho_0 c}{\rho_1 c_1} p(a)$ for $r = a$ (see equation 3.26). Using the same procedure as in section 4.2.1.1, we have:

$$A_n = -\frac{(2n+1)(-\mathrm{i})^n\left[j_n'(ka) - \mathrm{i}k\frac{\rho_0 c}{\rho_1 c_1} j_n(ka)\right]}{h_n^{(2)\prime}(ka) - \mathrm{i}k\frac{\rho_0 c}{\rho_1 c_1} h_n^{(2)}(ka)} \tag{4.5}$$

4.2.2 Cylindrical scatterers

4.2.2.1 Perfectly rigid cylindrical scatterer in a homogeneous medium

Consider a plane wave of unit amplitude scattered by an infinite perfectly rigid cylinder of radius a. Let the global Cartesian x-axis be the axis of the cylinder and assume that the plane wave is propagating along the positive z-axis. Since the cylinder is of infinite length, the analysis need only be carried out in the y-z plane. Consider a local two-dimensional axis set in the y-z plane centred at the global origin where the position is defined by r and θ where $z = r\cos\theta$ and $y = r\sin\theta$. The spatial dependence of the incident pressure field may be expressed as (Abramowitz and Stegun 1964, p361):

$$p_i = e^{-ikr\cos\theta} = \sum_{n=0}^{\infty} \varepsilon_n (-\mathrm{i})^n J_n(kr)\cos(n\theta) \tag{4.6}$$

where

$$\varepsilon_n = \begin{cases} 1, n = 0 \\ 2, n > 0 \end{cases} \tag{4.7}$$

and J_n is the Bessel function of the first kind of order n.

The scattered wave may be expressed as (Morse and Ingard 1968, p401):

$$p_s = \sum_{n=0}^{\infty} A_n H_n^{(2)}(kr)\cos(n\theta) \tag{4.8}$$

where $H_n^{(2)}$ denotes the Hankel function of the second kind of order n.

The total acoustic pressure in the exterior domain is given by the sum of the incident and scattered pressures:

$$p(r,\theta) = \sum_{n=0}^{\infty} \varepsilon_n (-\mathrm{i})^n J_n(kr)\cos(n\theta) + \sum_{n=0}^{\infty} A_n H_n^{(2)}(kr)\cos(n\theta) \tag{4.9}$$

By noting that for a perfectly rigid cylinder, $\frac{\partial p}{\partial r} = 0$ for $r = a$, by differentiating equation (4.9) with respect to r and using the orthogonality of the cosine function, we have:

$$A_n = -\frac{\varepsilon_n(-\mathrm{i})^n J_n{}'(ka)}{H_n^{(2)\prime}(ka)} \tag{4.10}$$

The expressions derived in this section are also valid for wave numbers with a non-zero imaginary part.

4.2.2.2 Locally-reacting cylindrical scatterer in a homogeneous medium

For an infinite cylinder with a locally reacting surface impedance condition, we have $\frac{\partial p}{\partial r} = \mathrm{i}k\frac{\rho_0 c}{\rho_1 c_1}p(a)$ for $r = a$ (see equation 3.26). Using the same procedure as in section 4.2.2.1, the following expression for A_n is obtained:

$$A_n = -\frac{\varepsilon_n(-\mathrm{i})^n\left[J_n'^{(ka)} - \mathrm{i}\frac{\rho_0 c}{\rho_1 c_1}J_n(ka)\right]}{H_n^{(2)\prime}(ka) - \mathrm{i}\frac{\rho_0 c}{\rho_1 c_1}H_n^{(2)}(ka)} \tag{4.11}$$

As in the prior cases, this expression also applies to wave numbers with a non-zero imaginary part.

4.3 Validation of BEM against analytical solutions

4.3.1 Scattering of a plane wave by a perfectly rigid sphere in a non-attenuating medium

A mesh of a spherical scatterer was generated using CATIA v5 Advanced Meshing Tools (CATIA v5 website) with eight node quadrilateral elements. The sphere was chosen to be of 5 mm radius, which is representative of the dimension of the cross-section of human ribs (Mohr *et al* 2007). The external medium was assumed to have water-like properties. The speed of sound was assumed to be 1500 m s^{-1} and the medium density was taken as 1000 kg m^{-3}. The surface of the scatterer was meshed ensuring three elements per wavelength (corresponding to the wave speed in the exterior domain) at 1 MHz. This corresponds to element dimensions of 0.5 mm, resulting in a mesh containing 4610 nodes. A Burton-Miller formulation was used so that the non-uniqueness problem associated with the discretisation of the Kirchhoff-Helmholtz equation could be overcome. The scattering problem was solved at the first seven eigenfrequencies, corresponding to radial modes of the internal cavity of the sphere, to test the robustness of the Burton-Miller formulation. These occur at frequencies where

an integer number of half-wavelengths exists along the radius of the sphere, or for $ka = n\pi$, where a is the radius of the sphere and n is a positive integer. The first seven eigenfrequencies are therefore: 0.15 MHz, 0.30 MHz, 0.45 MHz, 0.60 MHz, 0.75 MHz, 0.90 MHz and 1.05 MHz. The sphere was centred at the global origin and the axis of propagation of the plane wave was chosen as the positive x-axis.

The value of the coupling coefficient α_c was varied between 0 and 1 in steps of 0.1. A fixed number of 40 iterations of the GMRES algorithm was used. The matrix-vector products in the GMRES scheme were parallelised over 150 cores of a dedicated Linux cluster. Each iteration of the GMRES algorithm took approximately two minutes to complete, leading to run times of around 80 minutes for each job. Figure 4.1 shows BEM results for the acoustic pressure magnitude along the x-axis. Results on the side of the shadow zone between 5 mm and 25 mm, resulted from the unit-amplitude plane wave excitation for the coupling coefficient being set to zero. These are compared against the analytical solution in equation (4.3). Throughout this section, the series in equation (4.3) was truncated at $n = 100$.

Figure 4.1 shows the results for the scattering of a plane wave by a perfectly rigid sphere along the x-axis, on the side of the shadow zone at the first seven eigenfrequencies corresponding to the internal radial modes of the sphere. The shadow zone is defined as the area behind the scatterer with no direct line-of-sight from the receptor to the source where the sound wave may diffract around the scatterer. BEM results using $\alpha_c = 0$ in the Burton-Miller formulation are displayed alongside results from the analytical solution in equations (4.3) and (4.4).

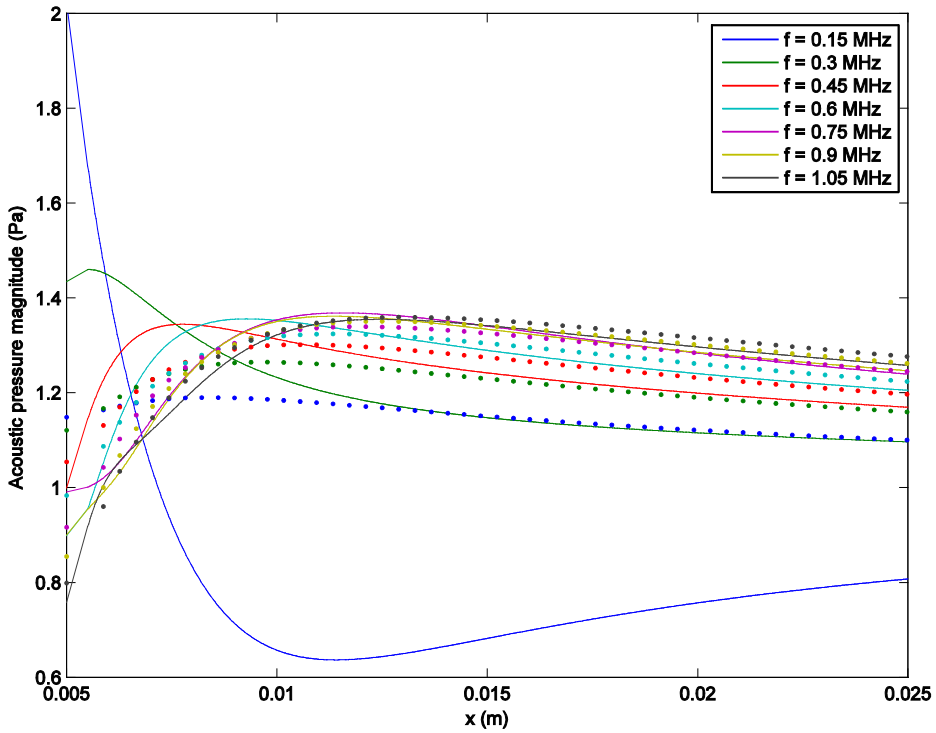

Figure 4.1 Surface Helmholtz formulation on a perfectly spherical scatterer of 5 mm radius in a non-attenuating medium. Incident field: unit amplitude 1 MHz plane wave travelling in positive x direction. Acoustic pressure magnitudes along the x-axis on the side of shadow zone. Solid lines: BEM. Dotted lines: analytical solution.

It can be seen that the results in figure 4.1 demonstrate very poor agreement against the analytical solution as a result of setting the coupling coefficient in the Burton-Miller formulation to zero. This confirms the necessity of having a non-zero coupling coefficient in this type of formulation when analysing scattering problems at frequencies close to those corresponding to the internal modes of the scatterer. The influence of the value of α_c on the acoustic pressure magnitude calculated using BEM is shown in figure 4.2. The BEM calculations were carried out at a location on the surface of the sphere, on the side of the shadow zone, positioned on the x-axis at x = 5 mm.

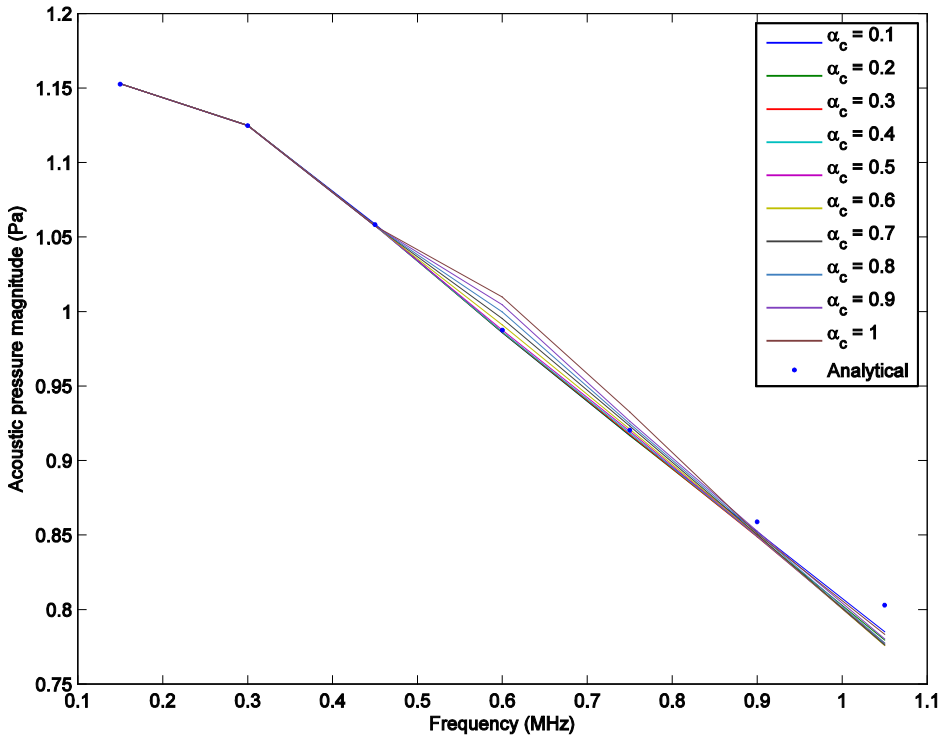

Figure 4.2 Burton-Miller formulation on a perfectly spherical scatterer of 5 mm radius in a non-attenuating medium. Incident field: unit amplitude 1 MHz plane wave travelling in positive *x* direction. Acoustic pressure magnitude calculated on the surface of the sphere, on the *x*-axis, on the side of the shadow zone. Comparison for ten values of the coupling coefficient with the analytical solution.

Figure 4.3 shows the resulting percentage difference in the BEM results in figure 4.2 compared to the analytical solution.

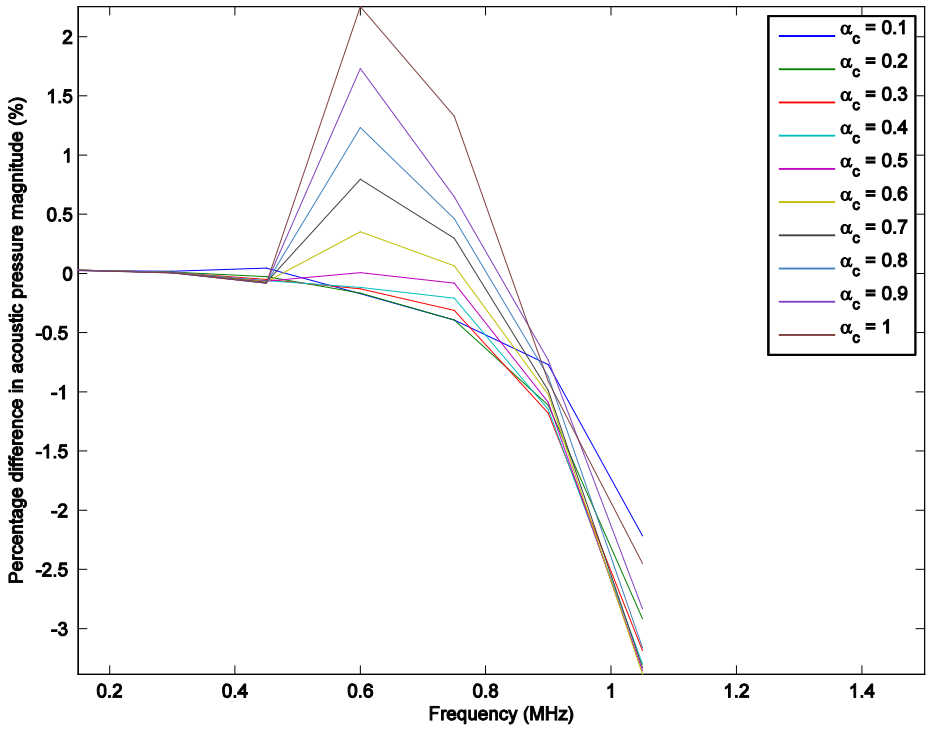

Figure 4.3 Percentage difference between acoustic pressure results in figure 4.2 and the analytical solution at the first seven eigenfrequencies, corresponding to interior radial modes of sphere. Comparison for ten values of the coupling coefficient with the analytical solution.

Figure 4.3 shows that the BEM results for the acoustic pressures on the surface of the sphere on the x-axis and on the side of the shadow zone are within -3.5% and $+2\%$ respectively of the analytical solution for all ten values of α_c and for all seven eigenfrequencies considered. However, of the values of α_c investigated here, the coupling coefficient which appears to provide the best agreement with the analytical solutions is $\alpha_c = 0.1$. For the mesh size considered here, and for 40 iterations of the GMRES algorithm, the acoustic pressure magnitude at (5, 0, 0) mm is underestimated by approximately 2%. Figure 4.4 shows the acoustic pressure magnitudes along the x-axis, on the side of the shadow zone for $\alpha_c = 0.1$ at the seven first eigenfrequencies of the interior cavity of the sphere, together with a comparison against the analytical solution.

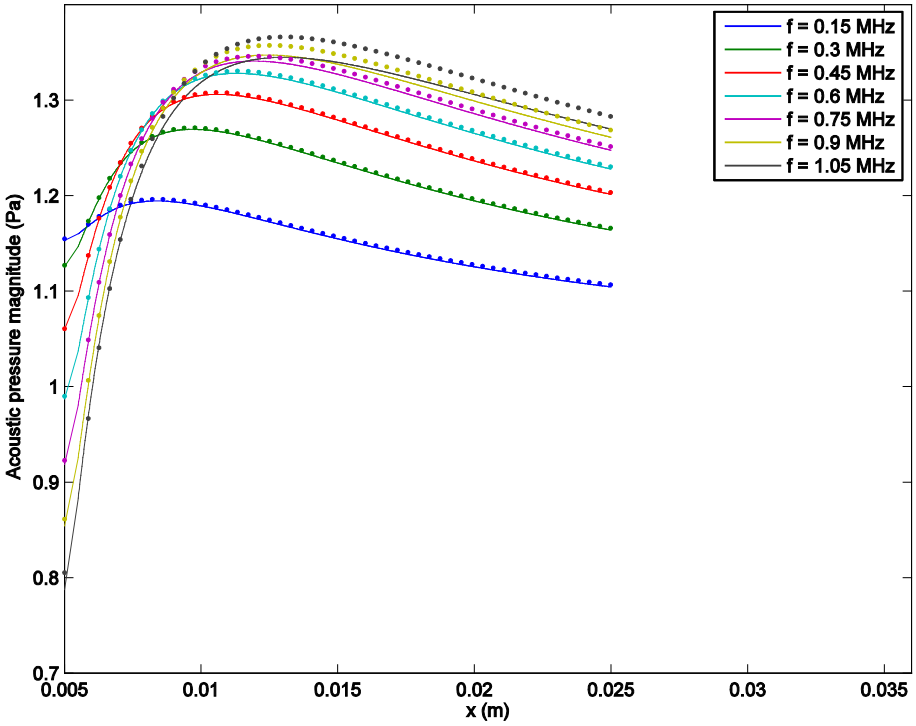

Figure 4.4 Burton-Miller formulation on a perfectly spherical scatterer of 5 mm radius in a non-attenuating medium for α_c = 0.1. Incident field: unit amplitude plane wave travelling in positive x direction. Acoustic pressure magnitudes along the x-axis on the side of the shadow zone. Solid lines: BEM. Dotted lines: analytical solution.

Figure 4.5 shows the percentage difference between the Burton-Miller BEM results in figure 4.4 and the analytical solution provided by equations (4.3) and (4.4).

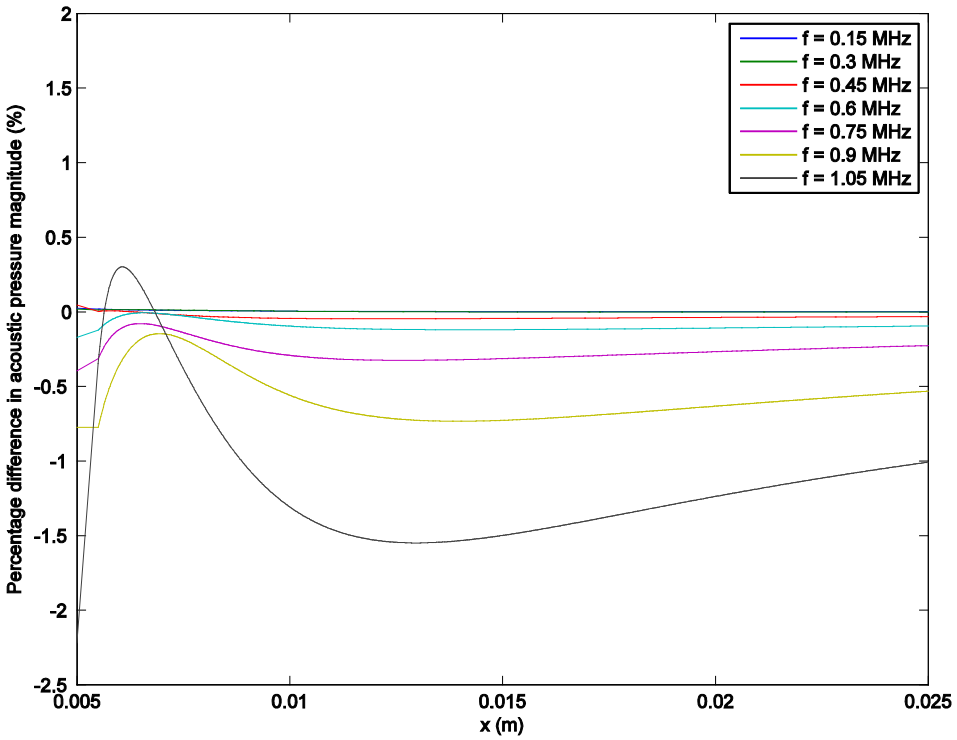

Figure 4.5 Percentage difference between acoustic pressure results in figure 4.4 and the analytical solution. Comparison along *x*-axis on the side of the shadow zone at seven first eigenfrequencies corresponding to interior modes of the sphere with analytical solution.

Figure 4.4 and 4.5 show agreement of the BEM results along the *x*-axis on the side of the shadow zone within −2% and +0.5% of the analytical solution at the seven first eigenfrequencies corresponding to interior radial modes of the sphere. It can be seen that the agreement deteriorates as the excitation frequency increases. This is expected, as the mesh density was kept the same throughout these analyses. Use of a finer mesh will yield better agreement against the analytical solution at higher frequencies, as will be demonstrated in section 4.3.3.

In order to justify the use of 40 iterations of the GRMES scheme, a graph of the acoustic pressure magnitude at (5, 0, 0) mm on the surface of the sphere was plotted as a function of the number of GMRES iterations (see figure 4.6). A coupling coefficient of $\alpha_c = 0.1$ was used.

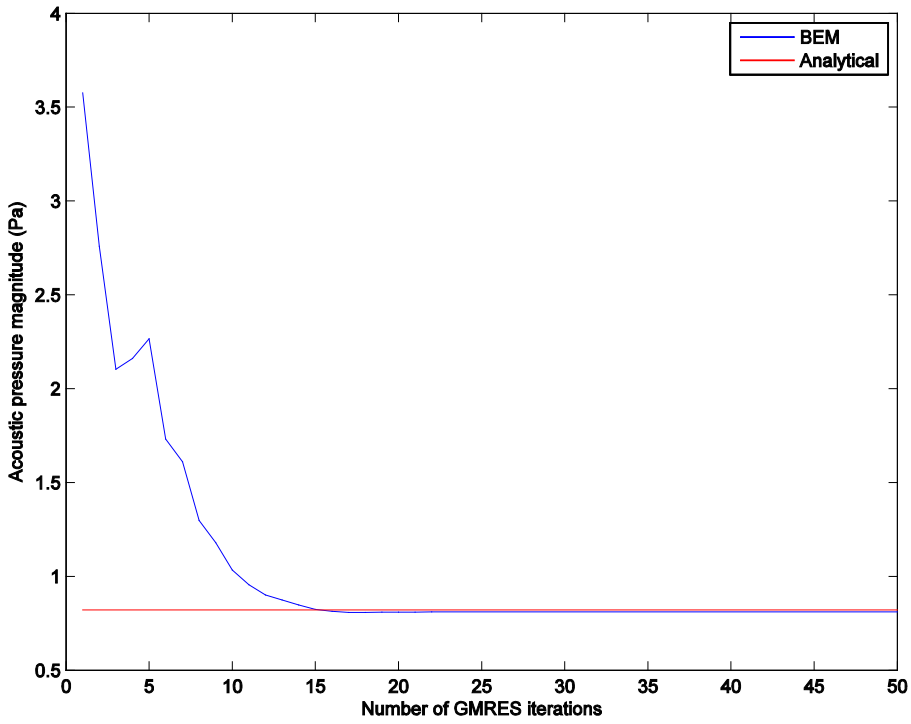

Figure 4.6 Burton-Miller formulation on a perfectly spherical scatterer of 5 mm radius in a non-attenuating medium for α_c = 0.1. Incident field: unit amplitude plane wave travelling in positive x direction. Acoustic pressure magnitude on the surface of the sphere at (5, 0, 0) mm as a function of the number of GMRES iterations. Comparison with analytical solution.

Figure 4.7 shows the percentage difference between the Burton-Miller BEM results in figure 4.6 and the analytical solution provided by equations (4.3) and (4.4).

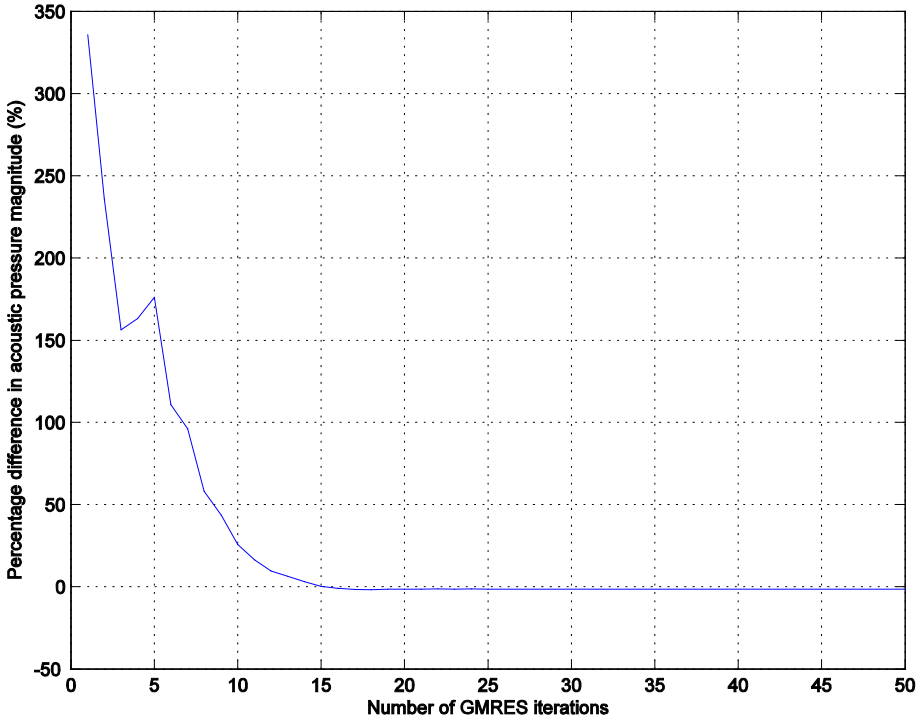

Figure 4.7 Percentage difference between acoustic pressure results in figure 4.6 and the analytical solution.

In this case, it can be seen that the GMRES scheme converges to within −1.4% of the analytical solution after 20 iterations. Beyond this number of iterations, there is little improvement in the accuracy of the BEM results. This is most likely due to discretisation errors in the mesh of the surface of the sphere.

4.3.2 Scattering of a plane wave by a perfectly rigid sphere in an attenuating medium

The calculations described in section 4.3.1 were repeated for the same sphere and incident pressure field, this time assuming a complex speed of sound in the exterior domain. The attenuation coefficient of plane waves was assumed to be 12.3 Np m^{-1} at 1 MHz. This value is representative of that of liver (Duck 1990, p104). The acoustic medium properties considered as part of the underlying work were chosen to be representative of those of soft tissue and are as follows: the medium density is $\rho = 1000$ kg m^{-3}. The complex wave number k is given by (Kinsler *et al*, p143):

$$k = \frac{\omega}{c_0} - \mathrm{i}\alpha \tag{4.12}$$

where c_0 = 1500 m s^{-1} and α is the attenuation coefficient in the propagating medium. The complex speed of sound in the medium is therefore $c = \frac{\omega}{k} = 1500 + 4.4046\mathrm{i}$ m s^{-1}. A linear dependency of the attenuation coefficient on frequency was assumed. This is also appropriate for liver tissue (Lin *et al* 1987). The GMRES scheme was again parallelised over 150 cores. Each GMRES iteration took about one minute to complete, as terms resulting from the discretisation of the hypersingular integral in equation (3.27) were not required to be evaluated. Run times for each job were therefore of the order of 40 min.

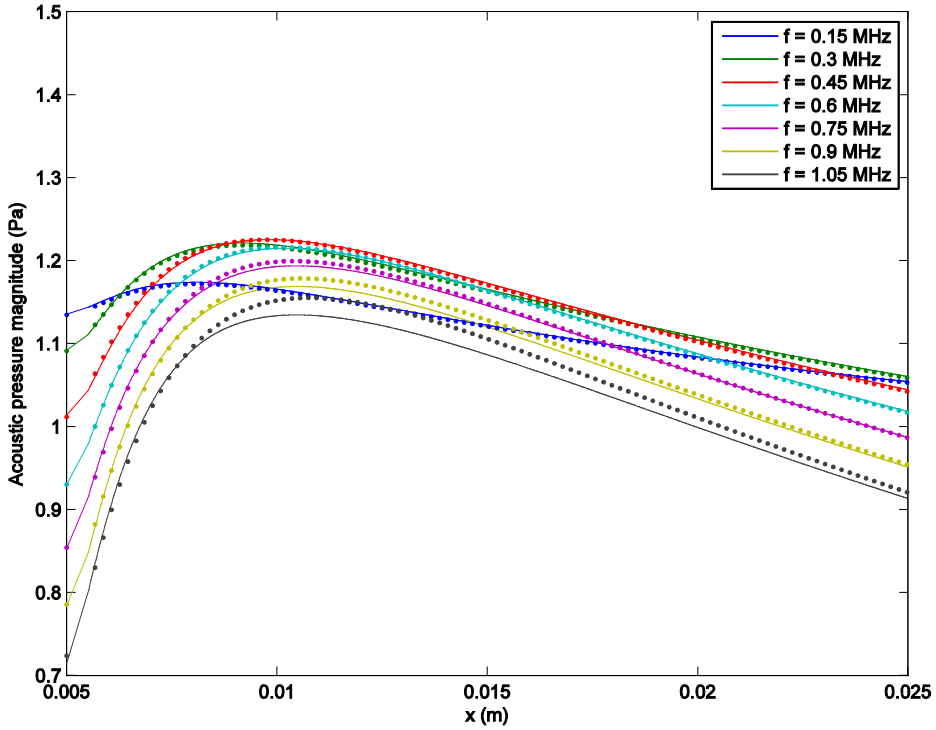

Figure 4.8 Surface Helmholtz formulation for a perfectly rigid spherical scatterer of 5 mm radius in an attenuating medium with properties representative of human liver. Incident field: unit amplitude plane wave travelling in positive x direction. Acoustic pressure magnitudes along the x-axis on the side of the shadow zone. Solid lines: BEM. Dotted lines: analytical solution.

Figure 4.9 shows the percentage difference between the BEM results in figure 4.8 and the analytical solution in equations (4.3) and (4.4).

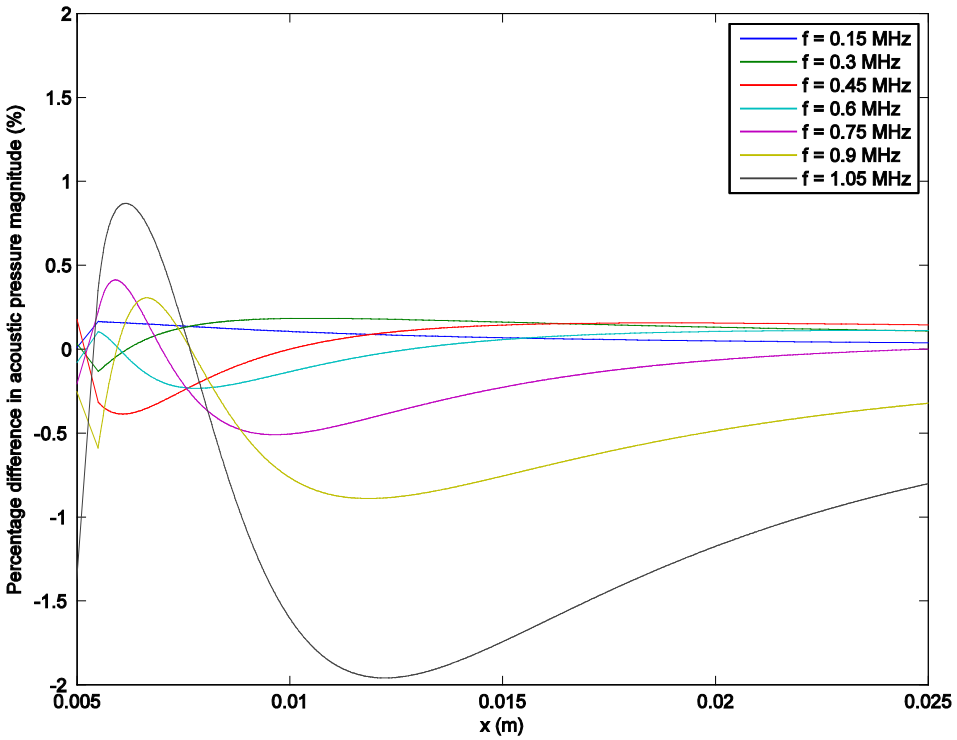

Figure 4.9 Percentage difference between acoustic pressure results in figure 4.6 and analytical solution. Comparison along *x*-axis on the side of the shadow zone at seven first eigenfrequencies corresponding to interior modes of sphere against analytical solution.

Figures 4.8 and 4.9 show agreement of the BEM results along the *x*-axis between –2% and +1% of the analytical solution at the seven first eigenfrequencies corresponding to interior radial modes of the sphere. It can be seen that, as described by Colton and Kress (1983, p81 and p84), using a wave number with a non-zero imaginary part can indeed help eliminate the non-uniqueness problem associated with the fictitious modes of the cavity inside the scatterer. For an attenuation coefficient which is representative of that of human liver, figure 4.9 demonstrates that a Burton-Miller formulation may not be required. As with results in section 4.3.2, the agreement of the BEM results with the analytical solution tends to worsen as the excitation frequency increases. Again, this is due to the mesh density being maintained at three elements per wavelength at 1 MHz.

4.3.3 Scattering of a plane wave by a locally reacting sphere in an attenuating medium

The term in the surface Helmholtz integral equation containing the normal derivative of the acoustic pressure was now introduced in order to implement a locally reacting surface with a known specific admittance, described by the Dirichlet boundary condition in equation (3.41). The properties of the scatterer were chosen to be representative of rib bone. The density of the scatterer was assumed to be 1912 kg m^{-3}

and the speed of sound of longitudinal waves 4080 m s^{-1} (Wein *et al* 2008). The attenuation coefficient of the scatterer was assumed to be 47.2 Np m^{-1} at 1 MHz (El-Brawany *et al* 2009). The analysis described in section 4.3.2 was then repeated. The comparison of the BEM results with the analytical solution in equations (4.3) and (4.5) is displayed in figure 4.10.

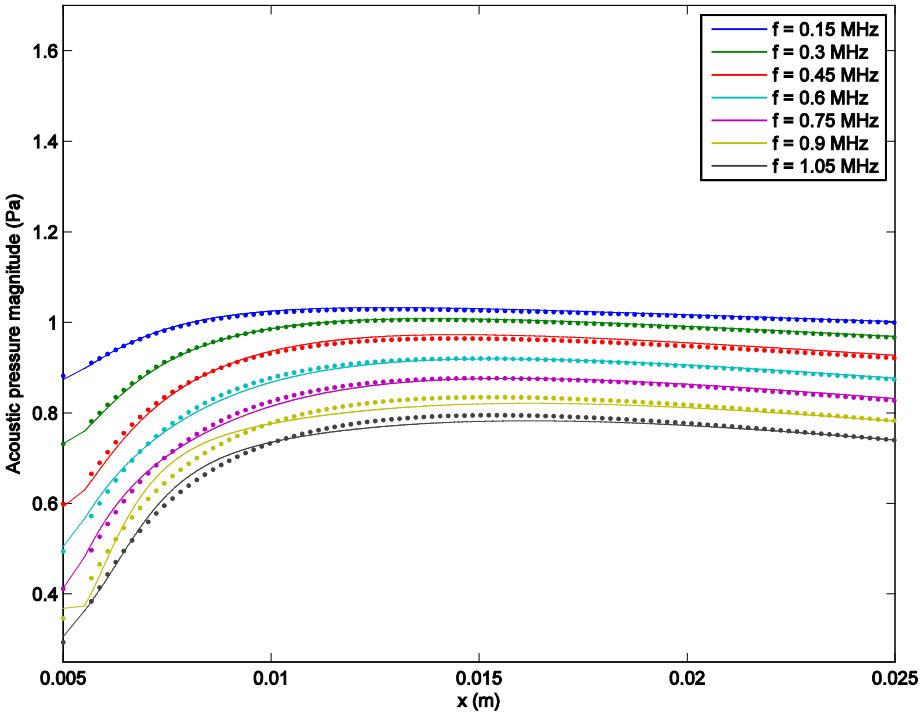

Figure 4.10 Surface Helmholtz formulation on a locally reacting spherical scatterer of 5 mm radius with properties representative of rib bone in an attenuating medium with properties representative of human liver. Incident field: unit amplitude plane wave travelling in positive x direction. Acoustic pressure magnitudes along the x-axis on the side of the shadow zone. Solid lines: BEM. Dotted lines: analytical solution.

Figure 4.11 shows the percentage difference between the BEM results in figure 4.10 and the analytical solution in equations (4.3) and (4.5).

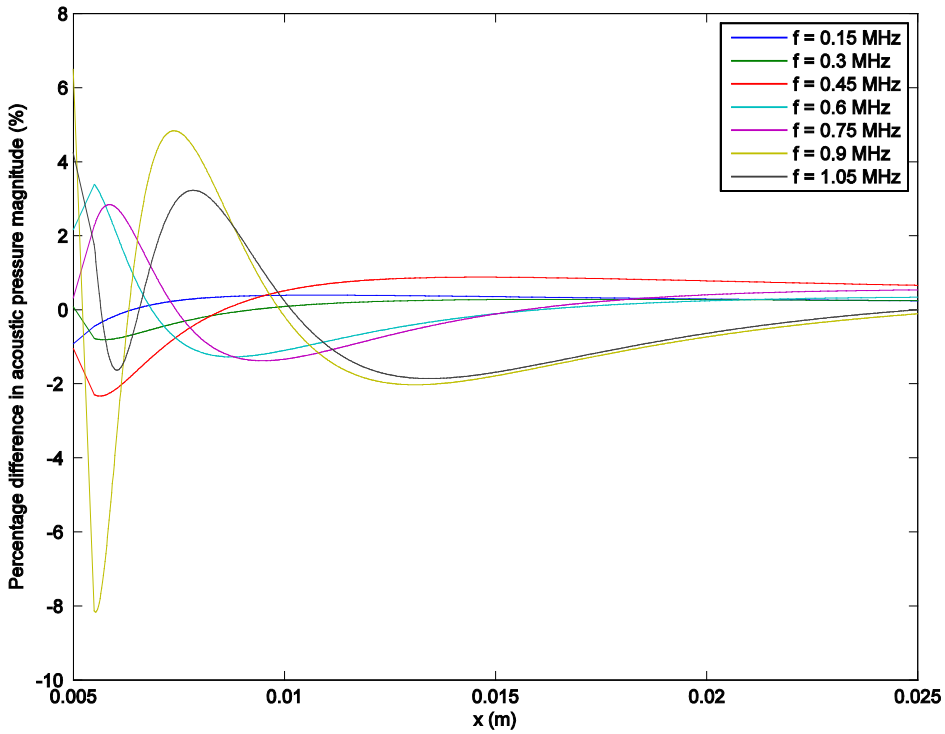

Figure 4.11 Percentage difference between acoustic pressure results in figure 4.10 and analytical solution. Comparison along *x*-axis on the side of the shadow zone at seven first eigenfrequencies corresponding to interior modes of sphere against analytical solution.

Figure 4.11 shows that BEM acoustic pressure predictions at distances between 10 mm and 25 mm from the surface of the sphere along the *x*-axis and the shadow zone are within ±2% of the analytical solution provided by equations (4.3) and (4.5). At an excitation frequency of 0.9 MHz, the BEM predictions disagree with the analytical solution by 8% between x = 5 mm and x = 0.01 mm. This suggests that, for the same scatterer size and incident field, a finer mesh is required than for a perfectly rigid scatterer when implementing a Dirichlet boundary condition.

Further results are shown below (see figure 4.12) for a 1 MHz incident plane wave for the same spherical scatterer but with varying mesh densities. In addition to the mesh density employed in previous examples, a finer mesh was generated ensuring six elements per wavelength (corresponding to the wave speed in the exterior domain) at 1 MHz, which corresponds to element dimensions of 0.25 mm. This resulted in a mesh containing 47036 nodes. A comparison of the BEM results along the *x*-axis and on the side of the shadow zone of the locally reacting sphere is displayed in figure 4.12 for the coarser and finer meshes, alongside results from the analytical solution in equation (4.3) and (4.5).

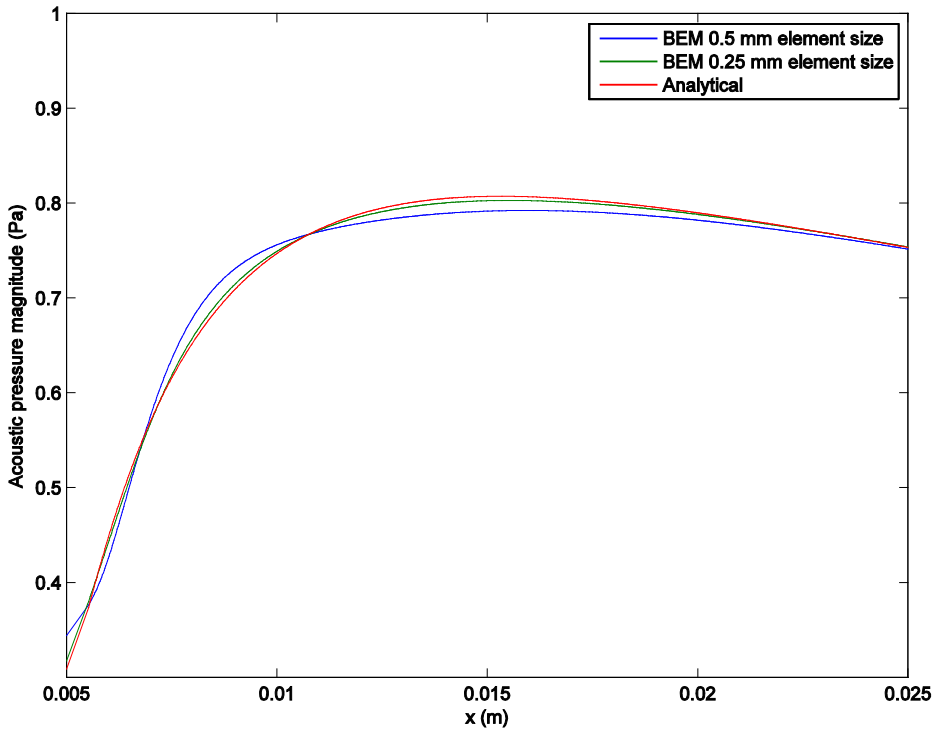

Figure 4.12 Surface Helmholtz formulation on a locally reacting spherical scatterer of 5 mm radius with properties representative of rib bone immersed in an attenuating medium with properties representative of human liver. Incident field: 1 MHz unit amplitude plane wave travelling in positive x direction. Acoustic pressure magnitudes along the x-axis on the side of the shadow zone.

The percentage difference between BEM results for both mesh densities and the analytical solution is shown in figure 4.13.

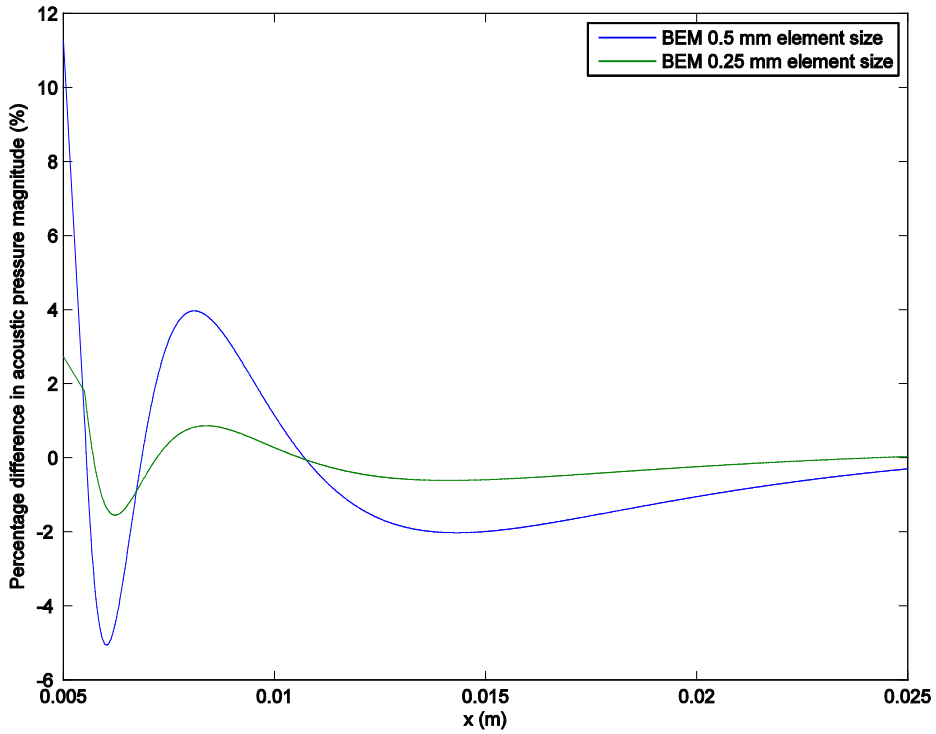

Figure 4.13 Percentage difference between acoustic pressure results in figure 4.12 and analytical solution. Comparison along *x*-axis on the side of the shadow zone at 1 MHz.

Figures 4.12 and 4.13 show that both mesh densities produce results for the acoustic pressure magnitude on the side of the shadow zone and on the *x*-axis that are within ±2% of the analytical solution for values of *x* between 10 mm and 25 mm away from the sphere. However, at the surface of the sphere, the BEM results for the lower mesh density case (i.e. 0.5 mm element size) show that the acoustic pressure on the surface of the sphere at $x = 5$ mm is overestimated by approximately 11%. Meshing scatterers of dimensions which are of the order of human ribs using a mesh density of six elements per wavelength is likely to result in BEM problems with a very large number of degrees of freedom, thus increasing both RAM requirements and computational times. Nevertheless, investigation of the case of a locally reacting scatterer in a dissipative medium is a crucial component of this thesis. At this stage, it is important that a compromise be sought between computational run times and accuracy. A factor which requires consideration for this compromise is the end-goal of this thesis. This is the prediction of the acoustic pressure on the surface of the ribs, the rate of energy absorption per unit mass (Nyborg 1981), and the investigation of means of reducing these quantities below a specified threshold, whilst also maintaining focal pressures above another specified threshold. Hence, although comparisons in the shadow zone are important, they are also more likely to be contaminated by numerical noise, since acoustic pressures here will be of a lower magnitude than at locations where the

wavefront is insonating the scatterer. Acoustic pressure magnitudes on the surface of the sphere are displayed in figures 4.14 and 4.15 for the case of 0.5 mm and 0.25 mm element sizes, respectively.

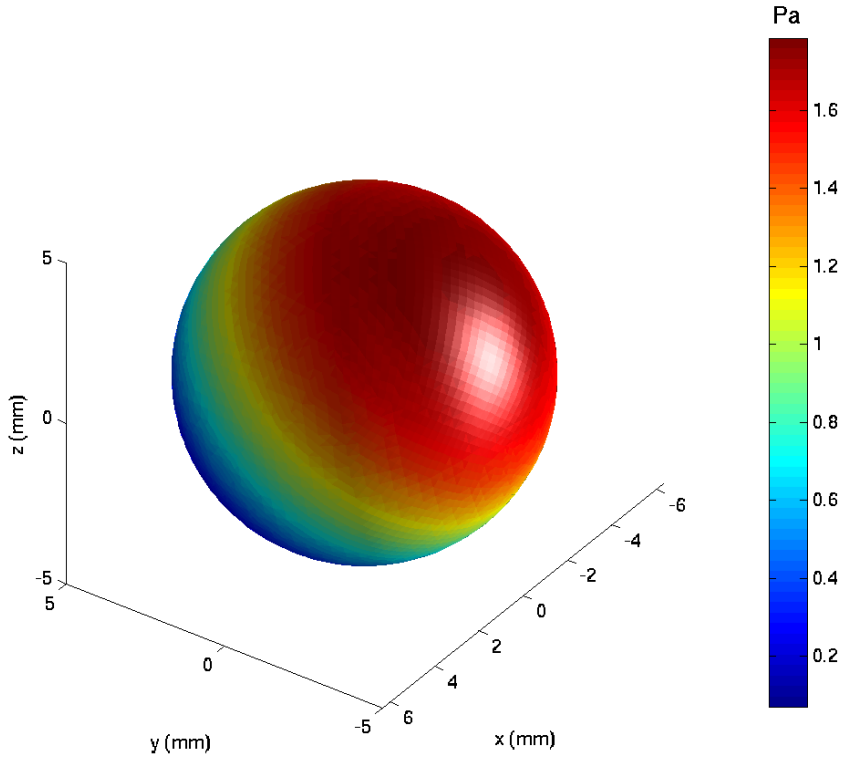

Figure 4.14 Acoustic pressure magnitude on the surface of a locally reacting 5 mm radius sphere insonated by a 1 MHz plane wave travelling in the positive *x* direction in a dissipative medium. Element dimensions: 0.5 mm (three elements per wavelength mesh density).

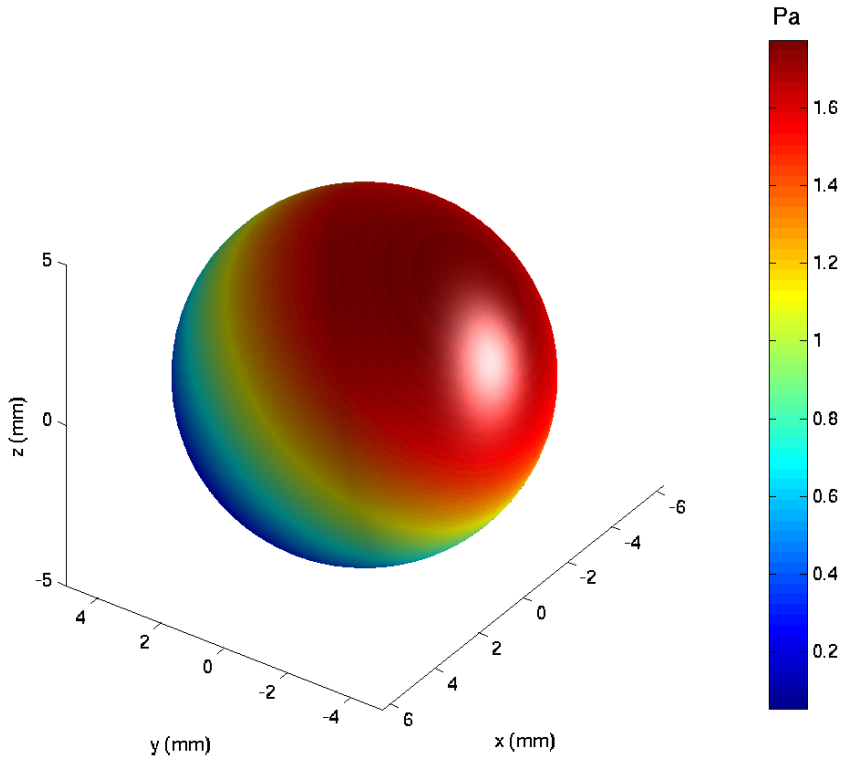

Figure 4.15 Acoustic pressure magnitude on the surface of a locally reacting 5 mm radius sphere insonated by a 1 MHz plane wave travelling in the positive *x* direction in a dissipative medium. Element dimensions: 0.25 mm (six elements per wavelength mesh density).

The acoustic pressure resulting from BEM calculations for these mesh densities was compared at locations (−5, 0, 0) mm, (0, 5, 0) mm and (0, 0, 5) mm. These locations were chosen as it is intuitively expected that high, moderate and low pressure magnitudes will respectively occur at the first, second and third location. The results are summarised in table 4.1.

Table 4.1: Acoustic pressure magnitude at selected locations on the surface of a 5 mm radius locally reacting sphere insonated by a 1 MHz plane wave travelling along the positive *x* direction in a dissipative medium. Comparison for two BEM mesh densities against the analytical solution.

Position on sphere surface (mm)	Acoustic pressure magnitude, BEM, 0.5 mm element size (Pa)	Acoustic pressure magnitude, BEM, 0.25 mm element size (Pa)	Acoustic pressure magnitude, Analytical solution (Pa)
(−5, 0, 0)	1.75	1.77	1.78
(0, 5, 0)	0.924	0.927	0.926
(0, 0, 5)	0.344	0.318	0.309

Table 4.1 shows that acoustic pressures are more accurately estimated using BEM at locations on the sphere which are not in the shadow zone. The acoustic pressure magnitude on the surface of the sphere at (–5, 0, 0) mm obtained using BEM with the coarser mesh is underestimated by around 1.3% when compared with the analytical solution.

4.3.4 Scattering of a plane wave by a perfectly rigid cylinder in a non-attenuating medium

Numerical experiments involving the scattering of a plane wave by a sphere are important as they provide a means of benchmarking BEM results against a known analytical solution. It is, however, useful to consider geometrical shapes which bear a closer resemblance to ribs, for which there are also known analytical solutions. One such shape is the infinite cylinder. Whilst the BEM implementation was carried out only in 3D, it is useful to consider a cylinder with hemispherical end-caps, whose height is much larger than its radius. The dimensions of this geometrical shape considered here will be of the order of those of a human rib. A total cylinder height of 22 cm was opted for (including the end-caps) and the radius was chosen as 1 cm. The radius of each hemispherical end-cap was chosen as 0.5 cm. It was assumed that the incident acoustic pressure field was that of a unit-amplitude plane wave travelling in the positive z direction. The axis of the cylinder was chosen to be the Cartesian x-axis (see figure 4.16).

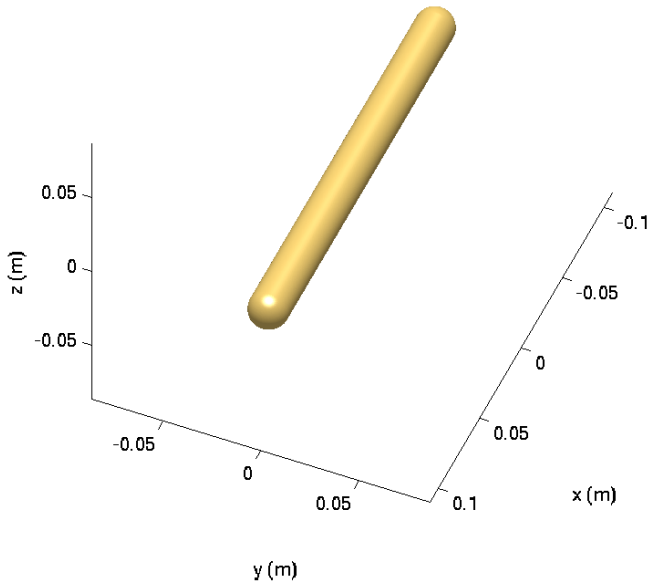

Figure 4.16 Cylindrical scatterer with hemispherical end-caps used for BEM validation: height 22cm and radius 1 cm.

When meshing the surface of this cylinder with three elements per wavelength for analysis at 1 MHz (i.e. using an element length of 0.5 mm), the resulting mesh contains 168655 nodes. While comparisons of BEM analyses on such a cylinder against the analytical solutions in equations (4.9), (4.10) and (4.11) would not be expected to yield exact agreement, in part due to effects of diffraction of the incident waves by the end-caps, features of the analytical solution can be expected to be reproduced. Furthermore, the large value of the cylinder height compared with its radius will help ensure comparison against the analytical solution for a plane wave scattered by an infinite cylinder at locations close to the scatterer. Figure 4.17 shows comparison of the BEM results against the analytical solution on the side of the shadow zone and along the z-axis between z = 1.2 cm and z = 20 cm. A Burton-Miller formulation was used, with the coupling coefficient set to 0.1. 40 iterations of the GMRES scheme were used. The analysis was parallelised over 150 cores of a dedicated computer cluster, resulting in run times of approximately 10 minutes per GMRES iteration.

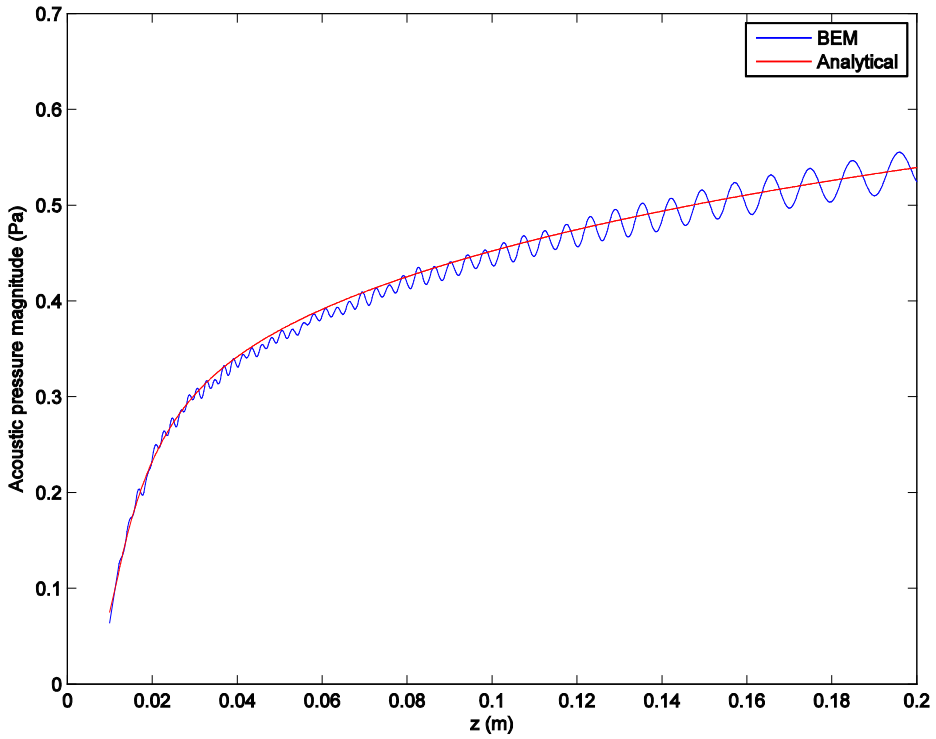

Figure 4.17 Burton-Miller formulation on a perfectly rigid cylindrical scatterer with hemispherical end-caps with α_c = 0.1. Cylinder height: 22 cm. Cylinder radius: 1cm. Incident field: unit amplitude 1 MHz plane wave travelling in positive z direction in a non-attenuating medium. Acoustic pressure magnitudes along the z-axis on the side of the shadow zone. The analytical solution for an infinite cylinder is shown for comparison.

Figure 4.17 shows good agreement between the analytical solution and the BEM formulation at distances less than 0.2 cm from the surface of the cylinder along the z-axis on the side of the shadow zone of the scatterer. At distances further away from the cylinder outer wall and on the side of the shadow zone, oscillations of the BEM results about the analytical solution are apparent. This is to be expected and corresponds to constructive and destructive interference of the edge wave at the hemispherical end-caps (Morse and Ingard 1968, p449). A bias is nevertheless present in which the BEM results appear somewhat shifted from the analytical solution. This is particularly noticeable in figure 4.17 at z = 5 cm where the BEM predicted pressure magnitudes are lower than those predicted by the analytical solution, even when accounting for the oscillations. This bias was also noticeable on rigid spherical scatterers, as discussed in section 4.3.1. As with the spherical scatterers, it is likely that refining the mesh would result in better agreement, although further calculations would be necessary to confirm this.

A 3D plot of the acoustic pressure magnitudes on the surface of this cylinder is shown in figure 4.18.

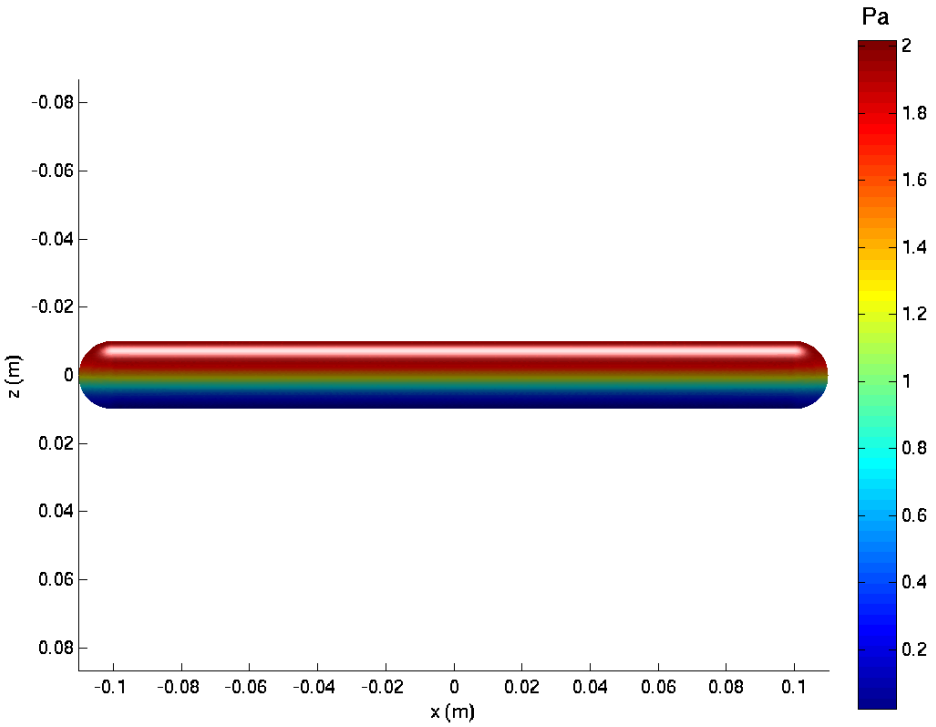

Figure 4.18 Burton-Miller formulation on a perfectly rigid cylindrical scatterer with hemispherical end-caps with α_c = 0.1. Cylinder height: 22 cm. Cylinder radius: 1cm. Incident field: unit amplitude 1 MHz plane wave travelling in positive z direction in a non-attenuating medium. Acoustic pressure magnitude on the surface of the scatterer is shown.

Figure 4.18 clearly shows a doubling of acoustic pressure at locations on the surface for which z = 1 cm, which are exposed to normal incidence of the plane wave. This result is expected for a perfectly reflecting surface.

Figure 4.19 shows a visualisation of the acoustic pressure magnitude in the exterior domain at locations in the y-z plane.

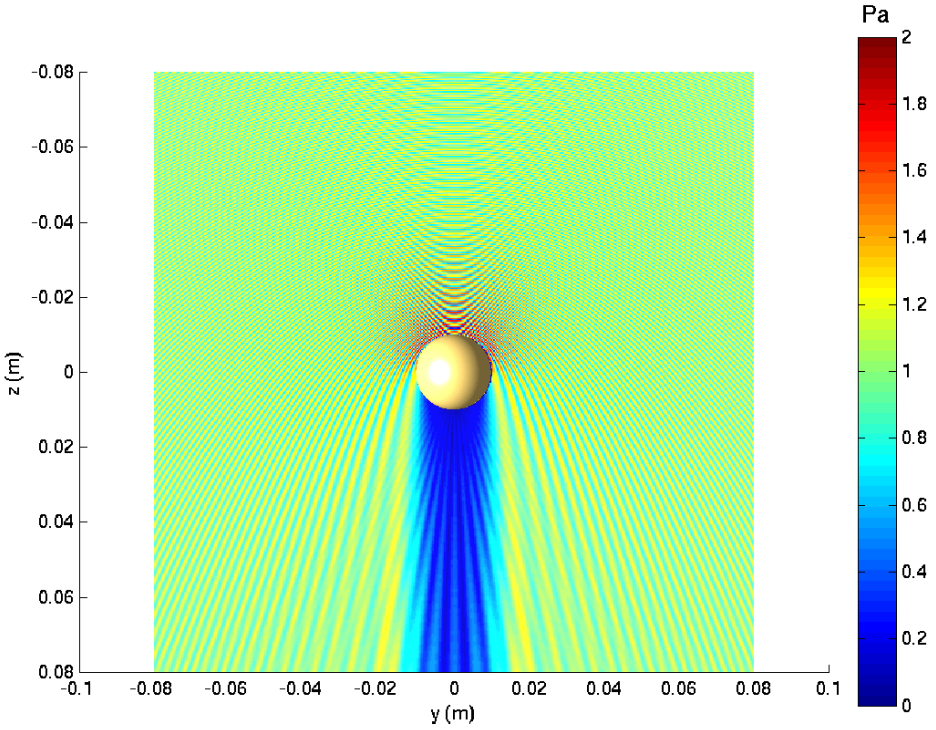

Figure 4.19 Burton-Miller formulation on a perfectly rigid cylindrical scatterer with hemispherical end-caps with α_c = 0.1. Cylinder height: 22 cm. Cylinder radius: 1cm. Incident field: unit amplitude 1 MHz plane wave travelling in positive z direction in a non-attenuating medium. Acoustic pressure magnitude in the y-z plane.

The shadow zone is clearly visible and is described by the region where acoustic pressures are significantly lower than at other field locations, i.e. at positive values of z close to the cylinder and for $y = 0$.

4.3.5 Scattering of a plane wave by a perfectly rigid cylinder in an attenuating medium

The calculations in section 4.3.4 were repeated for the same scatterer and incident pressure field, this time assuming a complex speed of sound of 1500 + 4.405i m s^{-1} in the exterior domain. This corresponds to an attenuation coefficient of plane waves of 12.3 Np m^{-1} at 1 MHz. This further validation was carried out to justify setting the coupling coefficient in the Burton-Miller formulation to zero. As in section 4.3.4, the analysis was parallelised over 150 cores of a dedicated computer cluster, resulting in approximately five minutes per GMRES iteration. The run times were about half of those for the scattering analysis of the cylinder in a non-attenuating medium. This is due to the fact that, in the surface Helmholtz formulation employed here, terms resulting

from the discretisation of the hypersingular integral in equation (3.27) need not be computed. A comparison between the analytical solution and BEM calculations on the side of the shadow zone is displayed in figure 4.20.

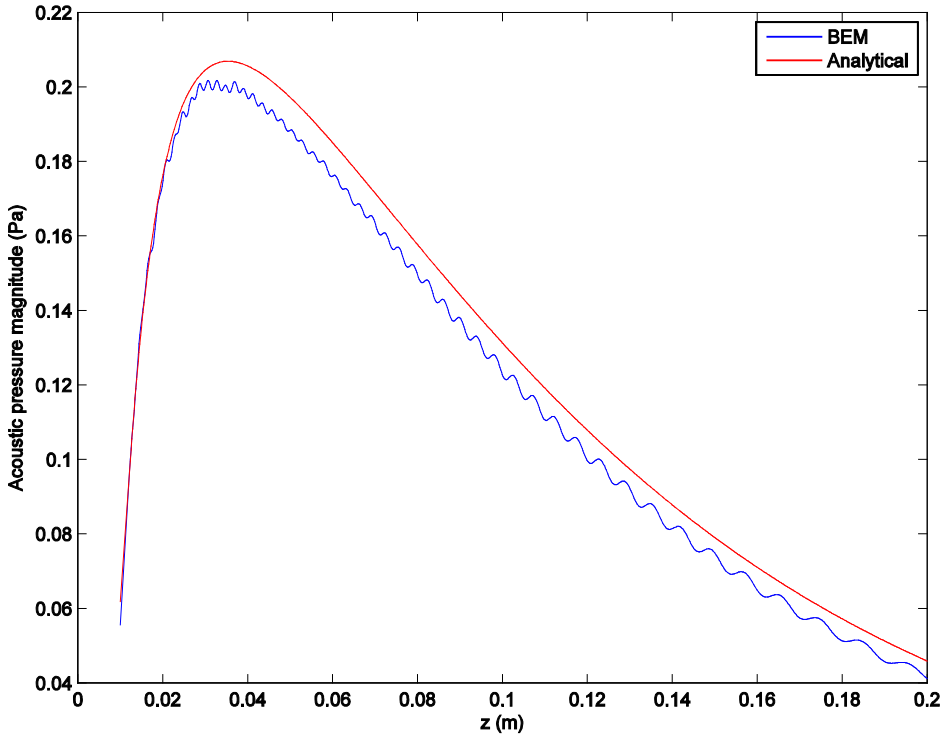

Figure 4.20 Surface Helmholtz formulation on a perfectly rigid cylindrical scatterer with hemispherical end-caps (α_c = 0). Cylinder height: 22 cm. Cylinder radius: 1cm. Incident field: unit amplitude 1 MHz plane wave travelling in positive z direction in an attenuating medium. Acoustic pressure magnitudes along the z-axis on the side of the shadow zone. Comparison against analytical solution for an infinite cylinder.

Figure 4.20 shows good agreement with the analytical solution for an infinite cylinder and the BEM implementation of the Helmholtz integral equation for a finite cylinder, at distances less than 0.2 cm from the surface of the cylinder along the z-axis on the side of the shadow zone. As in section 4.3.4, oscillations about the analytical solution can be observed in the BEM results. Again, these are due to constructive and destructive interference from the waves diffracted by the end-caps of the cylinder. Figure 4.20 displays no artefacts of numerical instability associated with the non-uniqueness of the solution of the discretised version of equation (3.27), demonstrating that any fictitious internal modes of the scatterers are being damped out, as was the case for the spherical scatterer (see section 4.3.2). As in figure 4.17, there appears to be a bias in the BEM results relative to the analytical solution. It is again likely that the BEM results are slightly underestimated due to the mesh density used.

The acoustic pressure magnitude on the surface of the locally reacting cylinder resulting from a unit amplitude 1 MHz incident plane travelling along the positive z-axis is displayed in figure 4.21.

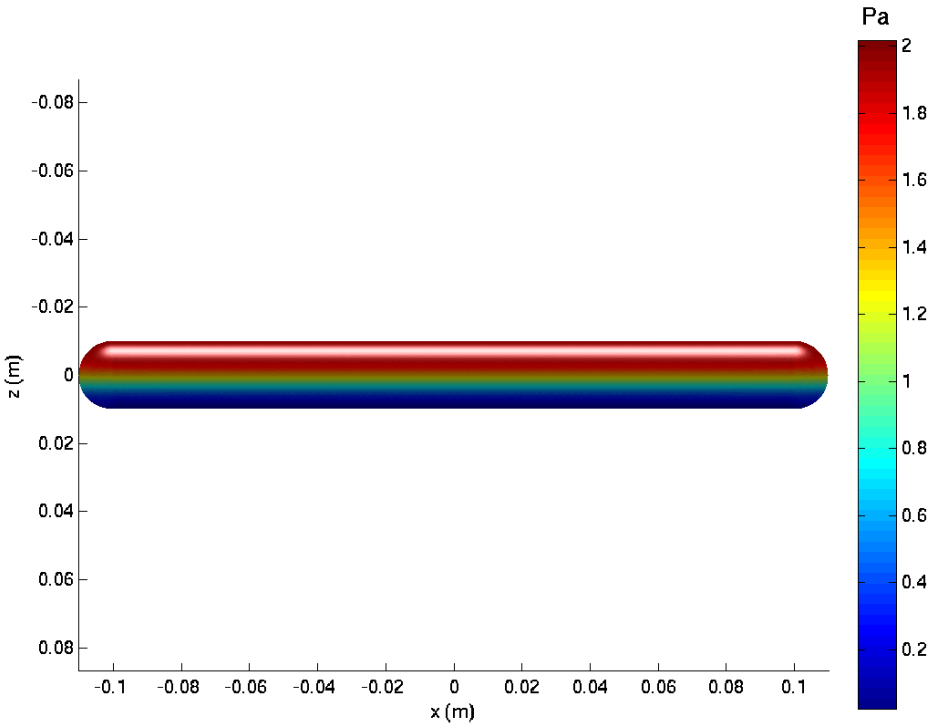

Figure 4.21 Surface Helmholtz formulation on a perfectly rigid cylindrical scatterer with hemispherical end-caps with α_c = 0.1. Cylinder height: 22 cm. Cylinder radius: 1cm. Incident field: unit amplitude 1MHz plane wave travelling in positive z direction in an attenuating medium. Acoustic pressure magnitude on the surface of the scatterer is displayed.

The corresponding acoustic pressure magnitudes in the exterior domain are displayed at locations in the y-z plane in figure 4.22.

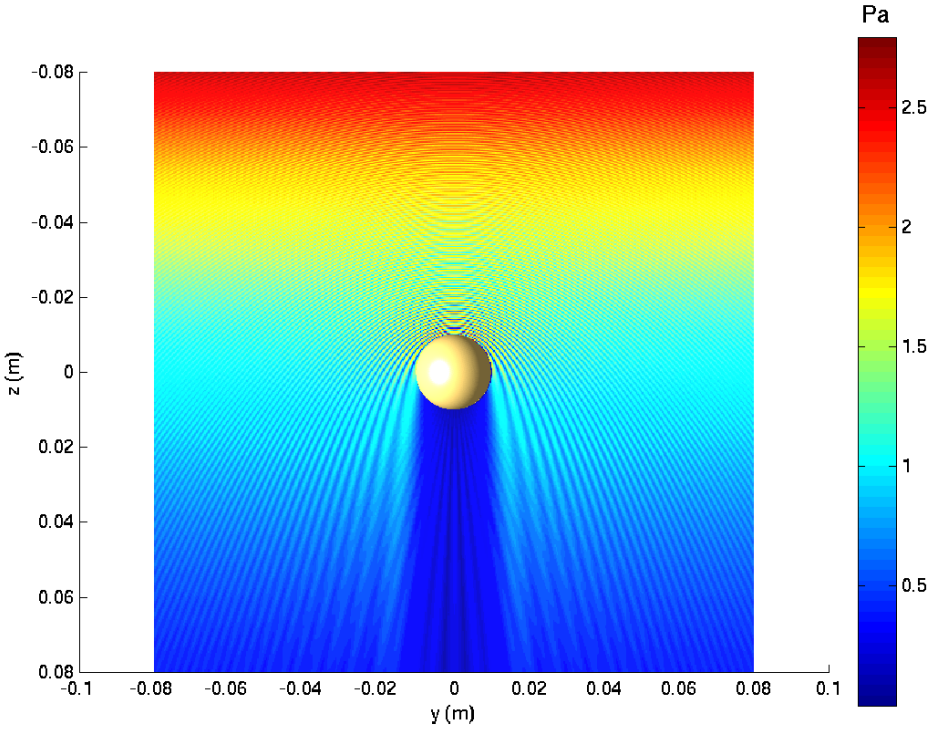

Figure 4.22 Surface Helmholtz formulation on a perfectly rigid cylindrical scatterer with hemispherical end-caps. Cylinder height: 22 cm. Cylinder radius: 1cm. Incident field: unit amplitude 1 MHz plane wave travelling in positive z direction in an attenuating medium. Acoustic pressure magnitude in the y-z plane.

As in figure 4.19, the shadow zone is clearly visible. The average acoustic pressure magnitude decays in the positive z direction, due to the implementation of a speed of sound with a non-zero imaginary part.

4.3.6 Scattering of a plane wave by a locally reacting cylinder in an attenuating medium

The term in the surface Helmholtz integral equation (3.19) which contains the normal derivative of the acoustic pressure was now accounted for, in order to implement the Dirichlet boundary condition described by equation (3.26). The properties of the scatterer were representative of rib bone, as described in section 4.3.3: the density of the scatterer was set to be 1912 kg m^{-3} and the speed of sound of longitudinal waves to 4080 m s^{-1}. An attenuation coefficient of 47.2 Np m^{-1} at 1 MHz was assumed. The analysis described in section 4.3.5 was then repeated. The results were compared against the analytical solution for scattering by an infinite cylinder in equations (4.9) and (4.11). When parallelised over 150 cores, run times were approximately 5 minutes

per GMRES iteration, thus indicating that the computation of terms involving the Dirichlet boundary does not add significant extra time to the analysis.

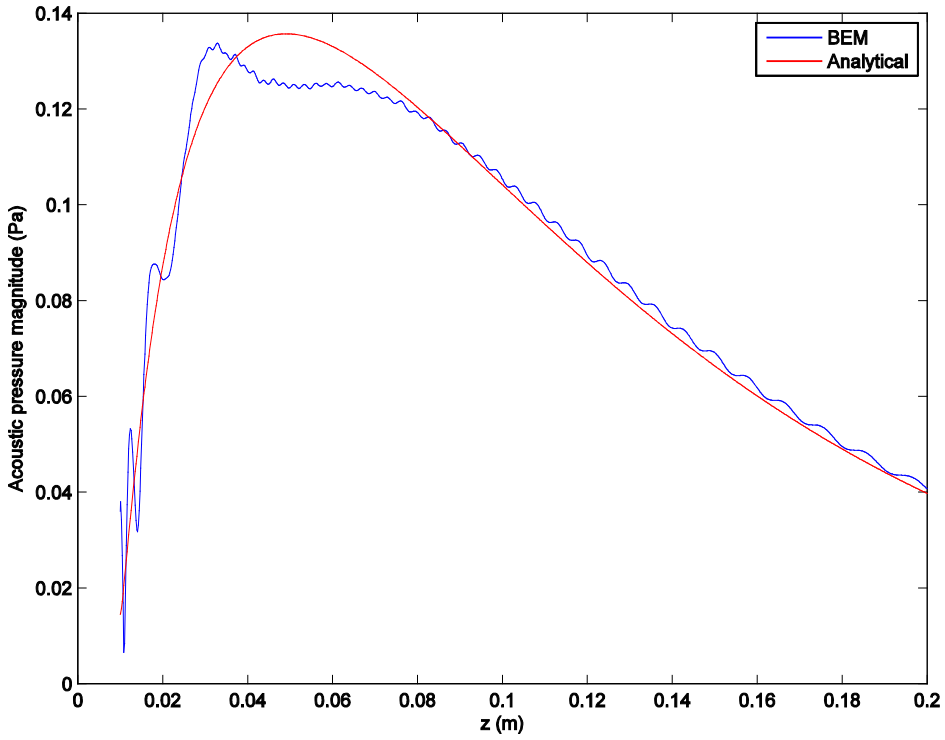

Figure 4.23 Surface Helmholtz formulation on a locally reacting cylindrical scatterer with hemispherical end-caps. Cylinder height: 22 cm. Cylinder radius: 1cm. Incident field: unit amplitude 1 MHz plane wave travelling in positive z direction in an attenuating medium. Mesh density: three elements per wavelength. Acoustic pressure magnitudes along the z-axis on the side of the shadow zone. Comparison against analytical solution for an infinite cylinder.

The acoustic pressure on the surface of the locally reacting cylinder resulting from a unit amplitude 1 MHz incident plane travelling along the positive z-axis is displayed in figure 4.24.

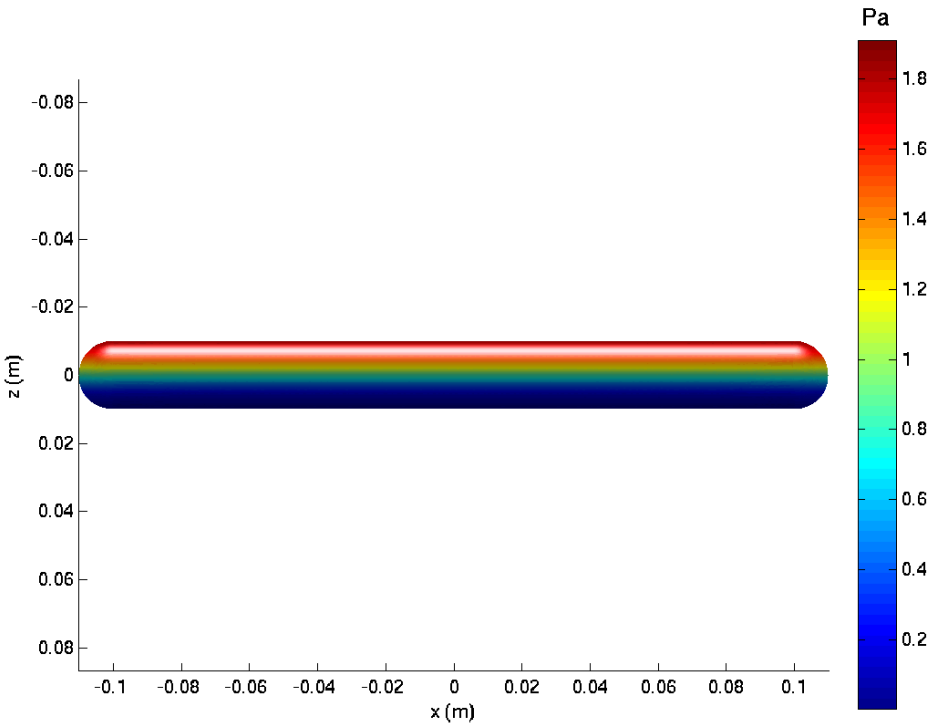

Figure 4.24 Surface Helmholtz formulation on a locally reacting cylindrical scatterer with hemispherical end-caps. Cylinder height: 22 cm. Cylinder radius: 1cm. Incident field: unit amplitude 1 MHz plane wave travelling in positive *z* direction in an attenuating medium. Mesh density: three elements per wavelength. Acoustic pressure magnitude on the surface of the scatterer.

The acoustic pressure magnitude at field locations in the *y*-*z* plane is displayed in figure 4.25.

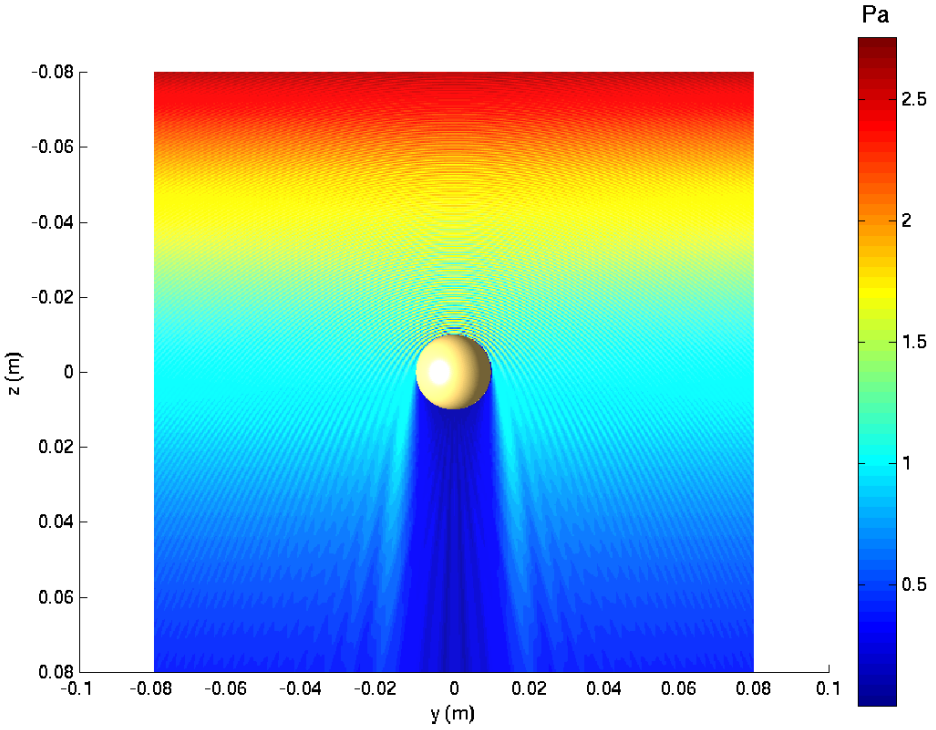

Figure 4.25 Surface Helmholtz formulation on a locally reacting cylindrical scatterer with hemispherical end-caps. Cylinder height: 22 cm. Cylinder radius: 1cm. Incident field: unit amplitude 1 MHz plane wave travelling in positive z direction in an attenuating medium. Mesh density: three elements per wavelength. Acoustic pressure magnitude in the y-z plane.

In addition to the oscillations caused by diffraction of the incident wave by the end-caps, additional oscillations with a lower spatial period are apparent in figure 4.23. The magnitude of these oscillations appears to decrease as the distance from the scatterer along the positive z-axis increases. In order to help identify the nature of this artefact, the mesh density on the surface of the scatterer was doubled to six elements per wavelength, resulting in a mesh containing 673850 nodes. The analysis was subsequently re-run. Run times per GMRES iteration were approximately one hour when parallelising the jobs over 150 cores. This represents a twelve-fold reduction in computational speed compared with the BEM analysis on the three element per wavelength mesh.

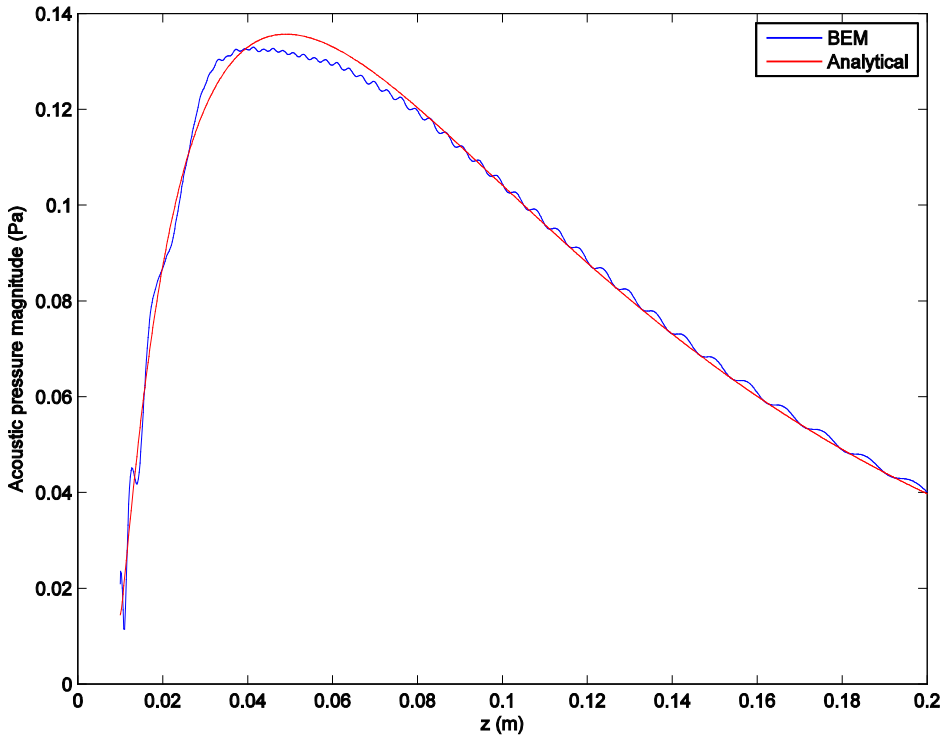

Figure 4.26 Surface Helmholtz formulation on a locally reacting cylindrical scatterer with hemispherical end-caps. Cylinder height: 22 cm. Cylinder radius: 1cm. Incident field: unit amplitude 1 MHz plane wave travelling in positive z direction in an attenuating medium. Mesh density: six elements per wavelength. Acoustic pressure magnitudes along the z-axis on the side of the shadow zone. Comparison against analytical solution.

The corresponding acoustic pressure magnitude on the surface of the cylinder is displayed in figure 4.27.

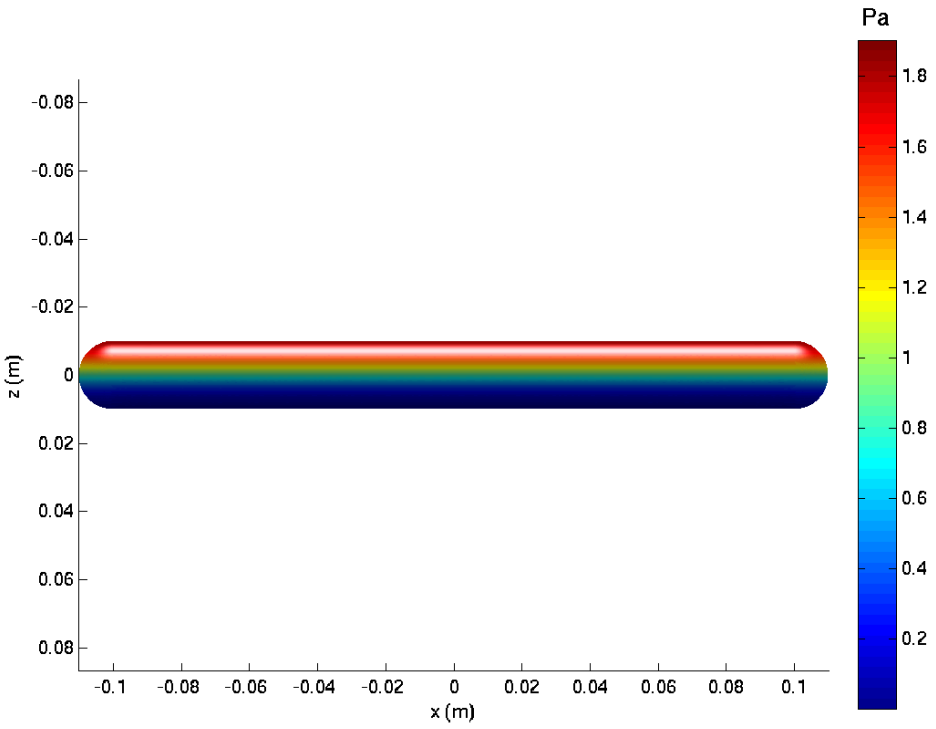

Figure 4.27 Surface Helmholtz formulation on a locally reacting cylindrical scatterer with hemispherical end-caps. Cylinder height: 22 cm. Cylinder radius: 1cm. Incident field: unit amplitude 1 MHz plane wave travelling in positive z direction in an attenuating medium. Mesh density: six elements per wavelength. Acoustic pressure magnitude on the surface of the scatterer.

Despite the differences in acoustic pressure on the side of the shadow zone between the coarser and finer mesh analysis, there is little percentage difference in the maximum acoustic pressure magnitudes predicted on the surface of the scatterer. The analyses on the mesh containing three elements per wavelength and six elements per wavelength both predict a maximum acoustic pressure magnitude of 1.9 Pa, located at (0, 0, −10) mm. These conclusions are similar to those reached for analyses on locally reacting spherical scatterers in section 4.3.3.

Figure 4.28 shows the acoustic pressure magnitude in the y-z plane for the analysis on the six-element-per-wavelength mesh.

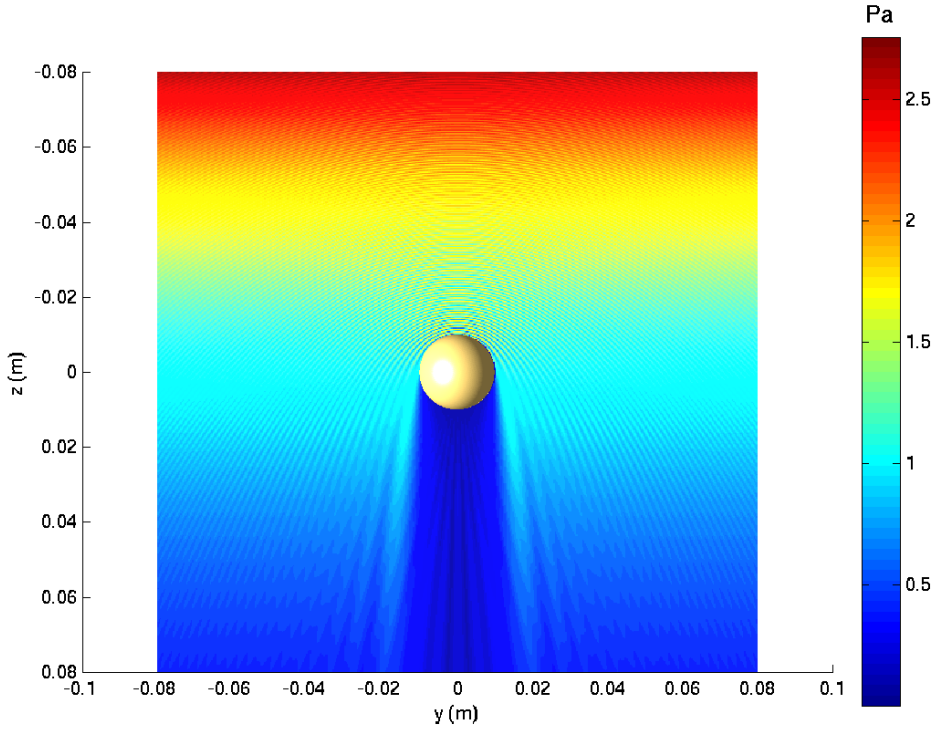

Figure 4.28 Surface Helmholtz formulation on a locally reacting cylindrical scatterer with hemispherical end-caps. Cylinder height: 22 cm. Cylinder radius: 1cm. Incident field: unit amplitude 1 MHz plane wave travelling in positive z direction in an attenuating medium. Mesh density: six elements per wavelength. Acoustic pressure magnitude in the y-z plane.

There is overall very good qualitative agreement between the pressure field plots in figures 4.25 and 4.28. This suggests that it is indeed at only locations in the shadow zone, where acoustic pressure magnitudes are low compared with those in other regions, that significant disagreement occurs. This is likely to be due to the fact that they are more prone to numerical noise. An additional useful comparison is that of the scatterered acoustic field. This represents the difference between the total acoustic pressure and the incident acoustic pressure and, as such, gives a clear indication of the effect of the scatterer. Figures 4.29 and 4.30 show the scattered pressure field magnitude at locations in the y-z plane for the BEM analysis on the three-element-per-wavelength mesh and the six-element-per-wavelength cylinder meshes, respectively.

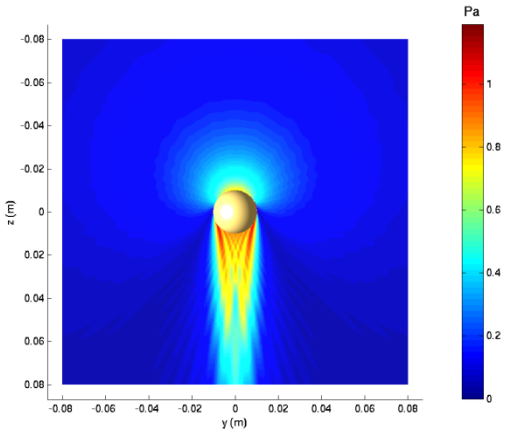

Figure 4.29 Scattered acoustic pressure magnitude in the *y*-*z* plane. Mesh density: three elements per wavelength. Surface Helmholtz formulation on a locally reacting cylindrical scatterer with hemispherical end-caps. Cylinder height: 22 cm. Cylinder radius: 1cm. Incident field: unit amplitude 1 MHz plane wave travelling in positive *z* direction in an attenuating medium.

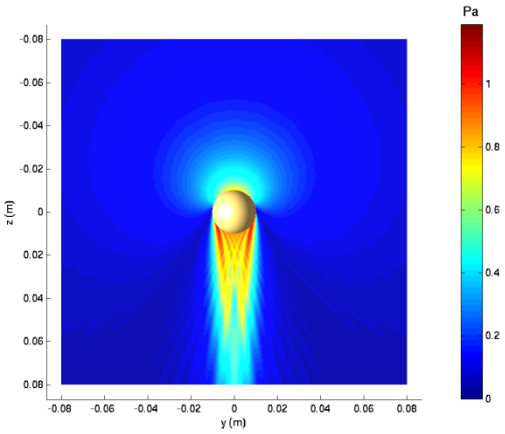

Figure 4.30 Scattered acoustic pressure magnitude in the *y*-*z* plane. Mesh density: six elements per wavelength. Surface Helmholtz formulation on a locally reacting cylindrical scatterer with hemispherical end-caps. Cylinder height: 22 cm. Cylinder radius: 1cm. Incident field: unit amplitude 1 MHz plane wave travelling in positive *z* direction in an attenuating medium.

Figures 4.29 and 4.30 demonstrate that when considering the effects of scattering by the cylinder independently from the incident plane wave, there is good qualitative agreement between the analysis using three elements per wavelength and that using six elements per wavelength at locations outside the shadow zone and close to the cylinder.

4.4 Modelling of the HIFU Source

4.4.1 Review of HIFU Sources

Many types of HIFU transducers have been used in a clinical context. Work performed by Fry *et al* (1954) involved concentrating high-energy ultrasound into a target volume and showed the ability to produce isolated deep-seated legions in animal brains using four quartz transducers, arranged to allow their beams to overlap within the tissue target. More commonly, HIFU transducers are of spherical-section shape so that the ultrasound beam is concentrated at the focal point, resulting in a local acoustic pressure maximum at this point. In its simplest form, the design of a HIFU transducer involves a single piezoceramic device where the focusing of the beam may be carried out either by machining the piezoceramic element into a spherically curved surface (Fry 1978, Hill and ter Haar 1995 and Rivens *et al* 1996), or by fronting a flat element with a suitably

designed lens (Hill 2004 and Fjield *et al* 1997). In the context of HIFU ablation, a commercially available system using such a source exists: the Chongqing Haifu JC system (Chongqing, China). A number of clinical trials have been conducted in liver with this device (for example Wu *et al* 2004, Kennedy *et al* 2004 and Leslie *et al* 2012). The Chongqing Haifu system, fully described by Wu *et al* (2001), employs an extracorporeal single element PZT–4 piezoceramic transducer operating at 0.8–1.6 MHz. The diameter of the device is 12 cm with a focal length of 9–16 cm, achieved using interchangeable treatment heads. Tumours are identified and targeted using a central 3.5–5 MHz diagnostic ultrasound probe mounted in a central aperture, which is aligned along the same axis as the therapeutic transducer. The diagnostic and therapeutic transducers are mounted in a reservoir of degassed water, under the treatment table. The ultrasound axis of propagation is directed upwards and the degassed water provides acoustic coupling between transducer and patient. Translational movement of the transducer is possible along the three orthogonal Cartesian axes, and rotational movement about the long axis of the bed is facilitated by the chains inside a cylindrical gantry at one end of the table. All movement is controlled electronically from the adjacent computer terminals. Although such a system, based on a single focused transducer, has the advantage of being relatively simple from the point of view of its construction and that it only requires a single channel of electronics to power the therapeutic device, it has a number of disadvantages. One of these is the requirement to steer the therapeutic transducer mechanically to treat clinically relevant volumes of tissue. This results in an increase in treatment time. In the context of trans-costal treatment of liver tumours, another is the limitations of focusing at the desired location through the ribcage whilst avoiding excessive heating of soft tissue and bone. As ribs strongly absorb and reflect ultrasound, trans-costal HIFU treatment may result in overheating of bone and overlying tissue during treatment, leading to skin burns (Wu *et al* 2004, Li *et al* 2007 and Leslie *et al* 2012). Hence, care must be taken so that sufficient energy is delivered through the ribcage to ensure that acoustic pressures at the treatment location are above the ablation threshold at the focus while at the same time maintaining the formation of side lobes to a minimal level. When using a single-element HIFU transducer, treatment planning variables are limited to the position of the device with respect to the treatment location, the ultrasonic intensity (governed by the electrical excitation of the transducer), the frequency of excitation, the duration of the ultrasonic pulses and the temporal delay between pulses. These variables may not alone be

sufficient to provide an adequate treatment plan which spares the ribs whilst causing tissue necrosis at the required locations.

For a given single-element device, there is a limit to the excitation frequency bandwidth. This is often limited to the frequency of the thickness extension mode of the piezoceramic element and its third harmonic. Acoustic beams produced by single-element devices are therefore fixed in shape at a given frequency of excitation, and modification of the focal size can only be accomplished by changing the physical properties of the transducer.

As a result of the limitations associated with single-element HIFU transducers, Ebbini *et al* (1988) suggested the use of a cylindrical-section ultrasound phased array applicator for hyperthermia cancer therapy in order to achieve precise control of localised heating patterns by electronic steering of the focused beam around the periphery of the tumour. The same group later proposed a spherical-section phased array for application in deep localised hyperthermia (Ebbini and Cain 1991). This array consisted of square elements forming a rectangular lattice on the surface of the sphere. These studies involved numerical simulations which demonstrated the potential of multi-element phased arrays for overcoming the limitations of single-element HIFU transducers. Building on this approach, Botros *et al* (1998) describe a method in which the design of a HIFU array was optimised using the pseudo-inverse technique (minimum norm least-squares solution) and by enforcing a constrained preconditioned pseudo-inverse method. The procedure calculates the required primary sources on the array while maintaining minimal power deposition over solid obstacles.

A known disadvantage of ultrasound phased arrays is the unwanted presence of grating lobes. These may be avoided by employing an inter-element spacing of half an acoustic wavelength in the propagating medium (Goss *et al* 1996). At MHz frequencies, which are generally used for therapeutic applications, the wavelength in tissue and water is approximately $1.5/f$ mm, where f is the frequency of excitation in MHz. This places severe limitations on the array element size. Whilst this is less of a problem for imaging arrays, therapeutic phased arrays are likely to require larger elements than do imaging applications, in order to induce the tissue heating required for ablation purposes, particularly if practical and financial constraints are placed on the number of channels available to drive the elements of the array. Goss *et al* (1996) considered a 108 multi-

element phased array with a hexagonal distribution of plane circular sources of 8 mm diameter, on a segment of the surface of a spherical shell. The driving frequency was 2.1 MHz. By randomly driving a subset of 64 of the 108 elements, they demonstrated both through numerical simulations and experimentally that the performance of the array improved in terms of grating lobe reduction. By simulating the performance of a spherical-section multi-element array with pseudo-random distribution of sources on its surface, they noted improved performance of the array in terms of both grating lobe magnitude with respect to focal peak and electronic steering capability. Goss *et al* (1996) also suggested that the use of a sparse arrangement of sources on a phased array may help lower the cost of the HIFU system and simplify its experimental implementation. Using the above study as a starting point Gavrilov and Hand (2000) carried out a theoretical sensitivity analysis involving the design of spherical-section multi-element arrays, where the number of elements, their spatial arrangement, their degree of sparseness, their diameter and the frequency of excitation were varied as follows:

- number of array elements: 64, 128, 255, 256 and 1024
- element diameter: 2.5, 5, 7 and 10 mm.
- frequency of excitation: 1, 1.5 and 2 MHz.

Pseudo-random, square, hexagonal and annular distributions of elements on a spherical shell of 12 cm radius of curvature were considered. Out of all the configurations, a pseudo-random spatial arrangement of 5 mm diameter elements on a spherical-section of 11 cm diameter with a radius of curvature of 12 cm and driven at frequencies of 1–1.5 MHz performed best in terms of suppression of grating lobes, steering capability in the vicinity of the geometric focus and ability to generate multiple foci.

The suppression of grating lobes using a spherical-section phased array with non-pseudo-random spatial distribution of elements was achieved by Lu *et al* (2005). A genetic optimisation algorithm was used on a phased array with 256 elements of quadrilateral shape. Off-axis steering of the beam together with the generation of multiple foci was also achieved. This study suggests that a pseudo-random array may not necessarily be a pre-requisite to eliminating grating lobes. This nevertheless requires adjustment of the velocity magnitude and phase for each element, including for focusing at the geometric focus of the array. This means that, to generate a field where grating

lobes are suppressed, some elements of the array have to be driven at lower amplitude compared to others. Hence, the acoustic pressure at the geometric focus resulting from the optimal source velocity distribution is likely to be reduced compared to that generated by an array with the same design specifications but with a pseudo-random spatial arrangement of the elements, which is known to supress side lobes for the spherical focusing case (Hand and Gavrilov, 2000). In applications which require the ablation of deep-seated tumours, and with elements and electronics featuring a finite dynamic range, this may be an unnecessary limiting factor. This may significantly reduce the ultrasonic power delivered at the focus and an increase in treatment time may occur as a result.

In the context of investigation of the scattering of a HIFU source by the ribs, and solving the problem of focusing through the ribcage, a number of considerations for the transducer design is required. These include the frequency of excitation, the size and shape of the array, the number of elements on the array, its radius of curvature, clinical considerations (e.g. resulting treatment time) and cost/benefit. From the studies reviewed in this section, it can be concluded that piezoelectric spherical-section HIFU phased arrays are suitable candidates for the trans-costal treatment of tumours of the liver. Furthermore, the advent of multi-element array transducers driven by multi-channel electronics offers significant advantages over concave single-element piezoelectric devices. Multi-element arrays have the ability to compensate for tissue and bone heterogeneities and to steer the beam electronically by adjusting the time delays in each channel to produce constructive interference at the required location, thus minimising the requirement for mechanical repositioning of the transducer (Sun and Hynynen 1999, Hand *et al* 2009). Hence, the HIFU transducer design considered in this thesis will be of spherical-section multi-element type. Furthermore, a pseudo-random arrangement of the elements on the surface of the device will be opted for.

4.4.2 Incident pressure field calculation

When solving the discretised form of the Kirchhoff-Helmholtz equation for receiver locations on the surface S of the ribs, the incident acoustic pressure p_i at nodal locations on S is required (see equation 3.41). This is the acoustic field resulting from the acoustic sources in the exterior volume V in the absence of scatterers. Additionally, if a Burton-

Miller formulation is chosen, we also require the normal derivative of the acoustic pressure at the centroid of the boundary element patches which discretise the surface *S*.

A rigorous simulation of a multi-element HIFU array would entail modelling the complex electrical and mechanical interactions which occur within the device and the acoustic interactions with the surrounding medium: it is well-known that applying a sinusoidal voltage at the electrodes of a piezoelectric element may not result in uniform vibrational behaviour at its front face (Ikegami *et al* 1974, Guo *et al* 1992). Whilst it is possible to develop a model which accounts for the full electrical to acoustical transfer characteristics using finite element modelling techniques (Hughes 2001), a full three-dimensional model of a multi-element phased array presents huge computational challenges due to the large dimensions compared with the wavelengths involved. To date, there does not appear to be any published work where this has been attempted. In this thesis, it is primarily the scattering of the HIFU acoustic pressure field by the ribs which is of interest. Hence, an accurate description of the electrical, mechanical and acoustic interactions which take place between the HIFU transducer and the acoustic medium remains beyond the scope of this work. Simplified descriptions of HIFU arrays, such as those described by Daum and Hynynen (1999), Gavrilov and Hand (2000), Pernot *et al* (2003) and Bobkova *et al* (2010) may be sufficient, based on the good agreement obtained between simulated and measured acoustic pressure fields. This type of description was chosen in this study, and is detailed below.

The incident acoustic pressure field p_i, (i.e. the field produced by the HIFU array in the absence of scatterers), was modelled as a superposition of plane circular piston sources, assumed to be rigidly vibrating in an infinite baffle. Piezocomposite technology has led to phased arrays with predictable beam patterns. The reduction of inter-element mechanical cross-talk has been made possible through reduction of transverse wave propagation across the surface of the device (Fleury *et al* 2003), so this approach is not unreasonable. This approach is valid if nonlinear propagation in the acoustic medium is ignored. The approach used by Daum and Hynynen (1999) and Gavrilov and Hand (2000) is based on a Rayleigh integral, where each element of the array was discretised into a finite number of point sources lying along a Cartesian grid in a coordinate system local to the element. Each point source is then weighted by the surface area ΔS_e of the square patch that it occupies, and by the velocity U_n of the element. At a field location

$\vec{r}$, an approximation to the acoustic pressure may be obtained by considering the following weighted sum:

$$p_i(\vec{r}) = \frac{\mathrm{i}\rho ck}{2\pi} \Delta S_e \sum_{n=1}^{N} U_n \sum_{m=1}^{N_S} \frac{e^{-\mathrm{i}k\|\vec{r}-\vec{r}_{0,m}\|}}{\|\vec{r}-\vec{r}_{0,m}\|} \tag{4.13}$$

- N is the total number of array elements
- N_S is the number of point sources used to represent each element
- $\vec{r}_{0,m}$ represents a location on the surface of the m^{th} circular source.

A similar approach was chosen here. There exists an analytical solution for the on-axis acoustic pressure generated by a plane circular piston, rigidly vibrating in an infinite baffle (Kinsler *et al* 1982, p179):

$$p_{\text{near field}}(\vec{r}) = \rho_0 cU \left(e^{-ik\|\vec{r}\|} - e^{-ik\sqrt{\|\vec{r}\|^2+a^2}} \right) \tag{4.14}$$

At distances corresponding to the far field of the source, this expression may be approximated as follows (Kinsler *et al* 1982, p179):

$$p_{\text{far field}}(\vec{r}) = \mathrm{i}\rho_0 cUka^2 \frac{e^{-\mathrm{i}k\|\vec{r}\|}}{2\|\vec{r}\|} \tag{4.15}$$

Figure 4.31 shows the analytical solution and far field approximation for the on-axis acoustic pressure resulting from a 1 m s^{-1} source velocity at 1 MHz for the above plane piston and acoustic medium properties. The properties of the acoustic medium were representative of liver tissue and are described in section 4.3.2.

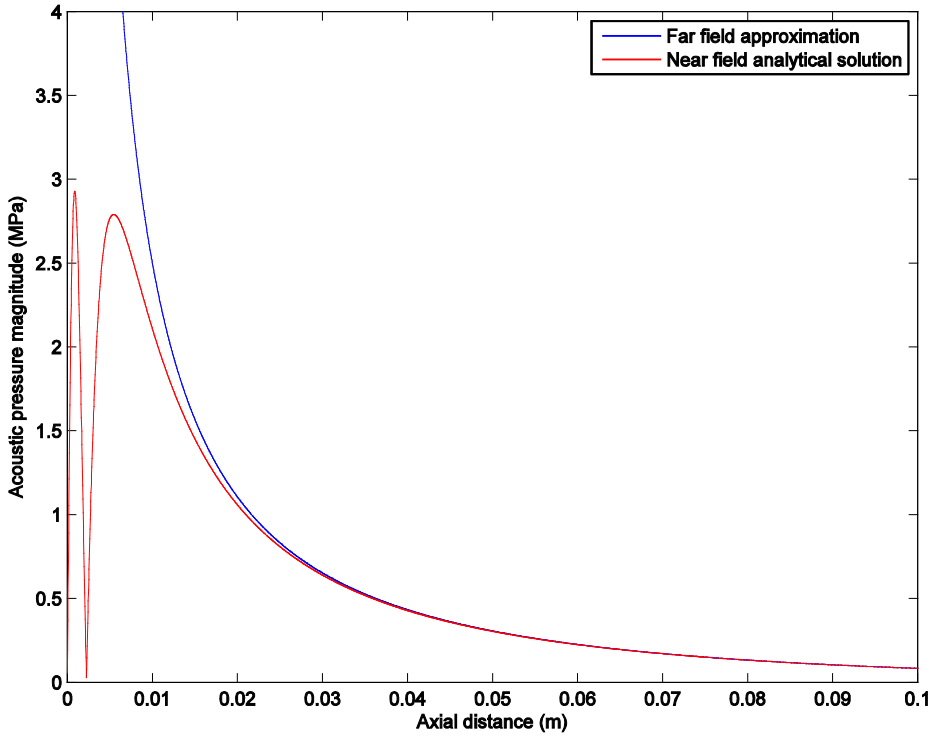

Figure 4.31 Near field and far field calculation of the on-axis acoustic pressure magnitude generated by a plane circular piston rigidly vibrating in an infinite baffle.

Analysing the results in figure 4.31 shows that, provided the on-axis field location is more than 5 cm away from the centroid of the piston, the far field approximation for the acoustic pressure magnitude is within 0.7% of the analytical near field solution. On the basis of these results, and by virtue of the fact that field locations which are in the near field of any element of the HIFU array are not of interest, the far field approximation will be used to compute the incident acoustic pressure field on the surface of the ribs in equation (3.41). Whilst equation (4.15) is valid on the axis of a transducer element, there also exists an approximate expression for the off-axis far field of the acoustic pressure (Kinsler *et al* 1982, p179).

For calculation of the acoustic pressure field generated by a multi-element HIFU array, consider the following. The main axis of the HIFU array is assumed to be the Cartesian z-axis, the global origin being positioned at the geometric focus of the array. Consider a circular source whose centroid is located at (0, 0, -F). The position of the centroid of each circular element on the array may then be inferred from a combination of two rotations:

- by β radians about the global Cartesian y-axis;
- by α radians about the global Cartesian x-axis.

In a local Cartesian axis set obtained by rotating the global axis set by β_j and α_j about the global y and x axes respectively, and translating by $-F$ in the global z-direction, the incident acoustic pressure $p_{i,j}$ radiated by the j^{th} element on the array is given by (Kinsler *et al* 1982, p179):

$$p_{i,j}(x_j', y_j', z_j') = \mathrm{i}\rho_0 caU_j \mathrm{J}_1\left(\frac{kaR_j}{\left\|\overrightarrow{r_j'}\right\|}\right)\frac{e^{-\mathrm{i}k\left\|\overrightarrow{r_j'}\right\|}}{R_j} \tag{4.16}$$

where

- x_j', y_j' and z_j' are the coordinates in the local Cartesian axis set corresponding to the j^{th} source
- $\overrightarrow{r_j'} = (x_j', y_j', z_j')$
- $R_j = \sqrt{x_j'^2 + y_j'^2}$
- U_j is the piston velocity, which contains both magnitude and phase information
- J_1: is the Bessel function of the first kind, of order one.

For each piston source on the spherical bowl array, the transformation from local to global coordinates can be obtained as follows:

$$\begin{pmatrix} x \\ y \\ z \end{pmatrix} = \begin{bmatrix} 1 & 0 & 0 \\ 0 & \cos\alpha_j & -\sin\alpha_j \\ 0 & \sin\alpha_j & \cos\alpha_j \end{bmatrix}\begin{bmatrix} \cos\beta_j & 0 & \sin\beta_j \\ 0 & 1 & 0 \\ -\sin\beta_j & 0 & \cos\beta_j \end{bmatrix}\begin{pmatrix} x_j' \\ y_j' \\ z_j' \end{pmatrix} + \begin{pmatrix} 0 \\ 0 \\ -F \end{pmatrix} \tag{4.17}$$

The total incident pressure p_i radiated by the multi-element HIFU array at location $\vec{r} = (x, y, z)$ in the global Cartesian axis set is therefore given by:

$$p(\vec{r}) = \sum_{j=1}^{N} \mathrm{i}\rho caU_j \mathrm{J}_1\left(\frac{kaR_j}{\left\|\overrightarrow{r_j'}\right\|}\right)\frac{e^{-\mathrm{i}k\left\|\overrightarrow{r_j'}\right\|}}{R_j} \tag{4.18}$$

where R_j and $\overrightarrow{r_j'}$ can be determined from the global coordinate values using the transformation in equation (4.17). In the case where a Burton-Miller formulation is required, and the coupling coefficient α_c in equation (3.40) is non-zero, the derivative

of the acoustic pressure with respect to the outward normal vector $\vec{n}$ on S may be obtained as follows:

$$\frac{\partial p_i}{\partial n} = \vec{\nabla} p_i \cdot \vec{n} = \begin{pmatrix} \frac{\partial p_i}{\partial x} \\ \frac{\partial p_i}{\partial y} \\ \frac{\partial p_i}{\partial z} \end{pmatrix} \cdot \vec{n} \tag{4.19}$$

For the j^{th} piston source on the HIFU array, we have:

$$\begin{pmatrix} \frac{\partial p_{i,j}}{\partial x} \\ \frac{\partial p_{i,j}}{\partial y} \\ \frac{\partial p_{i,j}}{\partial z} \end{pmatrix} = \begin{bmatrix} \frac{\partial x'_j}{\partial x} & \frac{\partial y'_j}{\partial x} & \frac{\partial z'_j}{\partial x} \\ \frac{\partial x'_j}{\partial y} & \frac{\partial y'_j}{\partial y} & \frac{\partial z'_j}{\partial y} \\ \frac{\partial x'_j}{\partial z} & \frac{\partial y'_j}{\partial z} & \frac{\partial z'_j}{\partial z} \end{bmatrix} \begin{pmatrix} \frac{\partial p_{i,j}}{\partial x'_j} \\ \frac{\partial p_{i,j}}{\partial y'_j} \\ \frac{\partial p_{i,j}}{\partial z'_j} \end{pmatrix} \tag{4.20}$$

The partial derivatives in the Jacobian matrix in equation (4.20) can be obtained from the coordinate transformation outlined in equation (4.17). The total incident pressure derivative with respect to the outward normal vector $\vec{n}$ on S is therefore given by:

$$\frac{\partial p_i}{\partial n} = \sum_{j=1}^{N} \begin{bmatrix} \frac{\partial x'_j}{\partial x} & \frac{\partial y'_j}{\partial x} & \frac{\partial z'_j}{\partial x} \\ \frac{\partial x'_j}{\partial y} & \frac{\partial y'_j}{\partial y} & \frac{\partial z'_j}{\partial y} \\ \frac{\partial x'_j}{\partial z} & \frac{\partial y'_j}{\partial z} & \frac{\partial z'_j}{\partial z} \end{bmatrix} \begin{pmatrix} \frac{\partial p_{i,j}}{\partial x'_j} \\ \frac{\partial p_{i,j}}{\partial y'_j} \\ \frac{\partial p_{i,j}}{\partial z'_j} \end{pmatrix} \cdot \vec{n} \tag{4.21}$$

The analytical expressions for the partial derivatives of the incident acoustic pressure with respect to the Cartesian coordinates in local axis sets corresponding to each element on the HIFU phased array are as follows:

$$\frac{\partial p_{i,j}}{\partial x'_j} = U_j \rho c a x'_j e^{-\mathrm{i}k\left\|\overrightarrow{r'_j}\right\|} \left[\left(\frac{k}{\left\|\overrightarrow{r'_j}\right\|_{R_j}} + \frac{\mathrm{i}}{\left\|\overrightarrow{r'_j}\right\|^2_{R_j}} \right) \mathrm{J}_1\left(\frac{kaR_j}{\left\|\overrightarrow{r'_j}\right\|} \right) + \right.$$

$$\left. \mathrm{i}\left(\frac{ka}{\left\|\overrightarrow{r'_j}\right\|_{R_j{}^2}} - \frac{ka}{\left\|\overrightarrow{r'_j}\right\|^3} - \frac{2}{R_j{}^3} \right) \mathrm{J}_0\left(\frac{kaR_j}{\left\|\overrightarrow{r'_j}\right\|} \right) \right] \tag{4.22}$$

$$\frac{\partial p_{i,j}}{\partial y_j'} = U_j \rho c a y_j' e^{-\mathrm{i}k\left\|\overrightarrow{r_j'}\right\|}\left[\left(\frac{k}{\left\|\overrightarrow{r_j'}\right\| R_j} + \frac{\mathrm{i}}{\left\|\overrightarrow{r_j'}\right\|^2 R_j}\right)\mathrm{J}_1\left(\frac{kaR_j}{\left\|\overrightarrow{r_j'}\right\|}\right) + \mathrm{i}\left(\frac{ka}{\left\|\overrightarrow{r_j'}\right\| {R_j}^2} - \frac{ka}{\left\|\overrightarrow{r_j'}\right\|^3} - \frac{2}{{R_j}^3}\right)\mathrm{J}_0\left(\frac{kaR_j}{\left\|\overrightarrow{r_j'}\right\|}\right)\right] \tag{4.23}$$

$$\frac{\partial p_{i,j}}{\partial z_j'} = U_j \rho c a z_j' e^{-\mathrm{i}k\left\|\overrightarrow{r_j'}\right\|}\left[\left(\frac{1}{\left\|\overrightarrow{r_j'}\right\| R_j^2} + \frac{\mathrm{k}}{\left\|\overrightarrow{r_j'}\right\| R_j}\right)\mathrm{J}_1\left(\frac{kaR_j}{\left\|\overrightarrow{r_j'}\right\|}\right) - \mathrm{i}\frac{ka}{{R_j}^3}\mathrm{J}_0\left(\frac{kaR_j}{\left\|\overrightarrow{r_j'}\right\|}\right)\right] \tag{4.24}$$

4.4.3 HIFU array specifications

The HIFU transducer modelled in this thesis was of spherical-section with a central aperture (to allow for the insertion of a diagnostic treatment head for image guidance purposes), populated with N = 256 plane circular elements mounted onto its surface. Guidelines for the dimensions involved were obtained from the literature (Gavrilov and Hand 2000, Bobkova *et al* 2010) and from prior *in-vivo* applications (Visioli *et al* 1999). The elements were each of a = 3 mm radius. Larger values for a will result in an increased likelihood of scattering from the ribs whilst smaller values would be difficult to manufacture and may result in insufficient acoustic power generation to induce tissue necrosis. A radius of curvature of F = 18 cm was used to ensure applicability to deep-seated tumours. The diameter of the central aperture was 4 cm. The outer diameter of the HIFU transducer was 16 cm, giving an F-number of 1.125. Initially, a regular spatial arrangement of the transducer elements was chosen, with the centroids of the sources positioned along a lattice when projected onto the x-y plane. A frontal view of the array is shown in figure 4.32.

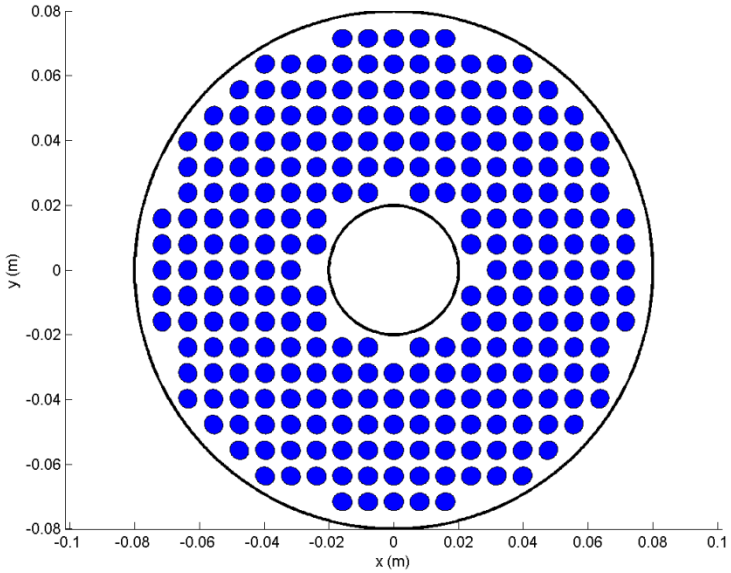

Figure 4.32 Frontal view of 256 element HIFU phased array with regular spatial arrangement of elements. 6 mm element diameter, 4 cm diameter central aperture, 16 cm array diameter, 18 cm focal length, 1 MHz frequency of operation.

Using equation (4.18), the acoustic pressure resulting from all elements of the array vibrating with 1 m s^{-1} velocity magnitude, and with uniform phase was calculated. Results in the *x*-*z* and *y*-*z* planes are shown in figures 4.33 and 4.34, respectively.

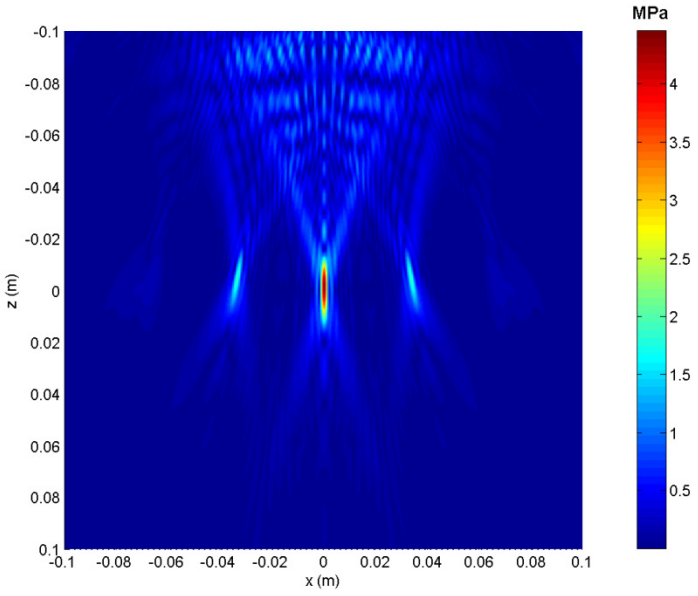

Figure 4.33 Acoustic pressure magnitude in *x*-*z* plane resulting from field of 256 element 1 MHz multi-element array with regular spatial arrangement of elements. Uniform unit amplitude velocity and zero phase.

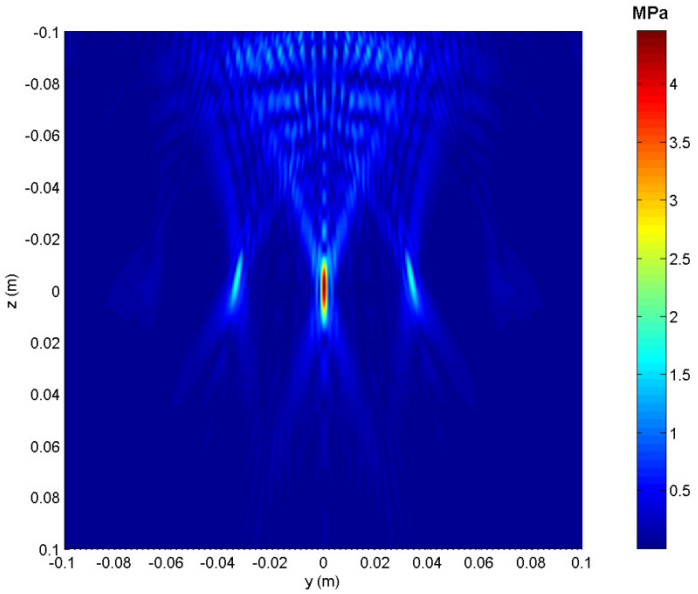

Figure 4.34 Acoustic pressure magnitude in *y*-*z* plane resulting from field of 256 element 1 MHz multi-element array with regular spatial arrangement of elements. Uniform unit amplitude velocity and zero phase.

The peak focal pressure generated by the regular array is approximately 4.45 MPa. Figures 4.33 and 4.34 clearly show that, in addition to the presence of the main focal lobe centred at the global origin, two grating lobes are located along the *x* and *y* axes, approximately 3.5 cm away from the main lobe in the *x*-*z* and *y*-*z* planes, respectively. These lobes are at −7.7 dB relative to the main lobe. The use of multiple foci can be desirable from the point of view in terms of minimising treatment times from the point of view of treatment planning. This approach has been suggested using phased array transducers by Ebbini and Cain (1989) and by Wan *et al* (1996) and has demonstrated the feasibility of enlarging the lesion size in both the lateral (*y*) and elevational (*x*) direction. Nevertheless, Melodelima and Cathignol (2004) have argued that in order to achieve a reduction in treatment times on a deep-seated tumour, it is desirable to increase the focal zone in the axial direction, or along the *z*-axis in this case. Furthermore, as the grating lobes produced by the HIFU array displayed in figure 4.32 are approximately 7 cm apart, the use of such an array would preclude the treatment of tumours less than 7 cm in diameter, as healthy tissue may be destroyed. Even so, it would be very difficult to treat a volume of 7 cm in diameter, as any mechanical steering of the array may also induce tissue necrosis in unwanted locations. Any steering would have to be achieved electronically.

The above simulations involving a multi-element array with regular spatial arrangement reinforce the findings outlined in section 4.4.1 and strengthen the case for using an array with a pseudo-random element arrangement of elements on its surface, which has the ability to reduce grating lobes when compared against the performance of arrays with a regular spatial distribution of elements (Pernot *et al* 2003). A spherical-section multi-element array with pseudo-random arrangement of the elements on its surface has been designed. Other than the distribution of the elements on its surface, the specifications of the pseudo-random array were the same as those of the regular array in figure 4.32. A frontal view of the array is shown in figure. 4.35.

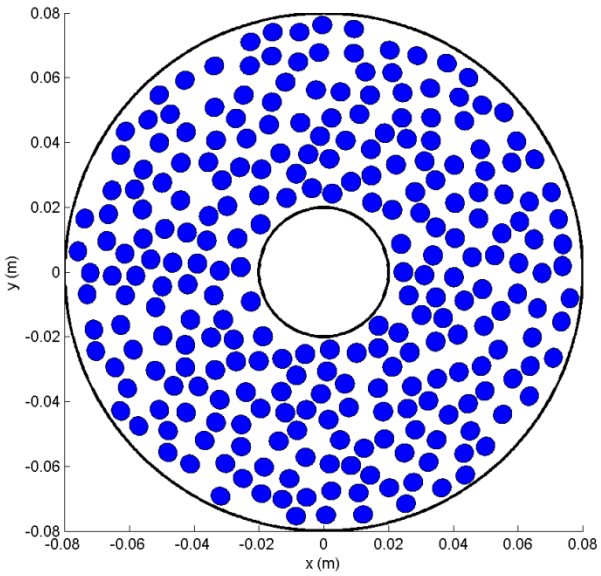

Figure 4.35 Frontal view of 256 element HIFU random phased array configuration. 6 mm element diameter, 4 cm diameter central aperture, 16 cm array diameter, 18 cm focal length, 1 MHz frequency of operation.

The acoustic pressure resulting from all elements of the array vibrating at 1 m s^{-1} velocity magnitude and with uniform phase was calculated using equation (4.18). Results in the *x*-*z* and *y*-*z* planes are displayed in figures 4.36 and 4.37, respectively.

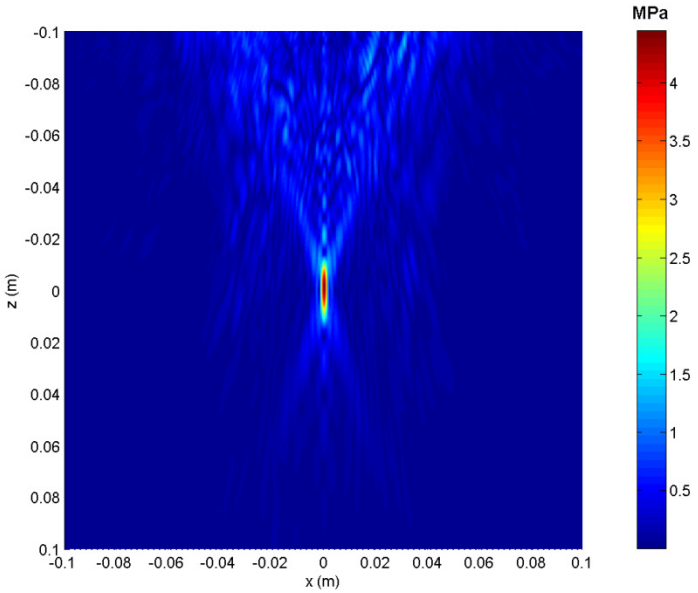

Figure 4.36 Acoustic pressure magnitude in *x*-*z* plane resulting from field of 256 element 1 MHz multi-element array with pseudo-random spatial arrangement of elements. Uniform unit amplitude velocity and zero phase.

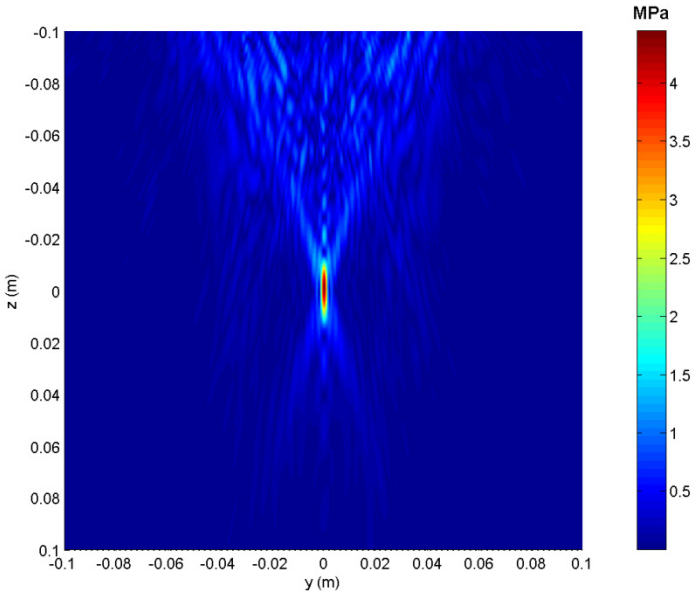

Figure 4.37 Acoustic pressure magnitude in *y*-*z* plane resulting from field of 256 element 1 MHz multi-element array with pseudo-random spatial arrangement of elements. Uniform unit amplitude velocity and zero phase.

The peak acoustic focal pressure in figures 4.36 and 4.37 is approximately 4.44 MPa, which is not significantly decreased compared with the 4.45 MPa produced by the regular array. More importantly, the grating lobes seen with regular element spacing are no longer visible when using a pseudo-random arrangement of the elements.

These features, together with the justification for the array specifications outlined earlier in this section, make the array in figure 4.35 a suitable candidate for investigation of the scattering of HIFU field by human ribs. This array will also be used when considering the inverse problem of optimising the magnitudes and phases of the transducer element velocities in order to induce tissue necrosis at the required foci, whilst keeping the pressure on the ribs below a chosen threshold, and ensuring minimal formation of side-lobes.

4.5 BEM calculations on human ribs

4.5.1 Rib mesh

The rib topology was obtained from an adult male human cadaver in STereoLithography (STL) format. This data is displayed in figure 4.38.

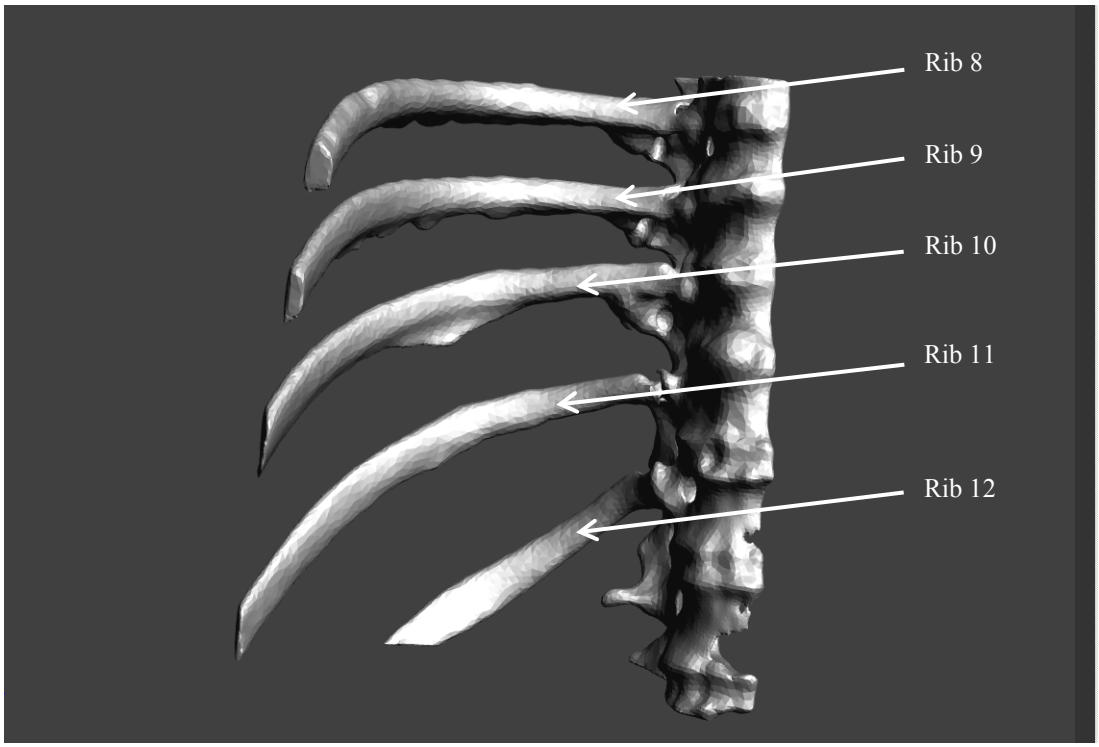

Figure 4.38 STL representation of ribs 8-12 of the right side of an adult male attached to the spine.

Ribs 9-12 on the right side were truncated from the spine and closed surfaces were fitted over each rib using Geomagic® (Geomagic website). CATIA v5 Advanced Meshing Tools (CATIA v5 website) were used to mesh the surfaces. The sections of the ribs which were meshed are displayed in figure 4.39. The mesh contains 200921 nodes.

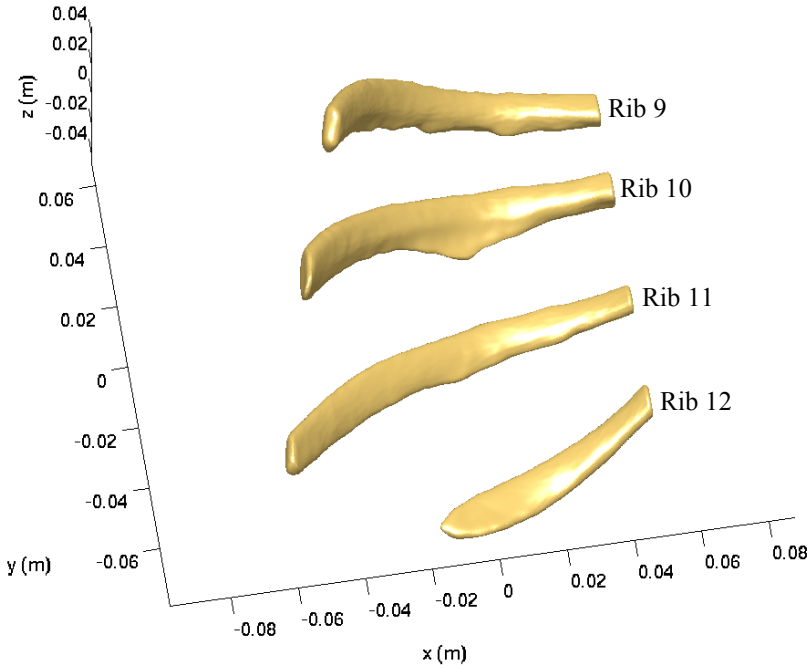

Figure 4.39 Section of ribs 9-12 of the right side of an adult male.

The position of the ribs with respect to the multi-element array described in section is shown in figures 4.40 and 4.41. The geometric focus of the array is approximately 3 cm behind the ribcage under the intercostal space between ribs 10 and 11. This configuration was in part chosen to assess the feasibility of the BEM technique, although it is relevant to clinical applications where shallow tumours may be targeted. These may be more problematic to treat than those lying deeper because the higher energy density at the skin increases the risk of skin burn.

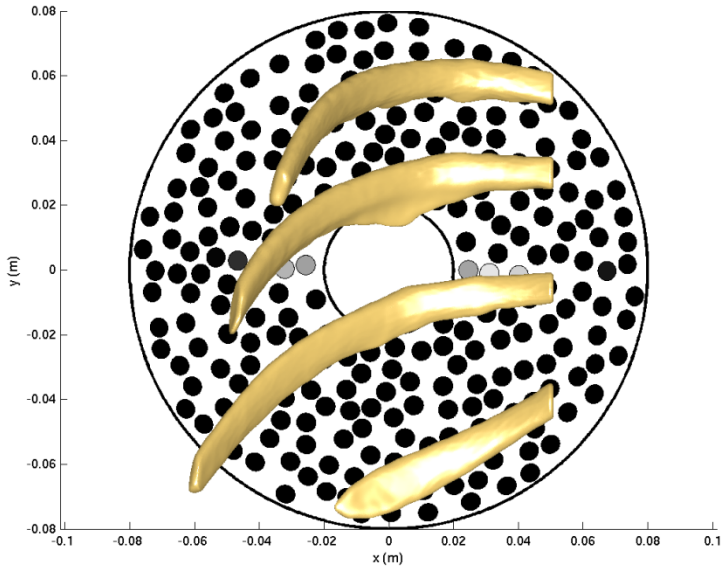

Figure 4.40 Position of ribs with respect to HIFU array looking through the ribs towards the transducer face, in the negative *z* direction.

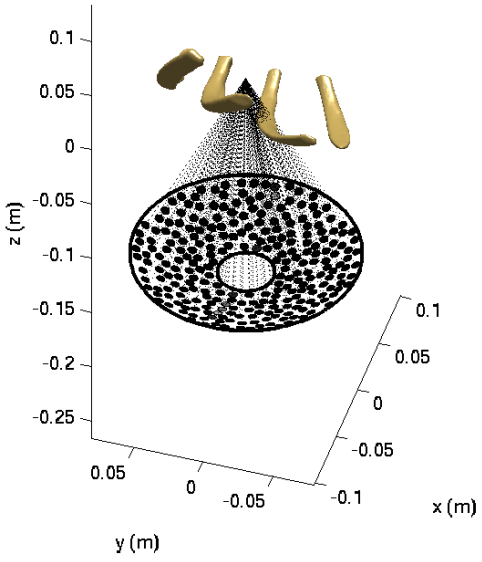

Figure 4.41 Position of ribs with respect to the HIFU array. Dotted lines join the centroid of each array element to the geometric focus of the array.

4.5.2 Meshing and convergence considerations

As described in section 4.2, numerical experiments carried out on spherical and cylindrical scatterers established that, at the excitation frequency of interest (1 MHz) and for perfectly rigid scatterers, it is generally sufficient to produce a mesh of the surface involving three elements per wavelength corresponding to the wave speed in the exterior domain, when using C^0 continuous eight node isoparametric quadrilateral patches. Furthermore, 40 iterations of the GMRES scheme appeared to provide sufficient accuracy for the BEM solution on the side of the shadow zone. Nevertheless, when imposing a Dirichlet locally reacting surface impedance condition, predictions of the acoustic pressure on the side of the shadow zone close to and on the surface of the scatterer were overestimated by up to 11%. Furthermore, oscillations were observed in the case of a finite cylindrical scatterer with hemispherical end-caps, which were not believed to originate from diffraction effects off the end-caps. These oscillations reduced as the surface mesh was refined thus suggesting that they may be numerical in nature. Despite these issues, acoustic pressures on the surface of the scatterer which are of higher magnitude, together with acoustic pressures further away from the scatterer, were estimated with good accuracy. For example, in the case of a locally reacting sphere, the acoustic pressure at the diametrically opposite end to the shadow zone on the surface was estimated within 2% of the analytical solution. Use of a finer mesh resulted in a large increase in computing times. This was approximately one order of magnitude greater in the case of the locally reacting cylindrical scatterer considered in section 4.3.5 where the mesh density was doubled. Whilst such run times for forward problems may not be particularly problematic, investigating mesh densities of six elements per wavelength when solving inverse problems on the computing platform used in the context of this thesis may present significant challenges. Hence, a compromise was adopted and all simulations discussed from hereon will involve scatterers meshed at three elements per wavelength of the wave speed in the medium in the exterior domain, together with 40 iterations of the GMRES scheme. An exception will be made on a reference case of a locally reacting rib mesh to ensure the validity of this approach, where a mesh density of six elements per wavelength will be used.

The use of fourth order Gaussian-Legendre quadrature routines (Zienkiewicz and Taylor 1994, p172) proved sufficient in terms of accuracy. This order was maintained for the remainder of the calculations.

4.5.3 Scattering of a multi-element spherical-section array by perfectly rigid human ribs immersed in a non-attenuating medium

Using the incident field described by equation (4.16), a Burton-Miller formulation was used to calculate the acoustic pressures on the surface of the rib topology described in section 4.5.1. The spherical focusing case was considered, where each element of the array was assumed to be vibrating at 1 m s^{-1} and with uniform phase. Acoustic properties representative of water were used, with a speed of sound of 1500 m s^{-1} and a density of 1000 kg m^{-3}. The computations were distributed over 100 cores of a dedicated cluster, which resulted in run times of approximately 16 minutes per iteration. The incident acoustic pressure field in the absence of the ribs is displayed in figure 4.42.

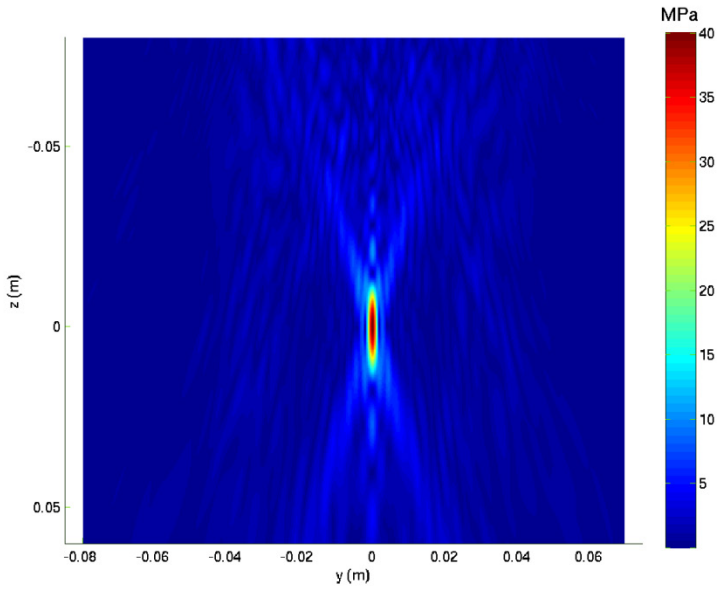

Figure 4.42 Incident acoustic pressure magnitude generated by the 1 MHz random phased HIFU array for spherical focusing case in the *y*-*z* plane.

The acoustic pressure magnitudes on the surface of the ribs are displayed in figure 4.43.

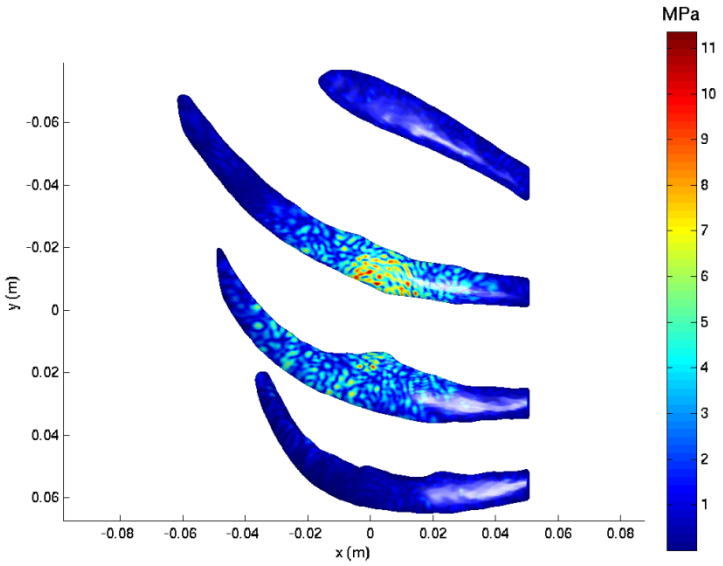

Figure 4.43 Acoustic pressure magnitude on the surface of the ribs resulting from sonication by the 1 MHz random phased HIFU array for an intercostal treatment location approximately 3 cm behind the ribcage, between ribs 10 and 11 on right side. Spherical focusing case on perfectly rigid ribs in a non-attenuating medium.

The acoustic pressure magnitudes generated in the *y-z* plane are shown in figure 4.44, where the ribs have been sectioned to aid the visualisation of the acoustic field.

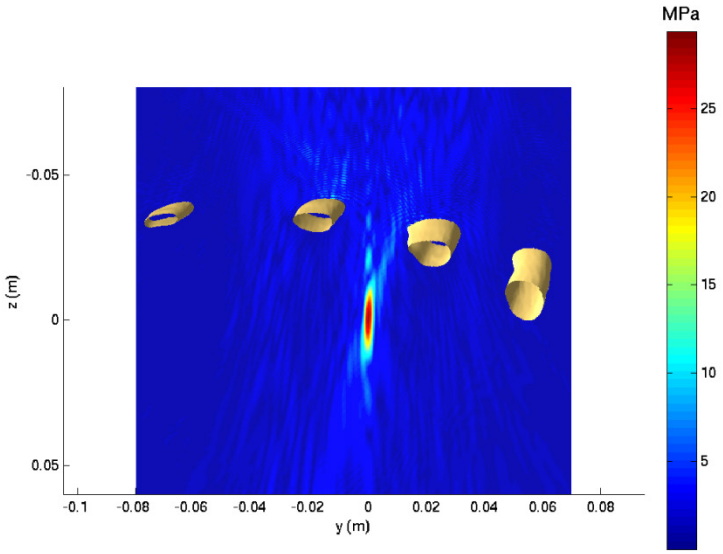

Figure 4.44 Acoustic pressure magnitude on the rib surface resulting from sonication by the 1 MHz random phased HIFU array for an intercostal treatment location approximately 3 cm behind the ribcage, between ribs 10 and 11 on right side. Spherical focusing case on perfectly rigid ribs in a non-attenuating medium. Contour of ribs shown in bone colour.

Inserting the ribs between the array and the focus causes the acoustic pressure magnitude to decrease from 40 MPa to 27 MPa at the focus, representing a 27% drop. Scattering in the acoustic medium in front of ribs 10 and 11 are observed. The maximum acoustic pressure on the surface of the ribs is 11.5 MPa. Unlike the case of cylindrical and spherical scatterers insonated by a plane wave, the multi-element array causes highly localised acoustic pressure magnitude maxima to occur on the surface of the ribs. In this particular array-element geometry rib 11 appears to experience the highest level of exposure to the incident field.

Through a qualitative comparison in the vicinity of the focal regions in the *y*-*z* plane in figures 4.42 and 4.44, it can be observed that, although the ribs introduce some mild aberrations, there is no splitting of the focus. This observation is inconsistent with the results reported by Khokhlova *et al* (2010), where the obstacles considered were not anatomical in shape, but were spatially periodic rectangular-shaped strips. This is likely to be due in part to the large intercostal spacing on the rib topology relative to the wavelength in the propagating medium. Furthermore, in human ribs, the intercostal spacing between two adjacent ribs is unlikely to be uniform throughout, which introduces more complexity in diffraction patterns than would occur when analysing periodic scatterers of regular shape. It will be demonstrated in Chapter 6 that effects of splitting of the focus do indeed occur when insonating specific rib topologies with the multi-element HIFU array described in figure 4.35.

The scattered field, i.e. the difference between the total acoustic pressure in figure 4.44 and the incident acoustic pressure in figure 4.42, is shown below, in figure 4.45.

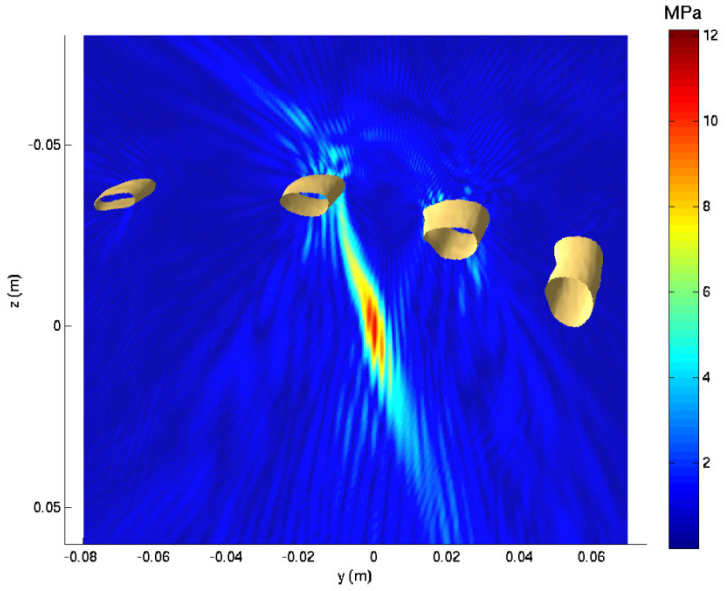

Figure 4.45 Magnitude of scattered acoustic pressure in the *y*-*z* plane resulting from sonication by the 1 MHz random phased HIFU array for an intercostal treatment location approximately 3 cm deep into ribcage between ribs 10 and 11 on right side. Spherical focusing case on perfectly rigid ribs in a non-attenuating medium. Contour of ribs shown in bone colour.

Figure 4.45 confirms qualitatively that rib 11 and, to a lesser extent rib 10, are responsible for a large part of the scattering of the incident field from the HIFU array. This conclusion can intuitively be reached by observing figure 4.41 and noting that it is only these two ribs which are in the "cone" of the HIFU array.

The methodology described in this chapter for analysing the scattering of a multi-element HIFU array by perfectly rigid ribs immersed in a non-dissipative medium has been published in *Physics in Medicine and Biology* (Gélat *et al* 2011) and in *Journal of Physics: Conference Series* (Gélat *et al* 2012). An earlier human rib topology was used in the above studies, which was generated from anatomical CT scan data obtained from *The Virtual Family* (Christ *et al* 2010) for ribs 9 to 12 on the right side of an adult male. A reprint of these publications is included in Appendix D.

4.5.4 Scattering of a multi-element spherical-section array by perfectly rigid human ribs immersed in an attenuating medium

The analysis in section 4.5.2 was repeated, this time using the complex speed of sound described in section 4.32 to account for effects of attenuation in the propagating medium. Again, the BEM calculations were parallelised over 150 cores resulting in run

times of approximately 8 minutes per GMRES iteration. These run times are shorter than for the Burton-Miller formulation, as the evaluation of the hypersingular integral in equation (3.27) was not required here. The resulting acoustic pressure magnitude on the surface of the ribs is shown in figure 4.46.

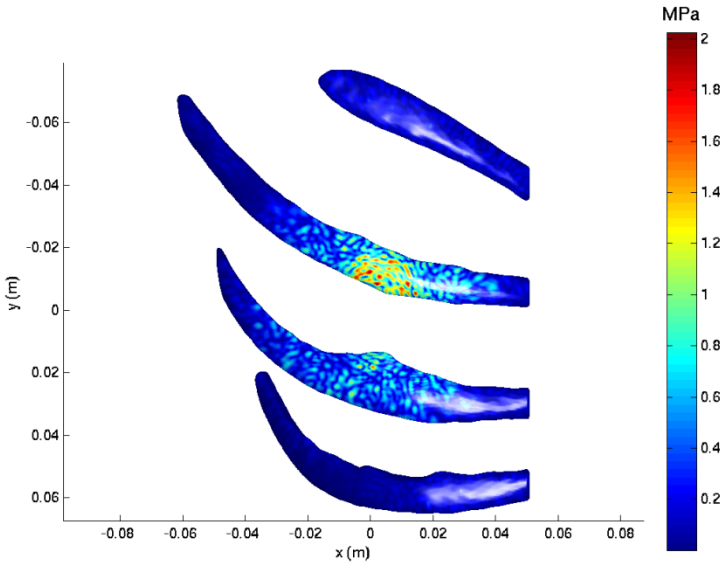

Figure 4.46 Acoustic pressure magnitude on the surface of the ribs resulting from sonication by the 1 MHz random phased HIFU array for an intercostal treatment location approximately 3 cm deep into ribcage between ribs 10 and 11 on right side. Spherical focusing case on perfectly rigid ribs in an attenuating medium.

Accounting for attenuation in the acoustic medium surrounding the ribs results in much lower maximum acoustic pressure amplitude on the surface of the ribs compared with the non-attenuating case displayed in figure 4.43. The maximum value of the acoustic pressure magnitude on the surface of the ribs is reduced from 11.5 MPa in figure 4.43 to 2.0 MPa in figure 4.46. It is nevertheless interesting to note that the pattern of local maxima looks similar from a qualitative point of view in both. In the context of investigating concepts of acoustic dose and acoustic dose rate, the peak acoustic pressure on the surface of the ribs is likely to be of crucial importance, since the rate of energy absorption per unit mass is proportional to the square of the acoustic pressure magnitude (Nyborg 1981, Duck 2009).

The acoustic pressure magnitude in the *y*-*z* plane is displayed in figure 4.47.

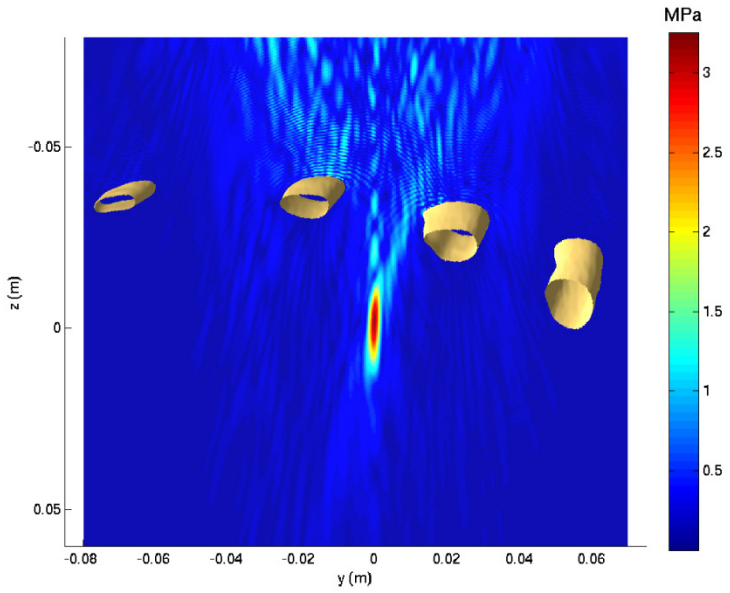

Figure 4.47 Acoustic pressure magnitude on the rib surface resulting from sonication by the 1 MHz random phased HIFU array for an intercostal treatment location approximately 3 cm behind the ribcage, between ribs 10 and 11 on right side. Spherical focusing case on perfectly rigid ribs in an attenuating medium. Contour of ribs shown in bone colour.

The acoustic pressure magnitude at the focus is reduced from 4.4 MPa in figures 4.36 and 4.37 to 3.3 MPa in figure 4.47, when ribs are inserted in front of the array. The effects of scattering of the acoustic field are more clearly visible than in figure 4.44, owing to the reduction in focal pressure arising from inclusion of attenuation in the propagating medium. Aside from this, the acoustic pressure magnitude pattern in the vicinity of the focus is qualitatively very similar to the non-attenuating medium case in figure 4.44.

The scattered pressure field is displayed in figure 4.48, again showing that ribs 10 and 11 are responsible for most of the backscatter.

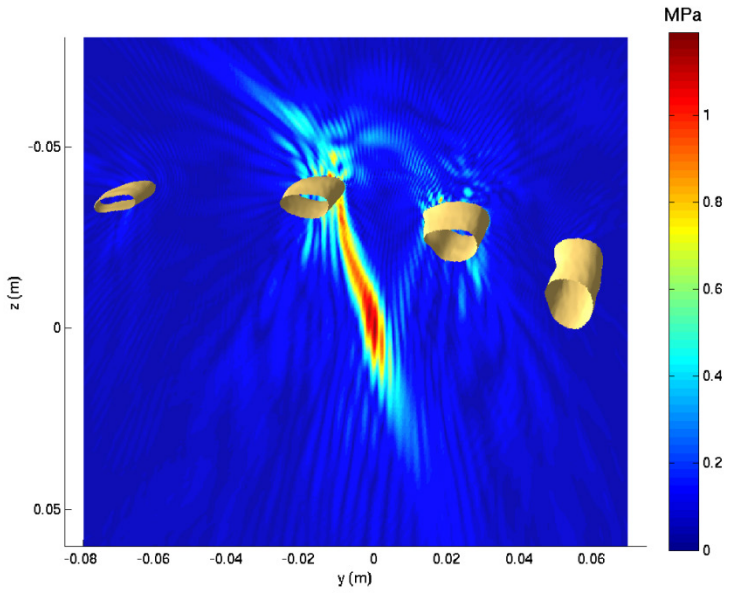

Figure 4.48 Magnitude of scattered acoustic pressure in the *y*-*z* plane resulting from sonication by the 1 MHz random phased HIFU array for an intercostal treatment location approximately 3 cm deep into ribcage between ribs 10 and 11 on right side. Spherical focusing case on perfectly rigid ribs in an attenuating medium. Contour of ribs shown in bone colour.

4.5.5 Scattering of a multi-element spherical-section array by locally reacting human ribs immersed in an attenuating medium

The locally reacting surface impedance Dirichlet boundary was investigated next. The impedance value at the surface of the ribs was obtained from a knowledge of the speed of sound, the attenuation and density for ribs described in section 4.3.3. The resulting acoustic pressure magnitude on the surface of the ribs is displayed in figure 4.49.

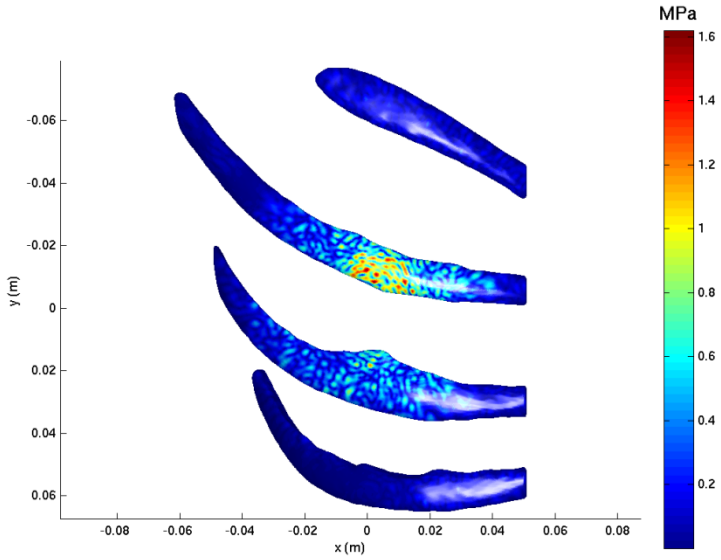

Figure 4.49 Acoustic pressure magnitude on the surface of the ribs resulting from sonication by the 1 MHz random phased HIFU array for an intercostal treatment location approximately 3 cm deep into ribcage between ribs 10 and 11 on right side. Spherical focusing case on locally reacting ribs in an attenuating medium.

The pattern of local maxima on the surface of the ribs in figure 4.49 is qualitatively similar to that in figures 4.43 and 4.46. The maximum value of the acoustic pressure magnitude is nevertheless reduced from 2.0 MPa in figure 4.46 to 1.6 MPa in figure 4.49. The fact that the ribs are no longer considered to be perfectly rigid implies that not all the acoustic energy is being reflected, and some energy is being transmitted and/or absorbed by the ribs. The rate of energy absorption per unit mass is overestimated by 56% if the ribs are considered as being perfectly rigid. This will have important ramifications in the context of treatment planning.

The acoustic pressure magnitude in the *y*-*z* plane is displayed in figure 4.50.

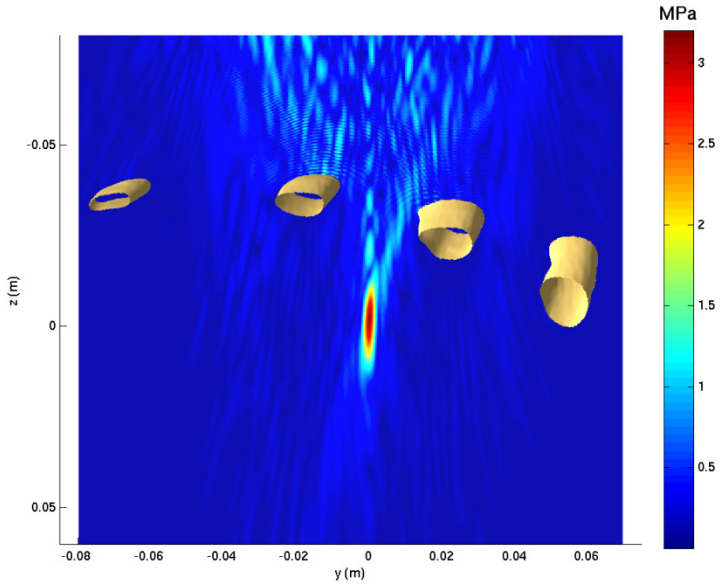

Figure 4.50 Acoustic pressure magnitude on the rib surface resulting from sonication by the 1 MHz random phased HIFU array for an intercostal treatment location approximately 3 cm behind the ribcage, between ribs 10 and 11 on right side. Spherical focusing case on locally reacting ribs in an attenuating medium. Contour of ribs shown in bone colour.

The acoustic pressure magnitude at the focus is 3.2 MPa, which is approximately 0.1 MPa lower than for the case of perfectly rigid ribs immersed in an attenuating medium. Although the ribs absorb some of the acoustic energy generated by the HIFU source, the focal pressure is not greatly affected. This is likely to be due to the fact that, at the focus, there is minimal contribution from diffraction for this particular array-rib geometry.

The scattered component of the acoustic pressure field is displayed in figure 4.50, showing again that ribs 10 and 11 are responsible for most of the effects of scattering.

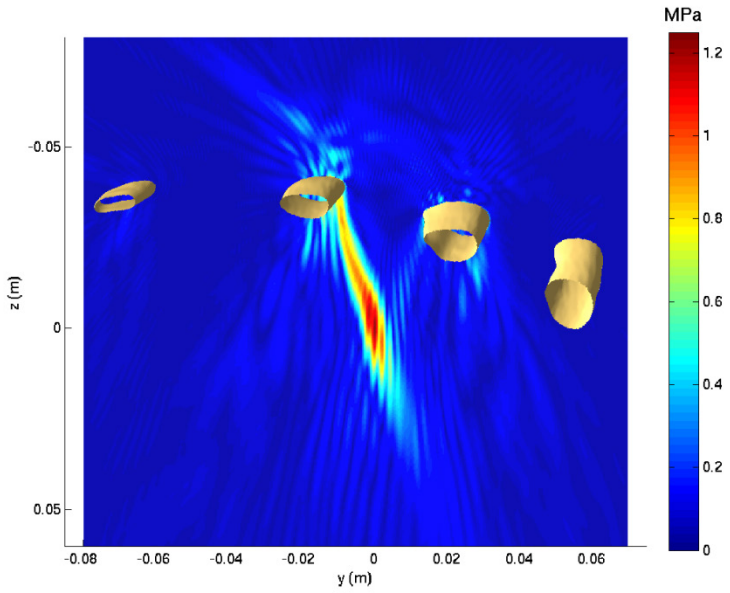

Figure 4.51 Magnitude of scattered acoustic pressure in the *y*-*z* plane resulting from sonication by the 1 MHz random phased HIFU array for an intercostal treatment location approximately 3 cm deep into ribcage between ribs 10 and 11 on right side. Spherical focusing case on locally reacting ribs in an attenuating medium. Contour of ribs shown in bone colour.

4.5.6 Scattering of a multi-element spherical-section array by locally reacting human ribs immersed in an attenuating medium: fine mesh

The calculations in section 4.5.5 were repeated using the same rib topology but meshed at six elements per wavelength corresponding to the wave speed in the exterior domain. As discussed in section 4.5.2, this was carried out in order to confirm the validity of using scatterers meshed at three elements per wavelength in conjunction with 40 iterations of the GMRES scheme. The resulting mesh contained 1213340 nodes and 404444 boundary element patches. Approximately one week of computing time was required to complete this job, when parallelising it over 150 cores.

The resulting acoustic pressure magnitude on the surface of the ribs is displayed in figure 4.52.

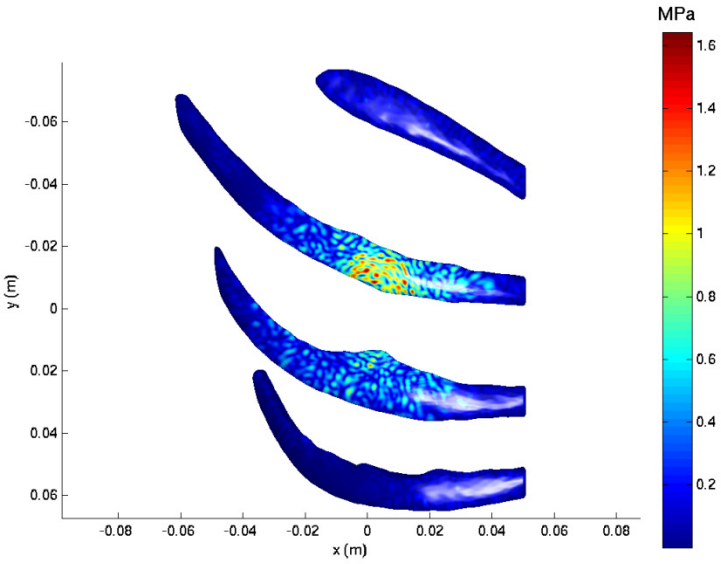

Figure 4.52 Acoustic pressure magnitude on the surface of the ribs resulting from sonication by the 1 MHz random phased HIFU array for an intercostal treatment location approximately 3 cm deep into ribcage between ribs 10 and 11 on right side. Spherical focusing case on locally reacting ribs in an attenuating medium. Fine mesh (six elements per wavelength).

The pattern of local maxima on the surface of the ribs in figure 4.52 is qualitatively similar to that in figure 4.49, which displayed results for the coarser mesh. The maximum value of the acoustic pressure magnitude remains 1.6 MPa. When accounting for significant figures to double precision, the coarse mesh results represent a percentage difference of –0.7% relative to those provided by the fine mesh.

The acoustic pressure magnitude in the *y*-*z* plane is displayed in figure 4.53.

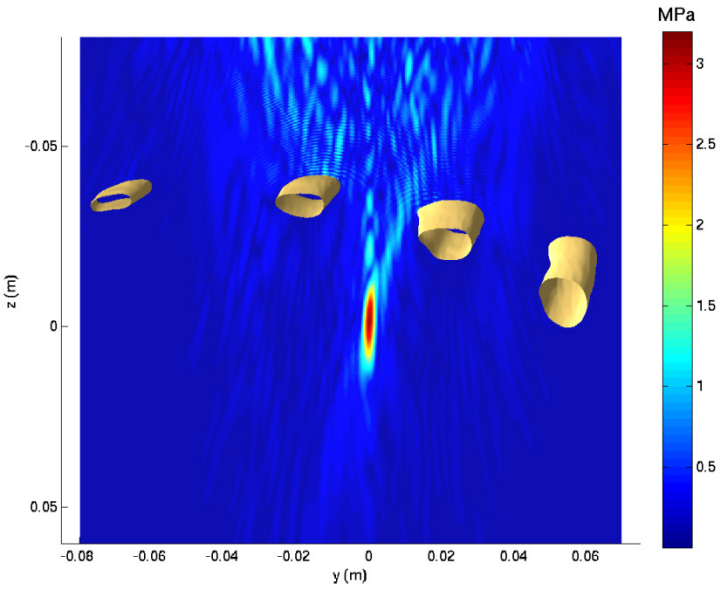

Figure 4.53 Acoustic pressure magnitude on the rib surface resulting from sonication by the 1 MHz random phased HIFU array for an intercostal treatment location approximately 3 cm behind the ribcage, between ribs 10 and 11 on right side. Spherical focusing case on locally reacting ribs in an attenuating medium. Contour of ribs shown in bone colour. Fine mesh (six elements per wavelength).

The acoustic pressure magnitude at the focus is 3.2 MPa. When including significant figures to double precision, the coarse mesh results in figure 4.50 correspond to a percentage difference of +0.1% relative to the finer mesh case. It can be concluded that, for this specific transducer array and rib configuration, there is minimal benefit in doubling the surface mesh density when it comes to evaluating maximum values of the acoustic pressure magnitude on the surface of the ribs and in the focal plane.

4.6 Summary

This chapter discusses the methodology employed in solving the forward problem of the scattering of a multi-element spherical-section HIFU array by human ribs, using BEM. Initially, numerical experiments involving the scattering of plane waves by spherical scatterers and cylindrical scatterers with hemispherical end-caps were conducted. Three types of analyses were considered:

- perfectly rigid scatterers in a homogeneous non-attenuating medium (Neumann boundary condition)
- perfectly rigid scatterers in a homogeneous attenuating medium (Neumann boundary condition)

- locally reacting scatterers with a surface impedance condition in a homogeneous attenuating medium (Dirichlet boundary condition).

In the case of scattering of plane waves by spheres, a direct comparison with analytical solutions was possible. The scattering of plane waves by cylindrical scatterers with hemi-spherical end-caps was also investigated. The results were compared against the analytical solution for the scattering of a plane wave by an infinite cylinder. At an excitation frequency of 1 MHz and for perfectly rigid scatterers, the numerical experiments demonstrated that it is generally sufficient to produce a mesh of the surface involving three elements per wavelength corresponding to the wave speed in the exterior domain, when using C^0 continuous eight node isoparametric quadrilateral patches. Furthermore, 40 iterations of the GMRES scheme appeared to provide sufficient accuracy of the BEM solution on the side of the shadow zone. Nevertheless, when imposing a Dirichlet locally reacting surface impedance condition, predictions of the acoustic pressure on the side of the shadow zone close to, and on, the surface of the scatterer were overestimated by up to 11% in the case of spheres. Furthermore, oscillations which were not believed to originate from diffraction effects were observed in the case of a finite cylindrical scatterer with hemispherical end-caps. These oscillations were diminished as the mesh of the surface was refined thus suggesting that they may be numerical in origin. Despite these issues, acoustic pressures on the surface of the scatterer which were not located in the shadow zone, together with acoustic pressures further away from the scatterer, were estimated with good accuracy.

An important aim of this thesis is to use the forward BEM model to investigate methods of minimising acoustic pressure magnitudes on the surface of ribs whilst maintaining high focal pressures. Hence, it is likely to be the surface locations at which highest values of the acoustic pressure magnitude occur and the pressures in the vicinity of the focus which are of most relevance. On the basis of this premise, the results on locally reacting spherical and cylindrical scatterers described above suggest that the use of a three-element-per-wavelength mesh of the scatterer is a suitable for BEM analyses on locally reacting human ribs. Use of a finer mesh was demonstrated to result in a large increase in computing times. This may render solving inverse problems on the computing platform used in the context of this thesis difficult.

Through a literature search, a suitable phased array transducer design for trans-costal HIFU simulations was determined. The transducer is of spherical-section type, with a central aperture. It features 256 circular elements of 3 mm radius, with a pseudo-random spatial arrangement of the elements on its surface. The frequency of operation is 1 MHz and the transducer F-number is 1.125, with a radius of curvature of 18 cm.

BEM calculations on human ribs were performed using the above HIFU array to provide the incident acoustic field, modelled as a superposition of plane circular pistons vibrating rigidly in an infinite baffle. The transducer was positioned so that its geometric focus was approximately 3 cm deep, behind the intercostal space between ribs 10 and 11. The phased array was assumed to be spherically focusing, so that all elements were vibrating at 1 m s^{-1} and with uniform phase. Acoustic pressure magnitude maps on the surface of the ribs were obtained, together with acoustic pressure magnitude plots in the *y*-*z* plane. Calculations were carried out for perfectly rigid ribs in a lossless medium and subsequently in an attenuating medium, with properties representative of those of human liver. A final set of calculations was carried out on locally reacting ribs in an attenuating medium with properties representative of human liver. The ribs were assumed to have surface impedance properties representative of rib bone. These calculations demonstrated the limitations of assuming that the ribs are perfectly rigid scatterers. Indeed, the rate of energy absorption per unit mass, which is proportional to the square of the acoustic pressure magnitude (Nyborg 1981, Duck 2009), was overestimated by 56% when considering the ribs to be perfectly rigid. A calculation involving a mesh density of six elements per wavelength, corresponding to the wave speed in the exterior domain, was carried out on this set of locally reacting human ribs in an attenuating medium. Post-processing of the results demonstrated that there was little benefit in refining the mesh by a factor of two, considering the large increase in computational time, which was increased by a factor of approximately 30 when using the finer mesh. The percentage difference between the peak focal and maximum rib surface pressures for the finer mesh were both within ±1% of those for the coarser mesh. This provided further justification for maintaining a mesh density of three elements per wavelength.

Chapter 5

The Inverse Problem: Methods

5.1 Overview

Chapters 3 and 4 have dealt with the description and validation of a forward modelling BEM approach to investigate the scattering of a multi-element spherical-section HIFU phased array by human ribs. The implementation of this BEM approach is described in Appendix A. The forward model is an important goal for this thesis work. This chapter is concerned with methodologies used for exploiting this forward modelling technique to solve the following inverse problem: optimal values for the real and imaginary parts of the element velocities of each element of the HIFU array are required so that the acoustic pressures at specified locations in the exterior domain best fit a required field distribution. At the same time, we wish to ensure that acoustic pressure magnitudes on the surface of the ribs are maintained below a specified threshold. Several approaches have been suggested in the literature to help solve this problem. These include binarised apodisation based on geometric ray tracing, phase conjugation (i.e. the frequency domain equivalent of time-reversal acoustics), an approach based on the decomposition of the time-reversal operator (DORT method), as well as a constrained optimisation approach. Binarised apodisation, phase conjugation and the DORT method will first be described and reviewed, after which the advantages and the limitations of each will be discussed. A method of solving the inverse problem using a constrained optimisation approach will then be described and tested on a reduced complexity problem. It will be demonstrated that the implementation of a constrained optimisation method as proposed in this thesis presents specific advantages as a treatment planning strategy, when compared with the other approaches investigated.

5.2 Description of focusing methods

5.2.1 Binarised apodisation based on geometric ray tracing

The use of a linearly segmented spherical-section transducer, in which all active elements were driven in phase to achieve a beam profile which avoids excessive heat deposition at the surface of the ribs, was proposed by Civale *et al* (2006). A significant decrease in the temperature rise on the surface of the ribs was observed when three edge segments directly over the position of the ribs were switched off compared with when all segments were active, thereby indicating potential for treating liver tumours. This concept was extended by Liu *et al* (2007), who proposed a method where the application of a dynamic element activation strategy on a spherically curved two-dimensional array would decrease the absorption of ultrasonic energy by the ribs and prevent them from overheating during the HIFU treatment. They carried out a numerical study based on a modified Rayleigh-Sommerfeld integral approach in which the feasibility of using a spherical-section ultrasound phased array for trans-rib liver tumour thermal ablation was investigated. This approach was implemented in multi-layered media and was based on the formulation described by Fan and Hynynen (1992, 1994). The acoustic and thermal responses were investigated, with ensuing thermal dose calculations (Sapareto and Dewey 1984, Dewey 1994). Based on the feedback from anatomical imaging, array elements obstructed by the ribs were deactivated in an effort to minimise heat deposition on the ribs. These elements were identified by means of a geometric ray tracing approach between the focus and the array elements. Liu *et al* (2007) compared the specific absorption rate at the focus and on the surface of the ribs to assess the efficacy of the method. The specific absorption rate (SAR), also known as the acoustic dose rate (Duck 2009), may be defined as the time-averaged relaxational absorption per unit volume. Under continuous wave conditions and for linear wave propagation, this quantity $\langle q_v \rangle$ is equivalent to the time-averaged rate of heat generation by relaxational absorption per unit volume and may be expressed as follows (Nyborg 1981):

$$\langle q_v \rangle = \alpha_a \frac{|p|^2}{\rho_0 c_0} \tag{5.1}$$

where

- α_a is the absorption coefficient arising from relaxation mechanisms when the shear viscosity is set to zero
- $|p|$ is the acoustic pressure magnitude
- ρ_0 is the medium equilibrium density
- c_0 is the equilibrium velocity of sound.

The brackets $\langle \quad \rangle$ denote a temporal average. These will be omitted in the remainder of this thesis and the specific absorption rate will be referred to as q_v or SAR. It should be noted that α_a and the attenuation coefficient of plane waves α (which is used to define the complex wave number) are distinct quantities. The attenuation coefficient accounts for effects of scattering in a propagating medium as well as those of absorption (Duck 1990, p100). In tissue, the scattering coefficient is not always negligible compared to the attenuation coefficient. This is particularly true of fatty liver, where methods of characterising abnormal retention of lipids within the hepatic cells have been suggested, exploiting the echogenicity of the fatty tissue (Ribeiro and Sanches 2009). A rigorous treatment of absorption and scattering mechanisms in tissue is beyond the scope of this thesis, and the approach used by Liu *et al* (2007) and Cochard *et al* (2009) will be used, in which it is assumed that backscatter is negligible so that the attenuation coefficient and the absorption coefficient may be equated to one another.

Quesson *et al* (2010) have described a method for selecting which elements of a HIFU transducer array to deactivate, based on the relative location of the focal point and the ribs as identified from anatomical MR data. This method was implemented both *ex vivo* and *in vivo* in pig liver and was compared against the case in which all elements were activated. Temperature variations near the focus and ribs were monitored using MR thermometry, and the benefit of deactivating selected array elements for sparing the ribs from excessive heating whilst still ensuring high enough temperatures for tissue ablation at the focus was demonstrated. A similar approach has been adopted by Marquet *et al* (2011), who described investigations of trans-rib HIFU using both *ex vivo* human ribs immersed in water, and *in vivo* in pigs (with 3D movement detection and compensation implemented).

The deactivation of transducer elements obstructed by ribs, or so-called binarised apodisation, described by Liu *et al* (2007), Quesson *et al* (2010), Bobkova *et al* (2010) and Marquet *et al* (2011), may be suboptimal, although practical in a clinical setting, as acknowledged by Quesson *et al* (2010). This approach does not directly address the inverse problem of optimising the magnitudes and phases of the transducer element drive voltage for transmission of sufficient energy through the ribcage to induce tissue necrosis at the required focus, whilst keeping the pressure on the ribs below a chosen threshold and ensuring minimal formation of side lobes. Furthermore, binarised apodisation may hamper the treatment of deep-seated abdominal tumours in humans, since deactivation of elements may significantly reduce the ultrasonic intensities delivered at the focus. Additionally, in order to reach the temperature rise required for tissue necrosis, an increase in treatment time may occur as a result of deactivation of transducer elements.

Given its widespread use in trans-costal HIFU applications, binarised apodisation based on geometric ray tracing was selected as one of the methods against which to compare and benchmark results from the constrained optimisation approach developed in this thesis (described in section 5.2.4). The binarised apodisation technique employed here was similar to that described by Quesson *et al* (2010). Rays were traced from the geometric focus of the array onto the surface of each element of the HIFU array. Each element was discretised into 276 points positioned along a regular Cartesian grid within the plane of each element. Rays traced from each point to the focus which came within 0.25 mm of any node on the rib mesh were discarded: this distance corresponds to half the maximum quadratic patch dimension on the rib mesh. Elements with over 50% of their surface shadowed were deactivated. Other elements were assigned 1 m s^{-1} normal velocity and zero phase. The resulting array element velocity distribution was then used as input data for the BEM forward model described in Chapter 3.

5.2.2 Time-reversal acoustics and phase conjugation

The time reversal process is based on the time invariance of the linear wave equation in a non-dispersive medium (Fink 1992). Consider the propagation of transient acoustic waves in a lossless inhomogeneous medium. It is assumed that the speed of sound c and the density ρ are both functions of the position vector $\vec{r}$. The propagation equation for an acoustic pressure field $p(\vec{r}, t)$ may be written as (Fink 1992):

$$\vec{\nabla} \cdot \left(\frac{\vec{\nabla} p}{\rho_0}\right) - \frac{1}{\rho_0 c^2} \frac{\partial^2 p}{\partial t^2} = 0 \tag{5.2}$$

It is easily shown that, if $p(\vec{r}, t)$ is a solution to equation (5.2), so is $p(\vec{r}, -t)$. This property denotes the invariance under a time reversal process. If the medium has a frequency-dependent attenuation, the propagation equation may contain odd-order time derivatives of the acoustic pressure (Nachman *et al* 1990), and the invariance under time reversal would then be lost (Fink 1992). Nevertheless, if attenuation is implemented in the form of a complex wavenumber, invariance under time reversal is retained as there are no odd order time derivatives.

The concept of a time-reversal mirror allows for the focusing of a multi-element transducer array at a specified location. The elements are assumed to work in pulse-echo mode, so that they can both emit and record signals. The process of time-reversal focusing involves three steps. The first step involves transmitting pulses from each array element through the medium to the target. The target will then generate a scattered pressure field that propagates through the medium back to the transducer array elements. The second step then involves each element of the array recording the backscattered signal received. In the final step, the signals are time-reversed and forward-propagated. The acoustic pressures will then propagate through the medium, and aberrations will be compensated for, thus causing the wavefront to focus on the target.

Consider an array of N transmit-receive transducers. The time reversal process may be described in matrix notation, in the frequency domain. Let $k_{lm}(t)$ represent the impulse response from element m to element l of the array. Let $e_m(t)$ be the input signal corresponding to the m^{th} element of the array, with $1 \leq m \leq N$. The output signal $r_l(t)$ at the l^{th} array element, for $1 \leq l \leq N$, is given by (Prada 1996):

$$r_l(t) = \sum_{m=1}^{N} k_{lm}(t) \otimes e_m(t) \tag{5.3}$$

where $\otimes$ denotes a convolution operation in time. By taking the Fourier transform of equation (5.3), we have:

$$R_l(\omega) = \sum_{m=1}^{N} K_{lm}(\omega) E_m(\omega) \tag{5.4}$$

where the upper-case letters denote Fourier transforms of the received (R) and emitted (E) signals. Since equation (5.4) is valid for $1 \leq l \leq N$, it may be re-written in matrix notation as follows:

$$\{R(\omega)\} = [K(\omega)]\{E(\omega)\} \tag{5.5}$$

where $\{R(\omega)\}$ and $\{E(\omega)\}$ are the vectors of the transmitted and received signals, respectively. $[K(\omega)]$ is the inter-element array transfer matrix and is of dimension $N \times N$. From the reciprocity principle, the inter-element transfer function from element l to element m is the same as that from element m to element l. Hence,

$$K_{lm}(\omega) = K_{ml}(\omega) \tag{5.6}$$

and the matrix $[K(\omega)]$ is symmetrical. At a given frequency, the time reversal process may be described as follows. Consider the initial input vector $\{E^0(\omega)\}$. The resulting output vector is then, according to equation (5.5):

$$\{R^0(\omega)\} = [K(\omega)]\{E^0(\omega)\} \tag{5.7}$$

Phase conjugation represents the frequency domain equivalent of the time reversal operation (Prada *et al* 1996). Hence, the updated vector of input signals $\{E^1(\omega)\}$ which focuses on the target is:

$$\{E^1(\omega)\} = [K(\omega)]^*\{E^0(\omega)\}^* \tag{5.8}$$

and the resulting output signal at a given angular frequency is therefore:

$$\{R^1(\omega)\} = [K(\omega)][K(\omega)]^*\{E^0(\omega)\}^* \tag{5.9}$$

where * denotes the conjugate transpose for matrices and the complex conjugate for vectors.

In the context of the work in this thesis, we are dealing with monochromatic waves. Hence, it is appropriate to consider phase conjugation rather than time-reversal acoustics as a method of focusing through the ribcage. Furthermore, the methodology adopted in this thesis was formulated with the application of treatment planning based on anatomical data in mind. Whilst it may be desirable, it is therefore not essential to rely upon a procedure which can be implemented in real time. The phase conjugation method was therefore implemented as follows:

- a monochromatic 1 MHz point source was placed at the geometric focus of the HIFU array with a source strength of unity
- a BEM calculation was carried out with the ribs in place, thus providing the acoustic pressure on the surface of the scatterers
- at a post-processing stage, the acoustic pressures on the surface of each transducer element were obtained, at 276 discrete locations along a Cartesian grid within the plane of each element
- the acoustic pressures were averaged over the surface of each element, and their complex conjugate obtained
- the normal velocity of each element of the array was obtained by normalising the above acoustic pressures so that the maximum resulting velocity did not exceed the upper limit of the dynamic range, which was defined as 1 m s^{-1}
- using the above focusing vector, another BEM calculation was then carried out, thus obtaining updated acoustic pressures on the surface of the ribs and resulting field pressures.

If linearity and spatial reciprocity assumptions are valid in a heterogeneous medium, the time-reversal process corresponds to a spatially and temporally matched filter of the propagation operator (Tanter *et al* 2000, Tanter *et al* 2001). This implies that the time-reversal process maximises the output amplitude at a given location and at a given time for a given input energy. Nevertheless, the time-reversal process will only optimise the acoustic pressure amplitude at the focus. It does not impose any constraints on the field around the focus (Tanter *et al* 2001). It is nevertheless possible to extend the time-reversal focusing technique based on the inversion of the propagation operator. The latter is defined as the transfer matrix relating locations at elements of an array to a set of control points. This transfer matrix is obtained in a similar way to the inter-element array transfer matrix $[K(\omega)]$, except that it is the responses between elements of the

array and a set of field locations which are considered. This has been carried out in the frequency domain (Tanter *et al* 2000) and in the time domain (Tanter *et al* 2001). This methodology could in principle be used to tackle the inverse problem of delivering ablation-level focal pressures whilst sparing the ribs, and would bear some resemblance to that proposed by Botros *et al* (1998), who described a method in which the design of a HIFU array was optimised using the pseudo-inverse technique (minimum norm least-squares solution) and by enforcing a constrained preconditioned pseudo-inverse method. The procedure calculates the required primary sources on the array while maintaining minimal power deposition over solid obstacles such as the ribs. In principle, the approaches proposed by Tanter *et al* (2000) and Botros *et al* (1998) could be implemented using BEM as the forward propagation model. Indeed, the forward model proposed by Botros *et al* (1998), suffers from limitations in that it is two-dimensional and that the shape of the rib contours is idealised. These approaches have not been attempted in this thesis study, and the phase conjugation methodology will be implemented as described earlier in this section.

5.2.3 Decomposition of the time reversal operator (DORT) method

The DORT method is based on an iterative time reversal process and consists of the construction of the wave fronts that are invariable under a time reversal process (Prada *et al* 1995, Prada *et al* 1996, Prada 2002). It is understood from the description of the three steps of time reversal described in section 5.2.2, and from equations (5.7) to (5.9), that the second emitted wave of a time reversal process can be used as the first emitted wave of the next time reversal process. If this operation is repeated in an iterative loop, this gives rise to the iterative time reversal process (Prada *et al* 1995). The iterative time reversal process can be shown to be convergent. It will converge towards a different value depending on whether the number of iterations is even or odd (Prada *et al* 1995). A consequence of the iterative time reversal process when implemented on well resolved point-like scatterers is that, after several iterations, the waves focusing on less reflective targets will tend to disappear, and the wavefront which focused on the most reflective target remains (Prada *et al* 1995). A scatterer is said to be well resolved if it can be focused on without sending energy to other scatterers. As such, effects due to multiple scattering are not accounted for.

For an array comprising *N* transducers functioning in both transmitting and receiving mode, the time reversal operator matrix can be obtained from the matrix of the inter-element transfer functions $[K(\omega)]$, for a time-invariant, linear system. The time reversal operator (TRO) is then defined as$[K(\omega)]^*$ $[K(\omega)]$ (see equation 5.9), where * denotes the conjugate transpose. The TRO is Hermitian and with positive eigenvalues, and its eigenvectors are invariant wave fronts of the time-reversal process. The diagonalisation of the TRO is equivalent to the singular value decomposition (SVD) of the array response matrix $[K(\omega)]$, from a mathematical point of view. This can be written as follows (Prada 2002):

$$[K(\omega)] = [V(\omega)][\Lambda(\omega)][W(\omega)]^* \tag{5.10}$$

where

- $[V(\omega)]$ and $[W(\omega)]$ are unitary matrices and the columns of $[W(\omega)]$ are the eigenvectors of the TRO
- $[\Lambda(\omega)]$ is a real diagonal matrix of the singular values.

In practice, the array response matrix $[K(\omega)]$ is measured by emitting a pulse on each array element successively and measuring the corresponding echoes from the scatterers on the *N* transducers, as described in section 5.2.2. Due to noise which is inherent in any measurement system, it may be the case that the measured matrix $[K(\omega)]$ is not symmetric. It is therefore common practice to replace the off-diagonal terms $[K_{lm}(\omega)]$ and $[K_{ml}(\omega)]$ with the average value of the two, i.e. $\frac{1}{2}[K_{lm}(\omega) + K_{ml}(\omega)]$ (Prada *et al* 1996). This practice may also have to be adopted on numerical simulations due to the presence of numerical noise.

The DORT method has been validated for the detection of and focusing on point-like scatterers (Prada *et* al 1996). Scatterers are however not generally isotropic or point-like. In such cases, the scatterer is associated with several invariants of the time-reversal operator. Aubry *et al* (2006) studied such invariants in the case of rigid cylinders, which were either well or poorly resolved. Nguyen and Gan (2010) developed the DORT method to solve the acoustic inverse scattering problem associated with a small metallic scatterer, where the approach estimated both the position of the scatterer and its physical properties. In the case of scatterers which are well resolved, each singular vector

associated with a significant singular value focuses on one portion of the scatterer. In the case of scatterers which are not well resolved, such as anatomical ribs, this gives rise to several singular vectors. As a result of the complex geometries arising in ribs, it is not possible to associate a particular singular vector with some part of the ribs without numerical re-propagation (Cochard *et al* 2011).

In the context of trans-rib HIFU treatment, the objective is not to focus selectively on the ribs, but rather to avoid energy depositions on the surface of the scatterer. Song *et al* (2007) describe how the emissions focusing on the scatterer in the DORT method may be removed from those that focus on the target using an orthogonal projection in the frequency domain. After carrying out an SVD on the array response matrix, as described in equation (5.10), the singular values of the diagonal matrix $[\Lambda(\omega)]$ need to be analysed and a threshold determined to separate the singular vectors into two categories: those associated with the higher singular values which focus on the ribs, and those associated with the lower singular values which do not send energy to the scatterer. This procedure is described by Cochard *et al* (2009).

By projecting the focusing vector orthogonally onto the first set of eigenvectors associated with the higher singular values, we have:

$$\{U_{\text{projected}}\} = \{U_{\text{focus}}\} - \sum_{i=1}^{i_{\max}} (\{W_i\}^* \{U_{\text{focus}}\}) \{W_i\} \tag{5.11}$$

where

- $\{W_i\}$ is the i^{th} column of $[W(\omega)]$
- $i_{\max}$ is the number of eigenvectors associated with the higher singular values.
- $\{U_{\text{projected}}\}$ represents the orthogonal projection of the array element normal velocity focusing vector $\{U_{\text{focus}}\}$.

$\{U_{\text{focus}}\}$ is generally chosen as the vector of array element velocities which will focus at the desired location in absence of the scatterer. Hence, for focusing at the geometrical centre of the spherical-section array, this would correspond to the spherical focusing case.

The application of the DORT method to focus through ribs immersed in water has been discussed by Cochard *et al* (2009) in 2D and by Cochard *et al* (2011) in 3D. Using a

singular value decomposition of the inter-element array response matrix, an excitation weight vector was obtained which is orthogonal to the subspace of emissions focusing on the rib. When applied to the array, this excitation vector enhances the acoustic energies deposited at the focal point compared with those on the ribs.

The DORT method has the advantage of not requiring any prior imaging of the scatterers. It however requires the measurement of N^2 transfer functions, where N is the number of array elements. If multi-channel electronics are available, this procedure may be parallelised, so that N responses may be acquired simultaneously for each excitation. Nevertheless, there are limitations associated with this method. In particular, multiple scattering is not accounted for. Whether or not this is significant when investigating anatomical ribs, is likely to be dependent on their geometry as well as their acoustic properties, and those of the surrounding medium. Furthermore, in the experiments described by Cochard *et al* (2009) and Cochard *et al* (2011), the SAR at the surface of the ribs was estimated by removing the ribs, placing a hydrophone at the location of the ribs to measure the acoustic pressure, and calculated using literature values for the properties of rib bone. Whilst alternatives to this approach may be challenging to implement in practice, it is nevertheless likely that this approach will introduce a considerable uncertainty in the measurement, as rib bone is not perfectly absorbing. Finally, there is an issue in determining the value of i_{max}, the number of eigenvectors associated with the higher singular values: unlike well resolved point-like scatterers, it is not straightforward to separate the 'signal' from the 'noise' in the singular values of the diagonal matrix.

The use of BEM as a forward model to analyse the scattering by ribs of the field from a multi-element HIFU array may prove to be a useful tool for further assessment of the efficacy of the DORT method for focusing into the ribcage whilst avoiding energy depositions at the surface of the ribs. Indeed, the scattered field at locations on the surface of the array elements is straightforward to obtain using BEM. Obtaining the $[K(\omega)]$ matrix numerically is however likely to be a time-consuming affair, since the contribution of each individual element on the array must be evaluated at the location of all elements of the array, thereby necessitating $N = 256$ forward calculations. The way in which the output from the BEM forward calculations feeds into the DORT method is described further in Appendix B.

5.2.4 Constrained optimisation using BEM as the forward model

5.2.4.1 Formulation of inverse problem

The DORT method has the advantage of not requiring CT or MR imaging of the ribs. Furthermore, Ballard *et al* (2010) proposed an experimentally validated method of an adaptive, image-based refocusing algorithm of dual-mode ultrasound arrays in the presence of scatterers. This approach and the DORT method both have the advantage of not requiring any prior knowledge of the location of the ribs. There is nonetheless a key limitation discussed by Cochard *et al* (2011) when it comes to using the DORT method applied to trans-costal HIFU applications. The SAR gain, which is defined as the logarithmic ratio of the SAR at the focus and at the ribs, was evaluated to assess the DORT method. However, this gain does not depend on the acoustic power emitted by the HIFU transducer. Whilst the DORT method may generate a vector of element velocities for which this gain is optimal, it may not be relevant in a clinical context if the acoustic pressures at the focus are insufficient to induce tissue necrosis and if the dynamic range of the elements and electronics prohibit scaling the element velocities so as to induce this. The DORT method may therefore proscribe the array from being used to its full potential, particularly when it comes to inducing tissue necrosis of deep-seated tumours. It was also seen that the binarised apodisation approach based on geometric ray tracing, whilst easy to implement, may be suboptimal (see section 5.2.1).

There is therefore a requirement to solve the inverse problem of focusing the field of a multi-element HIFU array inside the ribcage whilst ensuring that the acoustic dose rate on the surface of the ribs does not exceed a given damage threshold, using a suitable forward model capable of addressing the effects of scattering and diffraction on 3D anatomical data. A constrained optimisation approach for solving this inverse problem will be formulated using BEM as the forward model. This work was the subject of a peer-reviewed paper published in *Physics in Medicine and Biology* (Gélat *et al* 2012). A reprint of this paper is included in Appendix D. It is assumed that a surface Helmholtz formulation will be used throughout this chapter, so the Burton-Miller coupling coefficient α_c is set to zero. Recall equation (3.41) for a perfectly rigid scatterer:

$$[H]\{p_{\text{surf}}\} = -\{p_i\} \tag{5.12}$$

where $[H]$ is the boundary element matrix and the acoustic pressures on the surface S have been relabelled $\{p_{\text{surf}}\}$. Whilst the derivation in this section will only consider a perfectly rigid scatterer, it is straightforward to generalise this to a locally reacting one.

Let the incident field be a linear combination of plane circular pistons rigidly vibrating in an infinite baffle. The incident field on S is a linear combination of the source velocities of each piston. Equation (5.12) may therefore be rewritten as:

$$[H]\{p_{\text{surf}}\} = -[\beta]\{U\} \tag{5.13}$$

where the elements of $[\beta]$ may be obtained analytically in the far-field (see equation 4.16) or by solving the Rayleigh integral in the near-field. $[\beta]$ is of dimension $M \times N$, where M is the number of nodes on the surface S after its discretisation and N is the number of plane pistons. $\{U\}$ is the vector of source velocities and is of dimension $N \times 1$.

Consider equation (3.42), where the position vectors are located in the exterior volume V_{ext}. Again, the term on the left-hand-side of equation (3.42), involving the normal derivative of the acoustic pressure on S, was zero in this derivation. When evaluated numerically, the integral may be expressed as a weighted sum of the pressures on S. Additionally, the incident pressure at any given field location is a linear combination of the source velocities. Hence, for a specified number of locations in the exterior volume, we have:

$$[Q]\{p_{\text{surf}}\} = \{p_{\text{ext}}\} - [\gamma]\{U\} \tag{5.14}$$

where $[Q]$ is a matrix of weighting coefficients obtained from the Gaussian quadrature routines and the acoustic pressures in the exterior volume V_{ext} have been relabelled $\{p_{\text{ext}}\}$. The coefficients in $[\gamma]$ may be obtained from the Rayleigh integrals relating each plane piston on the multi-element array to each location in V_{ext}.

The vector of surface pressures may be eliminated by combining equations (5.13) and (5.14):

$$([\gamma] - [Q][H]^{-1}[\beta])\{U\} = \{p_{\text{ext}}\} \tag{5.15}$$

Equation (5.13) may be rewritten as follows:

$$-[H]^{-1}[\beta]\{U\} = \{p_{\text{surf}}\} \tag{5.16}$$

or

$$[A]\{U\} = \{p_{\text{surf}}\} \tag{5.17}$$

where $[A] = -[H]^{-1}[\beta]$.

Equations (5.15) may be re-written as follows:

$$[C]\{U\} = \{p_{\text{ext}}\} \tag{5.18}$$

where $[C] = [\gamma] - [Q][H]^{-1}[\beta]$.

All quantities in equation (5.18) will generally be complex. When investigating an inverse problem involving complex quantities, it is often convenient to reformulate in terms of purely real variables by rewriting equation (5.18) as follows:

$$\begin{bmatrix} \text{Re}[C] & -\text{Im}[C] \\ \text{Im}[C] & \text{Re}[C] \end{bmatrix} \begin{Bmatrix} \text{Re}\{U\} \\ \text{Im}\{U\} \end{Bmatrix} = \begin{Bmatrix} \text{Re}\{p_{\text{ext}}\} \\ \text{Im}\{p_{\text{ext}}\} \end{Bmatrix} \tag{5.19}$$

or

$$[\hat{C}]\{\hat{U}\} = \{\hat{p}_{\text{ext}}\} \tag{5.20}$$

We wish to obtain a set of real and imaginary parts of source velocities which best fit a prescribed field pressure distribution in a least-squares sense such that:

- the acoustic pressure magnitudes on *S* do not exceed a threshold defined by $p_{\text{surf}_{\max}}$
- the source velocity y magnitudes do not exceed the upper bound of the dynamic range of each element $U_{\max}$.

This may be expressed as a least-squares optimisation problem with nonlinear constraints:

$$\min_{\hat{U}} \frac{1}{2}\left\|[\hat{C}]\{\hat{U}\} - \{\hat{p}_{\text{ext}}\}\right\|_2^2 \text{ such that } \begin{cases} |\{p_{\text{surf}}\}| \leq p_{\text{surf}_{\max}} \\ |U| \leq U_{\max} \end{cases} \tag{5.21}$$

There are a number of commercially available and open source solvers which can solve the type of problem described by equation (5.21). The NAG® Numerical Library *e04us* (NAG® website) routine was used to carry out the constrained optimisation, as initial tests against other solvers, including the Matlab™ Optimisation Toolbox, demonstrated superior performance of the NAG® solver. Routine *e04us* is designed to minimise an arbitrary smooth sum of squares function subject to constraints, which may include simple bounds on the variables, linear constraints and smooth nonlinear constraints. It employs a sequential quadratic programming method described by Bonnans *et al* (2006 p490). A brief description of the algorithm is provided by Gill *et al* (2001). A full description of sequential quadratic programming methods is beyond the scope of this thesis, and the reader is referred to Gill *et al* (1981) for more information. The partial derivatives of the constraints and of the cost function with respect to the optimisation variables were supplied as input data to routine *e04us*. Providing the solver with this data generally greatly enhances the computational efficiency of the routine (Gill *et al* 2001). Details of the cost function and Jacobian matrices can be found in Appendix C.

5.2.4.2 Testing of inverse problem formulation on a reduced complexity model

The work described in this section was published in *Journal of Physics: Conference Series* (Gélat *et al* 2013). A reprint of this work is included in Appendix D. The reformulation of the boundary element approach described in section 5.2.4.1 was tested on a reduced complexity problem involving a 256 element spherical-section phased array with a pseudo-random distribution of the elements on its surface. Each element was vibrating at a frequency of 100 kHz, and a perfectly rigid cylindrical scatterer was placed between the array and its geometric focus. The elements on the array were each of radius a = 1 cm. A radius of curvature of F = 50 cm was used. The outer diameter of the HIFU transducer was 60 cm. A frontal view of the array is shown in figure 5.1.

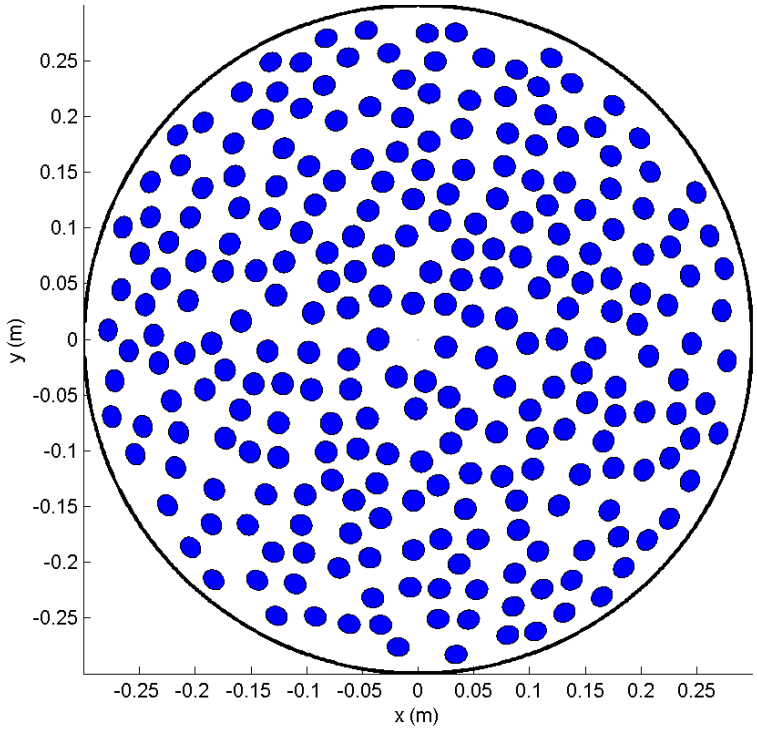

Figure 5.1 Frontal view of HIFU multi-element array configuration used for the reduced complexity problem. 1 cm element diameter, 60 cm array diameter, 50 cm focal length, 100 kHz frequency of operation.

It is acknowledged that both the frequency of operation of the array and its dimensions do not represent what is commonly used for trans-costal HIFU (Gavrilov and Hand 2000). Furthermore, it is not the intention to rescale the dimensions and frequency of operation of the array shown in figure 4.33. Investigation of a reduced-size problem such as this is however both relevant and beneficial prior to applying the methodology to trans-costal HIFU frequencies and dimensions, which demands much greater computational resources. Given the knowledge that beam characteristics are different in this reduced complexity problem compared to those associated with trans-costal HIFU, this approach nevertheless serves the purpose of establishing the efficiency of the inversion algorithm.

In order to obtain the coefficients of the $[A]$ matrix described by equation (5.17), we must solve equation (5.12). This is equivalent to launching a forward BEM calculation for N incident fields, each incident field vector representing a column of the matrix $[\beta]$. The current GMRES implementation of the BEM approach recalculates the coefficients of the boundary element matrices at each iteration of the algorithm (see Appendix A). It

is therefore more efficient to vectorise the process so that we may simultaneously solve for any number of right-hand-sides, depending on the RAM available.

The scatterer was meshed using isoparametric eight-node quadratic patches ensuring at least three elements per wavelength for a wave speed of 1500 + 4.405i m s^{-1}. This corresponds to an absorption coefficient of 47.2 Np per metre at 1 MHz (assuming a power law with a linear dependence on frequency). The density of the medium was assumed to be 1000 kg m^{-3}. The axis of symmetry of the cylindrical scatterer with hemispherical end-caps was chosen to be parallel to the *x*-axis located –5 cm away from the geometric focus of the array in the *z*-direction (towards the array). The mesh contained 6950 nodes. This arrangement is illustrated in figure 5.2.

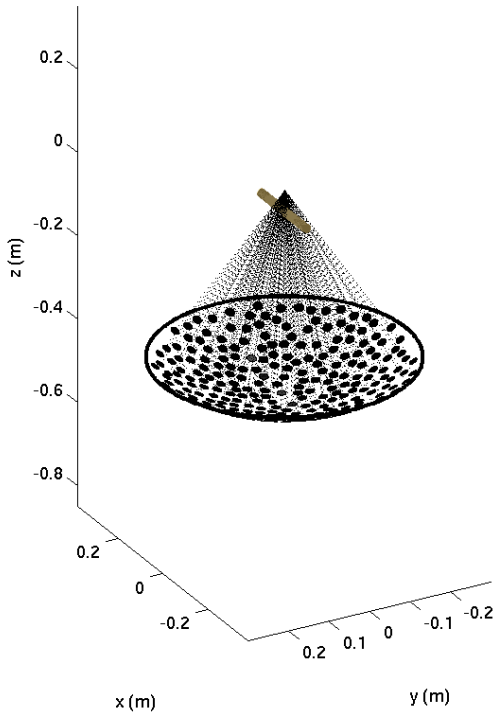

Figure 5.2 Position of cylindrical scatterer with respect to focused array.

From a knowledge of $[H]^{-1}[\beta]$, the acoustic pressure on the surface of the cylinder may be obtained using equation (5.16) for a given distribution of source velocities. In order to formulate the cost function and the constraints, the spherical focusing case of all elements vibrating in phase and with unit velocity amplitude was investigated. The acoustic pressure magnitudes at selected locations in the *y*-*z* plane are shown in figure

5.3. The corresponding incident pressure field (i.e. in absence of the scatterer) is shown in figure 5.4.

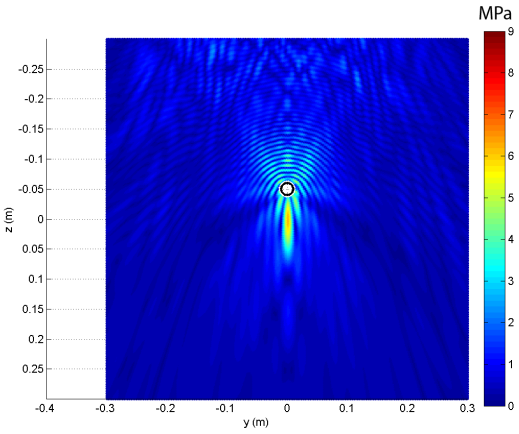

Figure 5.3 Acoustic pressure magnitude in *y-z* plane resulting from field of 100 kHz multi-element array. Uniform unit amplitude velocity and zero phase. Contour of cylinder shown in black.

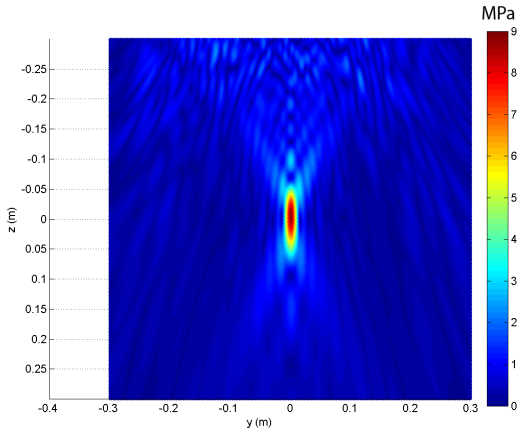

Figure 5.4 Incident acoustic pressure magnitude in *y-z* plane resulting from field of 100 kHz multi-element array (no scatterer). Uniform unit amplitude velocity and zero phase.

The resulting acoustic pressure magnitude on the surface of the cylinder is shown in figure 5.5.

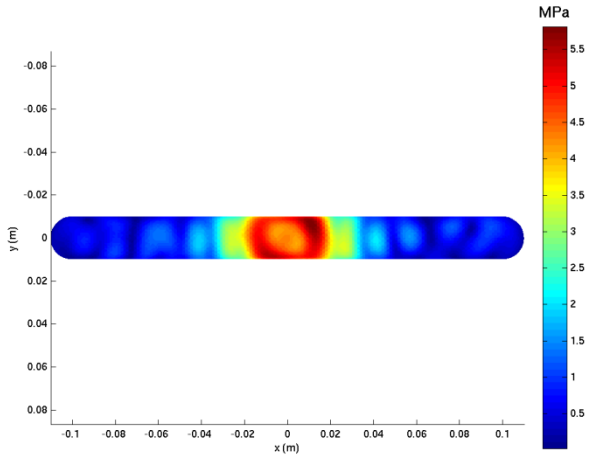

Figure 5.5 Acoustic pressure magnitude on surface of cylinder resulting from field of 100 kHz multi-element array. Uniform unit amplitude velocity and zero phase.

Figures 5.3 and 5.4 show that inserting the cylindrical scatterer between the array and the focus causes the acoustic pressure magnitude at the focus to drop from 9 MPa to 6 MPa. Figure 5.5 shows that the maximum pressure amplitude on the surface of the cylinder is 5.8 MPa for all elements of the array vibrating at an amplitude of 1 m s^{-1} and with uniform phase. The value of $p_{\mathrm{surf}_{\max}}$ in equation (5.21) was chosen so as to generate a 30% decrease in the acoustic pressure on the surface of the scatterer. U_{max} was taken as 1 m s^{-1}. The vector of pressures in the exterior volume in the cost function (i.e. the 'desired' field pressure distribution) was generated from incident pressure field values at 5192 equally spaced locations in the *y*-*z* plane such that $-3 \text{ cm} \leq y \leq 3 \text{ cm}$ and $-3 \text{ cm} \leq z \leq 3 \text{ cm}$, the focus of the array being at the global origin. Locations inside a 1.5 cm radius around the axis of the scatterer were removed.

According to the manual describing NAG® routine *e04us* (NAG website), scaling of the problem is likely to reduce the number of iterations required and make the problem less sensitive to perturbations in the data, thus improving the condition of the problem. It is suggested that, in the absence of better information, it is sensible to make the Euclidean lengths of each constraint of comparable magnitude. The problem was therefore scaled by a factor of 10^{-6} and the constraints involving the source velocities were scaled by a factor of 10^{6} so that they were of the same order of magnitude as those for surface pressure magnitudes. Initial values of the optimisation variables were all specified as $1/\sqrt{2}$ m s^{-1} so that the magnitudes of the source velocities were initially at the upper end of the specified dynamic range. This generated a solution for the optimisation variables where both sets of constraints were satisfied. If the rescaling was not carried out prior to the optimisation, the NAG® solver either became unstable or returned results which did not satisfy the constraints.

The real and imaginary parts of the velocities were subsequently rescaled and the surface and field pressures calculated. Figures 5.6 and 5.7 respectively display the magnitudes and phases of the element velocities of the array resulting from the constrained optimisation. It was verified that the velocity magnitudes did not exceed 1 m s^{-1}.

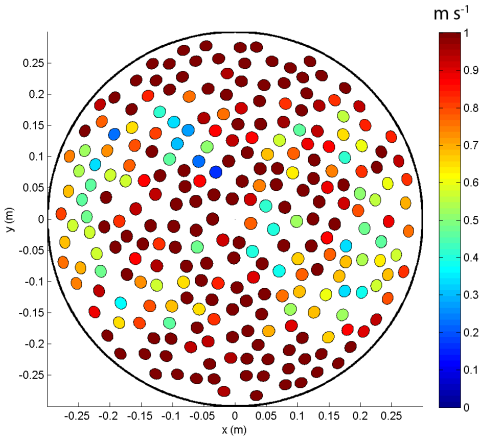

Figure 5.6 Source velocity magnitudes resulting from constrained optimisation.

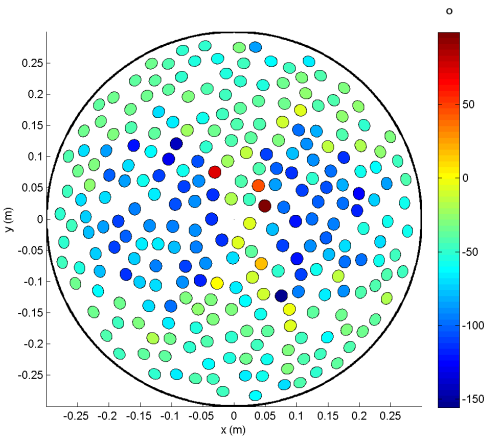

Figure 5.7 Source velocity phases resulting from constrained optimisation.

Figure 5.8 shows the acoustic pressure magnitude on the surface of the cylinder, resulting from the source velocity distribution displayed in figures 5.6 and 5.7. This acoustic pressure magnitude did not exceed 4 MPa. A 30% reduction in the acoustic pressure magnitude on the surface of the cylinder was therefore generated compared with the spherical focusing case.

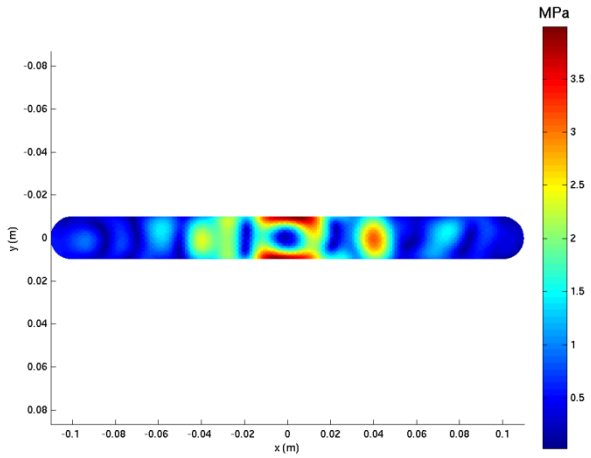

Figure 5.8 Acoustic pressure magnitude on surface of cylinder resulting from field of 100 kHz multi-element array. Source velocity distribution obtained from constrained optimisation.

Figure 5.9 shows the acoustic pressure magnitude in the *y-z* plane resulting from the source velocity distribution displayed in figures 5.6 and 5.7.

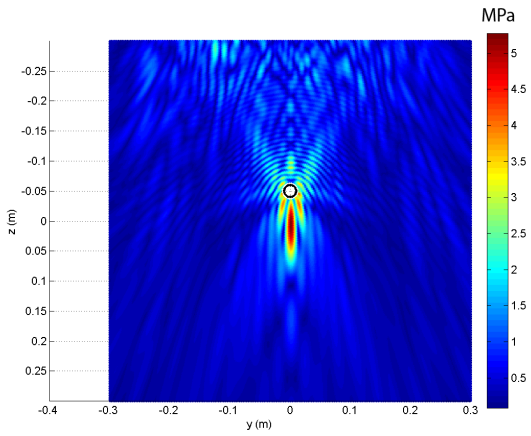

Figure 5.9. Acoustic pressure magnitude in *y*-*z* plane resulting from field of 100 kHz multi-element array. Source velocity distribution obtained from constrained optimisation.

This particular configuration makes it challenging for the majority of the acoustic energy to be transmitted to the vicinity of the focus, owing to the close proximity of the scatterer to the focal region of the array. This is further hindered by the cylinder's large diameter compared with the beam of the array, as shown in figure 5.3. The acoustic pressure magnitude at the focus shown in figure 5.10 is reduced by 14% compared with the spherical focusing case. To investigate how side lobes were affected by the constrained optimisation, the acoustic pressure magnitudes normalised to their value at the focus are displayed in figure 5.10, where all elements are vibrating with unit amplitude and uniform phase, and in figure 5.11, where the optimised velocity values were used.

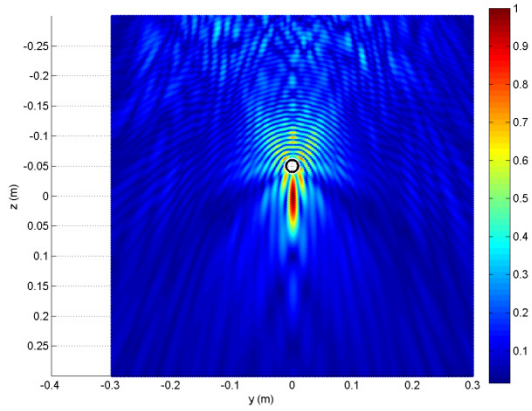

Figure 5.10 Normalised acoustic pressure magnitude in *y*-*z* plane resulting from field of 100 kHz multi-element array. Uniform unit amplitude velocity and zero phase (spherical focusing).

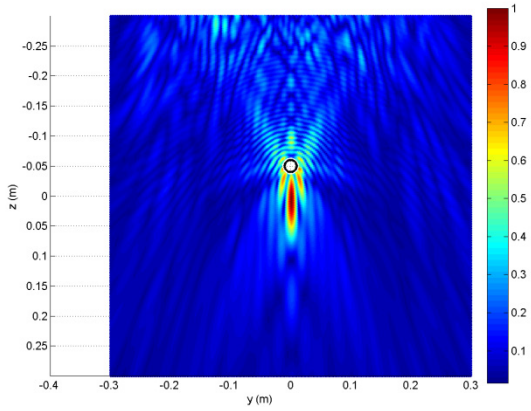

Figure 5.11 Normalised acoustic pressure magnitude in *y*-*z* plane resulting from field of 100 kHz multi-element array. Source velocity distribution obtained from constrained optimisation.

Figure 5.11 shows that an overall reduction in the side-lobes relative to the focus was achieved as a consequence of the constrained optimisation compared with the uniform amplitude and phase results displayed in figure 5.10. Furthermore, a reduction in the backscattered signal is clearly visible in figure 5.11 compared with figure 5.10.

5.3 Summary

This chapter has described methods for exploiting the forward BEM model to solve the inverse problem of focusing the field of a multi-element HIFU array through the ribcage. This procedure involves determining optimal values for the real and imaginary parts of the velocities of each element of the HIFU array so that the acoustic pressures at specified locations in the exterior domain best fit a required field distribution. Furthermore, the acoustic pressure magnitudes on the surface of the ribs should ideally be maintained below a specified threshold. The following approaches were initially identified:

- binarised apodisation based on geometric ray tracing
- phase conjugation (the frequency domain equivalent operation to time-reversal acoustics)
- the DORT method.

It was shown how the binarised apodisation approach, whilst practical to implement, may be suboptimal, as it does not directly address the inverse problem. Instead, it requires elements of the HIFU array to be switched off if they are occluded by a section of the ribs. This may be clinically effective but is also somewhat limiting. Indeed, switching off a large number of elements may significantly reduce focal pressures.

The phase conjugation process was seen to maximise the output amplitude pressure at a given location and at a given time for a given input energy. Nevertheless it will only optimise the acoustic pressure amplitude at the focus and does not impose any constraints on the field around the focus or on the ribs.

The DORT method has the advantage of not requiring any prior knowledge of the location of the scatterers, and only requires the measurement of the inter-element transfer matrix. It enables a vector focusing on point-like well resolved scatterers to be determined. The DORT method may be modified to separate and remove the emissions which focus on the scatterer from those that focus on the target, using an orthogonal projection in the frequency domain. It was explained that the DORT method may have limitations when applied to trans-costal HIFU applications: whilst it may generate a vector of element velocities for which the ratio of acoustic dose rate at the focus and on the ribs is optimal, it may not be relevant in a clinical context. Indeed, if the acoustic pressures at the focus are insufficient to induce tissue necrosis and if the dynamic range of the elements and electronics prohibit scaling of element velocities so as to induce this, the DORT method may limit the array from being used to its full potential.

Alongside these approaches, a constrained optimisation approach was proposed for solving the inverse problem, and has been formulated using BEM as the forward model. Using the discretised form of the Helmholtz integral equation for locations in the exterior volume and on the surface of the scatterer, the inverse problem of determining the complex velocities of a multi-element array which produces an acoustic pressure field that best fits a required acoustic pressure distribution in a least-squares sense was formulated such that:

- the pressure magnitude on the surface of the scatterer did not exceed a specified threshold

- the amplitude of the velocity of each element on the array was bounded by maximum value defined by the dynamic range.

This approach was tested on a reduced complexity model involving the scattering from a perfectly rigid cylinder with hemispherical end-caps by a 100 kHz 256 element spherical-section array. Employing a NAG® library solver, a least-squares optimisation with nonlinear constraints was carried out to solve the inverse problem, where the gradients of the objective function and of the constraints with respect to the optimisation variables were provided as input data. The solver returned a set of real and imaginary parts for the source velocities which satisfied both sets of constraints, hence reducing side lobes and acoustic pressures on the surface of the scatterer compared to the case when all elements are driven with uniform phase and amplitude. These results are encouraging and warrant the investigation of the constrained optimisation approach to focus the field of a multi-element phased array inside the ribcage whilst sparing the ribs and its comparison with other methods discussed in this chapter.

Chapter 6

The Inverse Problem: Results

6.1 Overview

Chapter 5 reviewed candidate methodologies for soling the inverse problem of focusing the field of a multi-element HIFU phased array through the ribcage, using BEM as the forward model. In this chapter, these methods were tested on a range of array-rib configurations. To test the validity and robustness of the focusing methods, a total of six configurations will be investigated, three of which will feature human ribs (or a variation thereof) and three others, idealised ribs. There are two principle reasons for including idealised ribs in this study. The first is because human anatomical rib data suitable for meshing was not straight forward to obtain. Clearly, a single configuration, realistic as it may be, cannot be relied upon for assessment of the various methods of focusing. Hence the requirement to carry out some simulations on idealised ribs. The second reason is that many trans-costal HIFU studies have used such idealised ribs both experimentally and theoretically (Botros *et al* 1998, Bobkova *et al* 2010, Khokhlova *et al* 2010, Ballard *et al* 2010) and have extrapolated their conclusions to human ribs. Whilst deductions from these studies may be of clinical significance, human ribs may differ significantly from idealised scatterers. The study in this chapter may therefore help evaluate whether studies on idealised ribs are relevant for assessment of trans-rib HIFU techniques.

As discussed in Chapter 5, results for the following focusing methods will be obtained, using BEM as the forward model.

- Binarised apodisation based on geometric ray tracing.
- Phase conjugation.
- The DORT method.
- The constrained optimisation method based on the NAG® *e04us* solver (NAG® website).

The exterior medium is assumed to be attenuating and to have properties representative of human liver. The ribs are assumed to be locally reacting, with a surface impedance representative of rib bone. All methods of focusing through the ribs will then be implemented on the six array-rib topologies discussed earlier. Results for spherical focusing will initially be obtained. The ability of each method to focus through the ribcage, whilst at the same time reducing local acoustic pressure maxima on the surface of the ribs, will be benchmarked against each other using the criteria based on the specific absorption rate (SAR) defined in equation (6.1). The SAR gain criterion G_{SAR} is defined by Cochard *et al* (2009) as the logarithmic ratio of the SAR on the target to the SAR on the point to be spared. In this work, we will consider the SAR gain relative to the maximum SAR observed on the surface of the ribs:

$$G_{\mathrm{SAR}} = 10 \log \frac{q_{v,\mathrm{focus}}}{\max(q_{v,\mathrm{ribs}})} \tag{6.1}$$

where $q_{v,\mathrm{focus}}$ denotes the SAR at the focus and $q_{v,\mathrm{ribs}}$ the SAR on the ribs. $\max(q_{v,\mathrm{ribs}})$ denotes the maximum value of $q_{v,\mathrm{ribs}}$. This SAR gain gives information about the hot spot level, but is masked by the spatial averaging and is relevant if heat diffusion is low (Cochard *et al* 2009). An SAR gain based on the spatial average of the SAR over the surface of the ribs was investigated by Cochard *et al* (2009), but is beyond the scope of this thesis. Ultimately, a heat transfer analysis would be required to relate the acoustic field distribution on the surface of the ribs to the temperature rise at required locations. This is also beyond the scope of this thesis.

In addition to the SAR gain, the peak focal pressure relative to the maximum level available from the phased array will also be used to assess the focusing quality.

6.2 Human ribs: Array-rib configuration 1

6.2.1 Description

The first configuration used to assess the trans-rib focusing methods was described in section 4.5.1. It corresponds to the geometric focus of the array being located on a line through the intercostal space equidistant between ribs 10 and 11 and approximately 3 cm deep behind the ribcage. This configuration was in part chosen to assess the

feasibility of the BEM technique, although it is relevant to clinical applications in which shallow tumours may be targeted. These may be more problematic to treat than more deep seated ones because the higher energy density at the skin increases the risk of skin burn. The configuration is shown again in figure 6.1.

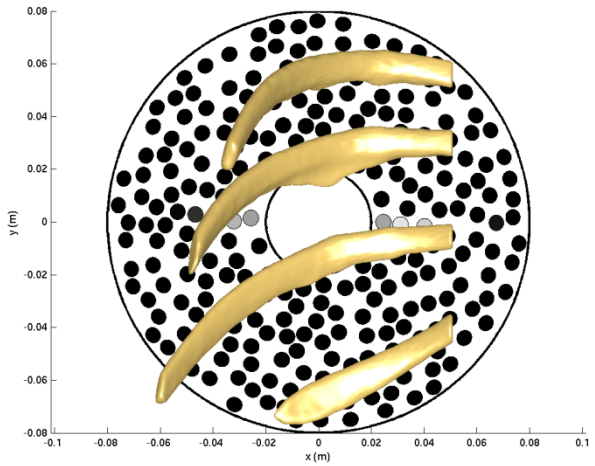

Figure 6.1 Position of ribs with respect to HIFU array looking in the negative *z* direction, through the ribs and towards the transducer. Array-rib configuration 1.

6.2.2 Spherical focusing

Whilst the spherical focusing on this rib-array configuration was already investigated in section 4.5.5, the results are recapitulated here for the sake of completeness.

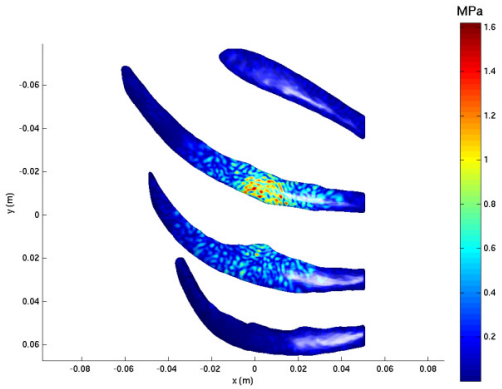

Figure 6.2 Acoustic pressure magnitude on surface of ribs resulting from field of 1 MHz multi-element array. Spherical focusing. Array-rib configuration 1.

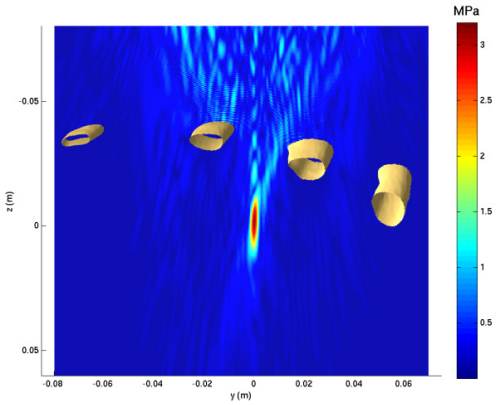

Figure 6.3 Acoustic pressure magnitude in *y-z* plane resulting from field of 1 MHz multi-element array. Spherical focusing. Array-rib configuration 1.

It can be seen that the maximum focal pressure is 3.2 MPa, and the maximum acoustic pressure on the surface of the ribs is 1.6 MPa. This results in an SAR gain of 7.2 dB.

6.2.3 Binarised apodisation based on geometric ray tracing

The method of binarised apodiation described in section 5.2.1 was applied to the current array-rib configuration, thus producing the source velocity distribution displayed in magnitude and phase in figures 6.4 and 6.5, respectively.

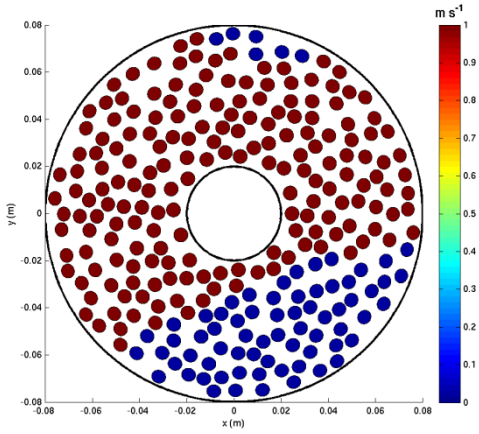

Figure 6.4 Source velocity magnitudes resulting from binarised apodisation based on ray tracing. Array-rib configuration 1.

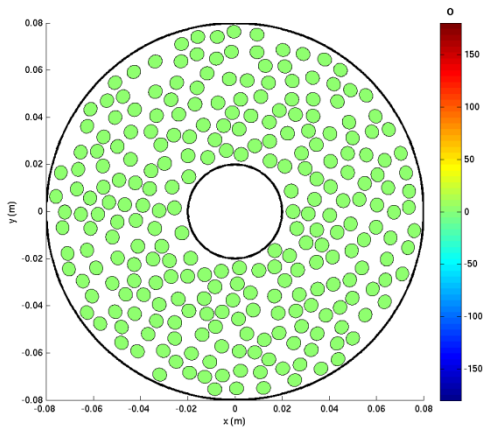

Figure 6.5. Source velocity phases resulting from binarised apodisation based on ray tracing. Array-rib configuration 1.

The above velocity distribution results in 73 elements of the phased array being switched off (approximately 29% of all elements). The velocity distribution in figures 6.4 and 6.5 was then used as input data to the forward BEM model, which generated the acoustic pressure magnitudes on the surface of the ribs shown in figure 6.6. The corresponding pressure magnitudes in the *y*-*z* plane, obtained at the post-processing stage, are displayed in figure 6.7.

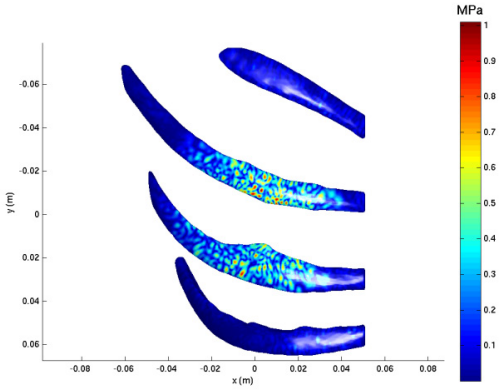

Figure 6.6 Acoustic pressure magnitude on surface of ribs resulting from field of 1 MHz multi-element array. Binarised apodisation based on geometric ray tracing. Array-rib configuration 1.

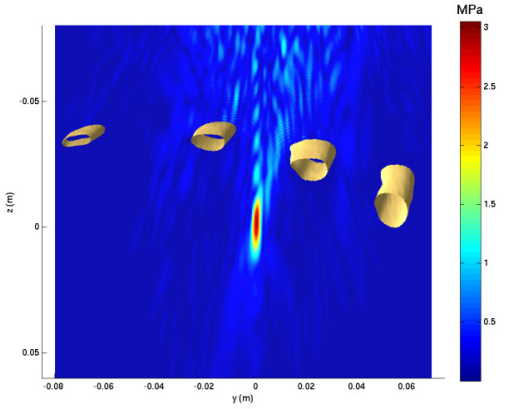

Figure 6.7 Acoustic pressure magnitude in *y*-*z* plane resulting from field of 1 MHz multi-element array. Binarised apodisation based on geometric ray tracing. Array-rib configuration 1.

The implementation of the binarised apodisation method on this rib-array configuration gives rise to a maximum acoustic pressure on the surface of the ribs of 1.0 MPa, with a peak focal pressure of 3.0 MPa. This produces an SAR gain of 11 dB. A qualitative reduction in the backscattered pressure can be observed when comparing figures 6.7 and 6.3.

6.2.4 Phase conjugation

The phase conjugation method described in section 5.2.2 first requires the calculation of the acoustic pressure field generated by a monochromatic point source. For focusing at the geometric centre of the array, the source must, in this case, be positioned at the global origin. The acoustic pressure field produced by such a point source in the presence of the ribs is displayed in the *y*-*z* plane in figure 6.8. Acoustic pressures at

locations within a 5 mm radius from the singularity at the global origin were removed from the plot, so as to allow better visualisation of the field.

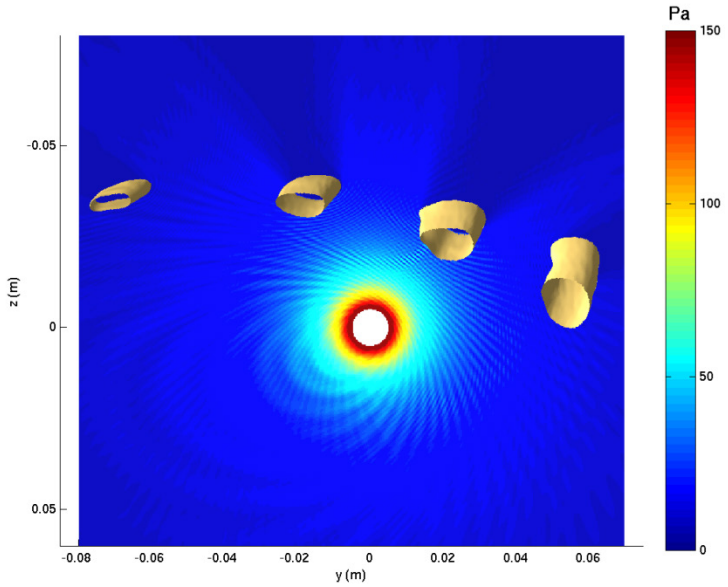

Figure 6.8 Acoustic pressure magnitude in *y*-*z* plane resulting from field of 1 MHz point source of unit source strength, positioned at the global origin. Array-rib configuration 1.

Figure 6.8 clearly shows the effect of shadowing by the ribs, particularly for ribs 10 and 11. The source element velocities required for the phase conjugation calculation were obtained following the procedure described in section 5.2.3. These are displayed in magnitude and phase in figures 6.9 and 6.10, respectively.

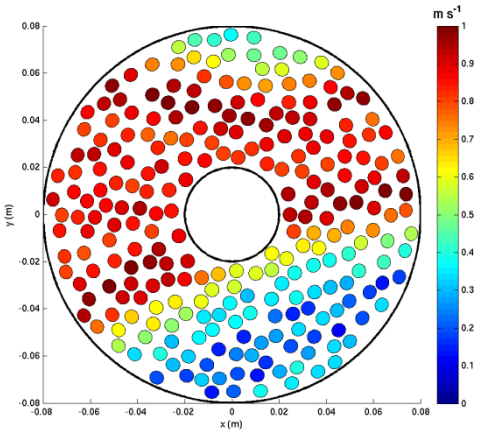

Figure 6.9 Source velocity magnitudes resulting from phase conjugation. Array-rib configuration 1.

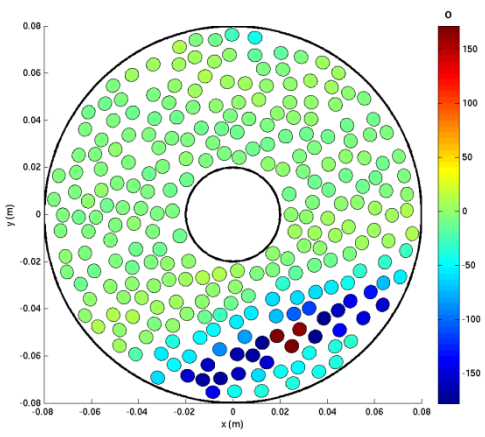

Figure 6.10 Source velocity phases resulting from phase conjugation. Array-rib configuration 1.

It can be seen that the pattern of velocity magnitudes in figure 6.9 is not dissimilar to that obtained in figure 6.4, when using binarised apodisation based on geometric ray tracing. The elements which are shadowed by the ribs are indeed ascribed lower velocity amplitudes by the phase conjugation process than those which are not. The focusing vector defined by the above source velocity distribution yields the acoustic pressure magnitude on the surface of the ribs shown in figure 6.11. The acoustic field pressures in the *y*-*z* plane are shown in figure 6.12.

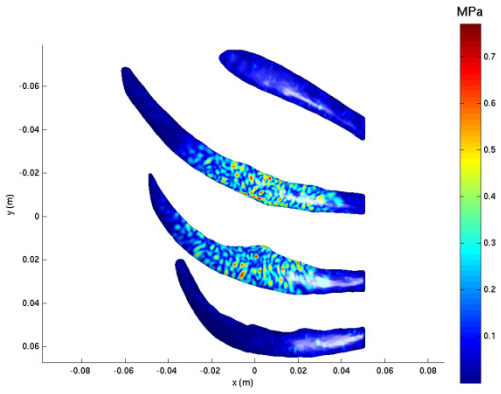

Figure 6.11 Acoustic pressure magnitude on surface of ribs resulting from field of 1 MHz multi-element array. Phase conjugation. Array-rib configuration 1.

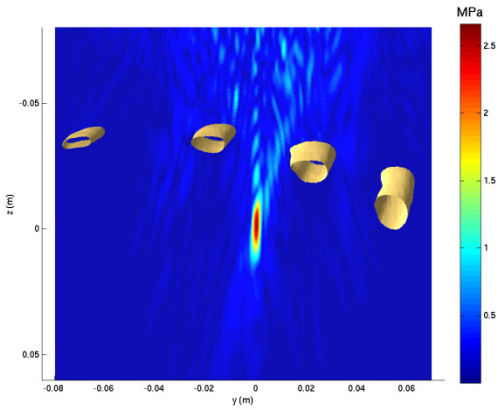

Figure 6.12 Acoustic pressure magnitude in *y*-*z* plane resulting from field of 1 MHz multi-element array. Phase conjugation. Array-rib configuration 1.

The phase conjugation method on this rib-array configuration gives rise to a maximum acoustic pressure on the surface of the ribs of 0.79 MPa, with a peak focal pressure of 2.7 MPa. This produces an SAR gain of 12 dB.

6.2.5 DORT

The DORT method was implemented as described in section 5.2.3 and in Appendix B. The value used for i_{max}, i.e. the number of eigenvectors associated with the higher singular values, was 25, as this maximised the SAR gain. This produced the focusing vector shown in terms of the magnitude of the array element velocity magnitudes and phases in figures 6.13 and 6.14, respectively.

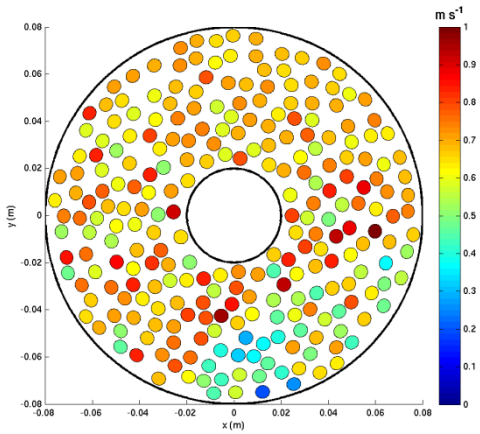

Figure 6.13 Source velocity magnitudes resulting from DORT method. Array-rib configuration 1.

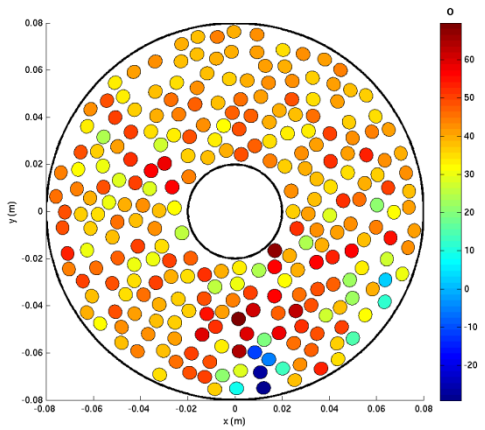

Figure 6.14 Source velocity phases resulting from DORT method. Array-rib configuration 1.

The corresponding BEM acoustic pressure magnitudes on the surface of the ribs and in the *y*-*z* plane are displayed in figures 6.15 and 6.16, respectively.

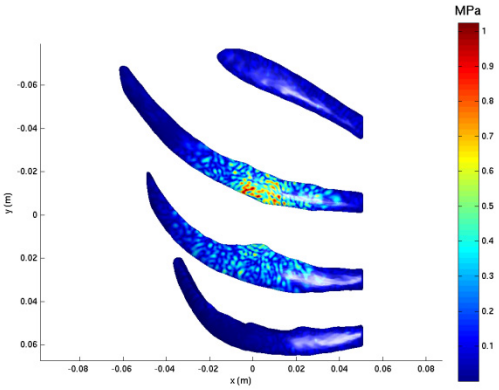

Figure 6.15 Acoustic pressure magnitude on surface of ribs resulting from field of 1 MHz multi-element array. DORT method. Array-rib configuration 1.

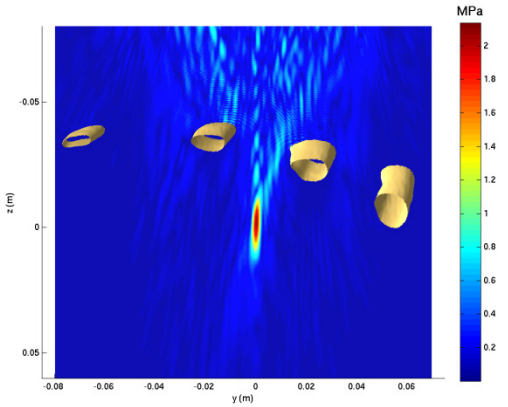

Figure 6.16 Acoustic pressure magnitude in *y*-*z* plane resulting from field of 1 MHz multi-element array. DORT method. Array-rib configuration 1.

The DORT method on this rib-array configuration gives rise to a maximum acoustic pressure on the surface of the ribs of 1.0 MPa, with a peak focal pressure of 2.1 MPa. An SAR gain of 7.6 dB is achieved.

6.2.6 Constrained optimisation

For this particular array-rib configuration, the value of $p_{\mathrm{surf}_{\max}}$ in equation (5.21) was chosen as 45% of the maximum value of the pressure magnitude on the surface of the

ribs resulting from spherical focusing. This 45% value is not necessarily of clinical significance and was chosen in part to illustrate the technique, but also because higher values would violate the constraints imposed on the element velocity magnitudes (recall that $U_{\max}$ in equation 5.21 is selected to be 1 m s^{-1}). It is understood that in clinical applications, a damage threshold related to a dose quantity would have to be established experimentally. Defining a damage threshold and a dose quantity remains beyond the scope of this thesis, as is providing a full treatment planning code. Nevertheless, the advantage of employing a constrained optimisation approach is that the option exists to set tailored upper and lower bounds to field and source quantities which may be specific to the patient and to the HIFU system employed.

The cost function was formed by choosing $\{\hat{p}_{\mathrm{ext}}\}$ in equation (5.21) as follows: the vector of pressures in the exterior volume featured in the cost function (i.e. the 'desired' field pressure distribution) was generated from pressure field values in absence of ribs at 9261 equally spaced locations in a 21×21×21 cubic Cartesian grid such that -1.5 cm ≤ x, y, z ≤ 1.5 cm, the focus of the array being at the global origin.

The surface mesh of the ribs contains 200921 nodes (see section 4.5.2). It is both impractical and unnecessary to impose a constraint at all these locations on the surface of the scatterer. Too high a number of constraints may result in numerical instability and some locations on the surface of the ribs are highly unlikely to exceed $p_{\mathrm{surf}_{\max}}$, in particular those not directly facing the array. Hence, surface locations associated with pressure magnitudes below 40% of the maximum pressure resulting from spherical focusing (i.e. locations on the rib surface where the pressure was less than 0.64 MPa) were not included in the constraints. This resulted in only 3390 constraints associated with the pressure magnitude on the ribs being required, along with the 256 constraints for the magnitude of the element velocities. After the optimisation, it was verified that the acoustic pressure magnitude at all nodes on the surface of the ribs was below the chosen threshold.

For reasons specified in section 5.2.4.2, initial values of the optimisation variables were all specified as $1/\sqrt{2}$ m s^{-1} and the problem was scaled by a factor of 10^{-6}. In addition to this, the constraints involving the source velocities were scaled by a factor of 10^{6} so that they were of the same order of magnitude as the surface pressure magnitude constraints.

With the above input conditions, a solution was obtained for the focusing vector by following the procedure outlined in section 5.2.4. The real and imaginary parts of the velocities were subsequently rescaled and the surface and field pressures calculated. Figures 6.17 and 6.18 respectively display the magnitudes and phases of the element velocities of the array resulting from the constrained optimisation. It was verified that the velocity magnitudes did not exceed 1 m s^{-1}.

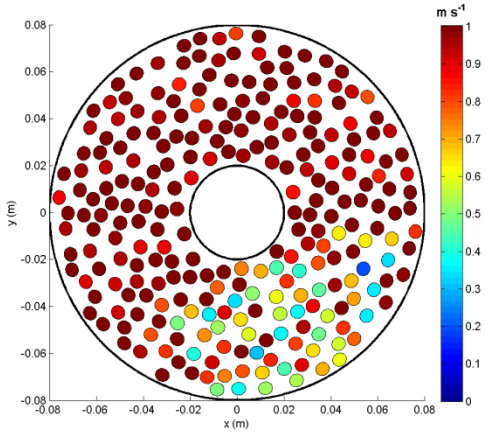

Figure 6.17 Source velocity magnitudes resulting from constrained optimisation. Array-rib configuration 1.

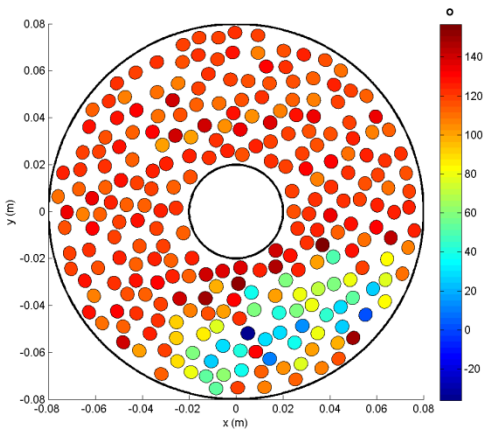

Figure 6.18 Source velocity phases resulting from constrained optimisation. Array-rib configuration 1.

The velocity distributions in figures 6.17 and 6.18 were then used as input data to the BEM formulation. The acoustic pressure magnitudes on the surface of the ribs and in the *y*-*z* plane are displayed in figures 6.19 and 6.20.

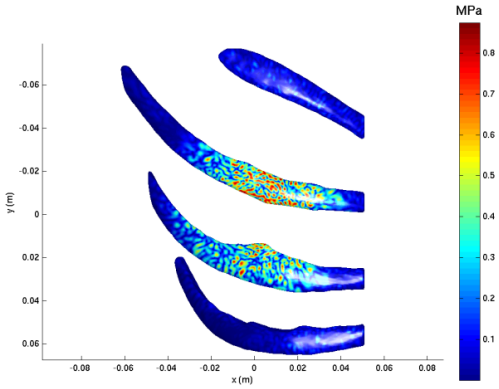

Figure 6.19 Acoustic pressure magnitude on surface of ribs resulting from field of 1 MHz multi-element array. Constrained optimisation. Array-rib configuration 1.

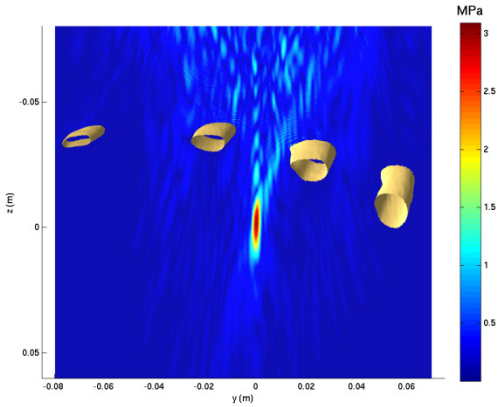

Figure 6.20 Acoustic pressure magnitude in *y*-*z* plane resulting from resulting. Constrained optimisation. Array-rib configuration 1.

It was verified that the maximum surface pressure magnitude was 0.88 MPa. The acoustic pressure magnitude at the focus is 3.1 MPa, hence providing an SAR gain of 12 dB. Figure 6.20 shows that an overall qualitative reduction in the back-scattered acoustic pressure is achieved as a consequence of the constrained optimisation, when compared against the uniform amplitude and phase results displayed in figure 6.3. Although the constrained optimisation algorithm is unsuccessful at rendering a peak pressure of 4.4 MPa which was obtained in the absence of ribs (see figures 5.34 and 5.35), it is now only 3% lower than in the case of spherical focusing in the presence of ribs (see figure 6.3).

6.3 Human ribs: Array-rib configuration 2

6.3.1 Description

Array-rib configuration 2 represents a variation on configuration 1 as follows. The ribs were translated by 2 cm and –3 cm in along the *y* and *z* axes, respectively, so that the geometric focus of the array was positioned approximately 6 cm directly behind rib 11, behind the ribcage. This scenario represents an extreme configuration where the target is directly behind one of the ribs, which is likely to result in a more challenging treatment planning situation. Indeed, as the transducer is now closer to the surface of the ribs, this is likely to result in a lower SAR gain for the spherical focusing case, which

may make the inverse problem more challenging. The configuration is shown in figure 6.21.

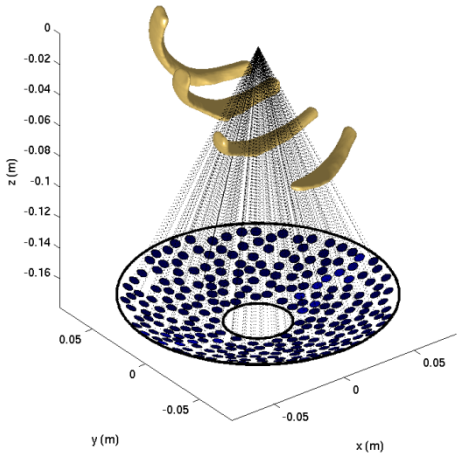

Figure 6.21 Position of ribs with respect to HIFU array for configuration 2.

6.3.2 Spherical focusing

Spherical focusing on array-rib configuration 2 results in the acoustic pressure magnitude on the surface of the ribs displayed in figure 6.22 and the field pressure magnitude in the *y*-*z* plane shown in figure 6.23.

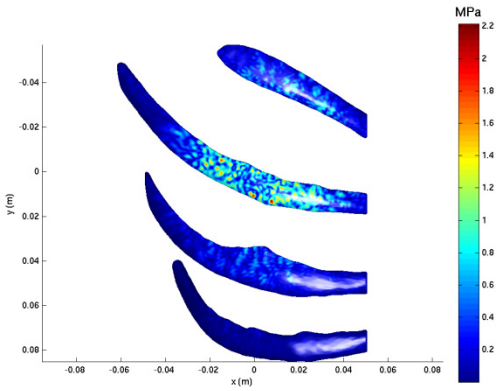

Figure 6.22 Acoustic pressure magnitude on surface of ribs resulting from field of 1 MHz multi-element array. Spherical focusing. Array-rib configuration 2.

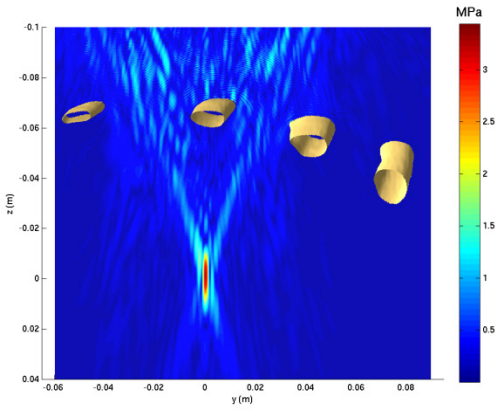

Figure 6.23 Acoustic pressure magnitude in *y*-*z* plane resulting from field of 1 MHz multi-element array. Spherical focusing. Array-rib configuration 2.

The data in figure 6.22 shows that the maximum acoustic pressure on the surface of the ribs is 2.2 MPa. The acoustic pressure at the focus in figure 6.23 is 3.4 MPa. This results in an SAR gain of 5.1 dB.

6.3.3 Binarised apodisation based on geometric ray tracing

The method of binarised apodiation described in section 5.2.1 was applied to the current array-rib configuration, thus producing the source velocity distribution displayed in magnitude and phase in figures 6.24 and 6.25, respectively.

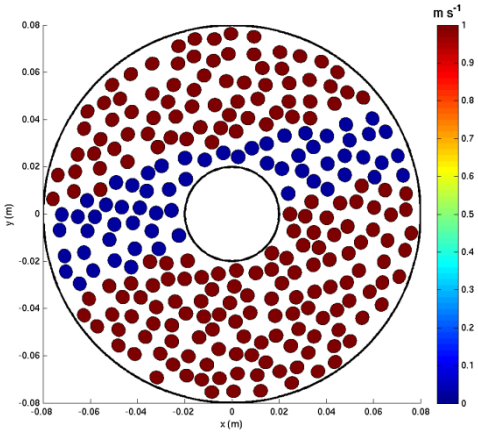

Figure 6.24 Source velocity magnitudes resulting from binarised apodisation based on ray tracing. Array-rib configuration 2.

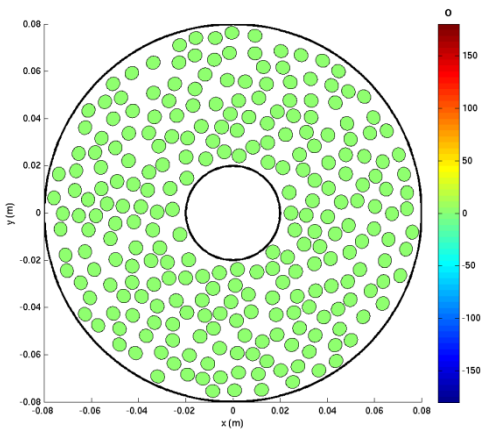

Figure 6.25. Source velocity phases resulting from binarised apodisation based on ray tracing. Array-rib configuration 2.

The above velocity distribution results in 62 elements of the phased array being switched off (approximately 24% of all elements). The velocity distribution defined by the data in figures 6.24 and 6.25 was then used as input data to the forward BEM model, which generated the acoustic pressure magnitudes on the surface of the ribs shown in figure 6.26. The corresponding pressure magnitudes in the *y*-*z* plane, obtained at the post-processing stage, are displayed in figure 6.27.

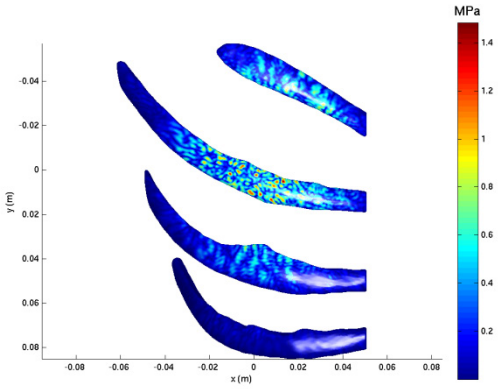

Figure 6.26 Acoustic pressure magnitude on surface of ribs resulting from field of 1 MHz multi-element array. Binarised apodisation based on geometric ray tracing. Array-rib configuration 2.

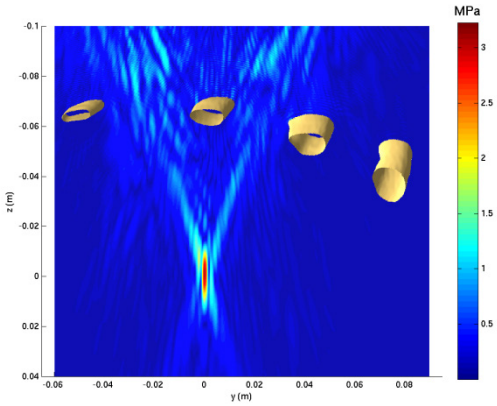

Figure 6.27 Acoustic pressure magnitude in *y*-*z* plane resulting from field of 1 MHz multi-element array. Binarised apodisation based on geometric ray tracing. Array-rib configuration 2.

The implementation of the binarised apodisation method on this rib-array configuration gives rise to a maximum acoustic pressure on the surface of the ribs of 1.5 MPa, with a peak focal pressure of 3.2 MPa. This produces an SAR gain of 7.9 dB. In addition to a qualitative reduction in the backscattered pressure when compared with the spherical focusing case, the pressure magnitude on rib 11 is reduced by 0.7 MPa.

6.3.4 Phase conjugation

The first stage of the phase conjugation calculation, i.e. the acoustic pressure field produced by a point source in the presence of the ribs, is displayed in the *y*-*z* plane in figure 6.28, with field locations within a 5 mm radius from the singularity removed.

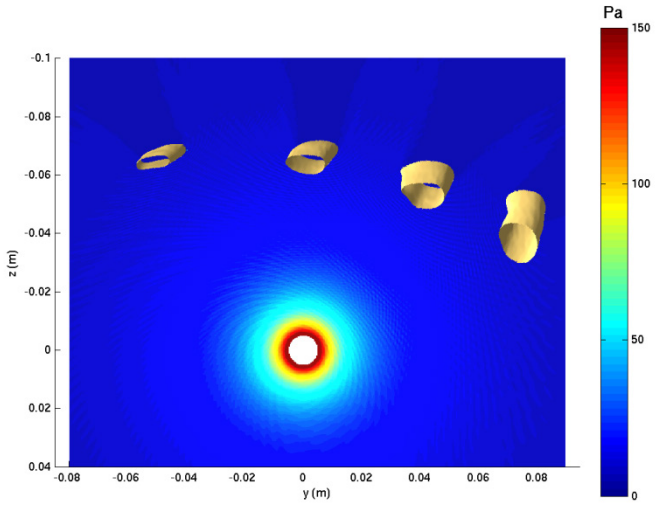

Figure 6.28 Acoustic pressure magnitude in *y*-*z* plane resulting from field of 1 MHz point source of unit source strength, positioned at the global origin. Array-rib configuration 2.

Figure 6.28 shows the effect of shadowing by the ribs. The source element velocities required for the phase conjugation calculation are displayed in magnitude and phase in figures 6.29 and 6.30, respectively.

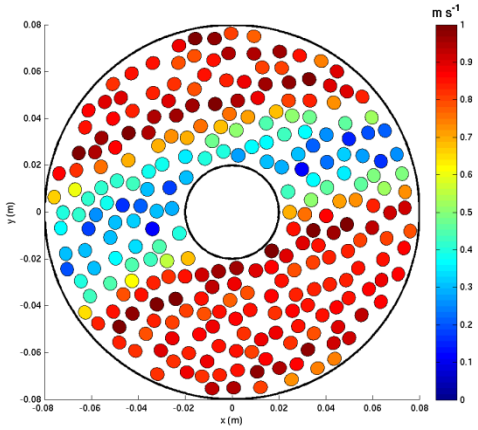

Figure 6.29 Source velocity magnitudes resulting from phase conjugation. Array-rib configuration 2.

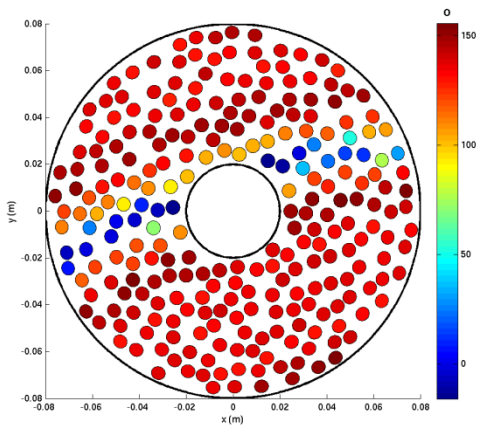

Figure 6.30 Source velocity phases resulting from phase conjugation. Array-rib configuration 2.

The pattern of velocity magnitudes in figure 6.29 bears some resemblance to that in figure 6.24. Clearly, much of the shadowing is caused by rib 11. At locations on the array where this shadowing is caused, the phase conjugation process generates lower values of the velocity amplitudes. The focusing vector defined by the above source velocity distribution yields the acoustic pressure magnitude on the surface of the ribs

shown in figure 6.31. The acoustic field pressures in the *y*-*z* plane are shown in figure 6.32.

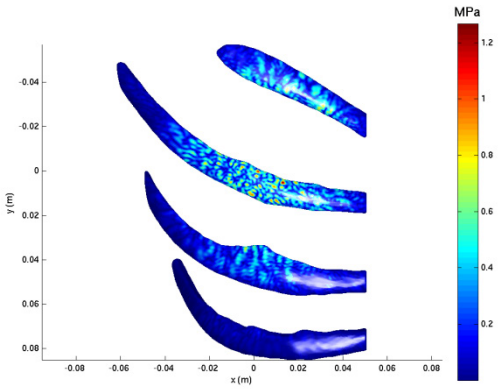

Figure 6.31 Acoustic pressure magnitude on surface of ribs resulting from field of 1 MHz multi-element array. Phase conjugation. Array-rib configuration 2.

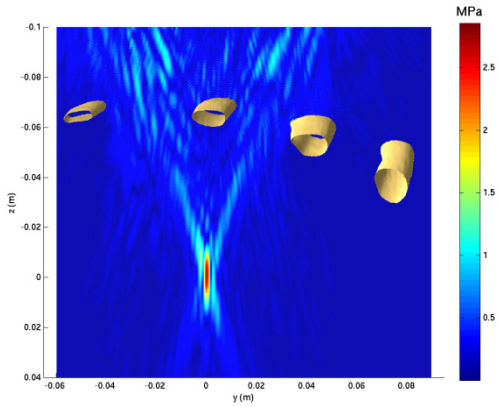

Figure 6.32 Acoustic pressure magnitude in *y*-*z* plane resulting from field of 1 MHz multi-element array. Phase conjugation. Array-rib configuration 2.

The phase conjugation method applied to this rib-array configuration gives rise to a maximum acoustic pressure on the surface of the ribs of 1.3 MPa, with a peak focal pressure of 2.8 MPa. This produces an SAR gain of 8.2 dB.

6.3.5 DORT

A value used for $i_{\max}$ of 30 was used in this implementation of the DORT method, as this maximised the SAR gain. This generated the focusing vector shown in terms of the magnitude of the array element velocity magnitudes and phases in figures 6.33 and 6.34, respectively.

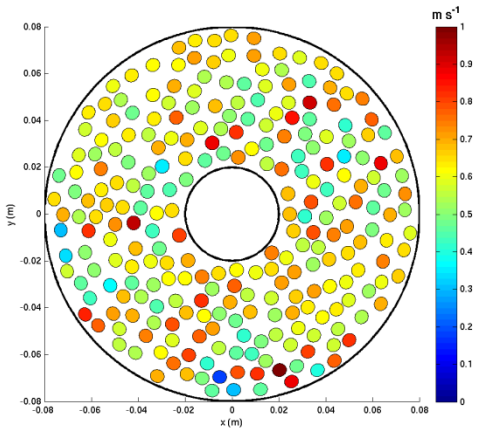

Figure 6.33 Source velocity magnitudes resulting from DORT method. Array-rib configuration 2.

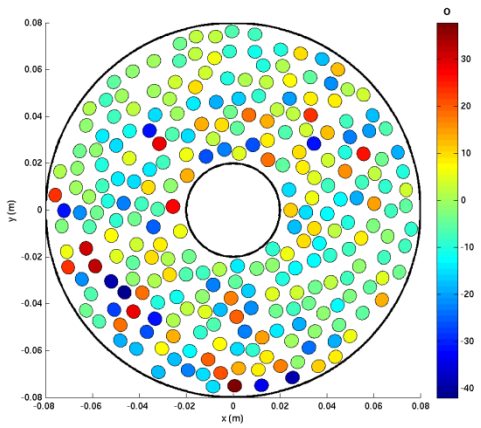

Figure 6.34 Source velocity phases resulting from DORT method. Array-rib configuration 2.

The corresponding BEM acoustic pressure magnitudes on the surface of the ribs and in the *y*-*z* plane are displayed in figures 6.35 and 6.36, respectively.

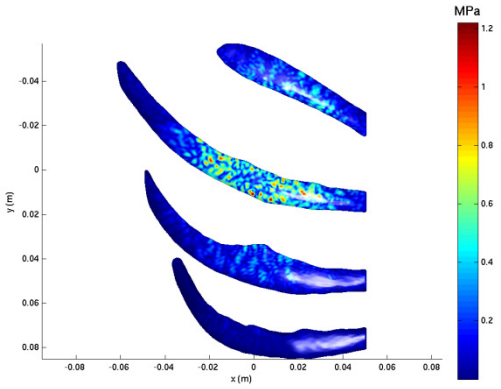

Figure 6.35 Acoustic pressure magnitude on surface of ribs resulting from field of 1 MHz multi-element array. DORT method. Array-rib configuration 2.

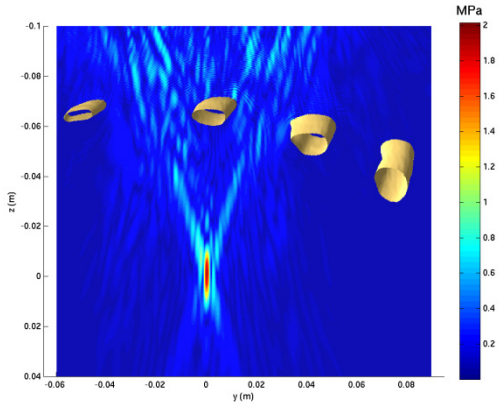

Figure 6.36 Acoustic pressure magnitude in *y*-*z* plane resulting from field of 1 MHz multi-element array. DORT method. Array-rib configuration 2.

The DORT method on this rib-array configuration gives rise to a maximum acoustic pressure on the surface of the ribs of 1.2 MPa, with a peak focal pressure of 2.0 MPa. An SAR gain of 5.6 dB is achieved.

6.3.6 Constrained optimisation

A solution was obtained for the focusing vector by following the procedure outlined in section 5.2.6 except that an additional constraint was added in the optimisation. This

was in the form of a lower bound value set on the focal pressure, equal to the pressure at the focus for the spherical focusing case. Implementing this additional constraint slightly improved the SAR gain. Figures 6.37 and 6.38 respectively display the magnitudes and phases of the element velocities of the array resulting from the constrained optimisation.

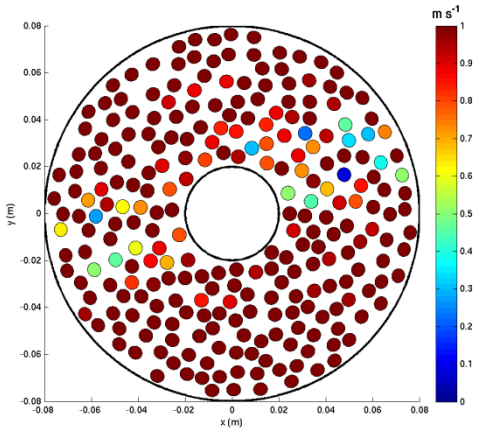

Figure 6.37 Source velocity magnitudes resulting from constrained optimisation. Array-rib configuration 2.

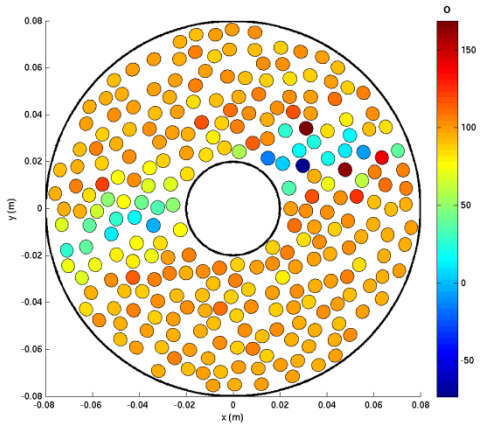

Figure 6.38 Source velocity phases resulting from constrained optimisation. Array-rib configuration 2.

The velocity distributions in figures 6.37 and 6.38 were subsequently used as input data to the BEM formulation. The acoustic pressure magnitudes on the surface of the ribs and in the *y*-*z* plane are displayed in figures 6.39 and 6.40.

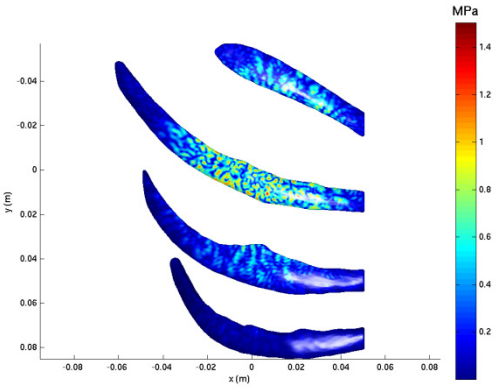

Figure 6.39 Acoustic pressure magnitude on surface of ribs resulting from field of 1 MHz multi-element array. Constrained optimisation. Array-rib configuration 2.

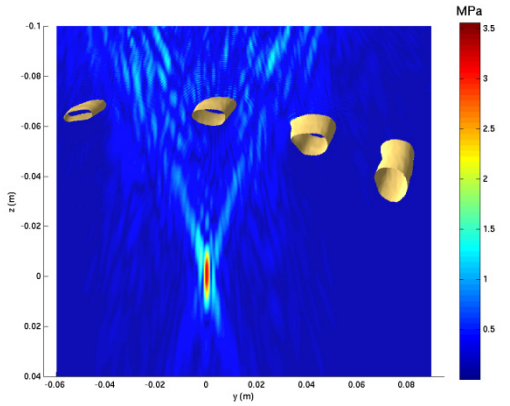

Figure 6.40 Acoustic pressure magnitude in *y*-*z* plane resulting from resulting. Constrained optimisation. Array-rib configuration 2.

For this particular array-rib geometry, the constrained optimisation routine could not locate a set of source velocities that would satisfy the constraints on the surface of the ribs. Indeed, the maximum surface pressure magnitude was 1.5 MPa, leading to only a 31% reduction in maximum pressure amplitude of the surface of the ribs instead of the requested 45%. Nevertheless, the acoustic pressure magnitude at the focus is 3.4 MPa, which is the same as for the spherical focusing case. An SAR gain of 8.3 dB is obtained, which is greater than that provided by the phase conjugation method.

6.4 Human ribs: Array-rib configuration 3

6.4.1 Description

Array-rib configuration 3 results from a modification in the rib topology used thus far in this thesis. Using CATIA v5 (CATIA v5 website), the ribs were rotated and translated to form an arrangement in which the intercostal spacing was as close as possible to 0.7 mm throughout. Some sections of the ribs had to be "shaved off" to achieve this. This particular intercostal distance was chosen because it is close to the smallest that might be expected to be encountered clinically (Nunn and Slavin 1980). Clearly, this configuration is not entirely realistic, as the intercostal spacing will vary throughout the ribcage. Nevertheless, this arrangement retains features of human ribs and provides a challenging situation for trans-rib HIFU treatment. The phased array was positioned so that its geometric focus was positioned approximately 3 cm behind rib 10, into the ribcage. The configuration is shown in figure 6.41.

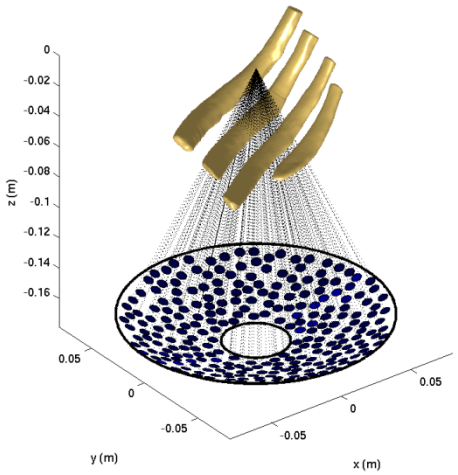

Figure 6.41 Position of ribs with respect to HIFU array for array-rib configuration 3.

6.4.2 Spherical focusing

Spherical focusing on array-rib configuration 3 results in the acoustic pressure magnitude on the surface of the ribs shown in figure 6.42 and the field pressure magnitude in the *y*-*z* plane shown in figure 6.43.

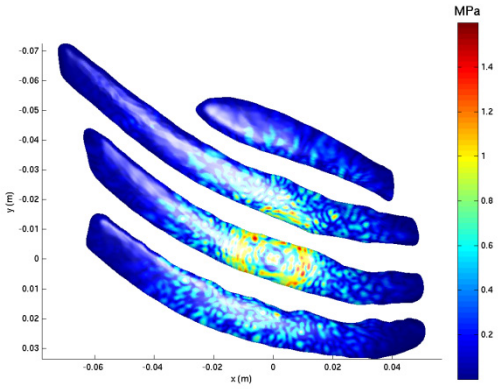

Figure 6.42 Acoustic pressure magnitude on surface of ribs resulting from field of 1 MHz multi-element array. Spherical focusing. Array-rib configuration 3.

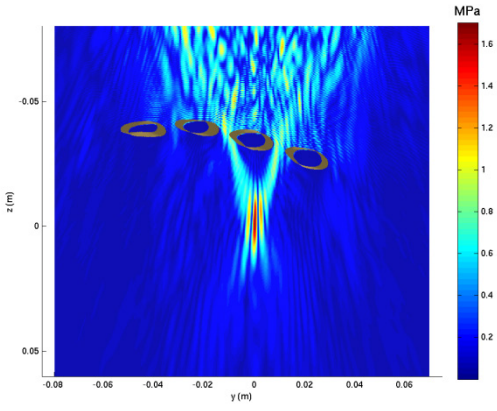

Figure 6.43 Acoustic pressure magnitude in *y*-*z* plane resulting from field of 1 MHz multi-element array. Spherical focusing. Array-rib configuration 3.

The data in figure 6.42 shows that the maximum acoustic pressure on the surface of the ribs is 1.6 MPa. The acoustic pressure at the focus in figure 6.43 is 1.7 MPa. This results in an SAR gain of 1.7 dB. Effects of scattering from the ribs are more prominant than for the spherical focusing cases on configurations 1 and 2, owing to the narrower

intercostal spacing in this configuration. Effects of splitting at the focus reported by Khokhlova *et al* (2010) are clearly visible, with side lobes approximately 3.7 dB relative to the main lobe, located ±2.5 mm along the *y*-axis from the global origin.

6.4.3 Binarised apodisation based on geometric ray tracing

The method of binarised apodiation based on geometric ray tracing apply to array-rib configuration 3 produces the source velocity distribution displayed in magnitude and phase in figures 6.44 and 6.45, respectively.

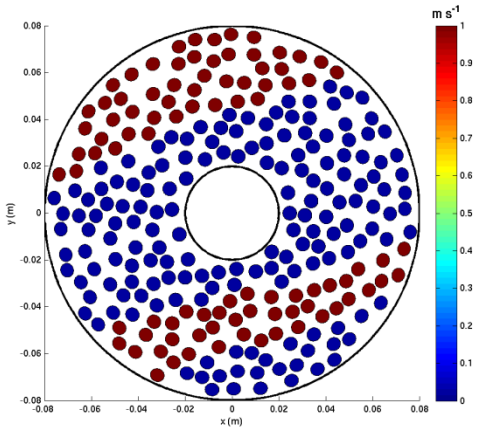

Figure 6.44 Source velocity magnitudes resulting from binarised apodisation based on ray tracing. Array-rib configuration 3.

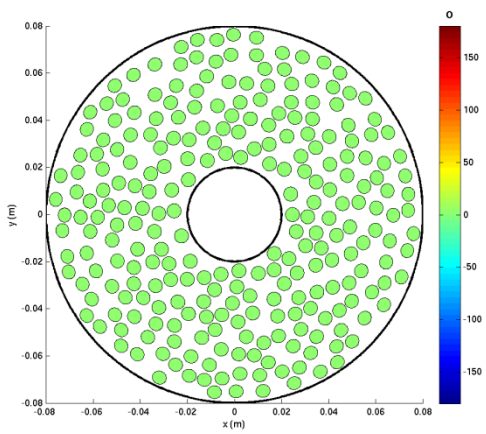

Figure 6.45. Source velocity phases resulting from binarised apodisation based on ray tracing. Array-rib configuration 3.

The above velocity distribution results in 165 elements of the phased array being switched off (approximately 64% of all elements). The velocity distribution defined by the data in figures 6.44 and 6.45 was then used as input data to the forward BEM model, which generated the acoustic pressure magnitudes on the surface of the ribs shown in figure 6.46. The corresponding pressure magnitudes in the *y*-*z* plane, obtained at the post-processing stage, are displayed in figure 6.47.

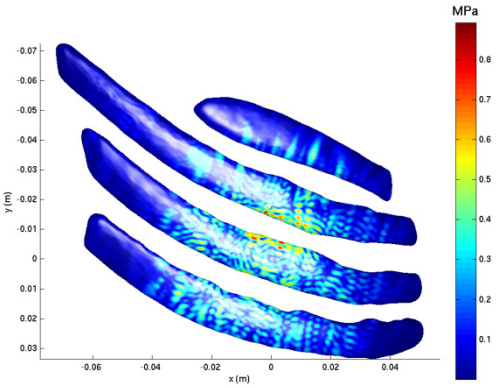

Figure 6.46 Acoustic pressure magnitude on surface of ribs resulting from field of 1 MHz multi-element array. Binarised apodisation based on geometric ray tracing. Array-rib configuration 3.

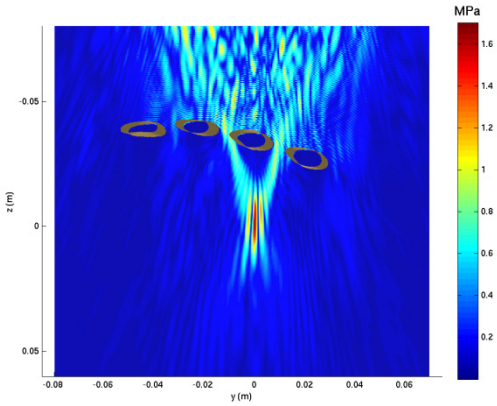

Figure 6.47 Acoustic pressure magnitude in *y*-*z* plane resulting from field of 1 MHz multi-element array. Binarised apodisation based on geometric ray tracing. Array-rib configuration 3.

The implementation of the binarised apodisation method on this rib-array configuration gives rise to a maximum acoustic pressure on the surface of the ribs of 0.92 MPa, with a peak focal pressure of 1.3 MPa. This produces an SAR gain of 4.2 dB.

6.4.4 Phase conjugation

The first stage of the phase conjugation calculation, i.e. the acoustic pressure field produced by a point source in the presence of the ribs, is displayed in the *y*-*z* plane in figure 6.48, with acoustic pressures at field locations in the vicinity of the singularity removed.

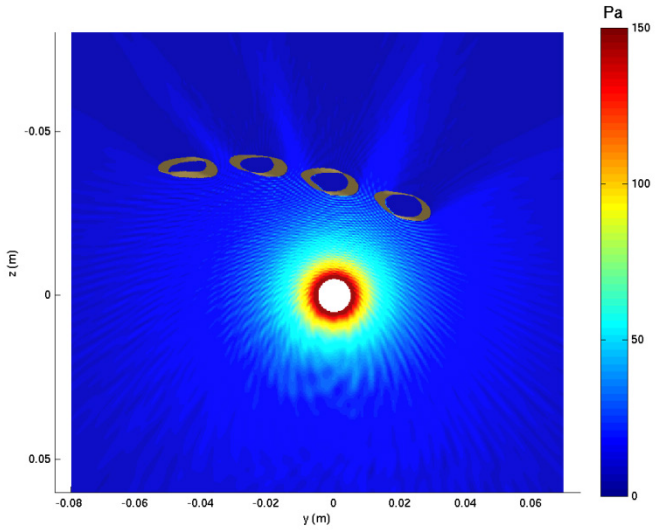

Figure 6.48 Acoustic pressure magnitude in *y*-*z* plane resulting from field of 1 MHz point source of unit source strength, positioned at the global origin. Array-rib configuration 3.

Figure 6.48 shows a stronger qualitative effect of shadowing by the ribs, compared with the point source calculation on array-rib configurations 1 and 2. The source element velocities required for the phase conjugation calculation are displayed in magnitude and phase in figures 6.49 and 6.50, respectively.

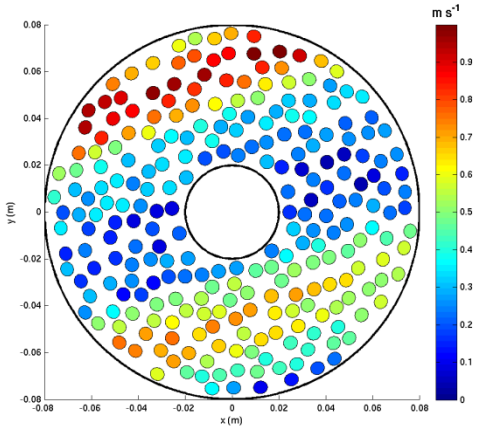

Figure 6.49 Source velocity magnitudes resulting from phase conjugation. Array-rib configuration 3.

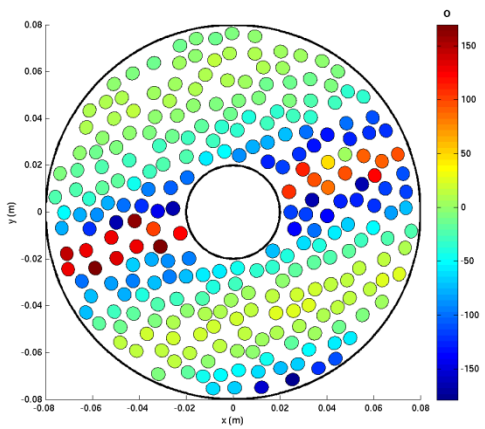

Figure 6.50 Source velocity phases resulting from phase conjugation. Array-rib configuration 3.

Again, it can be seen that the pattern of velocity magnitudes in figure 6.49 bears some resemblance with that in figure 6.44. The focusing vector defined by the above source velocity distribution yields the acoustic pressure magnitude on the surface of the ribs

shown in figure 6.51. The acoustic field pressures in the *y*-*z* plane are shown in figure 6.52.

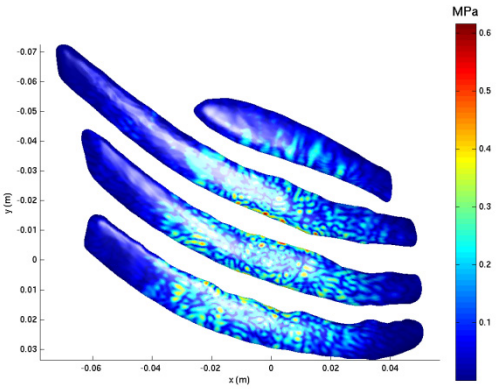

Figure 6.51 Acoustic pressure magnitude on surface of ribs resulting from field of 1 MHz multi-element array. Phase conjugation. Array-rib configuration 3.

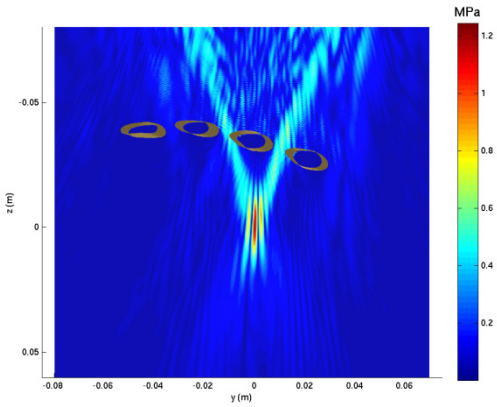

Figure 6.52 Acoustic pressure magnitude in *y*-*z* plane resulting from field of 1 MHz multi-element array. Phase conjugation. Array-rib configuration 3.

The phase conjugation method applied to this rib-array configuration gives rise to a maximum acoustic pressure on the surface of the ribs of 0.63 MPa, with a peak focal pressure of 1.2 MPa. This produces an SAR gain of 7.2 dB. Compared with spherical focusing and binarised apodisation, the phase conjugation method is successful in greatly reducing the acoustic pressure scattered by rib 10 (see figures 6.43, 6.47 and 6.52).

6.4.5 DORT

An $i_{\max}$ of 75 was used in this implementation of the DORT method. This value maximised the SAR gain. This generated the magnitude and phase of the focusing vector shown in figures 6.53 and 6.54, respectively.

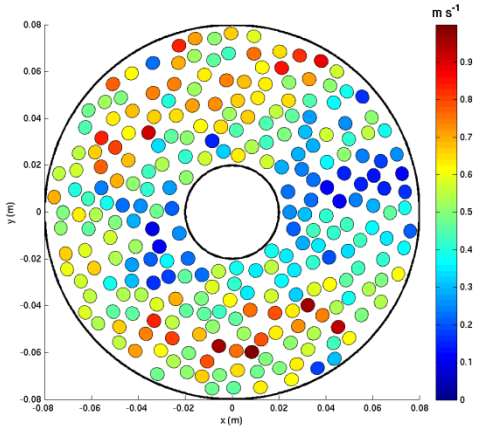

Figure 6.53 Source velocity magnitudes resulting from DORT method. Array-rib configuration 3.

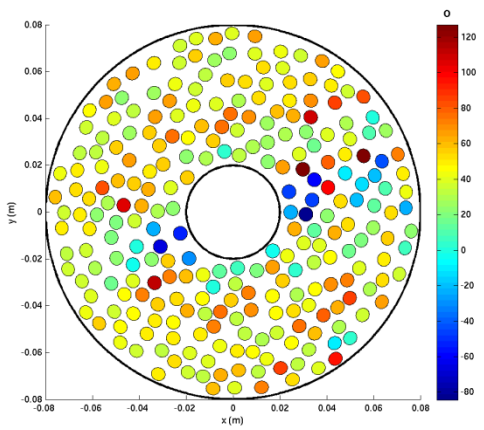

Figure 6.54 Source velocity phases resulting from DORT method. Array-rib configuration 3.

The corresponding BEM acoustic pressure magnitudes on the surface of the ribs and in the *y*-*z* plane are displayed in figures 6.55 and 6.56, respectively.

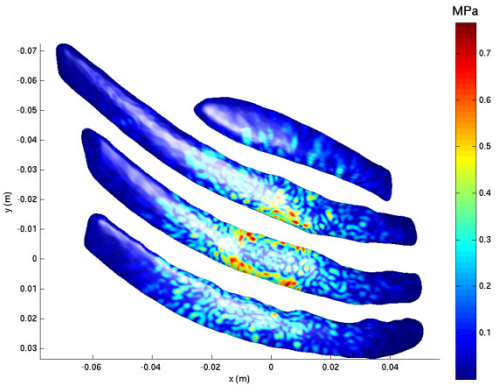

Figure 6.55 Acoustic pressure magnitude on surface of ribs resulting from field of 1 MHz multi-element array. DORT method. Array-rib configuration 3.

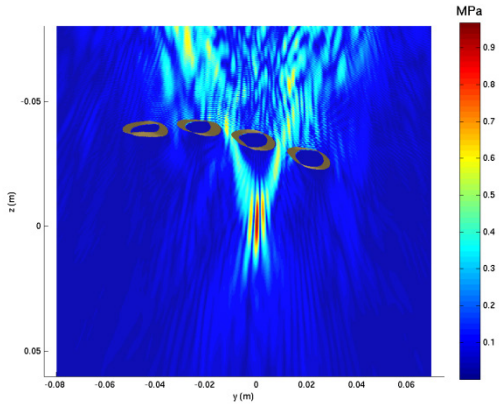

Figure 6.56 Acoustic pressure magnitude in *y*-*z* plane resulting from field of 1 MHz multi-element array. DORT method. Array-rib configuration 3.

The DORT method on this rib-array configuration generates a maximum acoustic pressure on the surface of the ribs of 0.77 MPa, with a peak focal pressure of 0.97 MPa. An SAR gain of 3.3 dB is achieved.

6.4.6 Constrained optimisation

A solution was obtained for the focusing vector by following the procedure outlined in section 5.2.6. An additional constraint in the form of a lower bound value set on the

focal pressure, equal to the pressure at the focus for the spherical focusing case was added in the optimisation. Furthermore, 1260 constraints were added at the locations of grating lobes in the form of lower bounds set to half of the acoustic focal pressure magnitude. These additional constraints were imposed to improve the SAR gain and reduce the magnitude of the grating lobes. The presence of grating lobes or multiple foci has been argued to reduce patient treatment times by producing large treatment volumes of thermally ablated tissue relative to single foci fields (Daum and Hynynen 1999, Filonenko *et al* 2004, Hand *et* al 2009). This may nevertheless complicate subsequent heat transfer analyses, so there is a requirement to try and minimise side lobes to cover the treatment volume with a more uniform temperature distribution. When setting the lower bound for the acoustic pressure magnitude at the locations of the grating lobes to less than half of the acoustic focal pressure, the optimisation routine did not yield a solution. Figures 6.57 and 6.58 respectively display the magnitudes and phases of the element velocities of the array resulting from the constrained optimisation.

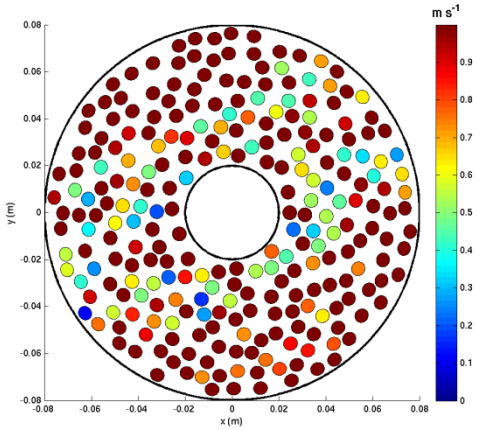

Figure 6.57 Source velocity magnitudes resulting from constrained optimisation. Array-rib configuration 3.

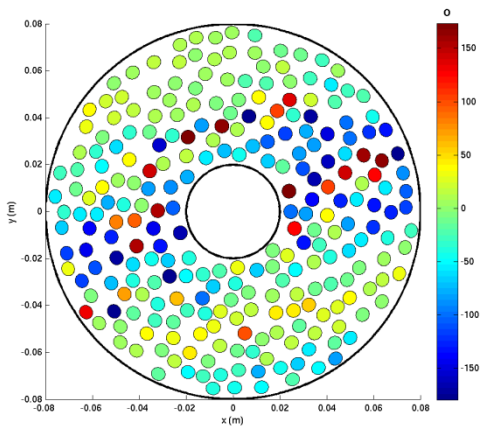

Figure 6.58 Source velocity phases resulting from constrained optimisation. Array-rib configuration 3.

The velocity distributions in figures 6.57 and 6.58 were subsequently used as input data to the BEM formulation. The acoustic pressure magnitudes on the surface of the ribs and in the *y*-*z* plane are displayed in figures 6.59 and 6.60.

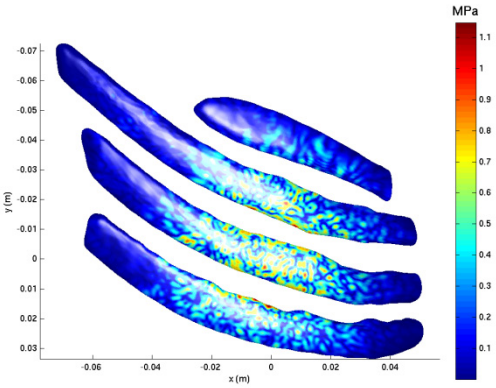

Figure 6.59 Acoustic pressure magnitude on surface of ribs resulting from field of 1 MHz multi-element array. Constrained optimisation. Array-rib configuration 3.

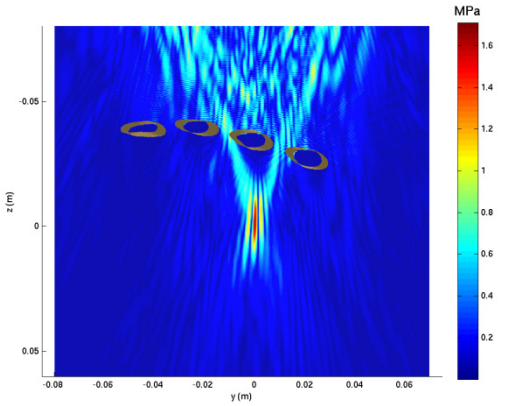

Figure 6.60 Acoustic pressure magnitude in *y*-*z* plane resulting from resulting. Constrained optimisation. Array-rib configuration 3.

Whilst the NAG® constrained optimisation solver found a local minimum, not all of the constraints were satisfied. Indeed, the maximum surface pressure magnitude is 1.2 MPa and the acoustic pressure magnitude at the focus is 1.7 MPa. This corresponds in a 26% reduction in the maximum acoustic pressure at the surface of the ribs, instead of the requested 45%. The resulting SAR gain is 4.6 dB, which is 2.6 dB lower than that provided by the phase conjugation method. Nevertheless, the peak focal pressure obtained in this instance is 0.5 MPa higher than that with the phase conjugation method. The narrow intercostal spacing compared with array-rib configurations 1 and 2, in this arrangement makes it challenging to retain high focal pressures alongside an SAR gain comparable with the phase conjugation method.

6.5 Idealised ribs: Array-rib configuration 4

6.5.1 Description

Due to limited availability of anatomical rib data in STL format, analyses of idealised rib geometries were considered. The configurations consisted of a regular spatial arrangement of three cuboid scatterers with rounded edges. The total height of the idealised ribs (i.e. the dimension along the *x*-axis) was 5 cm. The scatterers were positioned so that the geometric focus was located 3 cm behind the central idealised rib. The idealised ribs were considered to be symmetrical about the *y*-*z* plane. Whilst these scatterers are considerably shorter than the human ribs considered in configurations 1, 2

and 3, their position within the "cone" of the HIFU source was such that scattering by the end-caps was not significant. The thickness of the scatterers (i.e. the dimension along the axis of propagation) was 5 mm. Based on the range of rib dimensions described by Mohr *et al* (2007), the minimum rib width can be expected to vary between 4 mm and 10 mm. Furthermore, Liu (2000) reported that the intercostal space around the sternum can be expected to be less than 10 mm in most cases. Additionally, Nunn *et al* (1980) reported a lower limit for intercostal space in humans of approximately 6 mm. Based on this information, a "best case" array-rib configuration was arrived at, with a 4 mm rib width and a 10 mm intercostal spacing. This configuration is shown in figure 6.61.

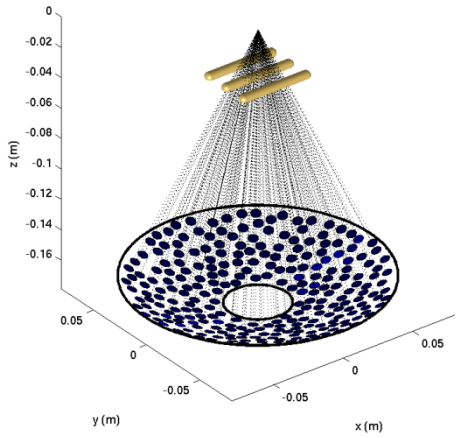

Figure 6.61 Position of ribs with respect to HIFU array for array-rib configuration 4.

6.5.2 Spherical focusing

Spherical focusing on array-rib configuration 4 resulted in the acoustic pressure magnitude on the surface of the ribs shown in figure 6.62 and the field pressure magnitude in the *y*-*z* plane shown in figure 6.63.

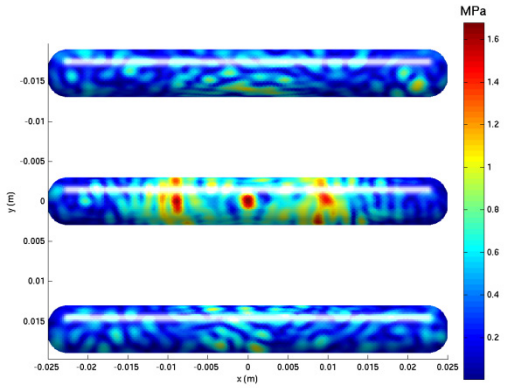

Figure 6.62 Acoustic pressure magnitude on surface of ribs resulting from field of 1 MHz multi-element array. Spherical focusing. Array-rib configuration 4.

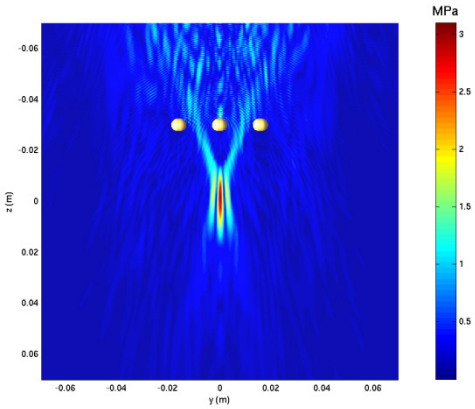

Figure 6.63 Acoustic pressure magnitude in *y*-*z* plane resulting from field of 1 MHz multi-element array. Spherical focusing. Array-rib configuration 4.

The maximum surface pressure on the idealised ribs is 1.7 MPa. The peak focal pressure is 3.0 MPa. This generates an SAR gain of 6.4 dB. It can be seen that effects of splitting at the focus are visible, with grating lobes approximately ±3 mm from the focal lobe. The magnitude of these grating lobes is approximately –4.8 dB relative to that of the main lobe.

6.5.3 Binarised apodisation based on geometric ray tracing

The method of binarised apodisation based on geometric ray tracing was applied to array-rib configuration 4. It produced the source velocity distribution displayed in magnitude and phase in figures 6.64 and 6.65, respectively.

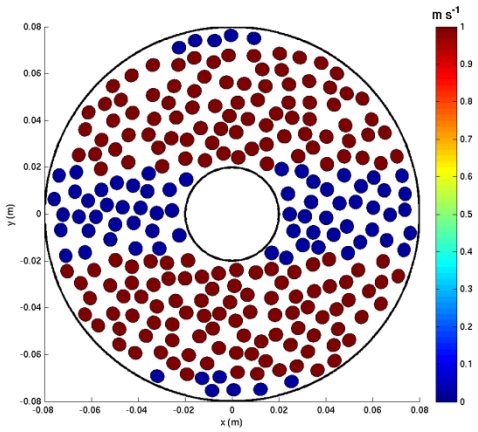

Figure 6.64 Source velocity magnitudes resulting from binarised apodisation based on ray tracing. Array-rib configuration 4.

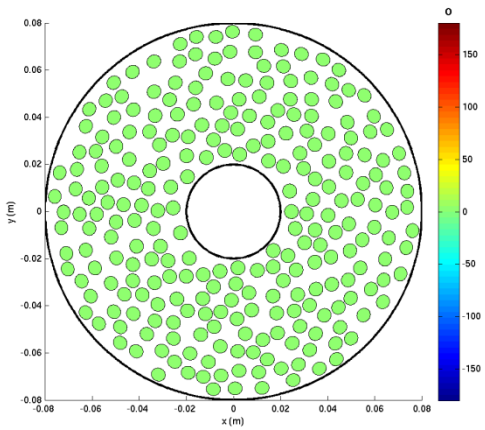

Figure 6.65. Source velocity phases resulting from binarised apodisation based on ray tracing. Array-rib configuration 4.

The above velocity distribution results in 179 elements of the phased array being switched on (or approximately 30% of all elements). The velocity distribution defined by the data in figures 6.64 and 6.65 was then used as input data to the forward BEM model, which generated the acoustic pressure magnitudes on the surface of the ribs shown in figure 6.66. The corresponding pressure magnitudes in the *y*-*z* plane, obtained at the post-processing stage, are displayed in figure 6.67.

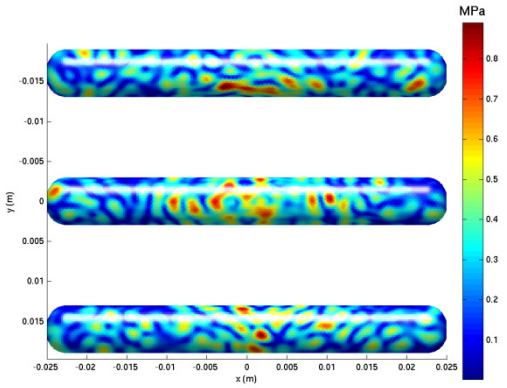

Figure 6.66 Acoustic pressure magnitude on surface of ribs resulting from field of 1 MHz multi-element array. Binarised apodisation based on geometric ray tracing. Array-rib configuration 4.

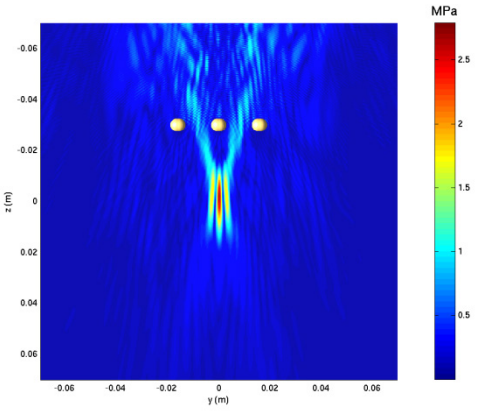

Figure 6.67 Acoustic pressure magnitude in *y*-*z* plane resulting from field of 1 MHz multi-element array. Binarised apodisation based on geometric ray tracing. Array-rib configuration 4.

The implementation of the binarised apodisation method on this rib-array configuration gives rise to a maximum acoustic pressure on the surface of the ribs of 0.90 MPa, with a

peak focal pressure of 2.7 MPa. Compared with the spherical focusing case, this improves the SAR gain by 5.6 dB, providing an SAR gain of 11 dB. Again, splitting of the focus is observed, with grating lobes positioned at ±3 mm along the *y*-axis from the main lobe. The magnitude of these grating lobes is approximately –3.7 dB relative to that of the main lobe. This represents a slight deterioration in the focusing of the array compared with the spherical focusing case, for which the side lobes were –4.8 dB lower than the main lobe.

6.5.4 Phase conjugation

The first stage of the phase conjugation calculation, i.e. the acoustic pressure field produced by a point source in the presence of the ribs, is displayed in the *y*-*z* plane in figure 6.68, with acoustic pressures at field locations in the vicinity of the singularity removed.

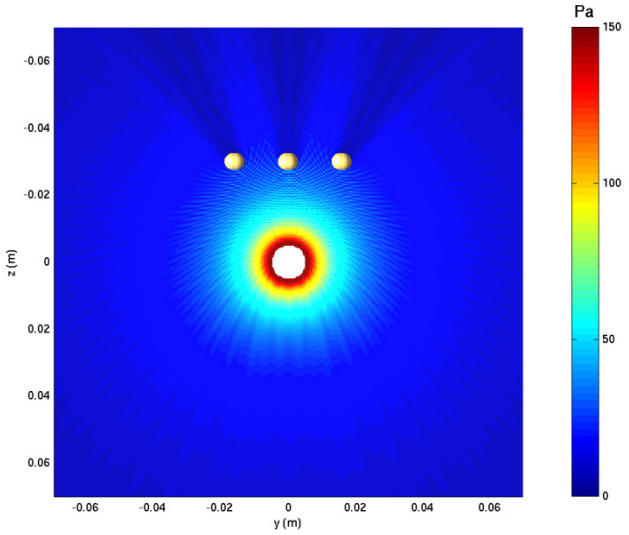

Figure 6.68 Acoustic pressure magnitude in *y*-*z* plane resulting from field of 1 MHz point source of unit source strength, positioned at the global origin. Array-rib configuration 4.

The source element velocities required for the phase conjugation calculation are displayed in magnitude and phase in figures 6.69 and 6.70, respectively.

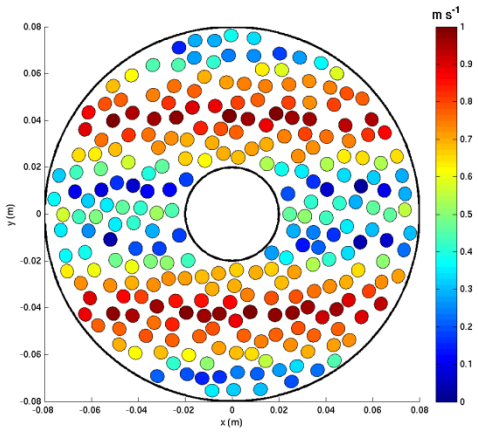

Figure 6.69 Source velocity magnitudes resulting from phase conjugation. Array-rib configuration 4.

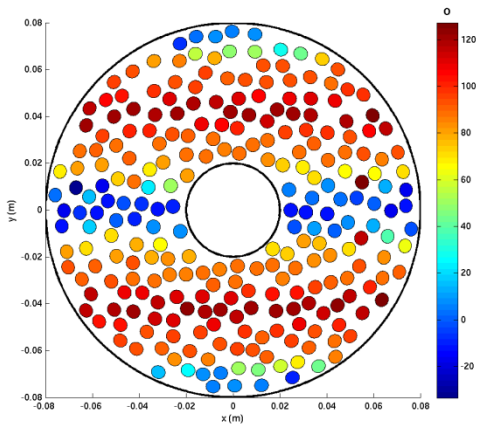

Figure 6.70 Source velocity phases resulting from phase conjugation. Array-rib configuration 4.

The focusing vector defined by the above source velocity distribution yields the acoustic pressure magnitude on the surface of the ribs shown in figure 6.71. The acoustic field pressures in the *y*-*z* plane are shown in figure 6.72.

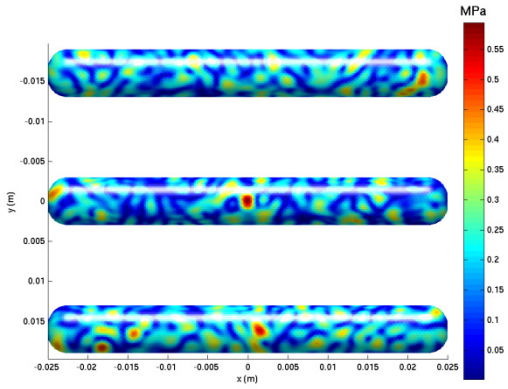

Figure 6.71 Acoustic pressure magnitude on surface of ribs resulting from field of 1 MHz multi-element array. Phase conjugation. Array-rib configuration 4.

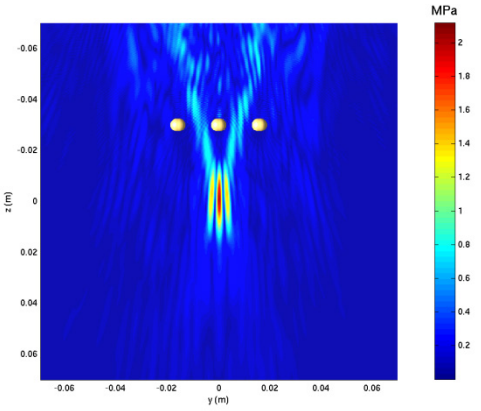

Figure 6.72 Acoustic pressure magnitude in *y*-*z* plane resulting from field of 1 MHz multi-element array. Phase conjugation. Array-rib configuration 4.

The phase conjugation method applied to this rib-array configuration gives rise to a maximum acoustic pressure on the surface of the ribs of 0.60 MPa, with a peak focal pressure of 2.1 MPa. This produces an SAR gain of 12 dB. For this specific array-rib configuration, the phase conjugation method provides an SAR gain comparable with that from the binarised apodisation method, although the peak focal pressure is reduced

by 0.6 MPa. The grating lobes are now –3.5 dB relative to the main lobe, which represents a deterioration by 1.3 dB compared against the spherical focusing case.

6.5.5 DORT

An i_{max} of 137 was used in this implementation of the DORT method, as this value maximised the SAR gain. This generated the magnitude and phase of the focusing vector shown in figures 6.73 and 6.74, respectively.

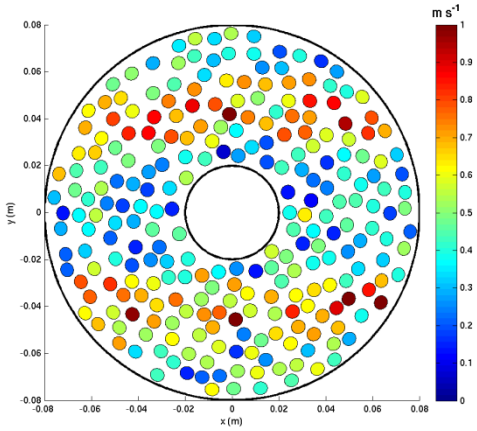

Figure 6.73 Source velocity magnitudes resulting from DORT method. Array-rib configuration 4.

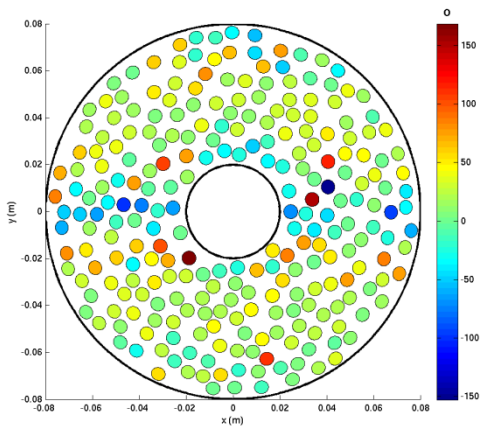

Figure 6.74 Source velocity phases resulting from DORT method. Array-rib configuration 4.

The corresponding BEM acoustic pressure magnitudes on the surface of the idealised ribs and in the *y*-*z* plane are displayed in figures 6.75 and 6.76, respectively.

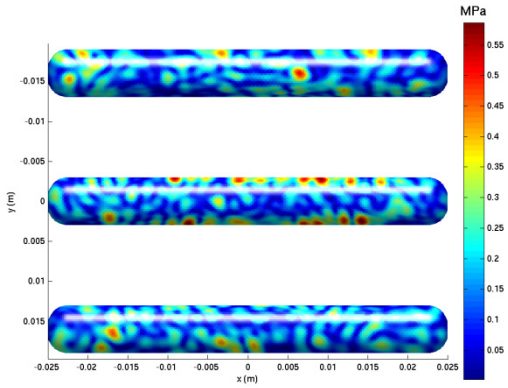

Figure 6.75 Acoustic pressure magnitude on surface of ribs resulting from field of 1 MHz multi-element array. DORT method. Array-rib configuration 4.

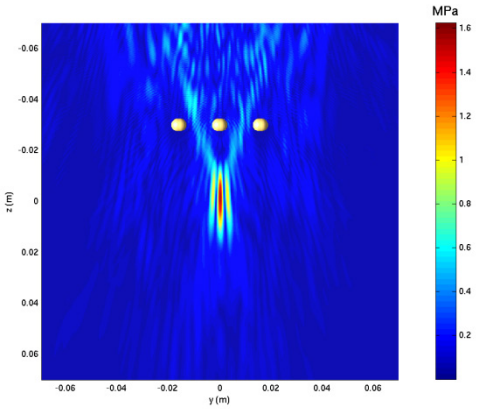

Figure 6.76 Acoustic pressure magnitude in *y*-*z* plane resulting from field of 1 MHz multi-element array. DORT method. Array-rib configuration 4.

The DORT method on this rib-array configuration generates a maximum acoustic pressure on the surface of the ribs of 0.59 MPa, with a peak focal pressure of 1.6 MPa. An SAR gain of 9.9 dB is achieved. Owing to the regular shape of the scatterers, these are perhaps closer to being well-resolved than human ribs. As such, better results are obtained in terms of the SAR gain than for human ribs, when using the DORT method. Furthermore, a qualitative reduction in the backscattered pressure can be observed compared with the spherical focusing case. The grating lobes are now –4.4 dB relative to the amplitude of the focal lobe.

6.5.6 Constrained optimisation

The procedure outlined in section 5.4.6 was followed, thus adding additional constraints to improve the SAR gain and reduce the magnitude of the grating lobes. Figures 6.77 and 6.78 respectively display the magnitudes and phases of the element velocities of the array resulting from the constrained optimisation.

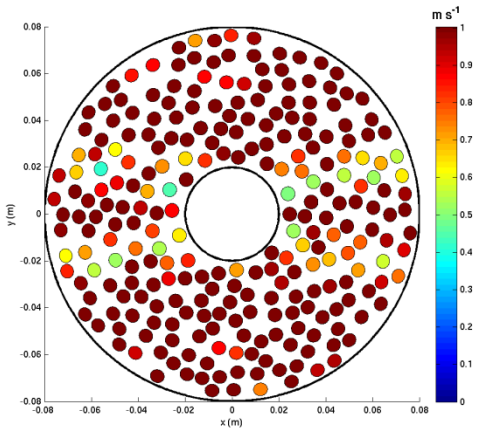

Figure 6.77 Source velocity magnitudes resulting from constrained optimisation. Array-rib configuration 4.

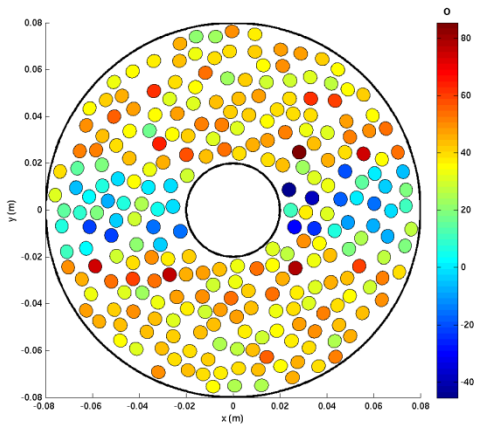

Figure 6.78 Source velocity phases resulting from constrained optimisation. Array-rib configuration 4.

The velocity distributions in figures 6.77 and 6.78 were subsequently used as input data to the BEM formulation. The acoustic pressure magnitudes on the surface of the idealised ribs and in the *y*-*z* plane are displayed in figures 6.79 and 6.80.

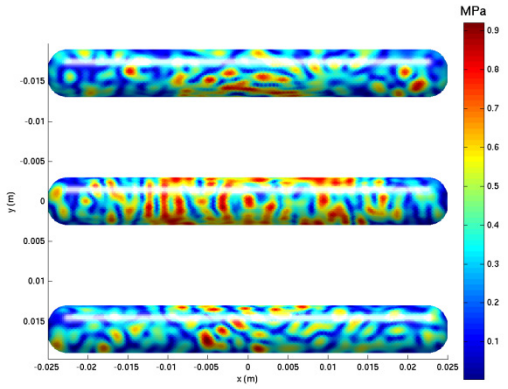

Figure 6.79 Acoustic pressure magnitude on surface of ribs resulting from field of 1 MHz multi-element array. Constrained optimisation. Array-rib configuration 4.

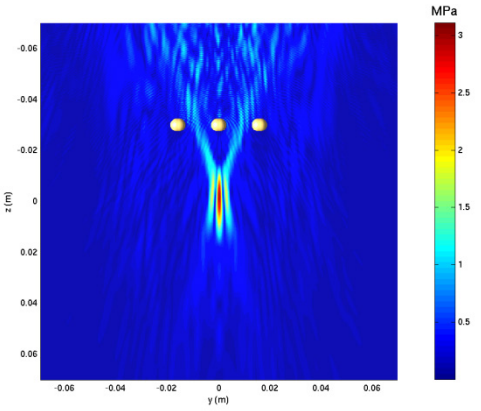

Figure 6.80 Acoustic pressure magnitude in *y*-*z* plane resulting from resulting. Constrained optimisation. Array-rib configuration 4.

The NAG® constrained optimisation solver found a local minimum satisfying the constraints associated with the acoustic pressure magnitude on the ribs. Indeed, the maximum surface pressure magnitude is 0.92 MPa and the acoustic pressure magnitude at the focus is 3.0 MPa. This achieves the required 45% reduction in the maximum acoustic pressure at the surface of the ribs compared with the spherical focusing case. The resulting SAR gain is 12 dB, which is effectively the same as that provided by the

phase conjugation method. Nevertheless, the peak focal pressure obtained here is almost twice that obtained with the phase conjugation method. Furthermore, the grating lobes are now 5.1 dB lower than the main lobe.

6.6 Idealised ribs: Array-rib configuration 5

6.6.1 Description

Based on the information given in section 6.5.1, a configuration of idealised ribs representing an "average case" was generated. The intercostal spacing and rib width were respectively chosen as the arithmetic mean of the upper and lower bounds described in section 6.5.1. This represented an intercostal spacing of 8 mm with a rib width of 7 mm. This configuration is displayed in figure 6.81.

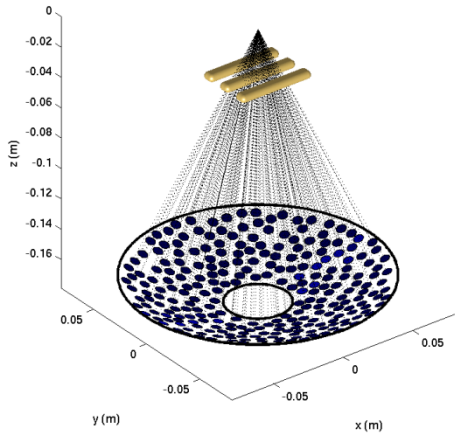

Figure 6.81 Position of ribs with respect to HIFU array for array-rib configuration 5.

6.6.2 Spherical focusing

Spherical focusing on array-rib configuration 5 resulted in the acoustic pressure magnitude on the surface of the ribs shown in figure 6.82 and the field pressure magnitude in the *y*-*z* plane shown in figure 6.83.

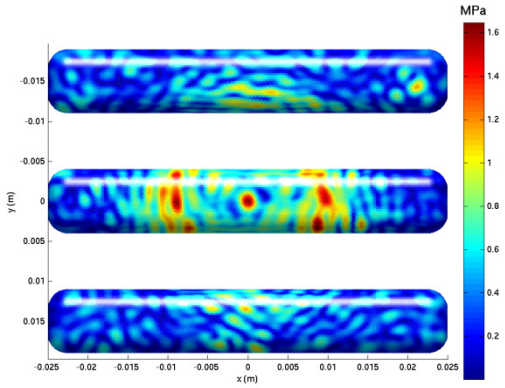

Figure 6.82 Acoustic pressure magnitude on surface of ribs resulting from field of 1 MHz multi-element array. Spherical focusing. Array-rib configuration 5.

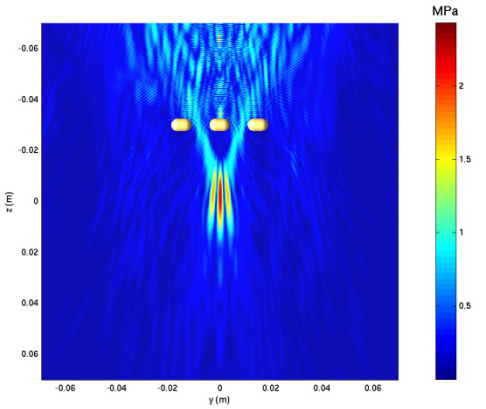

Figure 6.83 Acoustic pressure magnitude in *y*-*z* plane resulting from field of 1 MHz multi-element array. Spherical focusing. Array-rib configuration 5.

The maximum surface pressure on the idealised ribs is 1.7 MPa. The peak focal pressure is 2.3 MPa. This generates an SAR gain of 4.2 dB. Due to the increased shadowing produced by the wider scatterers and narrower space between them, deterioration in SAR gain and peak focal pressure is observed compared with the spherical focusing case for array-rib configuration 4. It can be seen that effects of splitting at the focus are visible, with grating lobes positioned approximately ±3 mm either side of the focal lobe. The magnitude of these is approximately –2.5 dB relative to that of the main lobe.

6.6.3 Binarised apodisation based on geometric ray tracing

The method of binarised apodisation based on geometric ray tracing applied to array-rib configuration 5 produces the source velocity distribution displayed in magnitude and phase in figures 6.84 and 6.85, respectively.

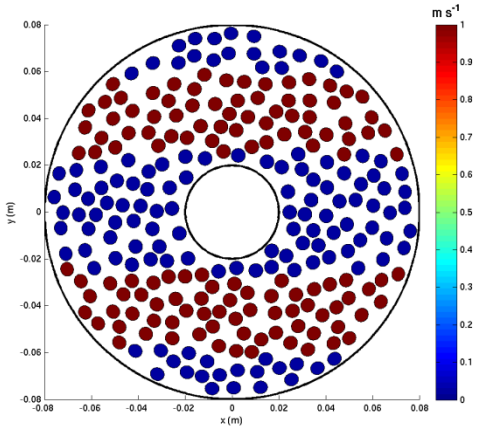

Figure 6.84 Source velocity magnitudes resulting from binarised apodisation based on ray tracing. Array-rib configuration 5.

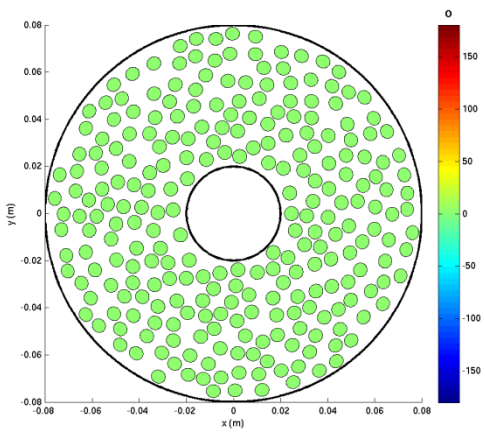

Figure 6.85. Source velocity phases resulting from binarised apodisation based on ray tracing. Array-rib configuration 5.

The above velocity distribution results in 129 elements of the phased array being switched off (approximately 50% of all elements). The velocity distribution defined by the data in figures 6.84 and 6.85 was then used as input data to the forward BEM model, which generated the acoustic pressure magnitudes on the surface of the ribs shown in figure 6.86. The corresponding pressure magnitudes in the *y*-*z* plane, obtained at the post-processing stage, are displayed in figure 6.87.

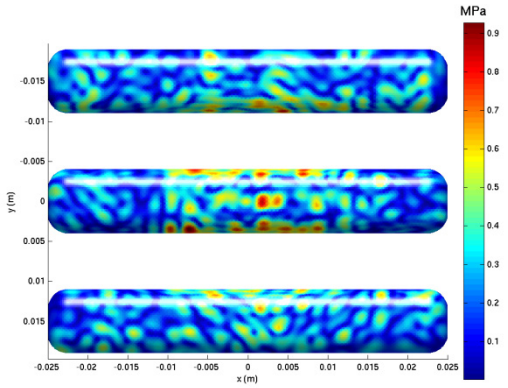

Figure 6.86 Acoustic pressure magnitude on surface of ribs resulting from field of 1 MHz multi-element array. Binarised apodisation based on geometric ray tracing. Array-rib configuration 5.

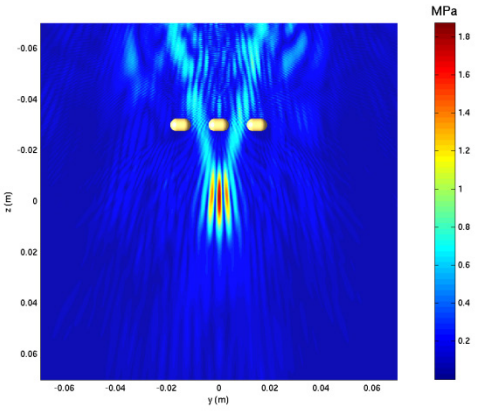

Figure 6.87 Acoustic pressure magnitude in *y*-*z* plane resulting from field of 1 MHz multi-element array. Binarised apodisation based on geometric ray tracing. Array-rib configuration 5.

The implementation of the binarised apodisation method on this rib-array configuration gives rise to a maximum acoustic pressure on the surface of the ribs of 0.94 MPa, with a

peak focal pressure of 1.8 MPa. This produces an SAR gain of 7.2 dB. The SAR gain is 3 dB better than for the spherical focusing case, and a qualitative reduction in the backscattered acoustic pressure is observed. The grating lobes centred at approximately ±3 mm from the main lobe along the *y*-axis are visible in figure 6.87. These are approximately –2.4 dB lower than the amplitude of the main lobe, as in the spherical focusing case.

6.6.4 Phase conjugation

The first stage of the phase conjugation calculation, i.e. the acoustic pressure field produced by a point source in the presence of the ribs, is displayed in the *y*-*z* plane in figure 6.88, with acoustic pressures at field locations in the vicinity of the singularity removed.

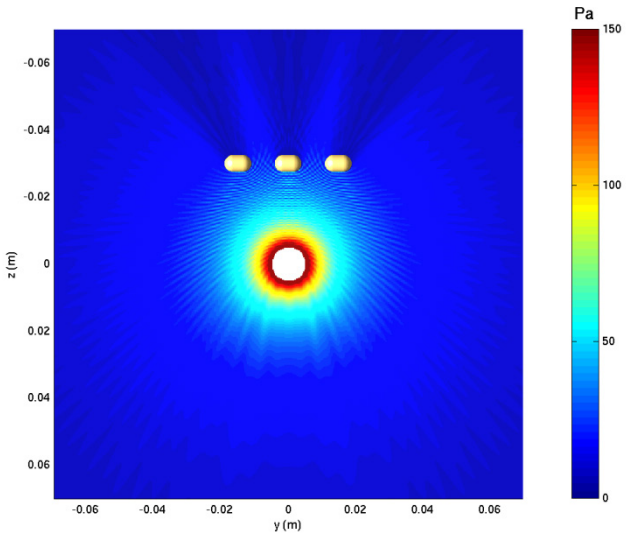

Figure 6.88 Acoustic pressure magnitude in *y*-*z* plane resulting from field of 1 MHz point source of unit source strength, positioned at the global origin. Array-rib configuration 5.

The source element velocities required for the phase conjugation calculation are displayed in magnitude and phase in figures 6.89 and 6.90, respectively.

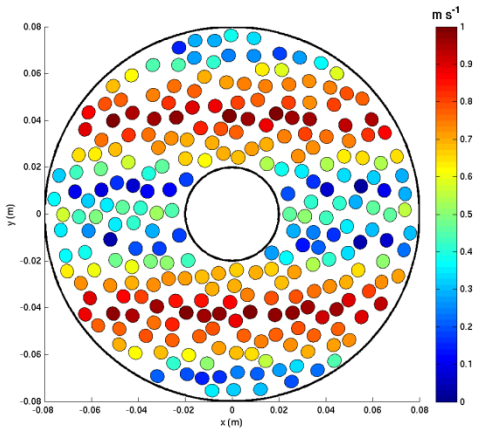

Figure 6.89 Source velocity magnitudes resulting from phase conjugation. Array-rib configuration 5.

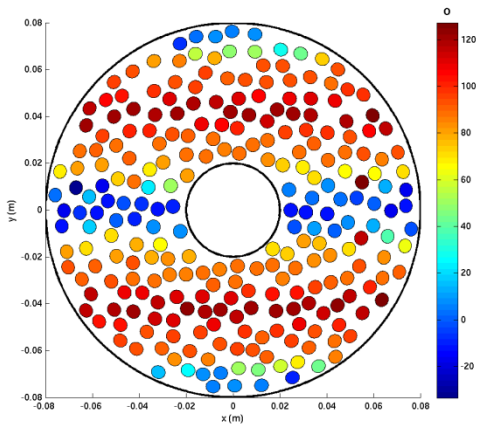

Figure 6.90 Source velocity phases resulting from phase conjugation. Array-rib configuration 5.

The focusing vector defined by the above source velocity distribution yields the acoustic pressure magnitude on the surface of the ribs shown in figure 6.91. The acoustic field pressures in the *y*-*z* plane are shown in figure 6.92.

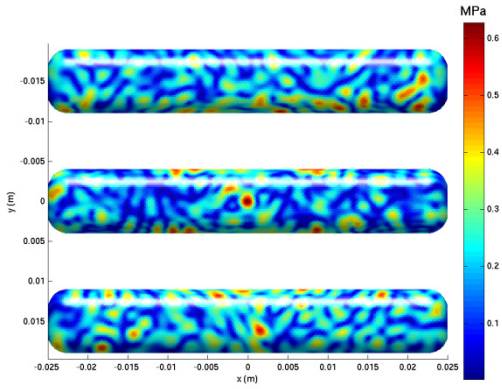

Figure 6.91 Acoustic pressure magnitude on surface of ribs resulting from field of 1 MHz multi-element array. Phase conjugation. Array-rib configuration 5.

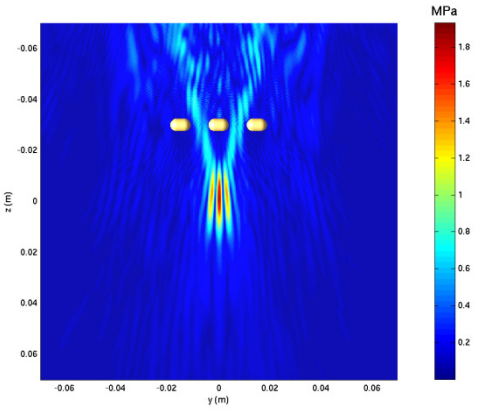

Figure 6.92 Acoustic pressure magnitude in *y*-*z* plane resulting from field of 1 MHz multi-element array. Phase conjugation. Array-rib configuration 5.

The phase conjugation method applied to this rib-array configuration gives rise to a maximum acoustic pressure on the surface of the ribs of 0.65 MPa, with a peak focal pressure of 1.9 MPa. This produces an SAR gain of 11 dB. The amplitude of the grating lobes at ±3 mm along the *y*-axis is now –2.8 dB relative to the main lobe.

6.6.5 DORT

An i_{max} of 130 was used in this implementation of the DORT method, as this value maximised the SAR gain. This generated the magnitude and phase of the focusing vector shown in figures 6.93 and 6.94, respectively.

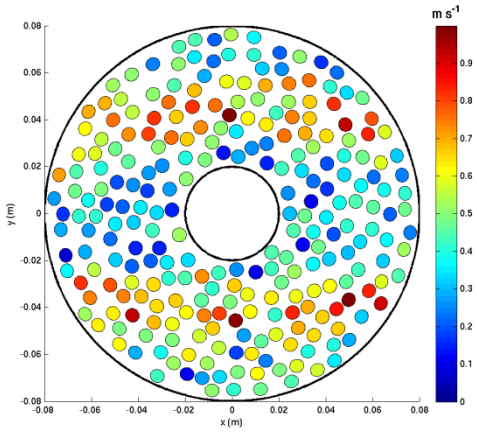

Figure 6.93 Source velocity magnitudes resulting from DORT method. Array-rib configuration 5.

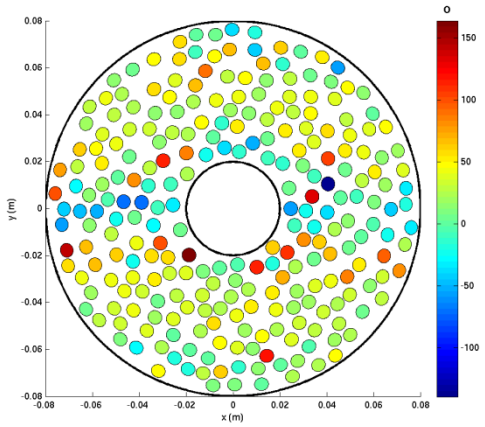

Figure 6.94 Source velocity phases resulting from DORT method. Array-rib configuration 5.

The corresponding BEM acoustic pressure magnitudes on the surface of the idealised ribs and in the *y*-*z* plane are displayed in figures 6.94 and 6.95, respectively.

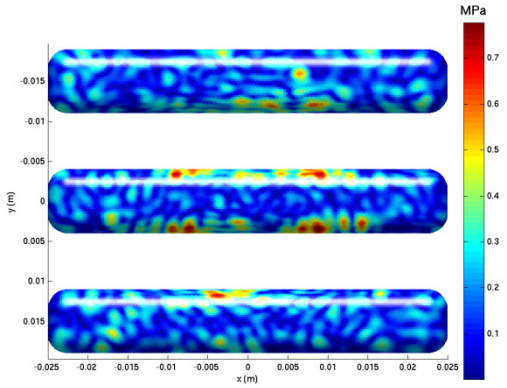

Figure 6.95 Acoustic pressure magnitude on surface of ribs resulting from field of 1 MHz multi-element array. DORT method. Array-rib configuration 5.

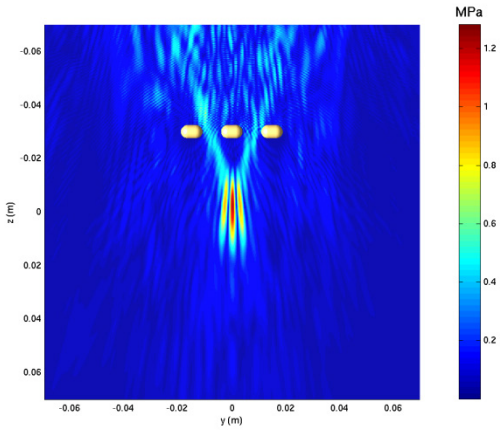

Figure 6.96 Acoustic pressure magnitude in *y*-*z* plane resulting from field of 1 MHz multi-element array. DORT method. Array-rib configuration 5.

The DORT method on this rib-array configuration generates a maximum acoustic pressure on the surface of the ribs of 0.78 MPa, with a peak focal pressure of 1.2 MPa. An SAR gain of 5.3 dB is achieved together with a qualitative reduction in the backscattered pressure compared with the spherical focusing case. Whilst the SAR gain is improved by 1.1 dB with respect to the spherical focusing case, it is still inferior to that provided by binarised apodisation and by phase conjugation. The grating lobes are now 2.7 dB below the amplitude of the main lobe.

6.6.6 Constrained optimisation

The procedure outlined in section 6.4.6 was repeated, thus adding additional constraints to improve the SAR gain and reduce the magnitude of the grating lobes. Figures 6.97 and 6.98 respectively display the magnitudes and phases of the element velocities of the array resulting from the constrained optimisation.

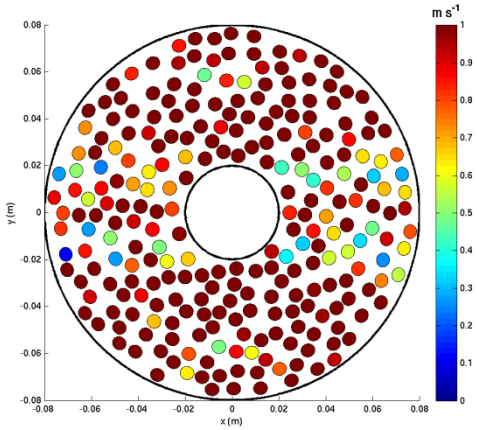

Figure 6.97 Source velocity magnitudes resulting from constrained optimisation. Array-rib configuration 5.

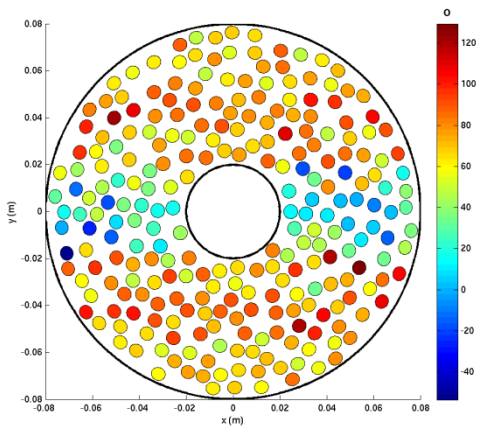

Figure 6.98 Source velocity phases resulting from constrained optimisation. Array-rib configuration 5.

The velocity distributions in figures 6.97 and 6.98 were subsequently used as input data to the BEM formulation. The acoustic pressure magnitudes on the surface of the idealised ribs and in the *y*-*z* plane are displayed in figures 6.99 and 6.100.

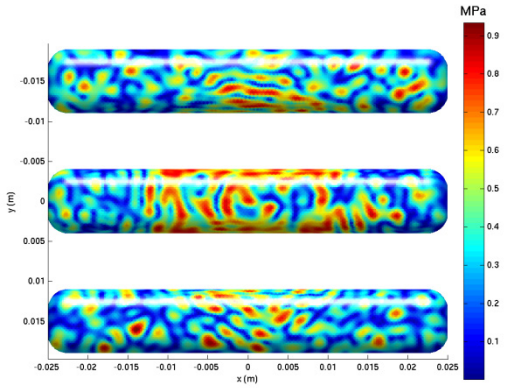

Figure 6.99 Acoustic pressure magnitude on surface of ribs resulting from field of 1 MHz multi-element array. Constrained optimisation. Array-rib configuration 5.

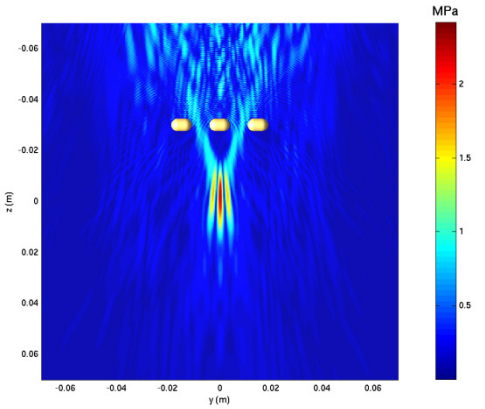

Figure 6.100 Acoustic pressure magnitude in *y*-*z* plane resulting from resulting. Constrained optimisation. Array-rib configuration 5.

The NAG® constrained optimisation solver finds a local minimum satisfying the constraints associated with the acoustic pressure on the surface of the ribs. Indeed, the maximum surface pressure magnitude is 0.94 MPa and the acoustic pressure magnitude at the focus is 2.3 MPa. This achieves the required 45% reduction in the maximum acoustic pressure at the surface of the ribs compared against the spherical focusing case. The resulting SAR gain is 9.2 dB, which is 1.8 dB lower than for phase conjugation. Nevertheless, the peak focal pressure obtained in this instance is 0.5 MPa higher than that obtained with the phase conjugation method. The grating lobes are 2.9 dB lower than the amplitude of the main lobe.

6.7 Idealised ribs: Array-rib configuration 6

6.7.1 Description

Based on the information described in section 6.5.1, a configuration of idealised ribs representing a “worst case” scenario was generated. The intercostal spacing and rib width were respectively chosen as the lower and upper bounds of the ranges depicted in section 6.5.1. This represented an intercostal spacing of 6 mm with a rib width of 10 mm. This configuration is displayed in figure 6.101.

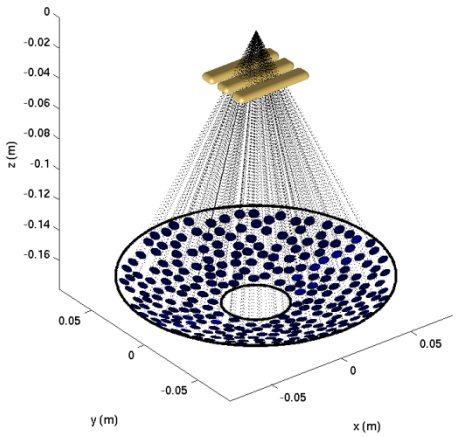

Figure 6.101 Position of ribs with respect to HIFU array for array-rib configuration 6.

6.7.2 Spherical focusing

Spherical focusing on array-rib configuration 6 resulted in the acoustic pressure magnitude on the surface of the ribs shown in figure 6.102 and the field pressure magnitude in the *y*-*z* plane shown in figure 6.103.

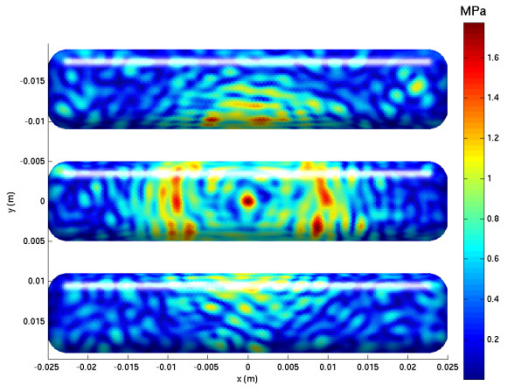

Figure 6.102 Acoustic pressure magnitude on surface of ribs resulting from field of 1 MHz multi-element array. Spherical focusing. Array-rib configuration 6.

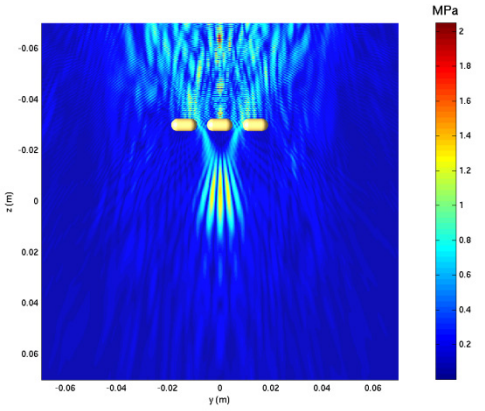

Figure 6.103 Acoustic pressure magnitude in *y*-*z* plane resulting from field of 1 MHz multi-element array. Spherical focusing. Array-rib configuration 6.

The maximum surface pressure on the idealised ribs is 1.8 MPa. The peak focal pressure is 1.3 MPa. This generates a negative SAR gain of −1.4 dB, due to the further increased shadowing produced by the wider scatterers and narrower space between

them compared with array-rib configurations 4 and 5. The backscattered signal is now so large that it interacts constructively with the incident field to generate a localised peak of 2.0 MPa along the *z*-axis between the scatterers and the phased array. The effects of splitting at the focus are further pronounced, with grating lobes approximately –0.75 dB and –4.5 dB relative to the main lobe, positioned respectively at ±3.3 mm and ±6.8 mm from the main lobe along the *y*-axis.

6.7.3 Binarised apodisation based on geometric ray tracing

The method of binarised apodiation based on geometric ray tracing applied to array-rib configuration 6 produces the source velocity distribution displayed in magnitude and phase in figures 6.104 and 6.105, respectively.

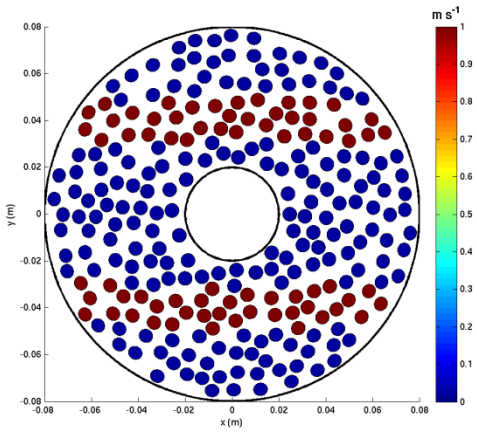

Figure 6.104 Source velocity magnitudes resulting from binarised apodisation based on ray tracing. Array-rib configuration 6.

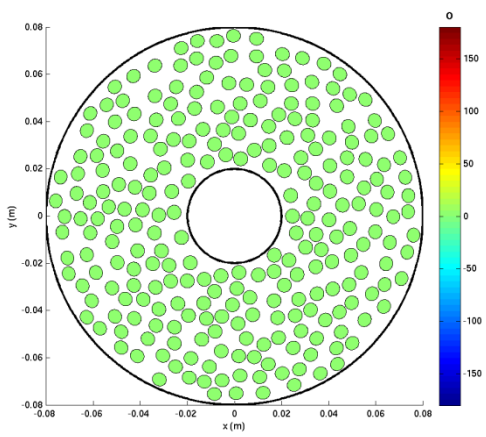

Figure 6.105. Source velocity phases resulting from binarised apodisation based on ray tracing. Array-rib configuration 6.

The above velocity distribution results in only 73 elements of the phased array being switched on (approximately 71% of the elements being switched off). The velocity distribution defined by the data in figures 6.104 and 6.105 was then used as input data to the forward BEM model, which generated the acoustic pressure magnitudes on the surface of the ribs shown in figure 6.106. The corresponding pressure magnitudes in the *y*-*z* plane, obtained at the post-processing stage, are displayed in figure 6.107.

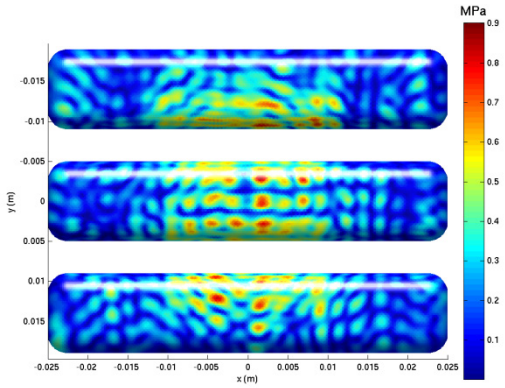

Figure 6.106 Acoustic pressure magnitude on surface of ribs resulting from field of 1 MHz multi-element array. Binarised apodisation based on geometric ray tracing. Array-rib configuration 6.

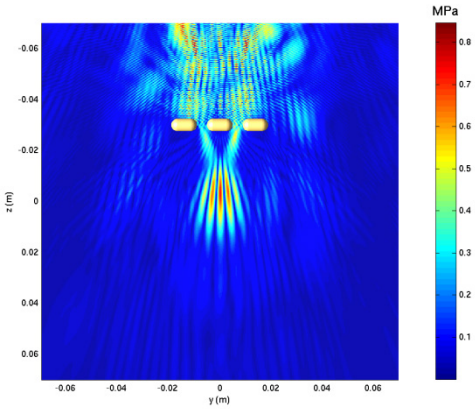

Figure 6.107 Acoustic pressure magnitude in *y*-*z* plane resulting from field of 1 MHz multi-element array. Binarised apodisation based on geometric ray tracing. Array-rib configuration 6.

The implementation of the binarised apodisation method on this rib-array configuration gives rise to a maximum acoustic pressure on the surface of the ribs of 0.91 MPa, with a peak focal pressure of 0.70 MPa. This produces an SAR gain of –0.96 dB. Clearly, due to effects of multiple scattering on this particular configuration of idealised ribs, the binarised apodisation method of focusing is only marginally more successful than the spherical focusing case, and still delivers a negative SAR gain. This is at the expense of a 46% reduction in peak focal pressure. The grating lobes are now –0.83 dB and –3.6 dB relative to the main lobe, positioned respectively at ±3.3 mm and ±6.8 mm from the main lobe along the *y*-axis.

6.7.4 Phase conjugation

The first stage of the phase conjugation calculation, i.e. the acoustic pressure field produced by a point source in the presence of the ribs, is displayed in the *y*-*z* plane in figure 6.108, with acoustic pressures at field locations in the vicinity of the singularity removed.

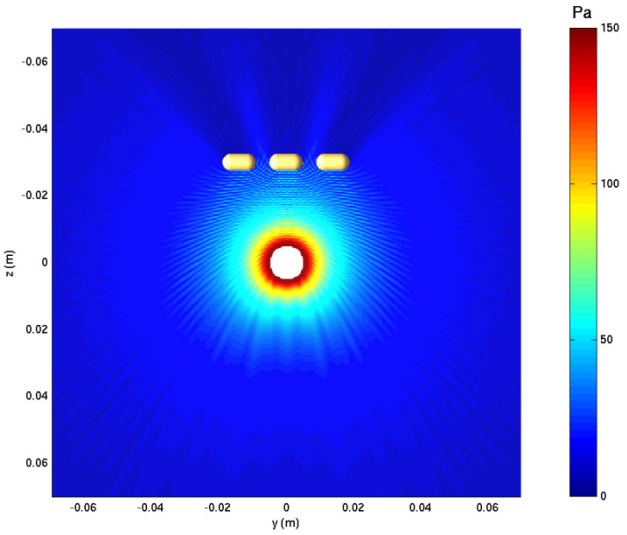

Figure 6.108 Acoustic pressure magnitude in *y*-*z* plane resulting from field of 1 MHz point source of unit source strength, positioned at the global origin. Array-rib configuration 6.

The source element velocities required for the phase conjugation calculation are displayed in magnitude and phase in figures 6.108 and 6.109, respectively.

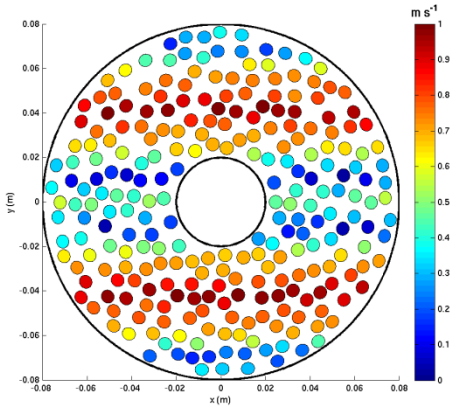

Figure 6.109 Source velocity magnitudes resulting from phase conjugation. Array-rib configuration 6.

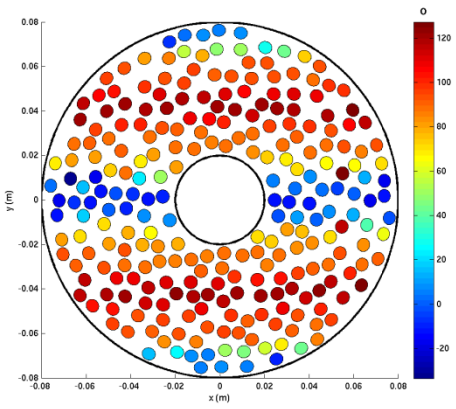

Figure 6.110 Source velocity phases resulting from phase conjugation. Array-rib configuration 6.

The focusing vector defined by the above source velocity distribution yields the acoustic pressure magnitude on the surface of the ribs shown in figure 6.111. The acoustic field pressures in the *y*-*z* plane are shown in figure 6.112.

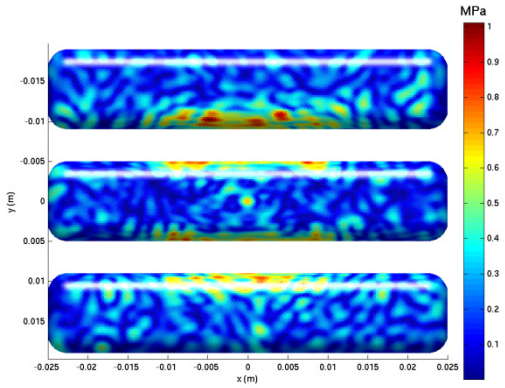

Figure 6.111 Acoustic pressure magnitude on surface of ribs resulting from field of 1 MHz multi-element array. Phase conjugation. Array-rib configuration 6.

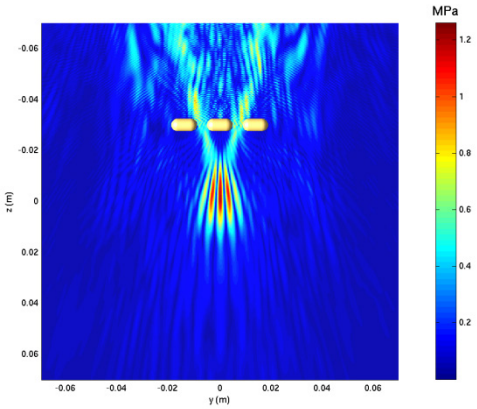

Figure 6.112 Acoustic pressure magnitude in *y*-*z* plane resulting from field of 1 MHz multi-element array. Phase conjugation. Array-rib configuration 6.

The phase conjugation method applied to this rib-array configuration gives rise to a maximum acoustic pressure on the surface of the ribs of 1.0 MPa, with a peak focal pressure of 1.2 MPa. This produces an SAR gain of 3.0 dB. The phase conjugation method of focusing is considerably more successful that the binarised apodisation method based on geometric ray tracing in terms of both SAR gain and peak focal pressure. Furthermore, the grating lobes are now –1.4 dB and –5.6 dB relative to the main lobe, positioned respectively at ±3.3 mm and ±6.8 mm from the main lobe along the *y*-axis.

6.7.5 DORT

A value used for i_{max} of 130 was used in this implementation of the DORT method, as this value maximised the SAR gain. This generated the magnitude and phase of the focusing vector shown in figures 6.113 and 6.114, respectively.

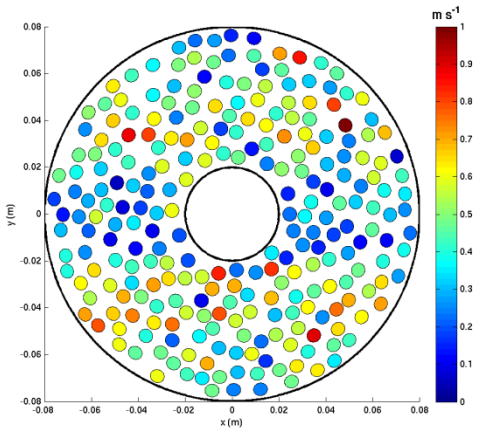

Figure 6.113 Source velocity magnitudes resulting from DORT method. Array-rib configuration 6.

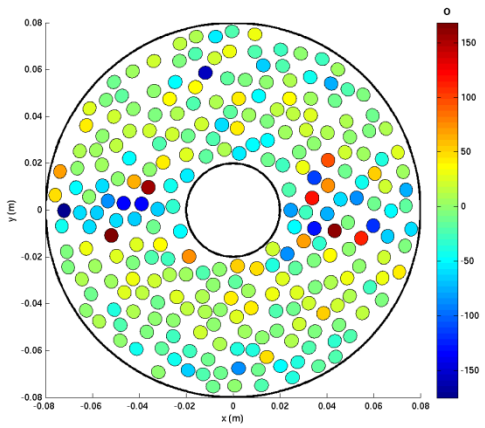

Figure 6.114 Source velocity phases resulting from DORT method. Array-rib configuration 6.

The corresponding BEM acoustic pressure magnitudes on the surface of the idealised ribs and in the *y*-*z* plane are displayed in figures 6.115 and 6.116, respectively.

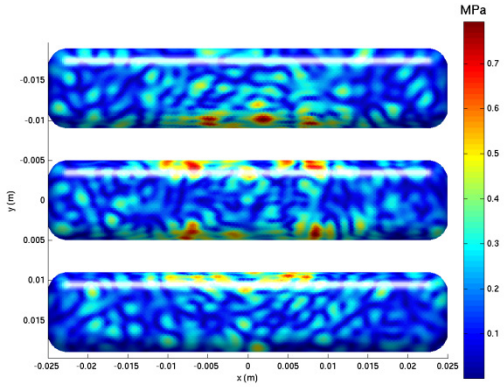

Figure 6.115 Acoustic pressure magnitude on surface of ribs resulting from field of 1 MHz multi-element array. DORT method. Array-rib configuration 6.

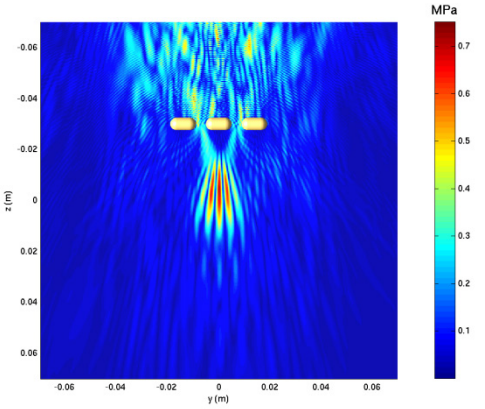

Figure 6.116 Acoustic pressure magnitude in *y*-*z* plane resulting from field of 1 MHz multi-element array. DORT method. Array-rib configuration 6.

The DORT method on this rib-array configuration generates a maximum acoustic pressure on the surface of the ribs of 0.80 MPa, with a peak focal pressure of 0.68 MPa. A negative SAR gain of –0.076 dB is achieved, which nevertheless represents an improvement compared with the spherical focusing case and binarised apodisation. The grating lobes are now –0.89 dB and –5.0 dB relative to the main lobe, positioned respectively at ±3.3 mm and ±6.8 mm from the main lobe along the *y*-axis.

6.7.6 Constrained optimisation

The procedure outlined in section 6.4.6 was repeated, thus adding additional constraints to improve the SAR gain and reduce the magnitude of the grating lobes. Figures 6.117 and 6.118 respectively display the magnitudes and phases of the element velocities of the array resulting from the constrained optimisation.

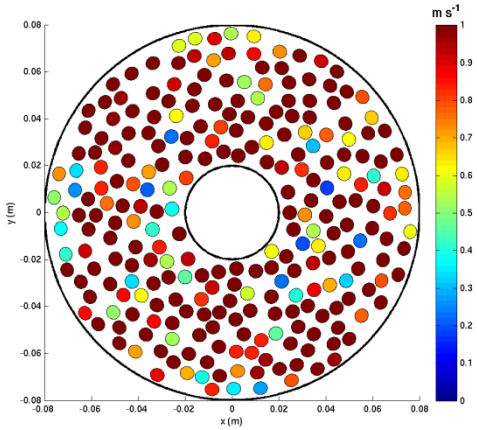

Figure 6.117 Source velocity magnitudes resulting from constrained optimisation. Array-rib configuration 6.

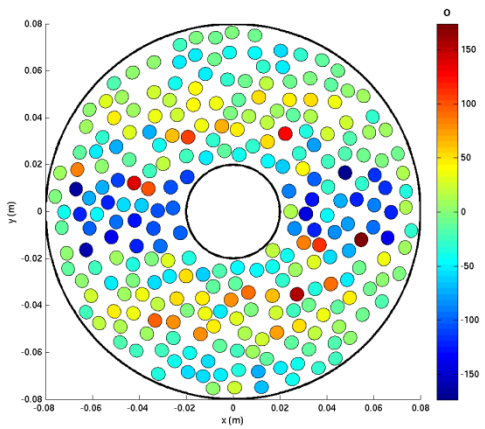

Figure 6.118 Source velocity phases resulting from constrained optimisation. Array-rib configuration 6.

The velocity distributions in figures 6.117 and 6.118 were subsequently used as input data to the BEM formulation. The acoustic pressure magnitudes on the surface of the idealised ribs and in the *y*-*z* plane are displayed in figures 6.119 and 6.120.

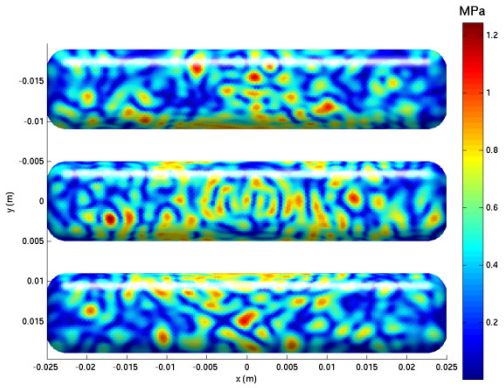

Figure 6.119 Acoustic pressure magnitude on surface of ribs resulting from field of 1 MHz multi-element array. Constrained optimisation. Array-rib configuration 6.

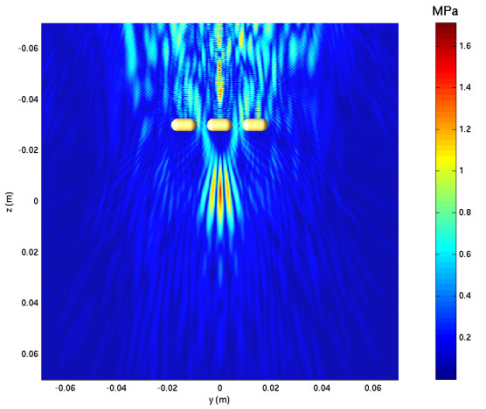

Figure 6.120 Acoustic pressure magnitude in *y*-*z* plane resulting from resulting. Constrained optimisation. Array-rib configuration 6.

Whilst the NAG® constrained optimisation solver found a local minimum, the constraints pertaining to the acoustic pressure magnitudes on the surface of the idealised ribs were not satisfied. Indeed, the maximum surface pressure magnitude is 1.3 MPa. This corresponds to a 29% reduction in the maximum acoustic pressure at the surface of the ribs, instead of the requested 45%. The acoustic pressure magnitude at the focus is 1.85 MPa, resulting in an SAR gain of 1.9 dB, which is 1.1 dB lower than that provided by the phase conjugation method. Nevertheless, the peak focal pressure obtained in this instance is 0.65 MPa higher that with the phase conjugation method. Owing to the narrow intercostal spacing compared with array-rib configurations 4 and 5, this arrangement makes it challenging to retain high focal pressures alongside an SAR gain comparable with the phase conjugation method. The grating lobes are comparable with those in the phase conjugation case and are –1.5 dB and –5.4 dB relative to the main lobe, positioned respectively at ±3.3 mm and ±6.8 mm from the main lobe along the *y*-axis.

6.8 Discussion

The SAR gain results on array-rib configurations 1 to 6 are summarised in table 6.1.

Table 6.1: SAR gain for the six array-rib configurations and for all methods of focusing.

Array-rib configuration	Spherical focusing	Binarised apodisation	Phase conjugation	DORT	Constrained optimisation
1	7.2 dB	11 dB	12 dB	7.6 dB	12 dB
2	5.1 dB	7.9 dB	8.2 dB	5.6 dB	8.3 dB
3	1.7 dB	4.2 dB	7.2 dB	3.3 dB	4.6 dB
4	6.4 dB	11 dB	12 dB	9.9 dB	12 dB
5	4.2 dB	7.2 dB	11 dB	5.3 dB	9.2 dB
6	–1.4 dB	–0.96 dB	3.0 dB	–0.076 dB	1.9 dB

Whilst the values expressed in table 6.1 give one indicator of the performance of a given focusing method on any given array-rib configuration, the peak focal pressures obtained are also important. These are displayed in table 6.2.

Table 6.2: Peak focal pressure the for six array-rib configurations and for all methods of focusing.

Array-rib configuration	Spherical focusing	Binarised apodisation	Phase conjugation	DORT	Constrained optimisation
1	3.2 MPa	3.0 MPa	2.7 MPa	2.1 MPa	3.1 MPa
2	3.4 MPa	3.2 MPa	2.8 MPa	2.0 MPa	3.4 MPa
3	1.7 MPa	1.3 MPa	1.2 MPa	0.97 MPa	1.7 MPa
4	3.0 MPa	2.7 MPa	2.1 MPa	1.6 MPa	3.0 MPa
5	2.3 MPa	1.8 MPa	1.9 MPa	1.2 MPa	2.3 MPa
6	2.0 MPa	0.70 MPa	1.2 MPa	0.68 MPa	1.8 MPa

The method of focusing which delivers the best overall performance in terms of maximising the SAR gain appears to be the phase conjugation method. Despite the fact that no constraints are placed on the maximum acoustic pressure magnitudes on the surface of the ribs, this method generally performs at least as well as the constrained optimisation approach. Nevertheless, the constrained optimisation method performs as well as the phase conjugation method for array-rib configurations 1, 2 and 4, where the intercostal spacing is large compared with the rib width. However, the phase conjugation method consistently results in focal pressures lower than those produced by the constrained optimisation method. This may be an issue if the phased-array does not

have a wide enough dynamic range that the source velocities may be increased sufficiently to produce the focal pressure magnitudes required for tissue ablation.

The binarised apodisation method based on a geometric ray tracing approach lowers SAR gains more than the phase conjugation method and the constrained optimisations approach. This is particularly true when applied to array-rib configurations 3, 5 and 6, which present significant treatment planning challenges due to the narrower intercostal spacing. Furthermore, the resulting peak focal pressure generated with binarised apodisation is up to 60% lower than that produced by the constrained optimisation approach in array-rib configuration 6. Owing to the narrow intercostal spacing, too many elements are perhaps deactivated unnecessarily. In a clinical context, this may hamper the treatment of deep-seated abdominal tumours in humans. The binarised apodisation method does however benefit from the fact that only anatomical data is required and no forward propagation model is needed. In the configurations with wide intercostal spacing (i.e. 1, 2 and 4), the binarised apodisation method delivers comparable performance to the constrained optimisation approach, albeit not quite as good.

The DORT method produces SAR gains superior to those generated through spherical focusing of the phased array. This is however at the expense of the peak focal pressures, which are the lowest out of all the focusing methods considered. The SAR gain also falls short of that delivered by the phase conjugation method by 5.7 dB for array-rib configuration 5. Overall, the DORT method does not appear to generate SAR gains of the same level as those produced by the phase conjugation or constrained optimisation approaches. This is likely to be due to the complex shape of the ribs and the fact that they cannot easily be assimilated to well-resolved point-like scatterers, an assumption generally required when using the DORT method (Prada 2002). It should also be noted that, in practice, there remains the issue of determining the value of $i_{\max}$, the number of eigenvectors associated with the higher singular values (see section 5.2.3). Unlike the case for well-resolved point-like scatterers presented in Appendix B, it is not straightforward to separate the "signal" from the "noise" in the singular values of the diagonal matrix in equation (5.10). In this chapter, the value of $i_{\max}$ was specifically chosen to maximise the SAR gain. This was possible because the DORT method was implemented using BEM as the forward model, and the acoustic pressures at the focus and at the surface of the ribs could readily be obtained at the post-processing stage for

all values of i_{max}. This procedure is described further in Appendix B. In a clinical context, however, such a procedure would be difficult to implement without a forward propagation model.

When assessing the relative merits of the focusing methods investigated in this thesis, an important factor to consider is the computational effort required for each method compared to its efficacy at generating the required focal pressures whilst keeping the SAR at the surface of the ribs below a specified threshold. In that respect, for the configurations investigated, phase conjugation appears to have the upper hand, since only two BEM calculations are required. Nevertheless, phase conjugation does not impose any constraints on the field around the focus (Tanter *et al* 2001) or in this case on the ribs. The constrained optimisation method, as implemented here, requires lengthier run times (of the order of two to five days, depending on the number of degrees of freedom in the configuration investigated). This is mainly due to the fact that 256 (the number of elements on the HIFU array) forward calculations must be carried out to form the matrices described in 5.2.4.1. Whilst the operations were vectorised, the process is still time-consuming. Nevertheless, the BEM code is currently not optimised for computational speed and methods exist which may help reduce both run time and memory requirements. These will be discussed further in Chapter 7. From a treatment planning point of view, the constrained optimisation is likely to provide greater flexibility than phase conjugation, particularly if patient-specific acoustic dose rates are established for safe and efficient treatments, along with ablation and damage thresholds. This data may then be used to define the constraints and plan the treatment accordingly. Furthermore, constrained optimisation may be useful when considering electronic steering of the beam, designed to enable a volume of tissue to be lesioned without, or with only minimal, mechanical repositioning of the transducer. Although the vector of pressures in the exterior volume in the cost function (i.e. the 'desired' field pressure distribution) was generated from the incident pressure field (i.e. in absence of the ribs, see equation 5.21), other options could easily be investigated.

Scans of the acoustic pressure magnitude along the x and y axes are shown for array-rib configurations 1 to 6 in figures 6.121 to 6.132. These scans are displayed in dB relative to the maximum focal acoustic pressure magnitude.

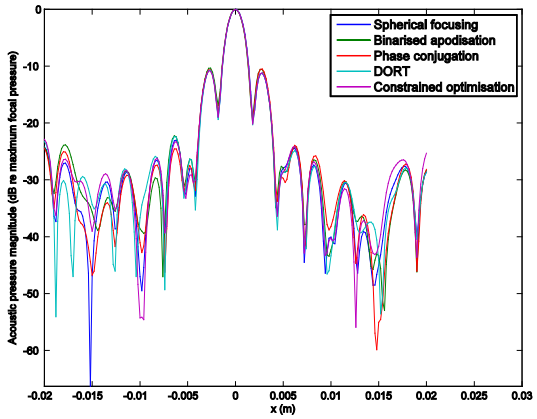

Figure 6.121 Acoustic pressure magnitude along the *x*-axis for all focusing methods. Array-rib configuration 1.

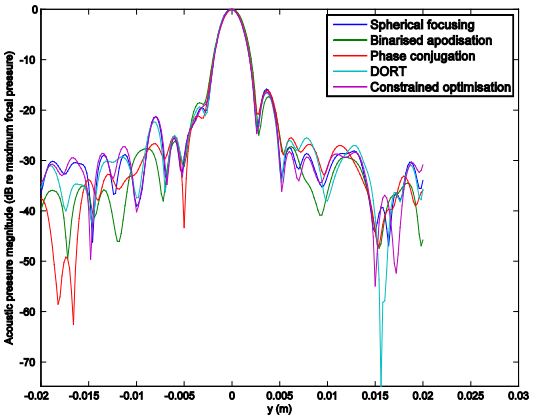

Figure 6.122 Acoustic pressure magnitude along the *y*-axis for all focusing methods. Array-rib configuration 1.

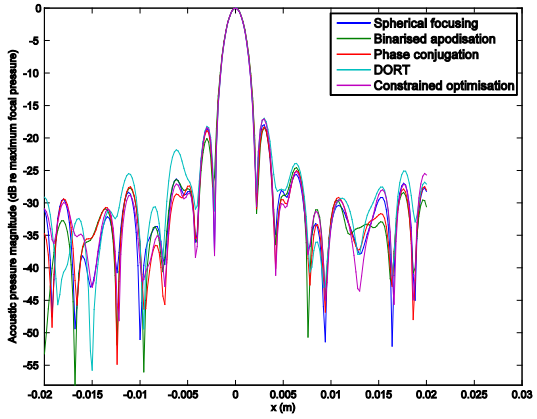

Figure 6.123 Acoustic pressure magnitude along the *x*-axis for all focusing methods. Array-rib configuration 2.

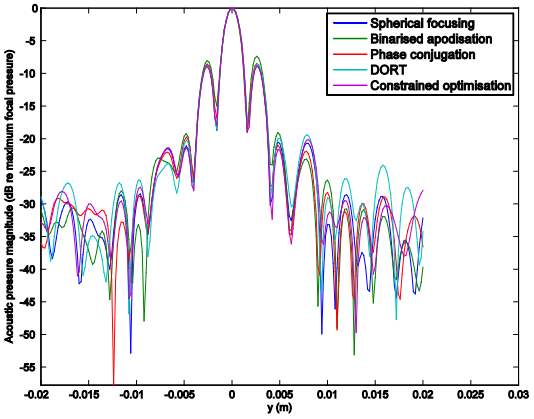

Figure 6.124 Acoustic pressure magnitude along the *y*-axis for all focusing methods. Array-rib configuration 2.

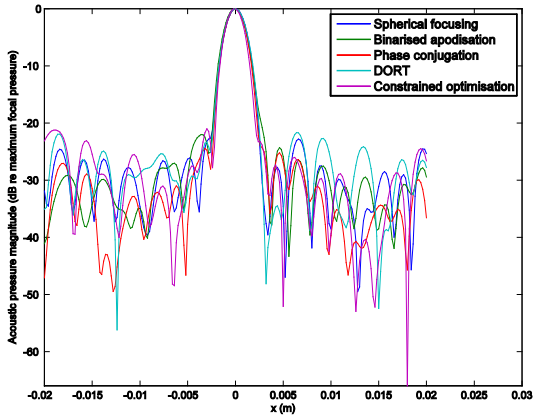

Figure 6.125 Acoustic pressure magnitude along the *x*-axis for all focusing methods. Array-rib configuration 3.

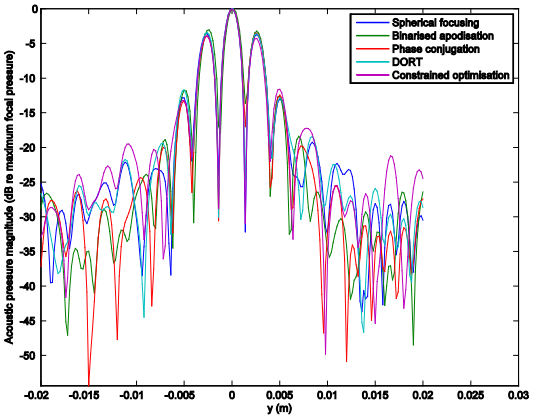

Figure 6.126 Acoustic pressure magnitude along the *y*-axis for all focusing methods. Array-rib configuration 3.

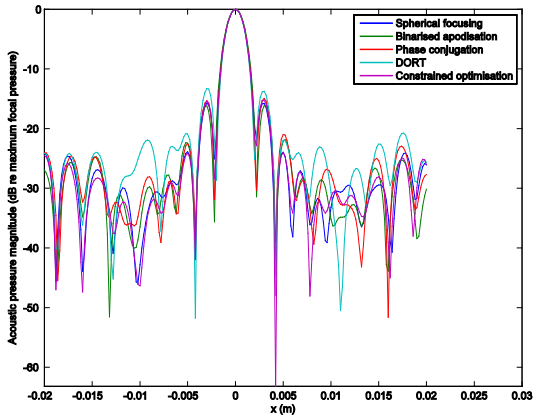

Figure 6.127 Acoustic pressure magnitude along the *x*-axis for all focusing methods. Array-rib configuration 4.

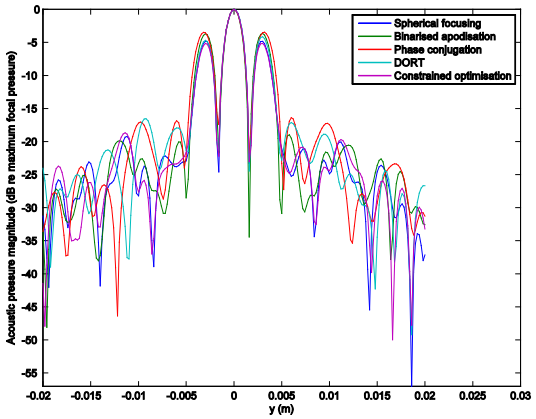

Figure 6.128 Acoustic pressure magnitude along the *y*-axis for all focusing methods. Array-rib configuration 4.

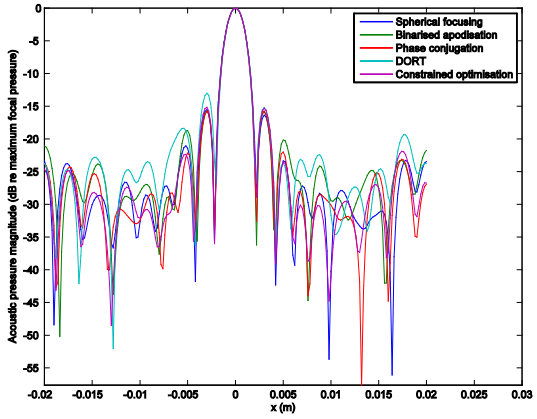

Figure 6.129 Acoustic pressure magnitude along the *x*-axis for all focusing methods. Array-rib configuration 5.

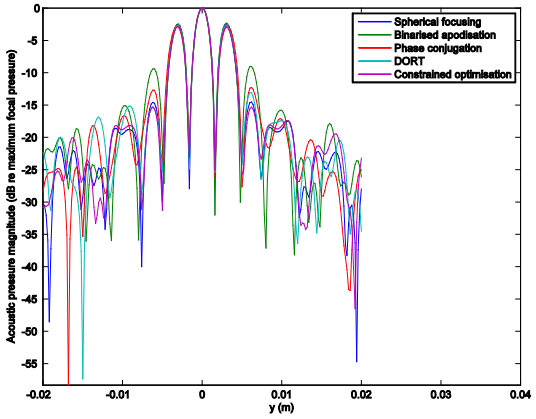

Figure 6.130 Acoustic pressure magnitude along the *y*-axis for all focusing methods. Array-rib configuration 5.

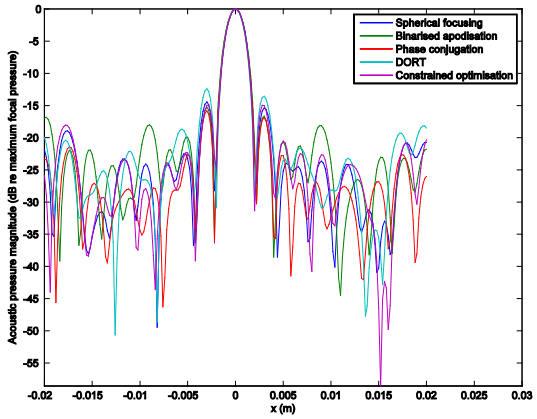

Figure 6.131 Acoustic pressure magnitude along the *x*-axis for all focusing methods. Array-rib configuration 6.

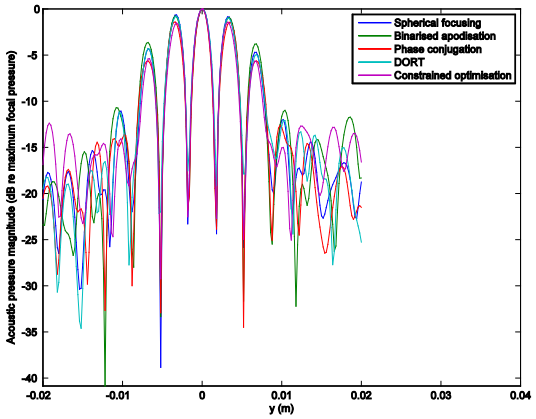

Figure 6.132 Acoustic pressure magnitude along the *y*-axis for all focusing methods. Array-rib configuration 6.

For rib-array configurations 1 to 6, an average of the amplitudes along the *x*-axis and the *y*-axis, respectively, of the two secondary lobes relative to the focal lobe is shown in tables 6.3 and 6.4,

Table 6.3: Average secondary lobe level along the *x*-axis relative to main lobe for the six array-rib configurations and for all methods of focusing.

Array-rib configuration	Spherical focusing	Binarised apodisation	Phase conjugation	DORT	Constrained optimisation
1	−11 dB	−10 dB	−11 dB	−11 dB	−11 dB
2	−18 dB	−19 dB	−19 dB	−18 dB	−18 dB
3	−25 dB	−23 dB	−25 dB	−27 dB	−24 dB
4	−16 dB	−16 dB	−15 dB	−13 dB	−15 dB
5	−16 dB	−16 dB	−16 dB	−14 dB	−15 dB
6	−15 dB	−16 dB	−16 dB	−13 dB	−15 dB

Table 6.4: Average secondary lobe level along the *y*-axis relative to main lobe for six array-rib configurations and for all methods of focusing.

Array-rib configuration	Spherical focusing	Binarised apodisation	Phase conjugation	DORT	Constrained optimisation
1	−17 dB	−18 dB	−18 dB	−18 dB	−18 dB
2	−8.8 dB	−7.7 dB	−8.5 dB	−8.7 dB	−9.0 dB
3	−3.7 dB	−3.1 dB	−3.7 dB	−3.5 dB	−4.1 dB
4	−4.8 dB	−3.7 dB	−3.5 dB	−4.4 dB	−5.1 dB
5	−2.5 dB	−2.4 dB	−2.8 dB	−2.7 dB	−2.9 dB
6	−0.75 dB	−0.83 dB	−1.4 dB	−0.89 dB	−1.5 dB

Figures 6.121 to 6.132, together with tables 6.3 and 6.4, demonstrate that secondary lobes are present in the focal plane along both the *x* and *y* axes. Along the *x*-axis, these are generally of considerably lower magnitude than the main lobe, for all methods of focusing (no more than −10 dB relative to the main lobe for all methods of focusing). This is a result of the chosen orientation of the ribs relative to the *y*-*z* plane. Along the *y*-axis, for array-rib configurations 1 and 2 (i.e. the configurations corresponding to human ribs from CT scans), the secondary lobes remain relatively low compared to the main lobe, for all methods of focusing (below −7.7 dB). For array-rib configurations 3,

4, 5 and 6, along the *y*-axis, the secondary lobes are of considerably higher magnitude than in for configurations 1 and 2, leading to visible splitting of the focus. This effect has been widely reported in trans-costal HIFU applications (Li *et al* 2007, Tanter *et al* 2007, Aubry *et al* 2008, Bobkova *et al* 2010), both theoretically and experimentally. In scatterers which exhibit spatial periodicity, the focal splitting parameters (e.g. the distance between the main and secondary lobe) can be obtained by considering the diffraction of spherically converging wave (Bobkova *et al* 2010). Using the parabolic approximation (discussed in Chapter 2 in the context of the KZK equation), an approximate relationship exists which predicts the acoustic pressure spatial distribution through parallel strips. In conjunction with the constrained optimisation approach, the multi-element array used here has been shown to lead to a modest reduction in the level of the secondary lobes relative to the main lobe (up to 1 dB – see table 6.4). Nevertheless, in cases where the intercostal spacing was too narrow compared to the rib width and to the wavelength in tissue (e.g. configuration 3), splitting at the focus could not be overcome with the current HIFU array owing to basic physics of diffraction. For array-rib configurations 1 and 2, which involve human data obtained from CT scans, it is interesting to note that focal splitting effects are not significant (see table 6.4). The ribs in configuration 3 were adapted from this topology and feature not only a narrower intercostal spacing, but one which is more or less constant throughout. This factor may significantly increase the magnitude of grating lobes. This is confirmed by the results in configuration 4, which involve idealised ribs based on a "best case" configuration (4 mm rib width and 10 mm intercostal spacing), where secondary lobes are approximately 5 dB lower than the main lobe for spherical focusing. Further BEM calculations on human ribs defined by CT scans on a range of subjects are necessary in order to fully underpin the extent of the occurrence of focal splitting in trans-costal HIFU. If it is found that focal splitting is indeed problematic, treatment planning strategies based on a multiple foci approach may have to be devised. For example, a criterion of 0.3 times the focal acoustic intensity magnitude was set by Gavrilov and Hand (2000) to estimate an acceptable level of grating lobes when steering multiple foci.

6.9 Summary

In this chapter, the following focusing methods of focusing the field of a multi-element HIFU transducer were investigated, using BEM as the forward model.

- Spherical focusing.
- Binarised apodisation based on geometric ray tracing.
- Phase conjugation.
- The DORT method.
- A constrained optimisation method based on the NAG® *e04us* solver (NAG® website).

These methods of focusing through the ribs were implemented on six array-rib configurations. All configurations featured the same 1 MHz spherical-section 256 element array, with pseudo-random spatial distribution of the sources on its surface. Three of the configurations featured human ribs (or a variation thereof), and three others, idealised ribs. The ability of each method to focus through the ribcage, whilst at the same time reducing local acoustic pressure maxima on the surface of the ribs, was compared using the criteria based on the specific absorption rate (SAR) defined in equation (6.1). Whilst the phase conjugation method delivered superior overall performance in terms of SAR gain, the constrained optimisation method was shown to provide greater flexibility than phase conjugation in treatment planning applications, particularly if patient-specific acoustic dose rates become established for safe and efficient treatments, along with ablation and damage thresholds.

It was seen that effects of splitting at the focus in configurations featuring narrow intercostal spacing relative to the rib width and to the wavelength in tissue were difficult to overcome. However, little splitting of the focus was observed on human ribs from CT scans, perhaps because of the variations in intercostal spacing in the anatomy of the ribcage. Further BEM calculations on human ribs resulting from CT scans on a range of subjects are necessary in order to underpin the extent of the occurrence of focal splitting in trans-costal HIFU fully. It was concluded that treatment planning strategies based on a multiple foci approach may have to be devised for the thermal ablation of trans-costal tumours.

Chapter 7

Conclusions

7.1 Overview

The first aim of the work described in this thesis was to develop and validate a forward BEM model which simulates the scattering by human ribs of the field of a multi-element HIFU array. The second aim was to use this forward BEM model to solve the inverse problem of focusing the field of the HIFU array inside the ribcage, whilst keeping the acoustic dose rate on the surface of the ribs below a specified threshold. A range of focusing methods reported in the literature was investigated, together with a constrained optimisation approach which was developed as part of this thesis work. The first goal of this chapter is to review the aims and objectives set out in Chapter 1, i.e. to assess the degree to which these have been achieved, and to summarise the contributions of the work. The second goal is to examine those areas requiring further investigation and to discuss new challenges arising from the work, together with possible solutions.

7.2 Contributions

This section will review the aims and objectives set out in Chapter 1 and compare them against the achievements accomplished in this body of work. The degree to which novel contributions have been made will be assessed.

Previous work on the modelling of ultrasound in biological media was reviewed in Chapter 2. A review of existing and potential trans-costal HIFU modelling approaches was then carried out. It was established that many of the existing approaches used to model the propagation of ultrasound in the presence of ribs were inadequate. It was determined that there was a requirement for linear approaches, which are capable of rigorously addressing acoustic scattering in 3D and on large problems, to be developed. The reasons why BEM is particularly suited to this task were discussed. Chapter 3 provided a theoretical description of

BEM applied to acoustic scattering problems. The model assumptions were stated and justified. The description and implementation of the BEM code used in this thesis (supplied by PACSYS Ltd, PAFEC website) is contained in Appendix A.

The validation of BEM code against known analytical solutions was described in Chapter 4. Good agreement with the analytical solutions was demonstrated. Furthermore, suitable numerical input parameters related to the accuracy, speed and convergence of the solution were chosen. This chapter also featured a review of HIFU sources, alongside a description of the multi-element transducer used in this thesis work. This was a 1 MHz spherical-section 256 element array, with pseudo-random spatial distribution of the sources on its surface. Finally, forward BEM calculations on human ribs were carried out. Initially, perfectly rigid ribs were assumed. A surface impedance boundary condition was then implemented with properties representative of rib bone. These calculations demonstrated the limitations of assuming ribs to be perfectly rigid scatterers. Indeed, the rate of energy absorption per unit mass, which is proportional to the square of the acoustic pressure magnitude (Nyborg 1981, Duck 2009), was overestimated by 56% when considering the ribs to be perfectly rigid.

Chapter 5 featured a review of the principal HIFU focusing methods for sparing ribs described in existing literature. These included binarised apodisation based on geometric ray tracing, the phase conjugation method and the DORT method. A novel constrained optimisation method using BEM as the forward model was suggested and described, and an example on a reduced complexity model presented.

Chapter 6 compared the efficacy of the inverse methods described in Chapter 5 on six different array-rib configurations, with the aim of assessing which method is most effective at sparing the ribs whilst maintaining high focal pressures. Three of these configurations involved human ribs (or a variation thereof) and three others, idealised ribs, consisting of cuboid scatterers with rounded edges. All true and idealised ribs were assumed to be locally reacting, with a surface impedance representative of rib bone. Results for spherical focusing were obtained initially. The first criterion used for assessing the efficacy of each focusing method was the SAR gain defined as the logarithmic ratio of the SAR at the target to the SAR at the point to be spared. The second criterion used to assess the quality of the focusing was the peak focal pressure relative to the maximum level available from the phased array. Whilst the phase conjugation method delivered superior overall performance in terms of SAR gain,

the constrained optimisation method was shown to provide greater flexibility than phase conjugation in treatment planning applications, particularly if patient-specific acoustic dose rates become established for safe and efficient treatments, along with ablation and damage thresholds. Effects of splitting at the focus were observed in configurations featuring narrow intercostal spaces relative to the rib width and to the wavelength in tissue. These were difficult to overcome owing to the basic physics of diffraction. However, little splitting of the focus was observed on human ribs from CT scans.

To the author's knowledge, this is the first time that BEM has been applied to trans-costal HIFU problems. Furthermore, other than the author's journal papers, there does not appear to be any published work on trans-costal HIFU simulations on human ribs in 3D to this date. Hence, the calculations presented in Chapters 4 and 6 represent a novel contribution to the field of trans-costal HIFU simulations. This thesis work demonstrated the limitations of simulating ribs as parallel thin strips or cuboid objects which are either perfectly reflecting or absorbing. It also highlighted the need to move towards an integrated treatment planning and protocol strategy based on the prior acquisition of MR or CT scans. The medical physicist will then benefit from a range of options when planning the HIFU treatment and will be able to assess which focusing method is the most appropriate for a given patient. The constrained optimisation method may prove to be particularly useful in this context.

7.3 Further work

In section 7.2, it has been shown that the aims and objectives outlined in Chapter 1 have been achieved, and that a number of novel contributions have been made as a result of this work. However, as indicated throughout this thesis, a number of assumptions have been made, and there are a number of areas which will benefit from further investigation. The aim of this section is to summarise these.

The BEM code used in this thesis work was neither optimised for computational speed, nor for minimising the use of RAM. It has been described how BEM leads to fully-populated, asymmetric and complex matrices, necessitating the use of an iterative solver. For trans-costal HIFU applications, run times for a forward problem are of the order of several hours, and of up to several days for inverse problems. Approaches based on hierarchical matrices methods (Bebendorf 2008) or on the fast multipole method (Liu 2009) may greatly reduce

both run times and problem sizes. Using the calculations in Chapter 4 and Chapter 6 as benchmarks, it would be highly relevant to investigate the extent to which these methods can improve the computational efficiency of BEM when applied to trans-costal HIFU simulations.

In the BEM formulation described in this thesis work, the acoustic medium surrounding the ribs is assumed to extend to infinity and the soft tissue (i.e. muscle, skin, cartilage and fat) is treated as a homogeneous medium. Whilst the speed of propagation of longitudinal waves is generally comparable in different soft tissues, and the same is true of the density, it has been shown that tissue inhomogeneities can cause aberrations of the focus (Treeby *et al* 2012). Multiple tissue volumes could in principle be implemented using BEM through a combination of interior and exterior formulations (Elysée 2011). This would necessitate meshing the closed surfaces associated with each region. Problem size may be considerably increased, so this should only be attempted once BEM is implemented with improved computational efficiently. The properties of rib bone were also considered to be constant as a function of positions. The current BEM implementation is in fact not restricted to this assumption, and separate complex values of speed of sound and density can be assigned to each boundary element patch. The spatial variation of rib bone properties and its impact on SAR and SAR gain could be investigated.

During HIFU treatment, the ultrasonic transducer is not coupled directly to the abdomen of the patient, as it is generally of spherical-section shape. Instead, a water region is placed between the transducer and the abdomen. Whilst the density and speed of sound in water are not dissimilar to those in soft tissue, the attenuation coefficient in liver is approximately three orders of magnitude higher than that in water at 20°C at 1 MHz (Duck 1990 p75 and p104, Fan and Hynynen 1994). Neglecting this will have an impact on the acoustic pressures calculated at the focus, which may be considerably underestimated. In order to account for this, a correction for the acoustic pressure transmitted at the water/tissue interface could be applied using a Rayleigh-Sommerfeld diffraction integral (Hynynen and Fan 1992 and 1994).

It is well known that both longitudinal and shear waves can be generated in bone (Kohles *et al* 1997, Mast *et al* 1999). As bone is a highly attenuating medium compared to soft tissue, absorption of shear waves may play an important part in heating of bone. A full

elastodynamic formulation would be required to deal with this phenomenon accurately. This could in principle be achieved using an elastodynamic BEM frequency domain formulation such as that proposed by Chaillat *et al* (2007). Another possible approach would consist of using a FEM/BEM method (Macey 1987), where the exterior domain would be modelled using BEM patches, and the interior domain using structural finite elements. These formulations are however likely to be computationally expensive.

The effects of nonlinear propagation have not been considered in this thesis. It is, however, well known that HIFU fields can result in highly nonlinear behaviour in the focal region (Wu *et al* 2004), leading to distortion of the acoustic waveform and transfer of energy from the fundamental frequency towards higher order harmonics. As nonlinear behaviour is likely to be mainly confined to the central focal lobe, a more rigorous treatment of the focal region could be envisaged, perhaps using a computational fluid dynamics approach or by propagating a source plane transverse to the direction of propagation using a Westervelt equation solver. Otherwise, a full-wave nonlinear 3D model for propagation of ultrasound in tissue, allowing for shock wave formation and for sharp discontinuities in the media interfaces (e.g. tissue/bone), would be required to deal with nonlinearities in the presence of ribs. If such a model is developed, it would be interesting to compare it against the BEM approach. Furthermore, optimised source velocities obtained using BEM as the forward model could serve as input data to such a model.

The focusing SAR gain was investigated in relation to the maximum SAR occurring on the surface of the ribs. Clearly, we require focusing criteria based on clinically established dose and exposure criteria. These are yet to be established. A heat transfer analysis would nevertheless provide insight relating the acoustic field distribution on the surface of the ribs to the temperature rise at required locations. This may also help refine the definitions of the constraints relating to thresholds and locations.

Finally, it is clear that experimental validation of the proposed method in water, with the use of a bone phantom, is required. Hydrophone measurements of acoustic pressures in the focal plane under linear excitation conditions and comparison against theoretical results would provide further confidence in the BEM approach.

This work was carried out as part of a wider project whose goal is the design of a prototype trans-costal HIFU system for the treatment of liver and pancreatic tumours. This features a multi-element array with electronic steering capabilities, together with a system for ultrasonic ablation/cavitation monitoring. The technique presented in this thesis is expected to help validate the treatment planning software and inform the treatment protocol. *In vivo* applications will be investigated and are expected to rely upon treatment plans generated using virtual propagation models based on anatomical data that has been obtained from CT or MR scans of the patient. Treatment monitoring will be performed using an ultrasonic probe which is either integrated into the HIFU transducer, or is placed in a separate position (e.g. to scan from a subcostal approach). Registration of the ribs from CT images to the patient will be carried out as follows: first, a diagnostic ultrasound probe, tracked by an optical 3D localiser, will be used to acquire a 3D ultrasound image of the rib surface (the 3D pose of each of a series of B-mode ultrasound images is calculated using the 3D tracking data, and the images combined to form a 3D image of the region of interest). The CT bone surface may then be registered directly and automatically to the ultrasound image using the method described by Penney *et al* (2006). Alternative methods could also be used since the CT scans are pre-segmented to produce a geometric representation of the bone surface as part of treatment planning and acoustic modelling tasks. Since the HIFU transducer is also tracked in 3D by the localiser, and registering the ribs using this procedure allows the ribs to be localised with respect to the 3D physical reference co-ordinate system of the localiser, the correct (planned) physical position and orientation of the HIFU transducer relative to the ribs may be determined.

Initially, effects of respiratory movement and organ deformation will be ignored and breath-hold or gating will be used. A subsequent version of the treatment planning software will feature motion compensation capabilities based on methods developed by Rijkhorst *et al* (2011).

7.4 Summary

It has been demonstrated in this chapter that the aims and objectives outlined at the start of the work have been achieved. A forward model using BEM, capable of simulating the scattering of the field of a multi-element HIFU array by human ribs has been developed. This forward BEM model was used to solve the inverse problem of focusing the field of the HIFU

array inside the ribcage whilst keeping the acoustic dose rate on the surface of the ribs below a specified threshold. A range of focusing methods reported in the literature has been investigated together with a constrained optimisation approach developed as part of this thesis work. This constrained optimisation method was shown to provide greater flexibility than other methods for treatment planning applications, particularly if patient-specific acoustic dose rates are to be established for safe and efficient treatments, along with ablation and damage thresholds. Areas for future study have been identified in this chapter. These include improving the computational efficiency of the BEM code, together with additional refinements to the model which would enable the incorporation of tissue inhomogeneities. A BEM elastodynamic formulation for modelling shear wave propagation in rib bone has been suggested, and the importance of heat transfer modelling outlined. Finally, it was emphasised that experimental and clinical validation of the modelling approach is essential.

References

Aanonsen S, Barkve T, Tjøtta J and Tjøtta S 1984 Distortion and harmonic generation in the nearfield of a finite amplitude sound beam *J. Acoust. Soc. Am.* **75** 749–768.

Abramowitz M and Stegun I 1964 *Handbook of Mathematical Functions* (Washington: National Bureau of Standards).

Ahmed H U, Cathcart P, Chalasani V, Williams A, McCartan N, Freeman A, Kirkham A, Allen C, Chin J, Emberton M 2012 Whole-gland salvage high-intensity focused ultrasound therapy for localized prostate cancer recurrence after external beam radiation therapy *Cancer* **118** 3071–3078.

Arnoldi W E 1951 The principle of minimized iteration in the solution of the matrix eigenvalue problem *Quart. Appl. Math.* **9** 17–29.

Aubry A, de Rosny J, Minonzio J-B, Prada C and Fink M 2006 Gaussian beams and Legendre polynomials as invariants of the time reversal operator for a large rigid cylinder *J. Acoust. Soc. Am.* **120** 2746–2754.

Aubry J-F, Pernot M, Marquet F, Tanter M, Fink M 2008 Transcostal high-intensity focused ultrasound: *ex vivo* adaptive focusing feasibility study *Phys. Med. Biol.* **53** 2937–2951.

Ballard J, Casper A J, Wan Y and Ebbini E S 2010 Adaptive Transthoracic Refocusing of Dual-Mode Ultrasound Arrays *IEEE T. Bio-med. Eng.* **57** 93–102.

Banerjee P K 1994 *The Boundary Element Methods in Engineering* (London: McGraw-Hill).

Bebendorf M 2008 *Hierarchical Matrices: A Means to Efficiently Solve Elliptic Boundary Value Problems* (Berlin and Heidelberg: Springer-Verlag).

Berenger J 1994 A perfectly matched layer for the absorption of electromagnetic waves *J.Comput. Phys.***114**185–200.

Berenger J 1996 Three-dimensional perfectly matched layer for the absorption of electromagnetic waves *J. Comput. Phys.* **127** 363–379.

Berntsen J 1990 *Numerical Calculations of Finite Amplitude Sound Beams*, in Hamilton M F and Blackstock D T, editors, *Frontiers of Nonlinear Acoustics: Proceedings of 12th ISNA*, Elsevier.

Bobkova S, Gavrilov L, Khokhlova, Shaw A and Hand J 2010 Focusing of high-intensity ultrasound through the rib cage using a therapeutic random phased array *Ultrasound Med. Biol*. **36** 888–906.

Bonnans J F, Gilbert J C, Lemaréchal C, Sagastizábal C A 2006 *Numerical optimization: Theoretical and practical aspects* (Berlin: Springer-Verlag).

Botros Y Y, Ebbini E S, Volakis J L 1998 Two-step hybrid virtual array-ray (VAR) technique for focusing through the ribcage *IEEE T. Ultrason. Ferr.* **45** 989–999.

Bridges J F, Gallego G, Blauvelt B M 2011 Controlling liver cancer internationally: A qualitative study of clinicians' perceptions of current public policy needs *Health Res. Policy Syst*. **9**:32.

Brillouin L 1964 *Tensors in Mechanics and Elasticity* (New York: Academic Press).

Burton A J and Miller G F 1971 The application of integral equation methods to the numerical solution of some exterior boundary-value problems *Proc. R. Soc. London. Ser.* A 323 *(London, UK)* pp 201–210.

Cancer Research UK website http://www.cancerresearchuk.org

Carpizo D R, D'Angelica M 2009 Liver resection for metastatic colorectal cancer in the presence of extrahepatic disease *Lancet Oncol.* **10** 801–809.

CATIA v5 website http://www.appliedgroup.com/catia

Cha C H, Saif M W Yamane B H 2010 Hepatocellular carcinoma: current management *Curr. Prob. Surg.* **47** 10–67.

Chaillat S, Bonnet M and Semblat J-F 2007 A fast multiple method formulation for 3D elastodynamics in the frequency domain *CR Mecanique* **335** 714–719.

Chen W and Holm S 2004 Fractional Laplacian time-space models for linear and nonlinear lossy media exhibiting arbitrary frequency power-law dependency *J. Acoust. Soc. Am.* **115** 1424–1430.

Chien C C, Rjiyah H and Atluri S N 1990 An effective method for solving the hypersingular integral equations in 3-D acoustics *J. Acoust. Soc. Am.* **88** 343–418.

Chinnery P A, Zhang J D and Humphrey V F 1997 Acoustic scattering by nonmetallic and metallic cubes in the elastic resonance regime: experimental and combined finite element/boundary element modelling *J. Acoust. Soc. Am.* **102** 60–66.

Christ A, Kainz W, Hahn E G, Honegger K, Zefferer M, Neufeld E, Rascher W, Janka R, Bautz W, Chen J, Kiefer B, Schmitt P, Hollenbach H-P, Shen J, Oberle M, Szczerba D, Kam A, Guag J W and Kuster N 2010 The Virtual Family—development of surface-based anatomical models of two adults and two children for dosimetric simulations *Phys. Med. Biol*. **55** N23–N38.

Chung T J 2002 *Computational Fluid Dynamics* (Cambridge: Cambridge University Press).

Civale J, Clarke R, Rivens I, terHaar G 2006 The use of a segmented transducer for rib sparing in HIFU treatments *Ultrasound Med. Biol.* **32** 1753–1761.

Cochard E, Prada C, Aubry J-F, Fink M 2009 Ultrasonic focusing through the ribs using the DORT method *Med. Phys.* **36** 3495–3503.

Cochard E, Aubry J-F, Tanter M and Prada C 2011 Adaptive projection method applied to three-dimensional ultrasonic focusing and steering through the ribs *J. Acoust. Soc. Am.* **130** 716-723.

Colton D and Kress R 1983 *Integral Equation Methods in Scattering Theory (Pure and Applied Mathematics)* (New York: Wiley).

Crum L, Bailey M, Hwang J H, Khokhlova V and Sapozhnikov O 2010 Therapeutic ultrasound: Recent trends and future perspectives. *Physics Procedia* **3** 25–34.

CyberLogic website http://www.cyberlogic.org/

Daum D R and Hynynen K 1999 A 256-element ultrasound phased array system for the treatment of large volumes of deep seated tissue *IEEE Trans. Ultrason. Ferroelectr. Freq. Control* **46** 1254–1268.

Deffieux T and Konofagou E E 2010 Numerical study of a simple transcranial focused ultrasound system applied to blood-brain barrier opening *IEEE Trans. Ultrason. Ferroelectr. Freq. Control* **57** 2637–2653.

Dewey W C 1994 Arrhenius relationships from the molecule and cell to the clinic *Int. J. Hyperthermia **10***, 457–483.

Dodd M and Oclee-Brown J 2007 A new methodology for the acoustic design of compression drive phase-plugs with concentric annular channels *J. Audio Eng. Soc.* **57** 771–787.

Duck F A 1990 *Physical Property of Tissues–A Comprehensive Reference Book* (Academic: London).

Duck F 2009 Acoustic dose and acoustic dose rate *Ultrasound Med. Biol.* **35** 1679–1685.

Ebbini E S, Umemura S-I, Ibbini M and Cain C A 1988 A cylindrical-section ultrasound phased-array applicator for hyperthermia cancer therapy *IEEE Trans. Ultrason. Ferroelectr. Freq. Control* **35** 561–572.

Ebbini E S and Cain C A 1991 A spherical-section ultrasound phased-array applicator for deep localized hyperthermia *IEEE Trans. Biomed. Eng.* **38** 634–43.

El-Brawany M A, Nassiri D K, Ter Haar G, Shaw A, Rivens I and Lozhken K 2009 Measurement of thermal and ultrasonic properties of some biological tissues *J. Med. Eng. Technol.* **33** 249–256.

Elysée J 2011 Innovative Boundary Integral and Hybrid Methods for Diffuse Optical Imaging, PhD Thesis, University College London, UK.

Emmerich H and Korn M 1987 Incorporation of attenuation into time domain computations of seismic waves *Geophys.* **52** 1252–1264.

Fan X and Hynynen K 1992 The effect of wave reflection and refraction at soft tissue interfaces during ultrasound hyperthermia treatments *J. Acoust. Soc. Am.* **91** 1727–1736.

Fan X and Hynynen K 1994 The effects of curved tissue layers on the power deposition patterns of therapeutic ultrasound beams *Med. Phys.* **21** 25–34.

Fink M 1992 Time reversal of ultrasonic fields–Part I: Basic principles *IEEE Trans. Ultrason. Ferroelectr. Freq. Control* **39** 555–566.

Filonenko E A, Gavrilov L R, Khokhlova V A, Hand J W 2004 Heating of biological tissues by two-dimensional phased arrays with random and regular element distributions *Acoust. Phys.* **50** 222–231.

Fjield T, Sorrentino V, Cline H and Hynynen K 1997 Design and experimental verification of thin acoustic lenses for the coagulation of large tissue volumes *Phys. Med. Biol.* **44** 1803–1813.

Fletcher R 1981 *Practical Methods of Optimization*. *Volume 2: Constrained Optimization* (New York: John Wiley & Sons; 1981).

Fleury G, Berriet R, Le Baron O and Huguenin B 2003 New piezocomposite transducer for therapeutic ultrasound *Proc. of SPIE* **4954** 227–236.

Fry W J, Mosberg Jr W H, Barnard J W, Fry F J 1954 Production of focal destructive lesions in the central nervous system with ultrasound *J. Neurosurg.* **11** 471–478.

Fry F J 1978 Intense focused ultrasound: Its production, effects and utilization in *Ultrasound: Its Applications in Medicine and Biology, Part II,* Fry F J Ed. New York: Elsevier, 1978 pp. 689–736.

Gaul L, Kögl M and Wagner M 2003 *Boundary Element Methods for Scientists and Engineers* (Berlin: Springer).

Gavrilov L R, Hand J W 2000 A theoretical assessment of the relative performance of spherical phased arrays for ultrasound surgery *IEEE T. Ultrason. Ferr.* **47** 125–139.

Geaves G P 1995 Modelling and Optimal Design of Loudspeaker Diaphragms using Numerical Methods, PhD Thesis, University of Brighton, UK.

Gélat P, ter Haar G and Saffari N 2011 Modelling of the acoustic field of a multi-element HIFU array scattered by human ribs *Phys. Med. Biol.* **56** 5553–5581.

Gélat P, ter Haar G and Saffari N 2012 Scattering of the field of a multi-element phased array by human ribs *J. Phys. Conf. Ser.* **353** Proceedings of the 10th Anglo-French Physical Acoustics Conference (AFPAC 2011) 19–21 January 2011, Fréjus, France.

Gélat P, ter Haar G and Saffari N 2012 The optimisation of acoustic fields for ablative therapies of tumours in the upper abdomen *Phys. Med. Biol.* **57** 8471-8497.

Gélat P, ter Haar G and Saffari N 2013 Towards the optimisation of acoustic fields for ablative therapies of tumours in the upper abdomen *J. Phys. Conf. Ser.* **457** Proceedings of the 11th Anglo-French Physical Acoustics Conference (AFPAC 2012) 18–20 January 2012, Brighton, UK.

Gentle J E 1998 *Gaussian elimination in numerical linear algebra for applications in statistics* (Berlin, Heidelberg and New York: Springer).

Geomagic™ website http://www.geomagic.com/en/

Gill P E, Murray W, and Wright M H 1981 *Practical Optimization* (London and New York: Academic Press).

Gill P E, Murray W, Saunders M A and Wright M H 2001 User's guide for NPSOL 5.0: A FORTRAN package for nonlinear programming *Technical Report SOL* **86-6**.

Griffith H B, Brownell B, Bowes J B, Halliwell M and Wells P N Arterial damage by trackless lesions in the spinal cord made by focused ultrasound 1967 *Meeting of the Surgical Society (Bristol, UK).*

Goss S A, Frizell L A, Kouzmanoff J T, Barich J M and Yang J M 1996 Sparse random ultrasound phased array for focal surgery *IEEE Trans. Ultrason. Ferroelectr. Freq. Control* **43** 1111–1121.

Guo N, Cawley P and Hitchings D 1992 The finite elements analysis of the vibration characteristics of piezoelectric discs *J. Sound. Vib.* **159** 115–138.

Hajihasani M, Farjami Y, Gharibzadeh S, and Tavakkoli J 2009 A novel numerical solution to the diffraction term in the KZK nonlinear wave equation. In *38th Annual Ultrasonic Industry Association Symposium* pages 1–9.

Hamilton M F and Blackstock D T 1998 *Nonlinear Acoustics* (San Diego: Academic Press).

Hand J W, Gavrilov L R Ultrasound transducer array. GB patent GB2347043A 23 August 2000.

Hand J W, Shaw A, Sadhoo N, Dickinson R J, Gavrilov L R 2009 A random phased array device for delivery of high intensity focused ultrasound (HIFU) *Phys. Med. Biol.* **54** 5675–5693.

Hill C R, The generation and structure of acoustic fields. In *Physical Principles of Medical Ultrasonics (2nd edn),* ed.by C R Hill, J C Bamber and G R ter Haar (Chichester: Wiley), Chapter 2. 2004.

Householder A S 1975 *Theory of Matrices in Numerical Analysis* (New York: Dover Publications).

Hugues M 2001 Finite element and boundary element modelling of a physiotherapy transducer and its near-field, PhD thesis, University of Bath, UK.

Ikegami A, Ueda I and Kobayashi S 1974 Frequency spectra of resonant vibration in disk plates of $PbTiO_3$ piezoelectric ceramics *J. Acoust. Soc. Am.* **55** 339–344.

Illing R O, Kennedy J E, Wu F, ter Haar G R, Protheroe A S, Friend1 P J, Gleeson F V, Cranston D W, Phillips R R and Middleton M R 2005 The safety and feasibility of extracorporeal high-intensity focused ultrasound (HIFU) for the treatment of liver and kidney tumours in a Western population *Brit J. Cancer* **93** 890–895.

Johnson L W, Reiss R D and Arnold J T 1989 *Introduction to Linear Algebra* (Reading: Addison-Wesley).

Kaufman J J, Luo G and Siffert R S 2008 Ultrasound simulation in bone *IEEE Trans. Ultrason. Ferroelectr. Freq. Control* **55** 1205–1218.

Kennedy J E, Wu F, ter Haar G, Gleeson F V, Phillips R R, Midleton M R and Cranston D 2004 High-intensity focused ultrasound for the treatment of liver tumours *Ultrasonics* **42** 931–935.

Kohles S S, Bowers J R ,Vailas A C and Vanderby, R 1997 Ultrasonic wave velocity measurement in small polymeric and cortical bone specimens J. Biomech. Eng. **119**, 232

Khokhlova V A, Bobkova S M and Gavrilov L R 2010 Focus splitting associated with propagation of focused ultrasound though the rib cage *Acoustical Physics* **56** 665–674.

Kinsler L E, Frey A R, Coppens A B and Sanders J V 1982 *Fundamentals of Acoustics 3rd ed.* (New York: John Wiley & Sons).

Kress R 1985 Minimizing the condition number of boundary integral operators in acoustic and electromagnetic scattering *Q. J. Mech. Appl. Math.* **38** 323–341.

Kreyszig E 1988 *Advanced Engineering Mathematics* (New York: John Wiley & Sons).

Kuznetsov V P 1971 Equations of nonlinear acoustics *Sov. Phys. Acoust.* **16** 467–470.

Lachat J C and Watson J O 1976 Effective numerical treatment of boundary integral equations: A formulation for three dimensional elastostatics *Int. J. Numer. Meth. Eng.* **10** 991–1005.

Landau L D and Lifshitz E M 2011*Fluid Mechanics* (Oxford: Elsevier).

Lapidus L and Pinder G F 1989 *Numerical solution of partial differential equations in science and engineering* (Beijing: China Coal Industry Publishing House).

Lee Y-S and Hamilton M F 1995 Time-domain modelling of pulsed finite-amplitude sound beams *J. Acoust. Soc. Am.* **97** 906–917.

Leslie T, Ritchie R, Illing R, ter Haar G, Phillips R, Middleton M, Wu F and Cranston D 2012 High-intensity focused ultrasound treatment of liver tumours: post-treatment MRI correlates well with intra-operative estimates of treatment volume *Brit. J. Radiol.* **85** 1363–1370.

Li J-L, X-Zh Liu, Zhang D, Gong X-F 2007 Influence of ribs on nonlinear sound fields of therapeutic ultrasound *Ultrasound Med. Biol.* **33** 1413–1420.

Lin T, Ophir J and Potter G 1987 Frequency-dependent ultrasonic differentiation of normal and diffusely diseased liver *J. Acoust. Soc. Am.* **82** 1131–1138.

Liu H-L, Chang Hsu, Chen W-S, Shih T-C, Hsiao J-K and Lin W-L 2007 Feasibility of transrib focused ultrasound thermal ablation for liver tumours using a spherically curved 2D array: A numerical study *Med. Phys.* **34** 3436–3448.

Liu Y 2009 *Fast Multipole Boundary Element Method: Theory and Applications in Engineering* (Cambridge: Cambridge University Press).

Liu Y and Rizzo F J 1992 A weakly singular form of the hypersingular boundary integral equation applied to 3-D acoustic wave problems *Comput. Method. Appl. M.* **96** 271–287.

Liu Y and Rudolphi T J 1991 Some identities for fundamental solutions and their applications to weakly-singular boundary element formulations *Eng. Anal. Boundary Elem.* **8** 301–311.

Liu Z 2000 Re-evaluation of normal people's rib cleft (801 X-ray measurements of normal people's rib cleft) *Chinese Journal of Medical Imaging Studies* **16** 589.

Lu M, Wan M, Xu F, Wang X and Zhong H 2005 Focused beam control for ultrasound surgery with a spherical-scation phased array: sound field calculation and genetic optimization algorithm *IEEE Trans. Ultrason. Ferroelectr. Freq. Control* **52** 1270–1290.

Lynn J G, Zwemer R L Chick A J and Miller A E 1942 A new method for the generation and use of focused ultrasound in experimental biology *J. Gen. Physiol.* **26** 179–319.

Lynn J G and Putman T J 1944 Histology of cerebral lesions produced by focused ultrasound. *Am. J. Path.* **20** 637–652.

Macey P 1987 Acoustic and structure interaction problems using finite and boundary elements, PhD Thesis, University of Nottingham, UK.

Macey P C 1994 Oblique incidence diffraction by axisymmetric structures *Proc. Ins. Ac.* **16** 67–74.

Markham J J, Beyer R T and Lindsay R B 1951 Absorption of sound in fluids *Rev. Mod. Phys.* **23** 353–411.

Marquet F, Aubry J F, Pernot M, Fink M and M Tanter 2011 Optimal transcostal high-intensity focused ultrasound with combined real-time 3D movement tracking and correction *Phys. Med. Biol.* **56** 7061–7080.

Mast D, Hinkelman L, Metlay L, Orr M and Waag R 1999 Simulation of acoustic pulse propagation and attenuation in the human chest wall *J. Acoust. Soc. Am.***106** 3665–3677.

Melodima A and Cathignol 2004 Cancer treatment by ultrasound: Increasing the depth of necrosis *Appl. Phys. Lett.* **54** 6353–6368.

Morgan S 2004 Efficient numerical methodologies for the performance prediction of active sonar arrays, PhD thesis, University of Birmingham, UK.

Mohr M, Abrams E, Engel C, Long W B and Bottlang M 2007 Geometry of human ribs pertinent to orthopaedic chest-wall reconstruction *J Biomech* **40** 1310–1317.

Morse P M and Ingard K U 1968 *Theoretical Acoustics* (New York: McGraw-Hill).

Nachman A, Smith J and Waag R 1990 An equation for the acoustic propagation in inhomogeneous media with relaxation losses *J. Acoust. Soc. Am.* **88** 1584–1595.

Nguyen D-Q and Gan W-S 2010 The DORT solution in acoustic inverse scattering problem of a small elastic scatterer *Ultrasonics* **50** 829–140.

Numerical Algorithms Group
website: http://www.nag.co.uk/numeric/numerical_libraries.asp

Nunn J F and Slavin G 1980 Posterior intercostals neverve block for pain after cholecystectomy. Anatomical basis and efficacy *Br. J. Anaesth.* **52** 253–260.

Nyborg W L 1981 Heat generation by ultrasound in a relaxing medium *J. Acoust. Soc. Am.* **70** 310–312.

Ochmann M, Homm A, Makarov S and Semenov S 2003 An iterative GMRES-based boundary element solver for acoustic scattering *Eng. Anal. Bound. Elem.* **27** 717–725.

O'Donnel M, Jaynes E T and Miller J G 1981 Kramers-Kroni relationship between ultrasonic attenuation and phase velocity *J. Acoust. Soc. Am.* **69** 696–701.

PAFEC VibroAcoustics, from PAFEC Ltd., Strelley Hall, Nottingham N686PE, UK.

Penney G P, Barratt D C, Chan C S K, Slomczykowski M, Carter T J, Edwards P J, Hawkes D J 2006 Cadaver validation of intensity-based ultrasound to CT registration *Med. Image Anal.* **10** 385–395.

Pernot M, Aubry J-F, Tanter M, Thomas J L, Fink M 2003 High power transcranial beam steering for ultrasonic brain therapy *Phys. Med. Biol.* **48** 2577–2589.

Pierce A D 1989 *Acoustics: an introduction to its physical principles and applications* (New York: McGraw-Hill)

Pinton G, Aubry J-F, Fink M and Tanter M 2011 Effects of nonlinear ultrasound propagation on high intensity brain therapy *Med. Phys.* **38** 1207–1216.

Piorkowsky N Y 2009 Europe hepatitis challenge: "Diffusing the viral time bomb" *J. Hepat.* **51** 1068– 1073.

Prada C, Thomas J-L and Fink M 1995 The iterative time reversal process: Analysis of the convergence *J. Acoust. Soc. Am.* **97** 62–71.

Prada C, Manneville S, Spoliansky D and Fink M 1996 Decomposition of the time reversal operator: Detection and selective focusing on two scatterers *J. Acoust. Soc. Am.* **99** 2067–2076.

Prada C, 2002 Detection and imaging in complex media with the DORT method *Top. Appl. Phys.* **84**, 107–133.

Quesson B, Merle M, Roujol S, de Senneville B D and Moonen C T 2010 A method for MRI guidance of intercostal high intensity focused ultrasound ablation in the liver *Med. Phys.* **37** 2533–2540.

Ribeiro R and Sanches J 2009 Fatty liver characterization and classification by ultrasound *Lect. Notes. Comput. Sc.* **5524** 354–361.

Rijkhorst E J, Rivens, I, ter Haar G, Hawkes,D and Barratt D 2011 Effects of respiratory liver motion on heating for gated and model-based motion-compensated

high-intensity focused ultrasound ablation. MICCAI proceedings, *Lect. Notes Comput. Sc.* **6891** 605–612.

Ritchie R W, Leslie T, Phillips R, Wu F, Illing R, ter Haar G, Protheroe A and Cranston D 2010 Extracorporeal high intensity focused ultrasound for renal tumours: a 3-year follow-up *BJU Int.* **106** 1004–1009.

Saad Y and Schultz M H 1986 GMRES: a generalised minimal residual algorithm for solving nonsymmetric linear systems *SIAM J. Sci. Statist. Comput.* **7** 856–869.

Sanghvi N T, Fry F J, Bihrle R, Foster R S, Syrus J, Zaitsev A V, Hennige C W 1996 Noninvasive surgery of prostate tissue by high-intensity focused ultrasound *IEEE Trans. Ultrason. Ferroelectr. Freq. Control* **43** 1099–1110.

Sapareto S A and Dewey W C 1984 Thermal dose determination in cancer therapy *Int. J. Radiat. Oncol*. **10** 787–800.

Shen L and Liu Y J 2007 An adaptive fast multipole boundary element method for three-dimensional acoustic wave problems based on the Burton-Miller formulation. *Comput. Mech.* **40** 461–472.

Shenck H 1968 Improved integral formulation for acoustic radiation problems *J. Acoust. Soc. Am.* **44** 41–58.

Song H C, Hodgkiss W S, Kuperman W A, Sabra K G, Akal T and Sevenson M 2007 Passive reverberation nulling for target enhancement *J. Acoust. Soc. Am.* **122** 3296–3303.

Sun J and Hynynen K 1999 The potential of transskull ultrasound therapy and surgery using the maximum available skull surface area *J. Acoust. Soc. Am.* **105** 2519–2527.
Szabo T L 2004 *Diagnostic Ultrasound Imaging* (Burlington: Elsevier).

Tabei M, Mast T D and Waag R C 2002 A k-space method for coupled first-order acoustic propagation equations *J. Acoust. Soc. Am.* **111** 53–63.

Tanter M, Thomas J-L and Fink M 2000 Time reversal and the inverse filter *J. Acoust. Soc. Am.* **96** 649–660.

Tanter M, Aubry J-F, Gerber J, Thomas J-L and Fink M 2001Optimal focusing by spatio-temporal inverse filter. I. Basic principles *J. Acoust. Soc. Am.* **110** 37–47.

Tanter M, Pernot M, Aubry J-F, Montaldo G, Marquet F, Fink M 2007 Compensating for bone interfaces and respiratory motion in high intensity focused ultrasound *Int. J. Hyperthermia* **23** 141–151.

Tappert F 1977 *The parabolic approximation method in wave propagation and underwater acoustics. Lectures in Physics* Keller J B and Papadakis J S (New York: Springer).

ter Haar G, Sinnett D and Rivens I 1989 High intensity focused ultrasound – a surgical technique for the treatment of discrete liver tumours *Phys. Med. Biol.* **34** 1743-1750.

ter Haar G and Coussios C 2007 High-Intensity Focused Ultrasound: Past, present and future *Int. J. Hyperthermia* **23** 85–87.

ter Haar G (communication) Therapeutic Ultrasound Group, Physics Department, Institute of Cancer Research, Sutton, UK. September 2013.

Tomlinson J S, Jarnagin W R, DeMatteo R P 2007 Actual 10-year survival after resection of colorectal liver metastases defines cure *J. Clin. Oncol.* **29** 4575– 4580.

Treeby B E, Jaros J, Rendell A P and Cox B T 2012 Modelling nonlinear ultrasound propagation in heterogeneous media with power law absorption using a *k*-space pseudospectral method *J. Acoust. Soc. Am.* **131** 4324–4336.

Treeby B E, Jaros J and Cox B T 2012 *k*-wave manual http://www.k-wave.org/manual/k-wave_user_manual_1.0.1.pdf

Vaezy S, Andrew M, Kaczkowski P, Crum L 2001 *Image-Guided Acoustic Therapy* Annual Review of Biomedical Engineering **3** 375–390.

van der Vorst H A 2003 *Iterative Krylov Methods for Large Linear Systems* (Cambridge: Cambridge University Press).

Visioli A G, Rivens I H, ter Haar G R, Horwich A, Huddart R A, Moskovic E, Padhani A, Glees J 1999 Preliminary results of a phase I dose escalation clinical trial using focused ultrasound in the treatment of localized tumours *Eur. J. Ultrasound* **9** 11–18.

Voogt M J, Trillaud H, Kim Y S, Th M Mali W P, Barkhausen J, Bartels L W, Deckers R, Frulio N, Rhim H, Lim H K, Eckey T, Nieminen H J, Mougenot C, Keserci B, Soini J, Vaara T, Köhler M O, Sokka S, Maurice A, J. van den Bosch A 2012 Volumetric feedback ablation of uterine fibroids using magnetic resonance-guided high intensity focused ultrasound therapy **22** *Eur Radiol* 411–417.

Wan H, VanBaren P, Ebbini E S and Cain C A 1996 Ultrasound surgery: Comparison of strategies using phased array systems *IEEE Trans. Ultrason. Ferroelectr. Freq. Control* **43** 1085–1098.

Wang W, Wang Y X and Tang J 2009 Safety and Efficacy of High Intensity Focused Ultrasound Ablation Therapy for Adenomyosis *Acad. Radiol*. **16** 1416–1423.

Wein W, Brunke S, Khamene A, Callstrom M R and Navab N 2008 Automatic CT-ultrasound registration for diagnostic imaging and image-guided intervention *Med. Image Anal.* **12** 577–585.

Westervelt P J 1963 Parametric acoustic array *J. Acoust. Soc. Am.* **35** 535–537.

White P J, Clement G T, and Hynynen K 2006 Longitudinal and shear mode ultrasound propagation in human skull bone *Ultrasound Med. Biol.***32** 1085–1096.

Wu F, Chen W-Z , Bai J, Zou J-Z, Wang Z-L, Zhu H and Wang Z-B 2001 Pathological changes in human malignant carcinoma treated with high-intensity focused ultrasound *Ultrasound Med. Biol.* **27** 1099–1106.

Wu F, Zhi-Biao W, You-De C, Wen-Zhi C, Jian-Zhong Z, Jin B, Hui Z, Ke-Quan L, Cheng-Bing J, Fang-Lin X, Hai-Bing S and Gen-Wu G 2003 Extracorporeal high

intensity focused ultrasound ablation in the treatment of patients with large hepatocellular carcinoma *Ultrasound Med. Biol.* **29** 1487–1492.

Wu F, Zhi-Biao W, Wen-Zhi C, Hui Z, Jin B, Jian-Zhong Z, Ke-Quan L, Cheng-Bing J, Fang-Lin X, Hai-Bing S 2004 Extracorporeal high intensity focused ultrasound ablation in the treatment of patients with large hepatocellular carcinoma *Ann. Surg. Oncol.* **11** 1061–1069.

Wu T W 2000 *Boundary Element Acoustics: Fundamentals and Computer Codes* (Boston: WIT Press).

Yan B C, Hart J A 2009 Recent developments in liver pathology *Arch. Pathol. Lab. Med.* **133** 1078–1086.

Yu K H, Kardaman A H and Djojodihardjo H 2010 Development and implementation of some BEM variants–A Critical review *Eng. Anal. Bound. Elem.***34** 884–899.

Yuan X, Member S, Borup D, Wiskin J W, Berggren M, Eidens R, and Johnson S A 1997 Formulation and Validation of Berengers PML Absorbing Boundary for the FDTD Simulation of Acoustic Scattering *IEEE Trans. Ultrason. Ferroelectr. Freq. Control* **44** 816–822.

Yuldashev P V and Khokhlova V A 2011 Simulation of three-dimensional nonlinear fields of ultrasound therapeutic arrays *Acoust. Phys.* **57** 337–347.

Yuldashev P V, Shmeleva S M, Ilyin S A, Sapozhnikov O A, Gavrilov L R and Khokhlova V A 2013 The role of acoustic nonlinearity in tissue heating behind a rib cage using a high-intensity focused ultrasound phased array *Phys. Med. Biol.* **58** 2537–2559.

Zel'dovich B Y, Pilipetsky N F, and Shkunov V V 1985 *Principles of Phase Conjugation* (Berlin: Springer-Verlag).

Zienkiewicz OC and Taylor RL 1994 *The Finite Element Method Volume 1 4th ed.* (London: McGraw-Hill) p 121.

Appendix A

Computational Considerations

A.1 Overview

Chapter 3 deals with the description of BEM for scattering problems. Specific boundary conditions at the surface of the scatterer, of relevance to the trans-costal HIFU simulations in this thesis, were described. In this appendix, the computational considerations pertaining to the implementation of BEM as the forward model are explained. Initially, an overview of the Program for Automatic Finite Element Calculations (PAFEC) is provided, including a description of its capabilities and a justification as to why it was chosen to tackle the BEM simulations in this thesis. It will be shown how HIFU simulations on anatomical ribs involving BEM are likely to lead to a system of linear equations which is too large to be solved on a single desktop machine and how conventional Gaussian elimination methods may be inefficient for this task. It will be demonstrated how an iterative solver, the generalised minimal residual (GMRES) method, is a highly efficient and stable scheme for solving large systems of linear equations involving fully-populated and complex matrices, which are not necessarily diagonally dominant, such as those which can be found in scattering problems using BEM. A detailed description of the GMRES method will be provided and it will be explained why it is particularly efficient for parallel computing. The implementation and parallelisation of the PAFEC BEM routines on a dedicated Linux computer cluster will then be described. It will be explained how data from a mesh resulting from an arbitrary smooth surface, along with the acoustic properties of the medium in the exterior domain and of the surface, feed into the PAFEC solver. Pre-processing, solving the scattering problem and post-processing will be explained.

A.2 Program for Automatic Finite Element Calculations

Program for Automatic Finite Element Calculations (PAFEC) is a general purpose commercially available finite element and boundary element analysis tool which has been established for over 25 years and is provided by PACSYS Ltd., Nottingham, UK. It addresses a number of specialist areas including structural vibration, acoustics, heat transfer analysis, lubrication, linear and nonlinear piezoelectric analysis. The section of the software dealing with acoustic and structure interaction problems using finite and boundary elements section was developed by Macey (1987) using FORTRAN. PAFEC has been extensively used to model fluid-structure interaction problems, particularly in loudspeaker design (Geaves 1995, Dodd and Oclee-Brown 2007). The modelling of physiotherapy transducers has also been carried out (Hughes, 2001). Additionally both scattering problems (Chinnery *et al* 1997) and diffraction problems (Macey, 1994) have been tackled. PAFEC has also been used in the defence sector to tackle the numerical modelling of active sonar arrays (Morgan, 2004). PAFEC has the capability to deal with the coupling between the elastic structure and the acoustic wave in a fluid by using a combined finite element/boundary element method.

In the context of the calculations in this thesis, boundary element methods based on either the Burton-Miller formulation with a purely real wave number, or the surface Helmholtz formulation with a complex wave number were required on C^0 continuous isoparametric eight node quadrilateral elements (see chapter 3). In its current commercially-available form, PAFEC does not feature a Burton-Miller formulation for such elements and only allows for the definition of a purely real wavenumber to characterise the propagation medium in the exterior domain. Nor does it have a distributed computing solver for boundary element problems. Nevertheless, PACSYS Ltd. were keen to develop their software to tackle large problems, such as those encountered in trans-costal HIFU and were interested in providing input to the work in this thesis. Given that the code in PAFEC is well documented, traceable, and extensively validated, this made PAFEC a suitable choice as a BEM solver. A licensing agreement was therefore struck between University College London, the National Physical Laboratory and PACSYS Ltd. to make the necessary modifications to the source code to provide stand-alone executable files which would enable the calculation of the coefficients of the boundary element matrices $[H]$ and $[G]$ (see equation 3.41) for the surface boundary conditions and formulations described earlier.

A.3 The GMRES method

A.3.1 Rationale for using an iterative solver

The matrices generated by the discretisation of the Kirchhoff-Helmholtz integral equation are generally complex, fully-populated and non-symmetric (see chapter 3). Hence, for large problem sizes, storing all the elements of the [H] and [G] matrices (see equation 3.41) simultaneously may potentially become problematic due to the limited availability of RAM on a computing platform. Consider a cylindrical scatterer of 1 cm diameter and of 22 cm height, with hemispherical end-caps. These dimensions are representative of those of a human adult rib (Mohr *et al* 2007). When meshing the surface of this cylinder with eight node quadrilateral patches, ensuring at least three elements per wavelength at 1 MHz (the fundamental frequency of excitation of the HIFU array considered in this thesis), this results in 168,655 degrees of freedom (see figure A.1).

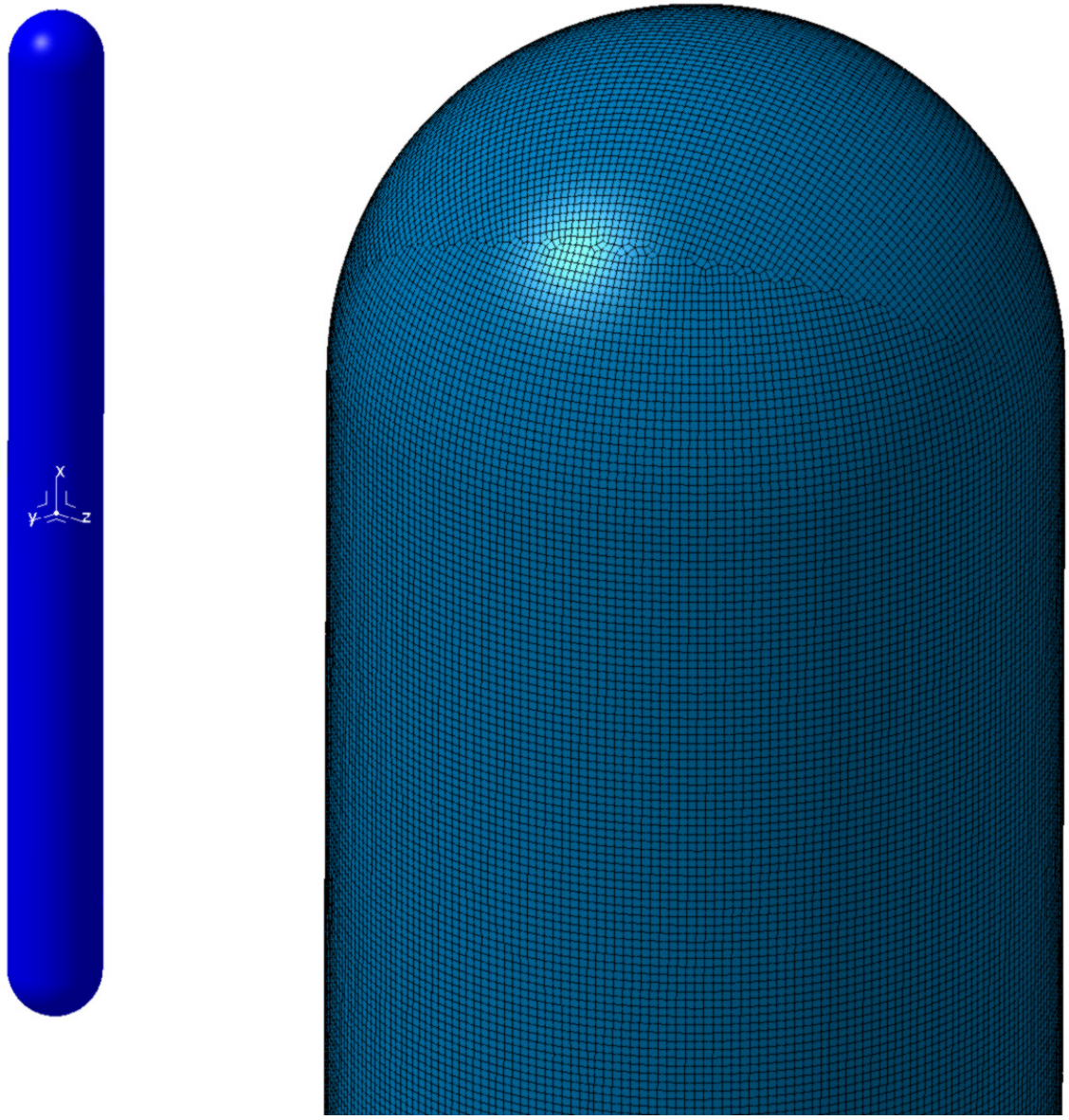

Figure A.1 Cylindrical scatterer with hemispherical end-caps. 1 cm radius, total height 22 cm (including an additional 0.5 cm radius for the hemispherical end-caps at either end). Meshed to include at least 3 elements per wavelength at 1 MHz.

The mesh in figure A.1 leads to RAM requirements of 400 GB just to store the coefficients of the $[H]$ matrix in equation (3.41). Clearly, using conventional Gaussian elimination methods (Gentle 1998, p87) to invert the matrices generated in this problem is inefficient. Also, using a single desktop computer to solve a scattering problem involving the above mesh is likely to be inadequate: a distributed computing approach implemented on a dedicated cluster is preferable. In general, solving a BEM system of equations requires $O(M^3)$ operations, where M is the number of unknowns, when a

direct solver such as the Gauss elimination method is used. Iterative solvers have been shown to be particularly beneficial for tackling BEM systems of equations (Ochmann *et al* 2003). One such iterative solver is the GMRES method, which was proposed by Saad and Schultz (1986). This iterative solver performs matrix-vector operations at each iteration which results in a reduction of operation counts from $O(M^3)$ to $O(M^2)$. An overview of the GMRES method is now presented.

The GMRES method is based on the minimisation of a residual vector over a Krylov subspace. The concept of a Krylov subspace stems from the observation that in any sequence of iterates, there exists a smallest set of consecutive iterates which are linearly dependent. The coefficients of a vanishing combination are the coefficients of a divisor to the characteristic polynomial. A detailed discussion on Krylov subspaces is provided by Householder (1975). Iterative Krylov methods for large linear systems of equations are reviewed in depth by van der Vorst (2003).

A.3.2 Arnoldi iteration method

Before reviewing the GMRES method, it is useful to consider the Arnoldi iteration method (Arnoldi, 1951) which forms the basis of the GMRES algorithm.

Consider a system of linear equations of the form:

$$\boldsymbol{A}\boldsymbol{x} = \boldsymbol{b} \tag{A.1}$$

where $\boldsymbol{A}$ is an $m \times m$ matrix and $\boldsymbol{x}$ and $\boldsymbol{b}$ are vectors of dimension $m \times 1$. In this appendix, matrix quantities will by depicted in upper case bold letters and vectors in lower case bold letters. In the context of matrix and vector notation, brackets will be generally be dispensed with.

Consider the Krylov sequence defined as follows.

$$\boldsymbol{K}_n = \{\boldsymbol{b} \quad \boldsymbol{A}\boldsymbol{b} \quad \boldsymbol{A}^2\boldsymbol{b} \quad \cdots \quad \boldsymbol{A}^{n-1}\boldsymbol{b}\} \tag{A.2}$$

The n^{th} order Krylov subspace is then defined as:

$$\mathrm{K}_n = \mathrm{span}\{\boldsymbol{b} \quad \boldsymbol{Ab} \quad \boldsymbol{A}^2\boldsymbol{b} \quad \cdots \quad \boldsymbol{A}^{n-1}\boldsymbol{b}\} \tag{A.3}$$

where span denotes the linear span, which corresponds to the intersection of all subspaces containing the set of vectors defined by the Krylov sequence.

The Arnoldi iteration method is applicable to solving both linear systems of equations and eigenvalue problems. Consider the similarity transformation of the following form:

$$\boldsymbol{A} = \boldsymbol{QHQ}^* \tag{A.4}$$

where $\boldsymbol{H}$ is an upper Hessenberg matrix and $\boldsymbol{Q}$ is a unitary matrix, so that

$$\boldsymbol{QQ}^* = \boldsymbol{Q}^*\boldsymbol{Q} = \boldsymbol{I} \tag{A.5}$$

where * denotes the conjugate transpose and $\boldsymbol{I}$ is the identity matrix. All matrices in equation (A.4) are of dimension $m \times m$.

By virtue of the properties of unitary matrices, equation (A.4) may be rewritten as follows:

$$\boldsymbol{AQ} = \boldsymbol{QH} \tag{A.6}$$

If we choose $n < m$, equation (A.6) may be written as:

$$\boldsymbol{A}[\boldsymbol{q}_1 \quad \boldsymbol{q}_2 \quad \cdots \quad \boldsymbol{q}_n \quad \boldsymbol{q}_{n+1} \quad \cdots \quad \boldsymbol{q}_m] = [\boldsymbol{q}_1 \quad \boldsymbol{q}_2 \quad \cdots \quad \boldsymbol{q}_n \quad \boldsymbol{q}_{n+1} \quad \cdots \quad \boldsymbol{q}_m]\boldsymbol{H} \tag{A.7}$$

where $\boldsymbol{q}_n$ is the n^{th} column of $\boldsymbol{Q}$ and the upper Hessenberg matrix is of the form:

$$\boldsymbol{H} = \begin{bmatrix} h_{11} & h_{12} & & \cdots & & h_{1,n} & \cdots & & h_{1,m} \\ h_{21} & h_{22} & & \cdots & & h_{2,n} & \cdots & & h_{2,m} \\ 0 & h_{32} & h_{33} & & & h_{3,n} & \cdots & & h_{3,m} \\ & 0 & h_{43} & \ddots & & & & & \\ & & 0 & \ddots & h_{n-1,n-1} & \vdots & & & \vdots \\ \vdots & & & \ddots & h_{n,n-1} & h_{n,n} & & & \\ & & & & 0 & h_{n+1,n} & & & \\ & & & & & 0 & \ddots & \ddots & \\ 0 & & & \cdots & & & 0 & h_{m,m-1} & h_{m,m} \end{bmatrix} \tag{A.8}$$

Consider only part of the system of equations defined in equation (A.7) so that

$$\boldsymbol{Q}_n = [\boldsymbol{q}_1 \quad \boldsymbol{q}_2 \quad \cdots \quad \boldsymbol{q}_n] \tag{A.9}$$

and

$$\boldsymbol{Q}_{n+1} = [\boldsymbol{q}_1 \quad \boldsymbol{q}_2 \quad \cdots \quad \boldsymbol{q}_n \quad \boldsymbol{q}_{n+1}] \tag{A.10}$$

The corresponding upper Hessenberg matrix is then:

$$\boldsymbol{H}_n = \begin{bmatrix} h_{11} & h_{12} & & \cdots & & h_{1,n} \\ h_{21} & h_{22} & & \cdots & & h_{2,n} \\ 0 & h_{32} & h_{33} & & & h_{3,n} \\ & 0 & h_{43} & \ddots & & \\ & & 0 & \ddots & h_{n-1,n-1} & \vdots \\ \vdots & & & \ddots & h_{n,n-1} & h_{n,n} \\ & & & & 0 & h_{n+1,n} \end{bmatrix} \tag{A.11}$$

We have:

$$\boldsymbol{A}\boldsymbol{Q}_n = \boldsymbol{Q}_{n+1}\boldsymbol{H}_n \tag{A.12}$$

$\boldsymbol{A}$ is of dimension $m \times m$, $\boldsymbol{Q}_n$ is $m \times n$, $\boldsymbol{Q}_{n+1}$ is $m \times (n + 1)$ and $\boldsymbol{H}_n$ is $(n + 1) \times n$.

Consider the n^{th} column on both sides of equation (A.12).

$$\boldsymbol{A}\boldsymbol{q}_n = h_{1,n}\boldsymbol{q}_1 + h_{2,n}\boldsymbol{q}_2 + \cdots + h_{n,n}\boldsymbol{q}_n + h_{n+1,n}\boldsymbol{q}_{n+1} \tag{A.13}$$

By re-writing equation (A.13), a recursive relationship for the vector $\boldsymbol{q}_{n+1}$ may be obtained as follows:

$$\boldsymbol{q}_{n+1} = \frac{A\boldsymbol{q}_n - \sum_{i=1}^{n} h_{i,n}\boldsymbol{q}_i}{h_{n+1,n}} \tag{A.14}$$

This recursive evaluation of the columns of the unitary matrix $\boldsymbol{Q}$ is known as the Arnoldi iteration. The first step of the Arnoldi iteration is as follows.

$$\boldsymbol{q}_2 = \frac{A\boldsymbol{q}_1 - h_{11}\boldsymbol{q}_1}{h_{21}} \tag{A.15}$$

where $\boldsymbol{q}_1$ is an arbitrary normalised vector. In order to have orthogonality of the columns of $\boldsymbol{Q}$, we require:

$$\boldsymbol{q}_1^* \boldsymbol{q}_2 = 0 \tag{A.16}$$

By pre-multiplying equation (A.15) by the conjugate transpose of $\boldsymbol{q}_1$, and noting that $\boldsymbol{q}_1$ is normalised, we have:

$$h_{11} = \boldsymbol{q}_1^* \boldsymbol{A}\boldsymbol{q}_1 \tag{A.17}$$

h_{21} is calculated by noting that $\boldsymbol{q}_2$ is also normalised, so that:

$$h_{21} = \|A\boldsymbol{q}_1 - h_{11}\boldsymbol{q}_1\| \tag{A.18}$$

The most expensive operation in the Arnoldi iteration algorithm is the evaluation of the matrix-vector product $\boldsymbol{A}\boldsymbol{q}_n$. Furthermore, it is only this product which is of interest in the algorithm and it is therefore unnecessary to store the elements of the matrix $\boldsymbol{A}$.

An alternative derivation of the Arnoldi iteration method may be carried out by considering the Krylov matrix:

$$\boldsymbol{K}_n = [\boldsymbol{b} \quad \boldsymbol{A}\boldsymbol{b} \quad \boldsymbol{A}^2\boldsymbol{b} \quad \cdots \quad \boldsymbol{A}^{n-1}\boldsymbol{b}] \tag{A.19}$$

By pre-multiplying both sides of equation (A.19) by $\boldsymbol{A}$, we have:

$$\boldsymbol{AK}_n = [\boldsymbol{Ab} \quad \boldsymbol{A}^2\boldsymbol{b} \quad \boldsymbol{A}^3\boldsymbol{b} \quad \cdots \quad \boldsymbol{A}^n\boldsymbol{b}] \tag{A.20}$$

The last $n-1$ columns of $\boldsymbol{K}_n$ correspond to the first $n-1$ columns of $\boldsymbol{AK}_n$. Equation (A.20) may therefore be rewritten as follows:

$$\boldsymbol{AK}_n = \boldsymbol{K}_n[\boldsymbol{e}_2, \boldsymbol{e}_3, \cdots, \boldsymbol{e}_n, -\boldsymbol{c}] \tag{A.21}$$

where $\boldsymbol{e}_i$ is a unit vector along the i^{th} direction. Provided that the Krylov matrix is invertible, $\boldsymbol{c}$ is given by:

$$\boldsymbol{c} = -\boldsymbol{K}_n^{-1}\boldsymbol{A}^n\boldsymbol{b} \tag{A.22}$$

Equation (A.21) will be re-written as follows:

$$\boldsymbol{AK}_n = \boldsymbol{K}_n\boldsymbol{C}_n \tag{A.23}$$

where $\boldsymbol{C}_n$ is given by:

$$\boldsymbol{C}_n = [\boldsymbol{e}_2, \boldsymbol{e}_3, \cdots, \boldsymbol{e}_n, -\boldsymbol{c}] \tag{A.24}$$

Consider a QR decomposition of the Krylov matrix as follows:

$$\boldsymbol{K}_n = \boldsymbol{Q}_n\boldsymbol{R}_n \tag{A.25}$$

where $\boldsymbol{Q}_n$ is an orthogonal matrix and $\boldsymbol{R}_n$ is an upper-triangular matrix. Both matrices are square and of the same dimension as $\boldsymbol{K}_n$. By pre-multiplying equation (A.23) by the inverse of the Krylov matrix, and by noting that $\boldsymbol{Q}_n$ is orthogonal, we have:

$$\boldsymbol{R}_n^{-1}\boldsymbol{Q}_n^*\boldsymbol{A}\boldsymbol{Q}_n\boldsymbol{R}_n = \boldsymbol{C}_n \tag{A.26}$$

or

$$\boldsymbol{Q}_n^*\boldsymbol{A}\boldsymbol{Q}_n = \boldsymbol{R}_n\boldsymbol{C}_n\boldsymbol{R}_n^{-1} \tag{A.27}$$

The upper Hessenberg matrix $\boldsymbol{H_n}$ is therefore:

$$\boldsymbol{H_n = R_n C_n R_n^{-1}} \tag{A.28}$$

Unless $\boldsymbol{A}$ is a Hermitian matrix, a disadvantage of Arnoldi's method is that it is both computationally expensive and may suffer from convergence issues (Saad and Schultz 1986). In the above form particularly, the Arnoldi iteration method generates a Krylov matrix that is often ill-conditioned, which may lead to difficulties in solving the system of linear equations in equation (A.25). Additionally, the inverse of $\boldsymbol{R}_n$ is also required, which may increase computational times.

A.3.3 The GMRES algorithm

To overcome some of the limitations of Arnoldi's iteration method, the GMRES algorithm, was proposed by Saad and Schultz (1986). The GMRES method has the ability to deal with arbitrary (nonsingular) square matrices which are not required to be diagonally dominant. The GMRES algorithm is a generalisation of the MINRES algorithm (Paige and Saunders, 1975) for solving nonsymmetric linear systems, and of Arnoldi's method. The basis for the GMRES scheme is the Arnoldi iteration algorithm, where a least squares problem is solved at each step of the iteration. The exact solution to the system of linear equations is approximated by a vector $\tilde{\boldsymbol{x}}_n \in \mathrm{K}_n$ so that the l_2 norm of the residual $\|\boldsymbol{r}_n\| = \|\boldsymbol{A}\tilde{\boldsymbol{x}}_n - \boldsymbol{b}\|$ is minimised. K_n is the n^{th} order Krylov subspace. Assume that $\tilde{\boldsymbol{x}}_n$ is related to a column vector $\boldsymbol{c}$ of length n via the Krylov matrix defined in equation (A.19):

$$\tilde{\boldsymbol{x}}_n = \boldsymbol{K}_n \boldsymbol{c} \tag{A.29}$$

The l_2 norm of the residual which is required to be minimised is:

$$\|\boldsymbol{r}_n\| = \|\boldsymbol{A}\boldsymbol{K}_n\boldsymbol{c} - \boldsymbol{b}\| \tag{A.30}$$

In Section A.2.1, it was established that:

$$\boldsymbol{H}_n = \boldsymbol{Q}_n^* \boldsymbol{A} \boldsymbol{Q}_n \tag{A.31}$$

This may be interpreted as an orthogonal projection of $\boldsymbol{A}$ onto $\boldsymbol{K}_n$, with the columns of $\boldsymbol{Q}_n$ as basis and we may write the approximate solution as:

$$\tilde{\boldsymbol{x}}_n = \boldsymbol{Q}_n \boldsymbol{y} \tag{A.32}$$

where $\boldsymbol{y}$ is an appropriate vector of length n. The l_2 norm of the residual is then:

$$\|\boldsymbol{r}_n\| = \|\boldsymbol{A}\boldsymbol{Q}_n \boldsymbol{y} - \boldsymbol{b}\| \tag{A.33}$$

Consider equation (A.12) in the Arnoldi iteration:

$$\boldsymbol{A}\boldsymbol{Q}_n = \boldsymbol{Q}_{n+1}\boldsymbol{H}_n \tag{A.34}$$

The l_2 norm of the residual may now be rewritten as:

$$\|\boldsymbol{r}_n\| = \|\boldsymbol{Q}_{n+1}\boldsymbol{H}_n \boldsymbol{y} - \boldsymbol{b}\| \tag{A.35}$$

Since pre-multiplication by a unitary matrix does not change the l_2 norm, we have:

$$\|\boldsymbol{r}_n\| = \|\boldsymbol{Q}_{\boldsymbol{n+1}}^{*}\boldsymbol{Q}_{n+1}\boldsymbol{H}_n \boldsymbol{y} - \boldsymbol{Q}_{\boldsymbol{n+1}}^{*}\boldsymbol{b}\| = \|\boldsymbol{H}_n \boldsymbol{y} - \boldsymbol{Q}_{\boldsymbol{n+1}}^{*}\boldsymbol{b}\| \tag{A.36}$$

Consider the matrix-vector product $\boldsymbol{Q}_{\boldsymbol{n+1}}^{*}\boldsymbol{b}$**:**

$$\boldsymbol{Q}_{n+1}^{*}\boldsymbol{b} = \begin{bmatrix} \boldsymbol{q}_{\boldsymbol{1}}^{*}\boldsymbol{b} \\ \boldsymbol{q}_{\boldsymbol{2}}^{*}\boldsymbol{b} \\ \vdots \\ \boldsymbol{q}_{\boldsymbol{n+1}}^{*}\boldsymbol{b} \end{bmatrix} \tag{A.37}$$

Since the columns of $\boldsymbol{Q}_n$ form an orthonormal basis to the Krylov subspace K_n, we have

$$\boldsymbol{q}_{\boldsymbol{i}}^{*}\boldsymbol{b} = \|\boldsymbol{b}\|, \text{ for } i = 1 \tag{A.38}$$

and

$$\boldsymbol{q}_{\boldsymbol{i}}^{*}\boldsymbol{b} = 0 \text{ for } i > 1 \tag{A.39}$$

Hence,

$$\boldsymbol{Q}_{\boldsymbol{n+1}}^{*}\boldsymbol{b} = \|\boldsymbol{b}\|\boldsymbol{e}_{\boldsymbol{1}} \tag{A.40}$$

We therefore wish to minimise the l_2 norm of the residual:

$$\|\boldsymbol{r}_n\| = \|\boldsymbol{H}_n\boldsymbol{y} - \|\boldsymbol{b}\|\boldsymbol{e_1}\| \tag{A.41}$$

where

$$\tilde{\boldsymbol{x}}_n = \boldsymbol{Q}_n\boldsymbol{y} \tag{A.42}$$

The minimisation may be carried out by using a QR factorisation process (Johnson *et al* 1989, p463). By cumulative multiplication of $\boldsymbol{H}_n$, by Givens rotation matrices of the form (Saad and Schultz 1986):

$$\boldsymbol{F}_j = \begin{bmatrix} 1 & 0 & & \cdots & & & 0 \\ 0 & 1 & & & & & 0 \\ & & \ddots & & & & \\ \vdots & & & c_j & -s_j & & \vdots \\ & & & s_j & c_j & & \\ & & & & & 1 & \\ & & & & & & \ddots \\ 0 & 0 & \cdots & & & & 1 \end{bmatrix} \tag{A.43}$$

$\boldsymbol{F}_j$ is of dimension (n +1) × (n +1) for n steps of the GMRES iterations and the scalars c_j and s_j are given by:

$$c_j = \frac{h_{jj}}{\sqrt{h_{jj}^2 + h_{j+1,j}^2}} \tag{A.44}$$

$$s_j = \frac{h_{j+1,j}}{\sqrt{h_{jj}^2 + h_{j+1,j}^2}} \tag{A.45}$$

Since $\prod_{j=n}^{1} \boldsymbol{F}_j$ is a unitary matrix, it does not modify the l_2 norm:

$$\|\boldsymbol{r}_n\| = \left\|\prod_{j=n}^{1} \boldsymbol{F}_j \left(\boldsymbol{H}_n\boldsymbol{y} - \|\boldsymbol{b}\|\boldsymbol{e}_1\right)\right\| \tag{A.46}$$

or

$$\|\boldsymbol{r}_n\| = \|\boldsymbol{X}_n\boldsymbol{y} - \boldsymbol{g_n}\| \tag{A.47}$$

where

$$\boldsymbol{X}_n = \left(\prod_{j=n}^{1} \boldsymbol{F_j}\right)\boldsymbol{H}_n \tag{A.48}$$

and

$$\boldsymbol{g}_n = \left(\prod_{j=n}^{1} \boldsymbol{F_j}\right)\|\boldsymbol{b}\|\boldsymbol{e_1} \tag{A.49}$$

The successive multiplication of the upper Hessenberg matrix by the Givens rotation matrices produces $\boldsymbol{X}_n$, which is an upper triangular matrix of dimension $(n + 1) \times n$ whose last row comprises of zeros (reference to linear algebra textbook). $\boldsymbol{g}_n$ is effectively the transformed right hand side. The minimisation of $\|\boldsymbol{r}_n\|$ may therefore be achieved by solving the upper triangular linear system of equations which results from removing the last row of zeros in $\boldsymbol{X}_n$. This provides the vector $\boldsymbol{y}$. $\tilde{\boldsymbol{x}}_{\boldsymbol{n}}$ may then be obtained by pre-multiplying $\boldsymbol{y}$ by $\boldsymbol{Q}_n$.

Let $\tilde{\boldsymbol{x}}_1$ be an arbitrary initial vector. Each iteration of the GMRES algorithm may therefore by summarised as follows:

(i) Carry out the n^{th} step of the Arnoldi iteration by computing new entries for H_n and Q_n.

For $n = 1, 2, 3, \ldots$

$q_n = \frac{\tilde{\boldsymbol{x}}_n}{\|\tilde{\boldsymbol{x}}_n\|}$

$\boldsymbol{v} = \boldsymbol{A}\boldsymbol{q}_n$

For $j = 1$ to n

$h_{jn} = \boldsymbol{q}_j^* \boldsymbol{v}$

$\boldsymbol{v} = \boldsymbol{v} - h_{jn}\boldsymbol{q}_j$

End

$h_{n+1,n} = \|\boldsymbol{v}\|$

$\boldsymbol{q}_{n+1} = \frac{\boldsymbol{v}}{h_{n+1,n}}$

End

(ii) Form the Givens rotation matrices F_j and their cumulative product with H_n, compute g_n and find y which minimises the l2 norm $\|r_n\| = \|X_n y - g_n\|$

$\tilde{x}_{n+1} = Q_n y$

The matrix inversion required for the minimisation of the residual norm is not computationally expensive, as the dimensions of the matrices and vectors correspond to the number of GMRES iterations required, which is typically much smaller than the dimension of $\boldsymbol{A}$. As with the Arnoldi iteration method, at each iteration, the largest operation involves the matrix-vector product $\boldsymbol{A}\boldsymbol{q}_n$. It is straightforward to parallelise this operation over a multi-core computer cluster.

A.3.4 Convergence of the GMRES algorithm

The GMRES algorithm will converge in at most m steps if $\boldsymbol{A}$ is of dimension $m \times m$. Furthermore, the convergence of the algorithm is monotonic (Saad and Schultz 1986). In Section A.2.1, we have seen that the trans-costal HIFU simulations are likely to generate matrices where m is of the order of 10^5. It may therefore be unrealistic to opt for full convergence of the GMRES algorithm, and a compromise in terms of accuracy *vs.* speed of computation may have to be sought. The number of iterations for simulations involving human ribs will be determined with the help of numerical experiments on scattering problems for which there are known analytical solutions. The dimensions of the scatterers involved and the frequency of excitation will be representative of the trans-costal problems under investigation. This work is described in chapter 4.

A.4 Parallelisation of PAFEC BEM routines on a dedicated Linux computer cluster

A.4.1 File format

In Section A.3, we have seen that the GMRES provides an efficient way of solving large systems of linear equations involving fully-populated and complex matrices, which are not necessarily diagonally dominant. This method is therefore particularly well-suited to large-scale BEM problems (Ochmann *et* al 2003, Shen and Liu 2007). In

this section, we will describe how the BEM routines were implemented and parallelised on a dedicated computer cluster. The main executable file provided by PACSYS Ltd. is entitled *SCATTER.exe*. Running this executable file requires the following input files.

jobname.SCA: this file contains information regarding the properties of the medium and the scatterer(s), the coordinates of the nodal positions on the mesh and the mesh topology. Assume that there are M nodes in the mesh and N_p BE patches. The layout is as follows:

Line 1: comment line
Line 2: number of first node in mesh, number of last node in mesh, total number of BE patches, number of iterations in GMRES method
Line 3: real and imaginary parts of density of medium in exterior domain in kg m^{-3}, real and imaginary parts of speed of sound in exterior domain in m s^{-1}.
Line 4: frequency of excitation in Hz, zero entry, coupling coefficient α_c in Burton-Miller formulation (see Section 3.4). For a surface Helmholtz formulation, the entry for α_c must be blank.
Lines 5 to M + 5 – 1: x, y and z values of nodal positions on the surface of the scatterer(s) in global Cartesian coordinates in m.
Lines M + 5 to $M + N_p$ + 4: patch reference number, number of nodes per patch (i.e. 8), sequence of nodes describing patch topology (as described in figure 3.3).

If a non-rigid boundary condition on the surface of the scatterer is required, in the form of a locally reacting surface, the file must be appended with the following lines

ADMITTANCE
TYPE=1
Real part of admittance and imaginary part of admittance (in m^2 s kg^{-1}).

jobname.INC file: this file contains the incident pressure field at nodal locations on the surface of the scatterer. The file format is as follows.

Column 1: node reference number
Column 2: real part of spatial component of incident acoustic pressure (i.e. in absence of the scatterer) at the node defined in column 1 (in Pa).

Column 3: imaginary part of spatial component of incident acoustic pressure (i.e. in absence of the scatterer) at the node defined in column 1 (in Pa).

jobname.IWG file: this file contains the normal derivative of the incident pressure field at nodal locations at the centroid of each BE patch on the surface of the scatterer. The file format is the same as for *jobname.INC*, except that the first column now refers to the BE patch number. This file is only required if a Burton-Miller formulation is invoked through a non-blank entry for the coupling coefficient α_c in the 4th line of *jobname.SCA*.

To obtain the normal derivative of the acoustic pressure at the centroids of the BE patches, we require the coordinates of the centroids together with the coordinates of the unit normal vectors (see equation 3.23). It should be noted that PAFEC requires the unit normal vectors to be inward pointing (i.e. from the surface towards the inside of the volume inside the scatterer rather than towards the exterior domain). The executable file *CENTREINFO.exe* can extract this information from the mesh topology and returns data in the following form.

Columns 1 to 3: *x*, *y* and *z* values for the coordinates of the BE patch centroids.
Columns 4 to 6: *x*, *y* and *z* values of the unit vectors normal to the surface at the patch centroids. The orientation of the vector is defined in chapter 3.

jobname.PR0 file: this file contains an initial guess for the acoustic pressures on the surface of the scatterer, which initialises the GMRES algorithm. The format is the same as for *jobname.INC*. Throughout this thesis, the content of this file was copied from *jobname.INC*.

A.4.2 Running of main executable file

SCATTER.exe must be run on a master core. Three executable communication files are invoked when running *SCATTER.exe*.

- *ANGCALC.com*: this file launches the calculation of the solid angles required for Gaussian quadrature. This is only executed once, as it is specific to the mesh topology.

- *BE-MATMUL.com*: this file carries out the multiplication of the matrix resulting from the discretisation of the integral term in equation (3.27), involving the first derivative of the Green's function, of the by the trial vector of acoustic pressures at the beginning of each GMRES iteration.
- *GRAD-MATMUL.com*: this file carries out the multiplication of the matrix resulting from the discretisation of the hypersingular integral term in equation (3.27), involving the second derivative of the Green's function, by the trial vector of acoustic pressures at the beginning of each GMRES iteration.

The solid angles from the outputs of each sub-job are then assembled into a file. After completion of *BE-MATMUL.com* and *GRAD-MATMUL.com* the matrix-vector product $\boldsymbol{Aq}_n$ described in Section A.2 is assembled from the output of the sub-jobs and a GMRES iteration is carried out on the master core from which the main programme *SCATTER.exe* has been lauched. At the end of each GMRES iteration, the acoustic pressure at nodal locations on the surface of the scatterer(s) is updated.

A.4.3 Pre-processing

Matlab™ script was used to generate the files *jobname.INC*, *jobname.PR0 and jobname.IWG*. A combination of Matlab™ script and shell script was used to generate the appropriate *jobname.SCA* file, based on the required input quantities. In the context of this thesis, the incident field in *jobname.INC* consisted of one of the three fields below.

- A unit amplitude plane with a spatial component of the acoustic pressure of the form $e^{-\mathrm{i}\vec{k}\cdot\vec{r}}$, where $\vec{k}$ is the propagation vector (Kinsler *et al* 1982, p108) so that $\vec{k} = \begin{pmatrix} k_x \\ k_y \\ k_z \end{pmatrix}$ and $\|\vec{k}\| = \frac{\omega}{c}$.
- A unit source strength point source with a spatial component of the acoustic pressure of the form $\frac{e^{-\mathrm{i}k\|\vec{r}-\vec{r}_q\|}}{\|\vec{r}-\vec{r}_q\|}$, where $\vec{r}_q$ defines the location of the point source.
- A multi-element spherical-section array modelled as is described in Section 4.4.2.

ANGCALC.com, *BE-MATMUL.com* and *GRAD-MATMUL.com* contain Linux Shell Script instructions which parallelise the operations over a user-defined number of cores on the cluster. Corresponding executable files *ANGCALC.exe*, *BE-MATMUL.exe* and *GRAD-MATMUL.exe* are then launched on each node. Specific files must be generated in advance which specify the nodal locations at which the solid angle will be calculated (in the case of *ANGCALC.exe*) and the columns of the matrices which will multiply the rows of the trial vector (in the case of *BE-MATMUL.exe* and *GRAD-MATMUL.exe*). The syntax is of the form:

$$./BE\text{-}MATMUL.exe\ jobname\ N_1\ N_2$$

which indicates that the matrix-vector multiplication will be carried out for columns N_1 to N_2 of the matrix. The same syntax applies to *GRAD-MATMUL.exe*. For *ANGCALC.exe*, the syntax is also the same and N_1 and N_2 define the range of nodes over which the solid angle is evaluated. N_{job} individual Linux Shell script files are automatically generated at the pre-processing stage via Matlab™ script, which contain commands to execute *ANGCALC.exe*, *BE-MATMUL.exe* and *GRAD-MATMUL.exe* for the required values of N_1 and N_2.

A combination of Matlab™ script and Linux Shell script was used to append templates of the *.com* files with the required job name information together with the number of cores over which the job was to be parallelised.

A.4.4 Post-processing

The output files to *SCATTER.exe* are *jobname.PR1* and *jobname.LOG*. *jobname.PR1* contains the vector of acoustic pressures on the surface of the scatterer(s) estimated after the required amount of GMRES iterations. The file format is the same as *jobname.PR0* and *jobname.INC*. *jobname. LOG* contains information about the residual norm at each GMRES iteration.

Acoustic field pressures in the exterior domain may be calculated from knowledge of the acoustic pressures on the surface of the scatterer(s) using equation (3.42). This is done using the executable file *PRFIELD.exe*, which requires the following input files.

- *jobname.SCA*
- *jobname.PR1*
- *jobname.FPT*

The format of *jobname.FPT* is as follows.

Line 1: number N_f of field locations
Lines 2 to N_f + 1: reference number of field location followed by x, y and z coordinates in the global Cartesian axis set (in m).
Lines N_f + 2 to 2N_f + 1: real and imaginary parts of spatial components of incident acoustic pressure at above field locations (in Pa).

PRFIELD.exe generates the output file *jobname.PR2*, which has the same format as *jobname.PR2*.

If acoustic pressures are required at a large number of field locations, it is straightforward to automate the generation of the required *jobname.FPT* files and launch *PRFIELD.exe* over a number of cores. The *jobname.PR2* files thus generated may then be concatenated so that all the required acoustic field information in the exterior domain is contained in one file.

A.5 Summary

The discretisation of the Kirchhoff-Helmholtz equation gives rise to a system of linear equations involving fully-populated complex non-symmetric matrices. When meshing the surface of a scatterer with dimensions of the order of those of human ribs, at three elements per wavelength at an excitation frequency of 1 MHz, problems containing of the order of 10^5 degrees of freedom are likely to be generated. It was established that the GMRES iterative algorithm is particularly well-suited to dealing with the nature of the matrices. The fact that the most computationally intensive step of the algorithm involves a matrix-vector product consequently makes it suitable for distributed computing. Hence, the GMRES method was chosen as part of this thesis and was implemented on a distributed computing platform to solve the systems of equations generated by the boundary element formulations.

Boundary element routines from the PAFEC software adapted for eight node isoparametric quadrilateral patches and made available as stand-alone executable files were used to generate the boundary element matrices. Both Burton-Miller and surface Helmholtz formulations were considered, depending on whether or not attenuation is accounted for in the exterior domain. Using a combination of Matlab™ script and Linux Shell script, an interface was created to conduct the calculations on a dedicated computer cluster where, at each iteration of the GMRES algorithm, the matrix-vector product of the $[H]$ and $[G]$ matrices by a trial vector (see equation 3.41) was distributed over a user-defined number of cores. A disadvantage of this approach is that the coefficients of $[H]$ and $[G]$ are re-calculated at the beginning of every iteration, as RAM limitations prohibit these matrices from being stored.

If $[H]$ and $[G]$ are $m \times m$, it can be shown that the GMRES algorithm will converge after m iterations. Since m is likely to be of the order of 10^5, a compromise may have to be sought between computational speed and required accuracy of the solution. This will be determined in chapter 4 via numerical experiments.

Appendix B

Test of the DORT Method on Two Spherical Scatterers

B.1 Overview

This appendix describes the implementation of the DORT method on two spherical scatterers. A 256 element spherical section HIFU array was used, with the same specifications as described in Chapter 4 in figure 4.33. This appendix serves two purposes. The first is to describe how the DORT method may be implemented from a knowledge of the scattered component of the acoustic field resulting from BEM calculations. The second is to validate this implementation against results published for the case of two well-resolved point-like spherical scatterers (Prada *et al* 1996).

The geometric focus of the array was located at the global origin. The spherical scatterers were both 5 mm in diameter with their centres located at (0, −2.5, −7.5) cm and (0, 2.5, −7.5) cm. The external medium featured acoustic properties representative of those of human liver described in 4.3.1. The spheres featured a locally reacting surface impedance condition. One sphere was assumed to have a surface impedance representative of that of rib bone impedance (see section 4.3.2). The surface impedance of the second sphere was set to twice that of the first. The location of the spheres with respect to the array is shown in figure B.1.

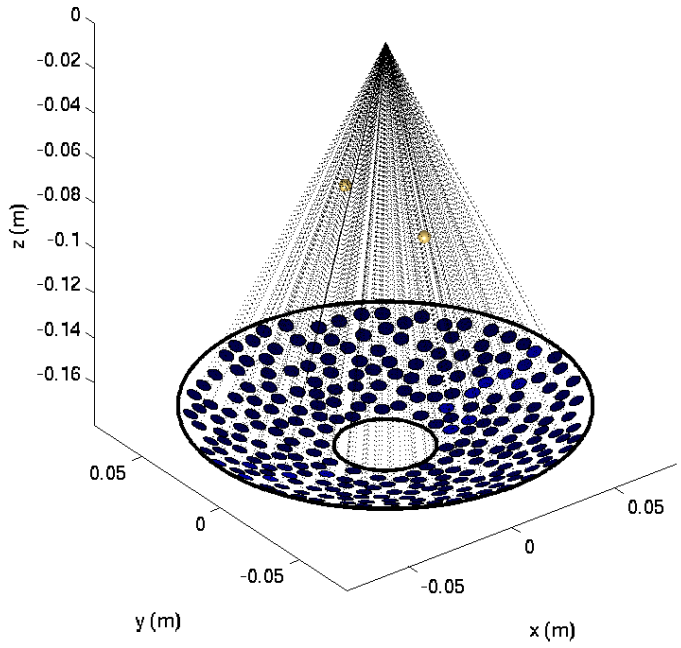

Figure B.1 Position of spherical scatterers with respect to focused array.

B.2 Spherical focusing

The acoustic pressure magnitude on the surface of the spheres is shown in figure B.2. The acoustic pressure magnitude in the *y*-*z* plane in the vicinity of the spheres is displayed in figure B.3.

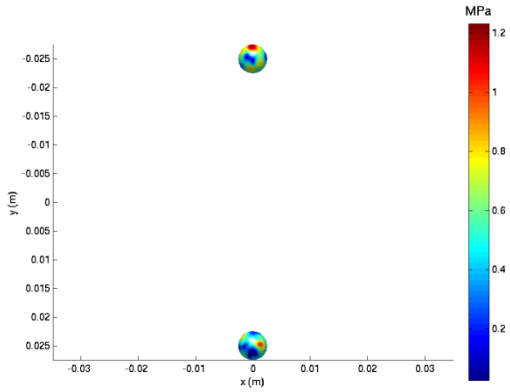

Figure B.2 Acoustic pressure magnitude on the surface of the spheres. Spherical focusing case.

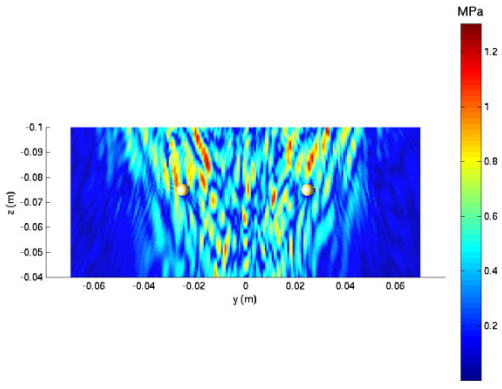

Figure B.3 Acoustic pressure field resulting from the spherical focusing.

B.3 DORT implementation and results

As described in section 5.2.3 the first stage of the DORT method is to obtain the inter-element transfer matrix $[K(\omega)]$. In practice, the array response matrix $[K(\omega)]$ is measured by emitting a pulse on each array element successively and measuring the corresponding echoes from the scatterers on the N transducers. Cochard *et al* (2009) employ a time window to select the back-scattered echo from the ribs, and carry out a Fourier transform of the selected signal at each frequency within the transducer bandwidth. Under continuous wave excitation conditions, $[K(\omega)]$ can be obtained from equation (5.15) by considering that the total pressure $\forall \vec{r} \in V_{\text{ext}}$ is the sum of the incident pressure and the scattered pressure.

$$([Q][H]^{-1}[\beta])\{U\} = \{p_{\text{scattered}}\} \tag{B.1}$$

where $\{p_{\text{scattered}}\}$ is the vector of scattered pressures at positions on the surface of the HIFU array elements. 276 locations on the surface of each element were considered. These were positioned along a regular Cartesian grid on the surface of each element. $\{p_{\text{scattered}}\}$ was then evaluated N = 256 times where all rows of $\{U\}$ were set to zero except for the row corresponding to the source being excited, which was successively set to unity. The scattered pressure was then averaged over the surface of each element, resulting in the $N \times N$ matrix of inter-element transfer functions $[K(\omega)]$.

The singular value decomposition of the array response matrix was then carried out.

$$[K(\omega)] = [V(\omega)][\Lambda(\omega)][W(\omega)]^{*} \tag{B.2}$$

where

- $[V(\omega)]$ and $[W(\omega)]$ are unitary matrices and the columns of $[W(\omega)]$ are the eigenvectors of the TRO.
- $[\Lambda(\omega)]$ is a real diagonal matrix of the singular values.

The singular values are plotted in figure B.4. They correspond the diagonal of the matrix $[\Lambda(\omega)]$. For well-resolved point-like scatterers, the number of significant singular values corresponds to the number of scatterers.

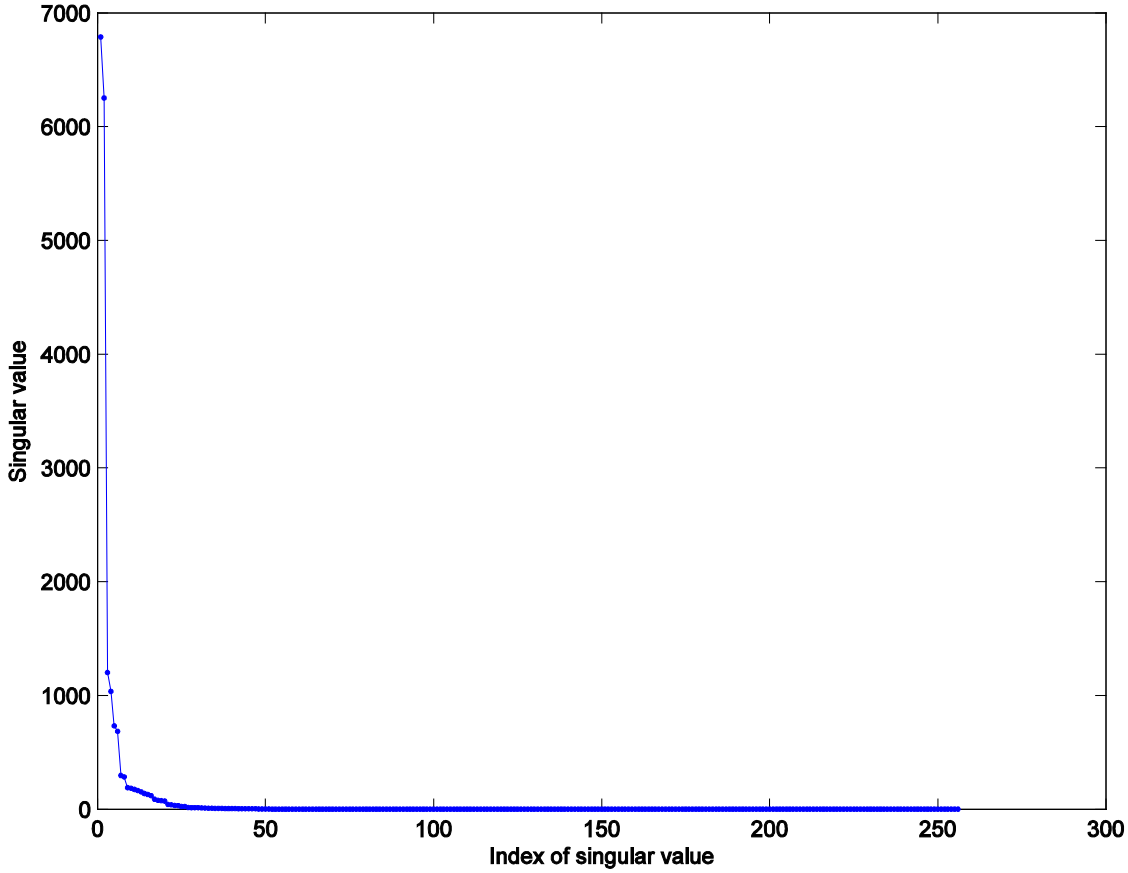

Figure B.4 Singular values of diagonal matrix

The above figure confirms that there are two obvious significant singular values (the first and the second). As the scatterers are not entirely point-like, there are four other singular values which appear to be above the noise floor and may therefore be significant. The first six columns of $[W(\omega)]$ are therefore likely to correspond to focusing vectors which focus on either of the spheres. When using them as input data into the forward BEM model, the plots in figures B.5 to B16 are obtained, confirming that the first six focusing vectors do indeed focus on one or both of the spheres.

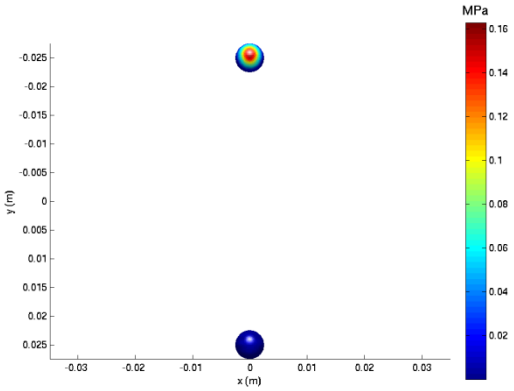

Figure B.5 Acoustic pressure on surface of spheres resulting from the focusing vector obtained from the first column of $[W(\omega)]$. This vector focuses on the least reflective scatterer.

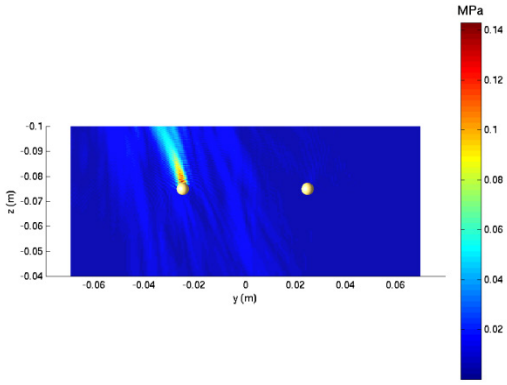

Figure B.6 Acoustic pressure field resulting from the focusing vector obtained from the first column of $[W(\omega)]$. This vector focuses on the least reflective scatterer.

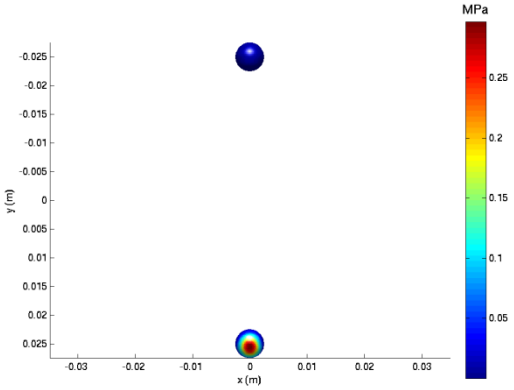

Figure B.7 Acoustic pressure on surface of spheres resulting from the focusing vector obtained from the second column of $[W(\omega)]$. This vector focuses on the most reflective scatterer.

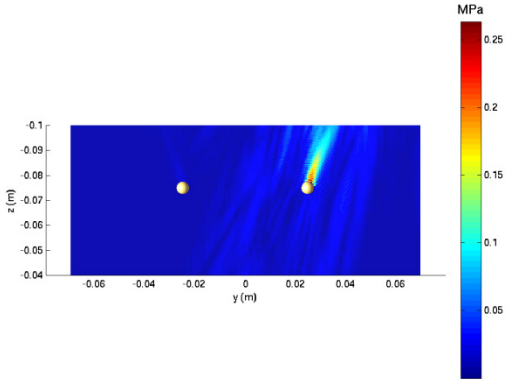

Figure B.8 Acoustic pressure field resulting from the focusing vector obtained from the second column of $[W(\omega)]$. This vector focuses on the most reflective scatterer.

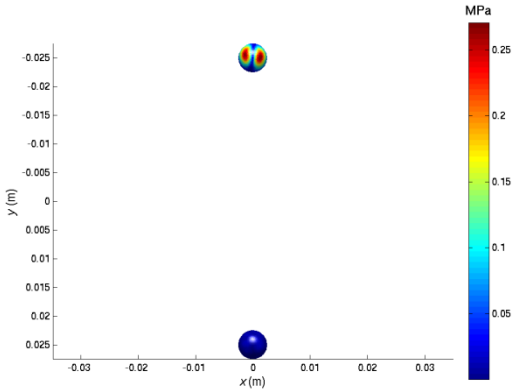

Figure B.9 Acoustic pressure on surface of spheres resulting from the focusing vector obtained from the third column of $[W(\omega)]$.

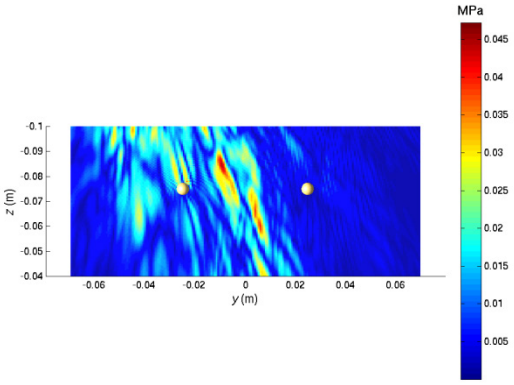

Figure B.10 Acoustic pressure field resulting from the focusing vector obtained from the third column of $[W(\omega)]$.

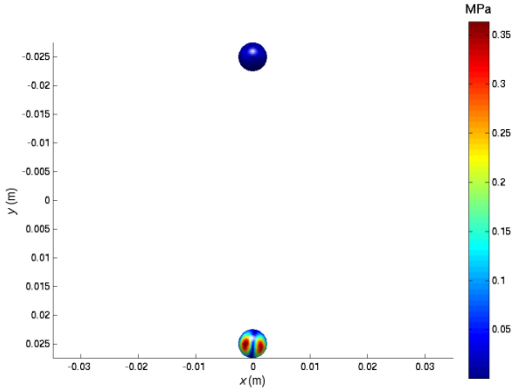

Figure B.11 Acoustic pressure on surface of spheres resulting from the focusing vector obtained from the fourth column of $[W(\omega)]$.

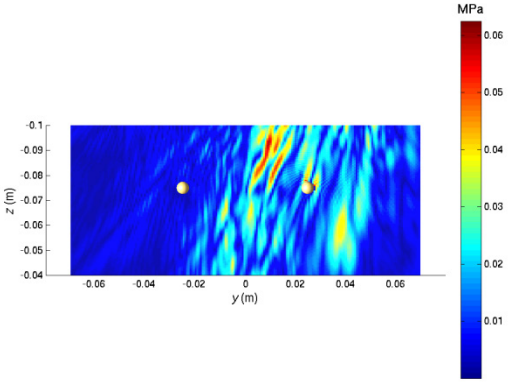

Figure B.12 Acoustic pressure field resulting from the focusing vector obtained from the fourth column of $[W(\omega)]$.

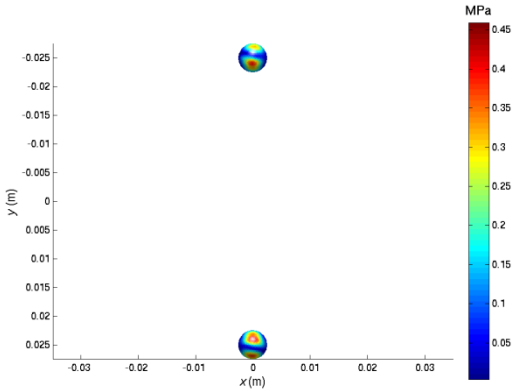

Figure B.13 Acoustic pressure on surface of spheres resulting from the focusing vector obtained from the fifth column of $[W(\omega)]$.

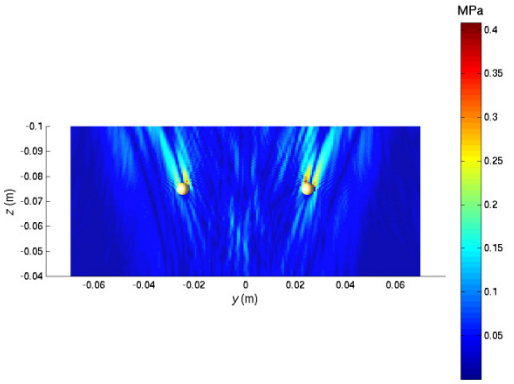

Figure B.14 Acoustic pressure field resulting from the focusing vector obtained from the fifth column of $[W(\omega)]$.

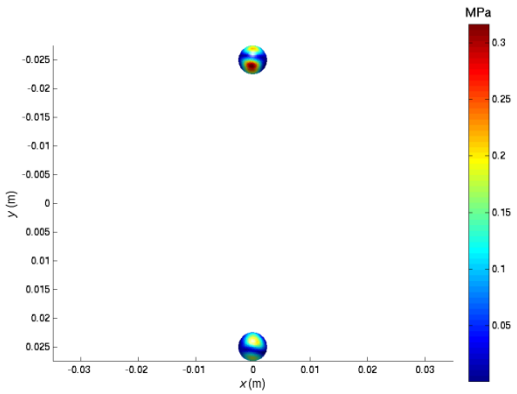

Figure B.15 Acoustic pressure on surface of spheres resulting from the focusing vector obtained from the sixth column of $[W(\omega)]$.

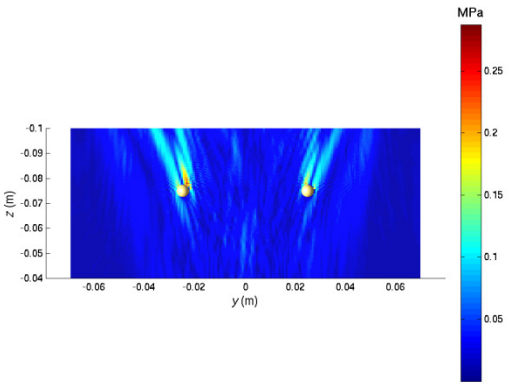

Figure B.16 Acoustic pressure field resulting from the focusing vector obtained from the sixth column of $[W(\omega)]$.

By projecting the focusing vector orthogonally onto the first set of eigenvectors associated with the higher singular values, we have:

$$\{U_{\text{projected}}\} = \{U_{\text{focus}}\} - \sum_{i=1}^{i_{\max}} (\{W_i\}^* \{U_{\text{focus}}\})\, \{W_i\} \tag{B.3}$$

where

- $\{W_i\}$ is the i^{th} column of $[W(\omega)]$
- $i_{\max}$ is the number of eigenvectors associated with the higher singular values (here, $i_{\max} = 6$)
- $\{U_{\text{projected}}\}$ represents the orthogonal projection of the array element normal velocity focusing vector $\{U_{\text{focus}}\}$
- * is the conjugate transpose

$\{U_{\text{focus}}\}$ is chosen as the vector of array element velocities which will focus at the desired location in absence of the scatterers, i.e. the spherical focusing vector for which figures B.2 and B.3 were obtained. The vector $\{U_{\text{projected}}\}$ which removes the effects of focusing onto the scatterers, was computed as described in equation (B.3). The resulting acoustic pressure magnitude on the surface of the spheres is shown in figure B.17. The acoustic pressure magnitude in the *y*-*z* plane in the vicinity of the spheres is displayed in figure B.18.

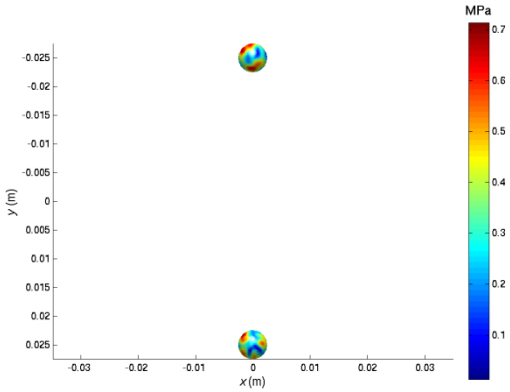

Figure B.17 Acoustic pressure magnitude on the surface of the spheres. DORT method.

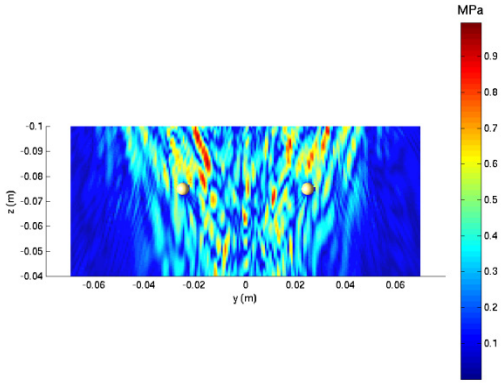

Figure B.18 Acoustic pressure field resulting from the DORT method.

By applying the projected vector resulting from the DORT method, the maximum acoustic pressure magnitude on the surface of the sphere is reduced from 1.2 MPa to 0.7 MPa compared with the spherical focusing case. Furthermore, there is a qualitative reduction in the backscattered signal in figure B.10 compared with figure B.3 (both figures have been plotted on the same colour bar scale).

The acoustic pressure magnitude in the vicinity focus is displayed in the *y*-*z* plane for the spherical focusing case and for the projected vector using the DORT method in figures B.11 and B.12, respectively.

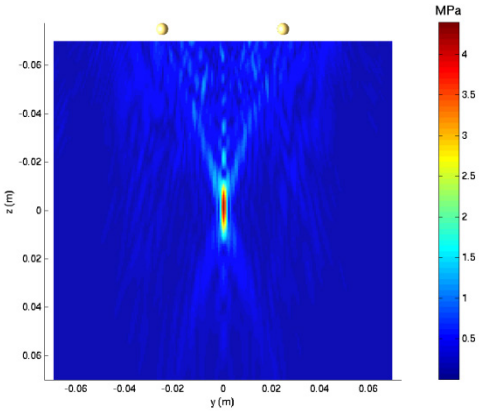

Figure B.19 Acoustic pressure field in the vicinity of the focus resulting from the spherical focusing.

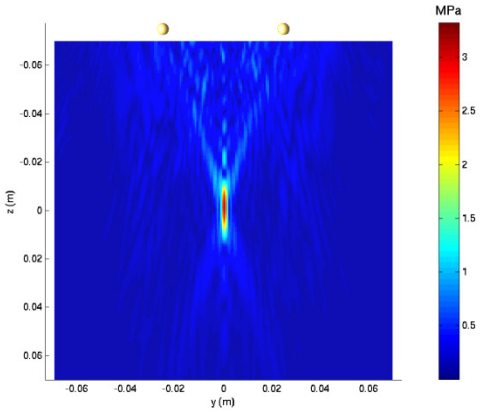

Figure B.20 Acoustic pressure field in the vicinity of the focus resulting from the application of the DORT method.

The SAR gain increases from approximately 13 dB for spherical focusing to 15 dB for the DORT method on the least reflective scatterer and from 15 dB to 18 dB on the most reflective scatterer.

B.4 Discussion

Figures B.2 and B.9 demonstrate that the acoustic pressure on the surface of the spheres displays some spatial variation. Furthermore, the location of the pressure maximum on each sphere for the spherical focusing case does not correspond with that in figures B.5 and B.7. The chosen diameter of the spheres compared with the wavelength in the exterior domain is perhaps too large for the scatterers to be considered point-like, in this case. The DORT method nevertheless delivers a 2 dB and 3 dB increase in SAR gain for the least reflective and most reflective scatterer, respectively. Using BEM as a forward model offers an opportunity to test the limit of validity of the DORT method so as to assess its range of applications in an experimental context.

Appendix C

Cost Function, Constraints and Gradients used in the Constrained Optimisation

C.1 Cost function

The cost function F is a function of $2N$ real variables (elements of the vector $\{\widehat{U}\}$), which returns a real scalar. It is defined as follows.

$$F(\{\widehat{U}\}) = \left\|[\hat{C}]\{\widehat{U}\} - \{\hat{p}\}\right\|^2 \tag{C.1}$$

or

$$F(\widehat{U}_1, \widehat{U}_2, \cdots, \widehat{U}_{2N}) = \sum_{i=1}^{2M'}\left(\sum_{j=1}^{2N} \hat{C}_{i,j}\widehat{U}_j - \hat{p}_i\right)^2 \tag{C.2}$$

C.2 Constraints

The constraints, denoted as c, are nonlinear and are require to be input in the format:

$$c_i \leq 0 \tag{C.3}$$

Equation (8) is rewritten as follows.

$$\begin{bmatrix} Re([A]) & -Im([A]) \\ Im([A]) & Re([A]) \end{bmatrix}\begin{Bmatrix} Re(\{U\}) \\ Im(\{U\}) \end{Bmatrix} = \begin{Bmatrix} Re(\{p_{surf}\}) \\ Im(\{p_{surf}\}) \end{Bmatrix} \tag{C.4}$$

or

$$[\hat{A}]\{\hat{U}\} = \{\hat{p}_{\text{surf}}\} \tag{C.5}$$

The i^{th} row and the j^{th} columns of Re([A]) and Im([A]) are defined as $A_{R\ i,j}$ and $A_{I\ i,j}$, respectively. Similarly, let the j^{th} row of Re({U}) and Im({U}) be defined as $U_{R\ i,j}$ and $U_{I\ i,j}$, respectively.

For all M nodes on the surface S, we require the acoustic pressure magnitude to be less than a specified threshold $p_{\text{surf}_{\max}}$. There are therefore M constraints associated with this condition. These can be expressed as follows.

For $i \leq M$

$$c_i = \left(\sum_{j=1}^{N} A_{R\ i,j} U_{R\ j} - \sum_{j=1}^{N} A_{I\ i,j} U_{I\ j}\right)^2 + \left(\sum_{j=1}^{N} A_{I\ i,j} U_{R\ j} + \sum_{j=1}^{N} A_{R\ i,j} U_{I\ j}\right)^2 - p^2_{\text{surf}_{\max}} \tag{C.6}$$

In practice, numerical instability may arise if M is too large. In some cases, a subset of the nodes on S may have to be chosen.

In addition, the source velocity magnitudes cannot be greater than the maximum amplitude $U_{\max}$ allowed by the dynamic range. This is equivalent to adding the N further constraints.

For $M < i \leq M + N$

$$c_i = U^2_{R\ i-M} + U^2_{I\ i-M} - U^2_{\max} \tag{C.7}$$

C.3 Gradient of cost function

The gradient of the cost function with respect to its input variables may be expressed as follows.

For $1 \leq k \leq 2$N,

$$\frac{\partial F}{\partial \hat{U}_k} = 2\sum_{i=1}^{2M'} \hat{C}_{i,k} \sum_{j=1}^{2N} \left(\hat{C}_{i,j}\hat{U}_j - \hat{p}_i\right) \tag{C.8}$$

C.4 Gradient of constraints

The gradient of the constraints with respect to the input variables forms a $2N$ by $M+N$ Jacobian matrix ($2N$ variables and $M + N$ constraints). Its elements are as follows.

For $k \le N$ and $i \le M$,

$$\frac{\partial c_i}{\partial \hat{U}_k} = 2A_{R\,i,k}\left(\sum_{j=1}^{N} A_{R\,i,j}U_{R\,j} - \sum_{j=1}^{N} A_{I\,i,j}U_{I\,j}\right) + 2A_{I\,i,k}\left(\sum_{j=1}^{N} A_{I\,i,j}U_{R\,j} + \sum_{j=1}^{N} A_{R\,i,j}U_{I\,j}\right) \tag{C.9}$$

For $k > N$ and $i \le M$,

$$\frac{\partial c_i}{\partial \hat{U}_k} = -2A_{I\,i,k-N}\left(\sum_{j=1}^{N} A_{R\,i,j}U_{R\,j} - \sum_{j=1}^{N} A_{I\,i,j}U_{I\,j}\right) + 2A_{R\,i,k-N}\left(\sum_{j=1}^{N} A_{I\,i,j}U_{R\,j} + \sum_{j=1}^{N} A_{R\,i,j}U_{I\,j}\right) \tag{C.10}$$

For $k \le N$ and $i > M$,

$$\frac{\partial c_i}{\partial \hat{U}_k} = 2U_{R\,k} \qquad \text{if } i = k + M \tag{C.11}$$

$$\frac{\partial c_i}{\partial \hat{U}_k} = 0 \qquad \text{if } i \ne k + M \tag{C.12}$$

For $k > N$ and $i > M$,

$$\frac{\partial c_i}{\partial \hat{U}_k} = 2U_{I\,k-M} \qquad \text{if } i = k + M - N \tag{C.13}$$

$$\frac{\partial c_i}{\partial \hat{U}_k} = 0 \qquad \text{if } i \ne k + M - N \tag{C.14}$$

Appendix D

Journal Paper Reprints

Appendix E

Programme Code